ECOLOGICAL CONDITIONS LEADING TO THE SWEEP OF ANTIBIOTIC RESISTANCE GENES IN THE MODEL-TYPE BACTERIUM *Escherichia coli*

Submitted by

Rafael Carlos Reding Román

to the University of Exeter as a thesis for the degree of

Doctor of Philosophy in Biological Sciences

September 14, 2015

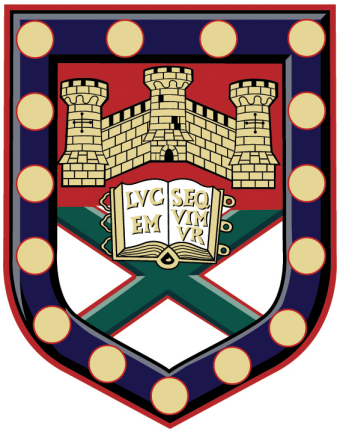

‘When you are studying any matter, or considering any philosophy, ask yourself *only* what are the facts. What is the truth that the facts bear out. Never let yourself be diverted either by what you wish to believe, or by what you think would have beneficient social effects if it were believed; but look only and solely at what are the facts.’

—Bertrand Russell. BBC interview on *Face to Face* (1959).

Summary. In antibiotic therapy design, conventional wisdom holds that higher antibiotic dosages always leads to the observation of fewer bacterial cells, resulting in a monotonic decay in cell number as a function of increasing antibiotic dose; accordingly, throughout this thesis, we will call this phenomenon a monotone dose-response profile. When we analysed the evolution of antibiotic resistance mediated by the multi-drug efflux pump AcrAB-TolC in *Escherichia coli* to study if such a monotone dose-response is maintained at all times, our analysis showed that higher dosages can, in fact, lead to higher bacterial loads. This is because selection for drug resistance is mediated by the duplication of the genes, AcrAB-TolC, that encode the aforementioned efflux pump. As explained in detail below, our work highlights the idea that Darwinian selection on additional copies of AcrAB-TolC is a non-linear function of antibiotic dose and that the observed transition from monotone to non-monotone dose-response is a consequence of AcrAB-TolC being strongly selected at very specific dosages. We term this phenomenon an 'evolutionary hotspot'.

Next, we extended the above experimental system to solid media to study how selection on resistance mediated by AcrAB-TolC leads to a 'spatio-genomic patterning' effect that we call a 'bullseye'. Using a bespoke culture device developed as part of this PhD, we show that spatial selection on resistance also depends non-linearly on the distance of the cell from an antibiotic source, and that the non-linearity can be multi-modal as a function of distance, and therefore also of antibiotic dose. This result also contradicts the aforementioned principle that higher antibiotic dosages necessarily lead to fewer bacterial cells.

Following on from this, we then studied the ability of microbial competitors for resources to modulate the antibiotic sensitivity of a particular strain of *E. coli*, namely Tet^s, using a range of multi-species experiments. We measured the sensitivity to antibiotics of Tet^s both with, and without, one bacterial or fungal competitor. When that competitor was equally sensitive to the antibiotic, we observed that Tet^s was less sensitive to it, in part due to an 'antibiotic sinking' effect carried out by the competitor strain. However, when the competitor was not sensitive to the antibiotic, Tet^s was, accordingly, more sensitive than in the absence of competition. In this latter case, the competitor seemed to reduce the growth of Tet^s by carbon theft as part of a phenomenon known as 'competitive suppression'. Moreover, this ecological effect is one that synergises with the action of the antibiotic.

Finally, we turned to a study of an ecological trade-off motivated by ribosome-binding antibiotics. So, by manipulating the content of ribosomal RNA in the *E. coli* cell, a large and essential molecule that is bound by antibiotics such as tetracycline or erythromycin, we could

subsequently manipulate what is known as a metabolic trade-off between growth rate and growth yield. The latter is the number of cells produced per molecule of carbon found in the extracellular environment of the bacterial population. Using glucose as carbon source we therefore constructed an empirical fitness landscape that shows how the optimum number of ribosomal rRNA operons depends on extracellular glucose concentration. Whilst this study does not relate directly to the presence of an antibiotic, it does show that by altering the number of operons in a manner that is known to affect antibiotic susceptibility, we can also mediate important growth parameters like cell yield, aka efficiency, and growth rate.

ACKNOWLEDGEMENTS

I never thought that the act of listening to a piece of advice would be such a difficult task. As expected this PhD was a challenge from day one, but what a truly gratifying challenge it was. I did not expect to enjoy it the way that I have. I cannot thank enough my supervisor, Rob Beardmore, for being so patient. 'Keep your eyes opened', 'Numbers don't lie', were just 2 of many cold and logic phrases/ways that I, as a biologist, found the most difficult yet useful to look at, think about and "do" things.

Exeter University introduced me to some supportive colleagues and friends especially those from Rob and Ivana Gudelj's groups. Francesca and Ayari taught me to be very strict with myself whilst "doing" science rather than act like a nutty scientist. Jess taught be that science is a debate and I have to be ready for it. Magdalena, Marta, Jérémie and everyone in the lab 309 who helped me to design the qPCR.

Ivana and her group were incredibly helpful with the brainstorming and problem-solving sessions/feedback during our joined lab meetings. I am very grateful to this group and Rob's group, where I learned how to communicate my work and deliver an understandable presentation. I have really enjoyed our meetings in the office and of course in the pub!

A special, and big thank you to Remy Chait, Tobias Bollenbach and Stuart Levy for providing me with the cool strains that I've used during the PhD, and to Emily Cook for helping us with the fungal pathogenic strains.

To my mum, my grandparents and my family all of which fed my passion for science with every single book/smart phone(!) they had in their hands, even if they didn't understand it, they helped to develop my *weirdness*. And finally to my "Miss Sunshine",

who took my hand and lit the path during the darkest moments of my journey, in a foreign country, and made the big problems small. Caroline, without your love, support and sacrifice this thesis would not exist.

PUBLICATIONS

- A. Fuentes–Hernandez, J. Plucain, F. Gori, R. Peña–Miller, C. Reding, G. Jansen, H. Schulenberg, I. Gudelj, and R. Beardmore. Using a Sequential Regimen to Eliminate Bacteria at Sub-Lethal Antibiotic Dosages. *PLoS Biol.* **13**(4), e1002104 (2015).
- R. Peña–Miller, A. Fuentes–Hernandez, C. Reding, I. Gudelj and R. Beardmore. Testing the optimality properties of a dual antibiotic treatment in a two-locus, two-allele model. *J. R. Soc. Interface*, **11**, 20131035 (2014).

CONTENTS

NOMENCLATURE

AST	Antibiotic Sensitivity Test.
CA	Casamino acids.
CFU	Colony Forming Unit.
Dox	Doxycycline.
Ery	Erythromycin.
Glc	Glucose.
IC$_n$	Inhibitory Concentration for n% of the culture.
LB	Lysogeny Broth.
M9	Minimal Media 9.
MIC$_k$	Minimum Inhibitory Concentration for strain k.
MSC	Minimum Selective Concentration.
MSW	Mutant Selection Window.
RPM	Rotations Per Minute.
Tet	Tetracycline.
WGS	Whole Genome Sequencing.
WHO	World Health Organization.

LIST OF FIGURES

LIST OF TABLES

I INTRODUCTION

"[resistance] is a purely chemical question which can only be solved by chemical means."
—Paul Ehrlich,[1] considered father of chemotherapy.

ANTIBIOTICS heralded a new era in the treatment of bacterial infections in which deadly infections, such as bacterial meningitis, could be cured. The discovery of the β-lactam penicillin and subsequently of other antibiotics defined the so-called *golden age* of antibiotic discovery,[2] when the drugs were classified in different classes (i.e. *tetracyclines* or *macrolides*) based on their biochemical properties. The ability of bacteria to become resistant to toxic substances, such as antibiotics, was well known since the early twentieth century,[3] but the variety of these drugs led "society and the scientific community to become complacent about the potential of bacterial resistance".[4] Such are the dimensions of resistance today that, during 2014, the World Health Organization (WHO) published a report stressing that resistance to commonly used antimicrobials is both widespread and, to quote the report directly, "few if any antimicrobial options are available".[5] The same report also highlights the "virtually empty pipeline for the development of new antibacterial drugs". Whilst the efforts to discover new antibiotics are of course an essential effort, perhaps it led us to overlook what has been termed "insufficient information about the conditions and factors that can lead to the mobilisation, selection and movement of these [resistant] bacteria".[6]

This was already asked in the 1950s. When doctors started to quantify antibiotic resistance in the clinic, feared that "if the supply [of antibiotics] should cease (...) the time may come when a few of the more enterprising [bacterial] species will flourish more or less unhindered".[7] An editorial note in the *British Medical Journal* then asked

about the conditions in which resistance was acquired.[8] Thus, very little progress has been made ever since. The small molecule antibiotic itself, in particular the discovery of new ones, will play an essential part of the ongoing fight in the antimicrobial crisis, but the clinical deployment of those molecules is an equally important part of the problem and we contend that this represents an under-studied set of scientific questions.

Therefore, in response, this thesis presents a theoretical and empirical study of such conditions, motivated by clinical treatments, and asks, exactly, what are the conditions that lead to the most rapid onset of bacterial resistance to antibiotics? A number of metabolic and physiological questions are addressed as a direct result of the questions we ask about antibiotics. More immediately, in this chapter, we will introduce a number of fundamental problems associated with antibiotic therapy design that we would like to resolve.

1.1 Antibiotic resistance (I): quantified within 24h, treated for weeks

Antibacterial drugs are, by definition, toxic to bacterial-type microorganisms. Antibiotic therapy design is based on a principle, assumed to be true for more than a century, whereby higher dosages of a drug necessarily lead to fewer observed bacterial cells in the presence of that drug.[9–12] Now, in practise, antibiotic sensitivity tests (ASTs) quantify the precise dosage *in vitro* prior to use in the clinic. In these standardised tests media, growth conditions and incubation times are clearcut, defined and, by now, almost seen by the community as immutable.[11] However, I contend that there is potential for a fundamental flaw in the relationship between ASTs and clinical therapies and it is this: the incubation time of ASTs is typically 24h, whilst therapies last substantially longer in the clinic.[13,14] Whether or not the sensitivity quantified by ASTs is maintained for longer incubation times has been experimentally demonstrated many times over in the field. However, this understanding has not been translated into improved clinical treatments. Whilst the latter is well beyond the purpose of this thesis, I will aim to show that prolonged treatments, beyond 24h, do lead to increases in resistance in a consistent, and even possibly, *a prior* predictable, manner.

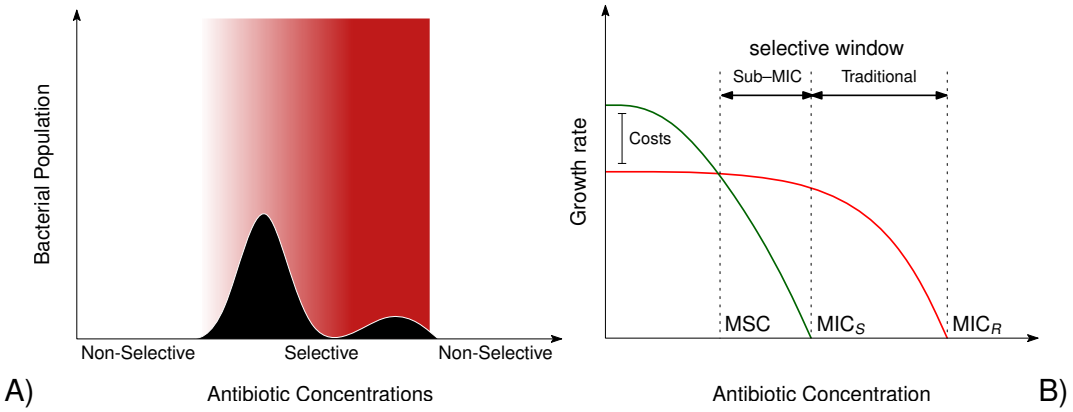

FIGURE 1.1. A) 'Mutant Selection Window' (MSW) model, adapted from REFERENCE 17. The black bars represent bacterial density in number of cells or strains. The selective gradient, as a function of antibiotic concentration, is represented in red. Below or above this window there is no selection on resistance. **B)** Sub-inhibitory selective window model. Growth rates of a sensitive (S, in green) and a resistant populations (R, in red) as a function of antibiotic dose. Assuming the existence of costs of resistance, here represented as the difference in growth rate in the absence of antibiotic, the minimum selective concentration (MSC) is defined as the concentration of antibiotic at which S and R have identical growth rates, and thus selection on R begins. Note that this selection takes places below the minimum inhibitory concentration of the wild-type strain (MIC$_S$). Adapted from REFERENCE 19.

1.2 SELECTION ON RESISTANCE IS PROPORTIONAL TO ANTIBIOTIC DOSE

Resistance to antibiotics is caused by transmissible genetic elements but also spontaneous chromosomal mutations.[15,16] But it is important to know at which drug dosages these genes are most selected for. This question has been studied and the outcome of those studies has concluded that the concept of a 'selection window' in which resistant mutants are strongly selected within a narrow range of concentrations of antibiotic resolves this question.[17] However, where this window, if it does indeed exist, resides remains a matter of some discussion in the field due to what could be said to be poorly supported criteria whereby the boundaries of the selective window are defined (FIG. 1.1).[17–19] In this thesis we therefore use a specific model system to address the question of where these windows can indeed be found.

But what does 'strongly' mean in terms of selection? The strength of selection can be objectively measured and quantified with the *selection coefficient*. In population genetics theory, selection "applies to the organism as a whole"[20] and therefore the selection coefficient is considered to be a "complicated function of the entire system of gene frequencies and can only be dealt with qualitatively".[20] Thus, the simplest case of study of selection in population genetics has typically been that of one gene with a

constant selection coefficient.[20–24] This concept has been applied to study antibiotic resistance in the clinic, and the strength of selection on resistance is considered to be proportional to antibiotic dose.[25–27] In this thesis, our data leads to a different conclusion, namely one whereby selection on specific resistance genes can be shown to vary in a nonlinear and, indeed, non-monotone fashion with respect to antibiotic dose. We will find hotspots and coldspots in the spectrum of dosages where selection is maximised and minimised, respectively.

1.3 Antibiotic resistance (II): tested on a specific strain, used against bacterial communities

A second likely flaw in the relationship between antibiotic sensitivity tests (ASTs) and their utility in terms of predicting the outcome of clinical therapies in hospital patients may stem from a fundamental property of microbial ecologies. These tests always, by design, quantify the sensitivity to antibiotics of a single, isolated strain of bacterium. Yet, in the clinic, antibiotics are not only deployed to target this particular strain, but they also target commensal microbes and the entire gamut of species that constitute the patient's microflora. Moreover, some infections can be polyclonal and, indeed, polymicrobial.[28–30]

Although therapies designed using isolated strains have been said some time ago to provoke a minimum disturbance on the microflora,[31] these microbes necessarily set the context for competition for resources with the bacteria being targeted. Whether or not the competition modifies the sensitivity to antibiotics of the targeted strain, previously quantified on isolation, is poorly understood.

Competition, and indeed cooperation, of the targeted species with other microbial species represents just one aspect of the ASTs that departs from the reality of a pathogen's lifestyle, but there are others. In particular, the immune system of a healthy host is known to play a large part in the success, and failure, of antibiotic treatments, but immunity plays almost no role in this thesis. This is not because it lacks importance, rather, it is a highly relevant part of the entire problem, however we have endeavoured to keep this work centred on a body of tractable experimental *in vitro* systems which has precluded the use of animal models.

1.4 In mixed populations, fast dividing cells outcompete slow dividing cells

The effect of antibiotics on bacteria is often measured as the reduction in bacterial *fitness*,[32] which is defined in terms of generation times (*per capita* growth rate).[19,32–35] Therefore, fitter types of bacteria divide quicker than less fit types. In the case of mixed populations of bacteria it has been proposed that, if mutations providing resistance to antibiotics have a cost associated so that resistant cells are less *fit*, sensitive stains of bacteria may outcompete resistant populations, less fit, when the use of antibiotics is interrupted.[36]

But slow dividing cells can also surpass fast dividing cells. Stemming from certain thermodynamic constraints,[37,38] it has been proposed that high growth rates are not compatible with simultaneous high growth yields (biomass produced per molecule of carbon source) and, hence, there must be a metabolic trade-off between rate and yield.[38] Under such circumstances, assuming the constant supply of resources, slow dividing but efficient cells can, in fact, outcompete fast dividing but inefficient cells.[38]

Now, bacterial growth rate is coupled to the cell's capacity to synthesise proteins,[39] and this capacity depends on the concentration of ribosomes within the cell.[40] So whilst the use of ribosome-binding antibiotics is expected to reduce bacterial fitness, and therefore the growth rate,[41] it is important to ask if the addition of such antibiotics leads to slow dividing, yet **more efficient**, resistant bacterial cells. This could be described as the potential for resistant cells to exploit an inevitable trade-off in growth. Empirical datasets supporting the aforementioned trade-off are scarce[42] meaning predictions based on these trade-offs, in terms of how antibiotic-resistant cells might outcompete drug sensitive cells, are very limited. We therefore sought to address this.

1.5 Questions and thesis outline

Using the bacterium *Escherichia coli* as a living model we answered a wide range of questions that can be summarised as follow.

First, we explored whether the previously introduced principle whereby high dosages always lead to low cell densities holds at all times during antibiotic treatment. *E. coli* is known to possess an operon (*acr*) that encodes a pump with which the bacterium is able to efflux a wide range of molecules, including antibiotics, from the cytoplasm of

the cell into extracellular space, thus providing a generic resistance mechanism on this operon. There are other mechanisms, more antibiotic-specific, that provide resistance through random changes in the genome or *mutations*. These mutations may affect, by chance, the molecule targetted by the antibiotic, or metabolic enzymes that can modify the antibiotic molecule.[43] Once these mutations occur *de novo*, they can be transmitted and acquired through vectors such as plasmids,[44] helping to spread resistance more rapidly. However, due to its unusually broad specificity,[45] we explored how selection on resistance provided by the aforementioned operon is mediated by the dosage of the ribosome-binding drug, erythromycin, supplied to the environment in which *E. coli* is cultured.

We then looked into how selection on resistance is mediated by the presence of a competitor microbial strain in the culture. Motivated by this question, we used a range of multi-species experiments, including fungal microbial species that are known to co-infect humans. We also sought to tackle the problem of determining the profile of selection as a function of antibiotic dose using strains of *E. coli* which harbour a plasmid that encodes the tetracycline resistance gene *tet36*. This gene provides ribosomal protection against the tetracycline class of antibiotics so we explored whether, or not, there is a minimal antibiotic dose at which selection on this plasmid begins.

Penultimately, we partially extended the first study (i.e. the one on *acr* selection) to a spatially-extended context to understand spatial patterning effects of the *acr* operon. For this we employed mathematical modelling, and used a bespoke spatial culture device that was constructed as part of this PhD project.

Finally, we were interested in how the number, or concentration, of targets within the cell of important antibiotics like erythromycin and tetracycline mediate key phenotypes like growth rate and cell efficiency (per supplied molecule of carbon). Whilst this does not relate directly to the presence of an antibiotic, we analysed whether by altering the number of operons in a manner that is known to affect antibiotic susceptibility, we could also mediate important growth parameters like cell efficiency and growth rate.

II EVOLVING AN ERYTHROMYCIN-SENSITIVE BACTERIUM TO DETERMINE SELECTION ON RESISTANCE BY ANTIBIOTIC EFFLUX: NONLINEAR SELECTION ON ACRB

ANOMALOUS DRUG activity, also known in the literature as a *paradoxical effect*, is a phenomenon whereby higher doses of antibiotic do not necessarily yield higher bactericidal, or indeed bacteriostatic, effects of that drug.[10,46–48] In other words, an inhibitor is not an inhibitor at all doses, but it can even appear to be a stimulant of vegetative growth. This phenomenon, observed many decades ago after short (in all likelihood, non-evolutionary) periods of 16 to 24h of exposure to antibiotics, has been known since the 1940s but still remains poorly understood.[49] In this chapter we will demonstrate that a similar 'paradox' can be produced through selection for a 'genomically scalable' multi-drug efflux pump system, AcrAB-TolC, caused by genome duplication events.

Previously this was deemed to be a paradox in the cited references and the so-called 'Eagle effect' is one observation that fits this particular description. From a more modern and evolutionary perspective, we will show that a paradox whereby greater drug doses also produce higher population densities of a bacterium can be the result of differential selection for a drug resistance mechanism. Such differential selection can, as we will demonstrate, lead to a strong non-linear and, more importantly, non-monotone relationship between selection on a resistance mechanism and the drug

dose applied to the microbial population under study.

The purpose of this chapter is to provide the data supporting the existence of such a non-monotone relationship. We will demonstrate that selection on resistance, in this case by antibiotic efflux, is subsequently maximised in a 'mid-dose region'. The latter term will be explained in the remainder of this chapter.

Determining the drug dosing regions where selection for a resistance mechanism is maximised is a key problem in the field of antibiotic pharmacology. As we discussed in the introductory chapter various different theories have been postulated for this, with a variety of empirical datasets put forward to support each view.[17–19] With the *minimum inhibitory concentration* of the wild-type (MIC) as the central parameter, these theories are mutually exclusive: one establishes that selection on resistance begins at concentrations above the MIC,[17,18] whereas for the other theory it begins at concentrations below the MIC.[19]

It is essential to determine which concentration maximises selection on resistance and to determine selection on resistance in a precise way, we used a simple experimental model based on *Escherichia coli*'s multi-drug efflux pump AcrAB-TolC. We now describe some of the features of this pump system.

2.1 Description of the multi-drug efflux pump AcrB-TolC and its regulation

The role played by efflux pumps in clinical multi-drug resistance (MDR) has been reconsidered in recent years.[50,51] In the bacterium *Escherichia coli* there is, perhaps, one of the best-described such pumps, the AcrAB-TolC efflux pump system (Fig. 2.1). Its components are encoded by an different operons, *acr*, and *tolC*. The products of these genes interact with each other to assemble the multi-drug efflux pump that connects the bacterial cytoplasm with extracellular space, as shown in Fig. 2.1.[45,52] With a proton-powered, rotational mechanism, this pump is able to collect antibiotics as well as a broad range of small molecule substrates from within the periplasm and translocate them to the outside of the cell. The specificity of this pump is known to be 'unusually broad'[45] and is believed that these pumps not only provide MDR but also a fitness advantage in their natural environments.[53]

The complex, regulatory architecture of this efflux system has been determined to

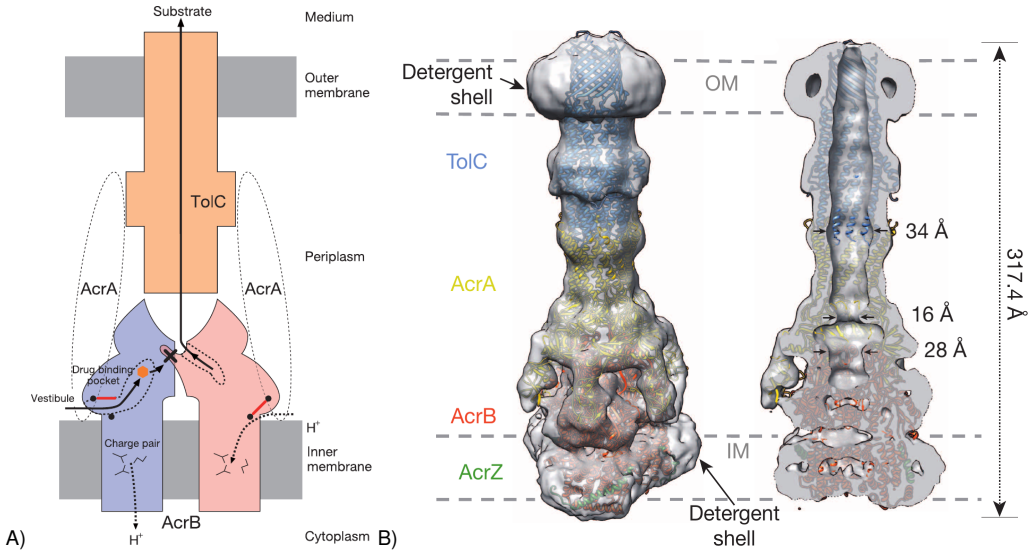

FIGURE 2.1. A) The proposed transport mechanism and (b) estimated structure of the multi-drug efflux pump AcrAB-TolC taken from REFERENCES 54 in the case of A) and 52 in the case of **B)**. The pump rests on a structure formed by proteins AcrB and AcrZ in the inner membrane, opening out to the cytoplasm. In the outer membrane lies TolC that forms a pore opened to the extracellular environment. AcrA connects both in the periplasm, and forms a vestibule in the periplasm with AcrB. The drug binding pocket is hidden in the vestibule. The drug is captured and ejected to the environment powered by protons (H^+) from the periplasm. Note that further studies of this pump[52] established the cytoplasmic section of AcrB as a completely different component, AcrZ that is also produced by the *acr* operon.

some extent, where a role is played by several genes within the *mar* regulon which mediate MDR levels via expression of the *acr* operon. From a literature search, we constructed just a part of the regulatory network of the *acr* operon, as shown in FIG. 2.2 in order to provide background to the complex dynamics of Acr protein expression that are likely following antibiotic challenge to the bacterial cell.

Using an even larger model of this regulatory network, we could also attempt to link metabolic processes, such as the response to nutrient limitation, oxidative stress molecules, or population densities to the expression level of the *acr* operon. We presented FIG. 2.2 only to illustrate the fact that it is not even clear whether, for example, *acr* expression is positively correlated with antibiotic dose. Nevertheless, we remark that in the absence of antibiotics and due to the accumulation of stress signals in the cell, this efflux pump system can be up-regulated to play a key role in 'detoxifying' the cell from hazardous metabolic byproducts, and down-regulated when such byproducts are absent.

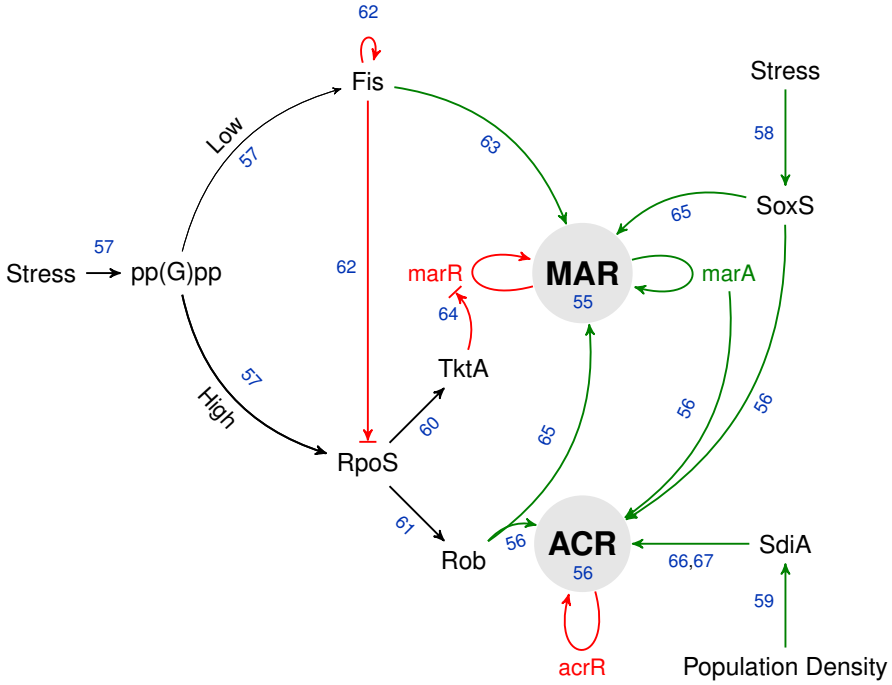

FIGURE 2.2. Partial regulatory network of the operons *mar* and *acr* composed through a reverse-literature research during this project (i.e. if *acr* is regulated by *rob*, what regulates *rob*?). There are at least three main signals for the *acr* operon. First is guanosine tetraphosphate (ppGpp), a small nucleotide 'alarmone' that acts as a global gene expression regulator in *E. coli*.[57] This signal is produced upon nutrient limitation and its accumulation leads to the down-regulation of basic processes such as DNA replication, and the up-regulation of processes such as glycolysis, oxidative stress and osmotic stress response.[57] Second is the response to oxidative stress specifically mediated by the *sox* operon. This operon is able to sense reactive oxygen species, known mutagenic byproducts of metabolism and activate a series of downstream genes to remove such mutagenic byproducts.[58] The third signal depends on population density, or a *quorum sensing* mechanism, mediated by *sdiA*. This gene is involved in the density-dependant regulation of cell division.[67]

2.2 QUANTIFYING THE DEGREE OF RESISTANCE PROVIDED BY THE ACRAB-TOLC EFFLUX PUMP SYSTEM

To determine the role of the AcrAB-TolC efflux pump system in multi-drug resistance, in *E. coli*, we used a number of strains with a modified AcrAB-TolC efflux pump (TABLE 2.1). Our wild-type strain here is one denoted AG100, a K-12 strain of *E. coli*. This strain was modified with the transposable element *Tn909* to interrupt the sequence of the genes *acrA* and *acrB* within the *acr* operon. Thus, this derivative strain, namely AG100-A, produces nonfunctional versions of the proteins AcrA and AcrB, which are two key components of the AcrAB-TolC efflux pump system. In order to measure the relative abundance of AcrAB-TolC within the cell exposed to different antibiotic

TABLE 2.1. Strains of *Escherichia coli* used to perform the experiments described in this chapter. The strain TB108 was kindly provided by Dr. Tobias Bergmiller.

Strain	***Genotype***	***Reference***
E. coli AG100	K-12 *argE3 thi-1 rpsL xyl mtl* Δ*(gal-uvrB) supE44*	68
E. coli AG100-A	AG100 Δ*acrAB::Tn903*	68
E. coli TB108	MG1655 *acrB-sfGFP-FRT*	Unpublished
E. coli eTB108	MG1655 *acrB-sfGFP-FRT* ± ***?***	This thesis

environments we used derivatives of a K-12 strain that we denote TB108.

The latter is derived from another K-12 type strain, this time MG1655, and in TB108 the original *acrB* is replaced with a copy of *acrB* which has been tagged (physically fused) with sfGFP (the superfolder green fluorescent protein), inserted downstream and in-frame. The result is a fully functional, although partially 'damaged', efflux protein AcrB with sfGFP attached in the cytoplasmic c-terminal end. By measuring the fluorescence produced by sfGFP, we will be able to measure the relative abundance of the AcrAB-TolC efflux pump system as a function of time and antibiotic dose. By doing so we can determine the strength of selection for this efflux system at different doses.

In order to quantify the loss of efflux efficacy due to the GFP construct imposed upon the cell relative to the wild-type strains, we measured the resistance to the macrolide erythromycin using the broth dilution method in 96-well microtiter plates, as shown in FIG. 2.3. The strain AG100 displayed the highest MIC for this protein synthesis-inhibiting drug, followed by TB108 and then AG100-A. This latter strain showed the lowest MIC, thus demonstrating that the lack of a functional AcrAB-TolC efflux pump system leads to an increased sensitivity to erythromycin. However, strain TB108 showed a phenotype that rests between the strain AG100 and that with the nonfunctional copy of *acrAB*, AG100-A. In order to verify that sfGFP was physically interfering with the function of AcrB, and to repair this if possible, we evolved this strain in the presence of 10µg/mL of erythromycin for seven days (experimental details are given below within this chapter). Our working hypothesis for this procedure was that sub-populations with a lower physical interference between these two components

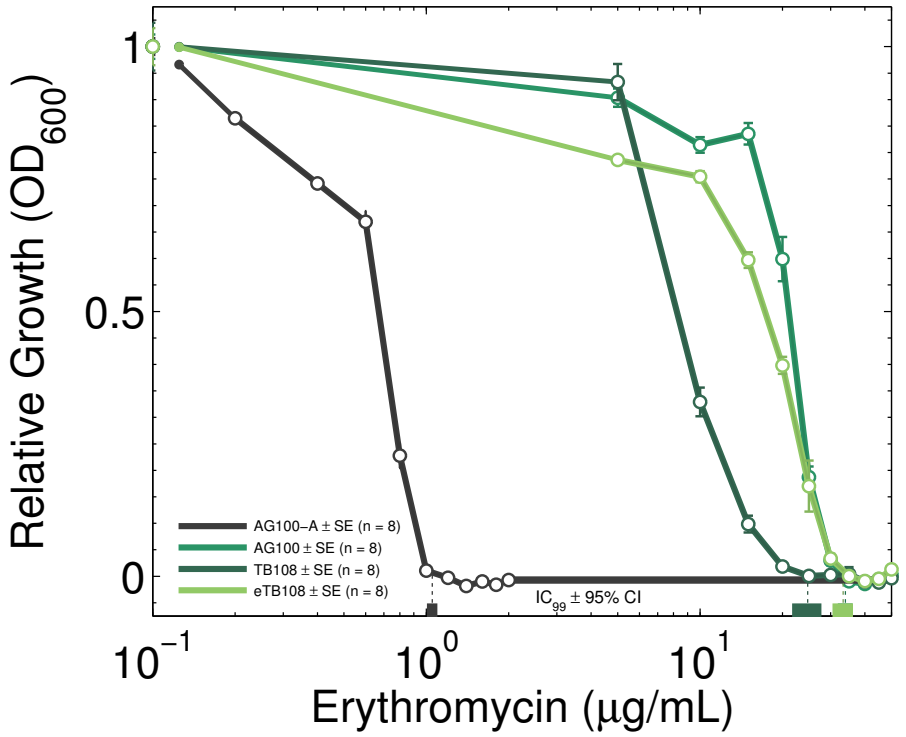

FIGURE 2.3. A comparative set of four dose-response profiles, using erythromycin, for the strains of *E. coli* AG100, AG100-A, TB108, and eTB108 where optical density data has been measured at 600nm (OD_{600}) after 24h of growth. Note that OD_{600} is shown on the *y*-axis whilst the concentration of erythromycin is represented in a logarithmic scale on the *x*-axis. The IC_{99} and its 95% confidence intervals, determined using $n = 8$, are shown for each strain on top of the *x*-axis. Only three of these are visible as two of the strains have overlapping confidence intervals for their IC_{99} values (eTB108 and AG100).

(AcrB and the GFP) would be preferentially selected in this evolutionary protocol. After the selection process, a new strain labelled eTB108 (meaning 'evolved TB108'), subsequently had a sensitivity (i.e. MIC) to erythromycin that is indistinguishable to that measured for the strain AG100. We labelled the resulting strain eTB108 and used this for the subsequent studies that we now describe.

2.3 QUANTIFYING ADAPTATION: RATE OF CHANGE IN GROWTH RATE AS A FUNCTION OF TIME AND DOSE

Whilst performing the aforementioned studies, we measured how these different strains adapted to their environment. One way of doing this relied on finding rates of change of growth rate as a function of time, and antibiotic dose, and calling this the rate of adaptation. This is an approach already used in the literature,[69] and the idea is based on the assumption that growth rates will change as a function of time as the bacterium

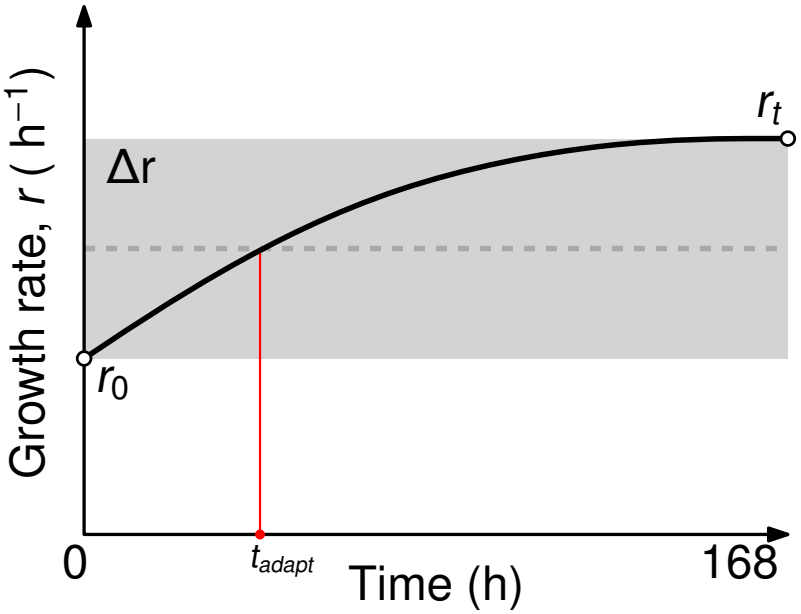

FIGURE 2.4. A shematic showing the key parameters involved in the quantification of the rate of adaptation with respect to any phenotype on the y-axis, here taken to be the growth rate. The rate of adaptation is denoted α throughout the text.

adapts to the environment. This phenotypic change can then be taken as a simple measure quantifying the complex processes of adaptation (FIG. 2.4).

A key parameter for producing such datasets is the 'adaptive time', denoted t_{adapt}. Here r_0 denotes the bacterial growth rate at the beginning of a bacterial culture experiment, $r(t)$ is the growth rate at some time t and $\Delta r(t)$ the difference between r_0 and $r(t)$. We can the define the adaptive time to be the time at which the condition $r(t) = r_0 + \Delta r(t)/2$ is satisfied. Lastly, the rate of adaptation (denoted α) is defined as the ratio between Δr and t_{adapt} so that $\alpha := (\Delta r/2)/t_{adapt}$; for further details of the calculation see REFERENCE 69.

2.4 HYPOTHESIS: IF THE STRENGTH OF SELECTION IS A LINEAR FUNCTION OF THE DOSE, THEN RESISTANCE MUST ALSO BE A LINEAR FUNCTION OF THE DOSE

In population genetics theory, the strength of selection on a novel trait encoded by some allelic variant is quantified by the *selection coefficient*. This coefficient, frequently denoted s, is usually assumed to be constant for a given trait.[20,21,23] One standard version of this theory proposes that 'sweeps to fixation' of a novel trait encoded by an advantageous allele occur in a manner that can be represented as a logistic function of the time.

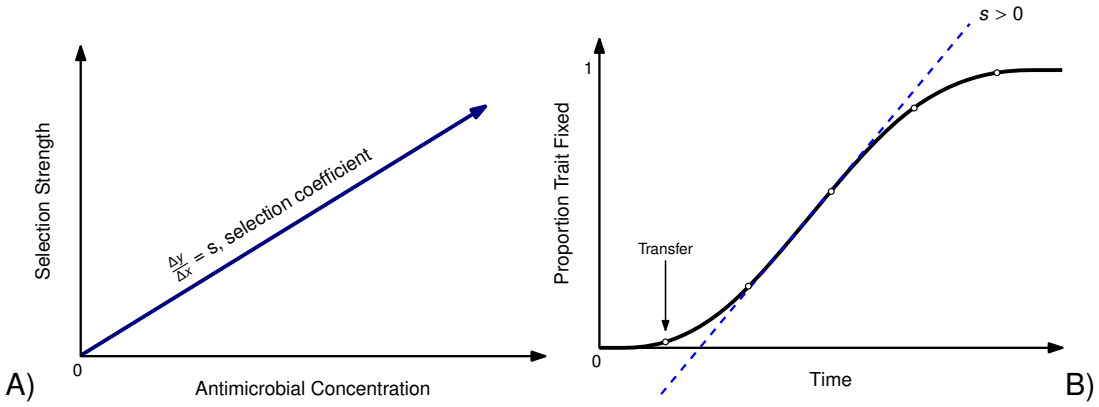

FIGURE 2.5. A) Variation in strength of selection on resistance as a function of the dose of an antimicrobial: it has been postulated to have a linear form.[26,27] Thus one might anticipate a form whereby $s(A) = \sigma \cdot A$ for some coefficient σ. **B)** The rate of the sweep to fixation of an advantageous trait of interest, assuming a constant selection coefficient *s*, see REFERENCE 23. This is a logistic curve whose steepness, and therefore the rate of fixation, is positively correlated with the value of *s*. From A) this rate of fixation is therefore also positively correlated with the value of *A*, if dose is indeed positively correlated with the selection coefficient.

If an allele provides resistance to an antibiotic drug, the strength of selective pressure exerted by the antibiotic has been frequently discussed in the literature, which recently has stated that it ought to be proportional to the drug dose applied, as depicted in FIG. 2.5, see REFERENCES 26 and 27.

If this rationale holds in practise, we should observe an increase of the frequency of resistance due to this allele, as a function of the dose of antibiotic supplied to the environment and as a function of time. However, much classical population genetics theory does not account for a dynamically changing population density; we address this below. However, antibiotics, by definition, have strong density-dependent suppression effects on growth and therefore control mutation supply because high doses will lead to small population sizes and therefore a reduced number of novel alleles with potential to provide resistance *de novo*. Our first approach to addressing these issues was theoretical. Next, with the results of that study, we went on to validate the resulting model experimentally.

So, the following model is a frequency- and density-dependent mathematical genetics model of the evolutionary dynamics of the operon *acr* at different antibiotic doses. We considered a situation whereby a monoclonal population of a bacterium, at density *B*, is exposed to an antibiotic, *A*, for a period of time *t*. To grow, *B* consumes a carbon source, *S*, supplied to the environment. To make our model compatible with

experimental methodologies such as batch transfers, we further assume that B is transferred to an environment with replenished S and A at time intervals indexed by the letter i, usually at 12h or 24h duration, satisfying the expression

$$B_i(t_{\text{start}}; S_{\text{start}}, A_{\text{start}}) = \eta \cdot B_{i-1}(t_{\text{start}}; S_{\text{start}}, A_{\text{start}}).$$

Here $\boldsymbol{B}(t, S, A) = (b_1(t, S, A), \ldots, b_n(t, S, A))$ denotes a time-series vector containing the density of n different genotypes that sum together to form B at time t, given S and A; $0 < \eta \ll 1$ denotes the fraction of B transferred (typically $\eta 0.01$), and $i \geqslant 1$ denotes the number of transfers, aka seasons or treatments. We will describe below how these different genotypes are defined. This is a relationship implemented as part of common evolutionary protocols that permit the propagation of a bacterial population indefinitely through time so that multiple antibiotic treatments can be administered. These are called 'batch transfer protocols' in which a small amount of biomass is transferred from one experimental vessel to another on a seasonal basis, each season typically lasting 24h, and indexed by i as mentioned above. Below we will write down explicit differential equations so that we can predict the behaviour of B as a function of t, S, A and i with the following rationale. Each cell contains a transporter that is able to take S from the environment and process it to grow. Assuming that each molecule of S is transformed into biomass (yield, c = 1), the growth rate function is defined to have the Michaelis-Menten form $G(S_0) = c\frac{VS_0}{(K_m+S_0)}$. Here V and K_m denote the maximal uptake and half-saturation constants, respectively. The antibiotic, at initial concentration A_0, diffuses into the cells at a rate controlled by φ and binds to the transporter, with affinity κ, reducing the growth of the cells. This type of inhibition (γ) can be modelled as $\gamma(A) = \frac{1}{1+\kappa A}$ [70] and the growth function is therefore redefined as $G(S, A) := c\frac{VS_0}{(K_m+S_0)} \cdot \gamma(A)$.

The reduction in growth thus becomes a function of the antibiotic concentration within each cell genotype and will be written A_{B_j}. Suppose the bacterium B may be resistant to the antibiotic A by means of an efflux pump,[51,71] whereby A_{B_j} is removed from the cytoplasm of the bacterium at the maximal rate v. Different cell genotypes are defined by the number of copies of this gene, $j \geqslant 1$, whereas the expression levels of this system will be denoted $1 \geqslant p \geqslant 0$. The abundance of this pump protein therefore

depends on number of genes encoding efflux pumps (j) and on the expression of these genes (p). The number of copies may change due to duplication mutations that we modelled as a Poisson process at a certain rate δ per cell per hour, whereas the rate of losing a copy of the gene is $\delta(1+\Delta) > \delta$.

We then impose the conditions $p_1 = 0$, and $p_2 > 0$. This means that cells with one gene copy must first express it before A_{B_j} can be pumped from the cell, thereafter that gene may be duplicated. Finally, we assume a functional form for p_j that is monotonically increasing and bounded in j, controlled by a dimensionless constant g in the Michaelis-Menten function $p_j = (j-1)/(1+g(j-1)$. Thus, the cell phenotype for which $j = 1$ has the gene for efflux pump, but does not express it. We based this on the limited abundance of the DNA polymerase transcription complex,[72] consequently it has to 'compete' for each gene copy providing a limit on the number of efflux genes that can be simultaneously expressed. If the genotypes within the vector B, namely b_j, represent the densities of bacteria that carry j copies of the efflux pump, a greater value of j implies a greater resistance. The genetics of the mechanism by which this occurs is represented by the following set of ordinary differential equations (ODEs):

$$\frac{d}{dt}b_1 = G(S, A_1)\cdot b_1 - \delta\cdot(b_1 - (1+\Delta)\cdot b_2), \tag{2.1a}$$

$$\frac{d}{dt}b_j = G(S, A_j)\cdot b_j - \delta\cdot((1+\Delta)\cdot b_j - b_{j-1} - (1+\Delta)\cdot b_{j+1}), \tag{2.1b}$$

$$\frac{d}{dt}b_n = G(S, A_n)\cdot b_n - \delta\cdot((1+\Delta)\cdot b_n - b_{n-1}), \tag{2.1c}$$

$$\frac{d}{dt}S = -\frac{V\cdot S_0}{K_m + S_0}\cdot\sum_{j=1}^{n} b_j, \tag{2.1d}$$

$$\frac{d}{dt}A_0 = -d\cdot A_0 - \sum_{j=1}^{n} b_j\cdot\left(\varphi\cdot(A_0 - A_j) - \frac{v\cdot p_j}{k_m + p_j}\cdot A_j\right), \tag{2.1e}$$

$$\frac{d}{dt}A_j = -d\cdot A_j + b_j\cdot\left(\varphi\cdot(A_0 - A_j) - \frac{v\cdot p_j}{k_m + p_j}\cdot A_j\right). \tag{2.1f}$$

We represented three different phenotypes (n = 3) containing a single but unexpressed efflux pump gene, a single and expressed efflux pump gene, and two copies of the efflux pump gene that are fully expressed. At the end of the 24h hours season, a sample of the current population is transferred to fresh medium where the next season

of growth occurs. We set this sample to be 1% of the bacterial population at the end of the season and repeated the protocol for a 7-season period in the model.

We solved this model numerically in Matlab using the function `ode15s`, which uses numerical differentiation formulas (NDFs).[73] The first prediction of the model is illustrated in FIG. 2.6. At the earliest times during the protocol, the density of the drug-susceptible population is seen to be decreasing monotonically, as a function of the increasing dose of antibiotic A_0. But the population density rapidly evolves to have a non-monotone profile. Also, the IC_{90} (the drug concentration inhibiting 90% of growth, defined at 24h for each day) clearly increases as a function of time as expected from adaptation to the presence of the antibiotic. This adaptation, according to the nature of the model, is an increase in frequency of cells that carry two or more copies of the efflux operon in their chromosome.

EQUATION 2.1 makes a second prediction that is illustrated in FIG. 2.7. In the case of a knockout strain, for example, meaning that the efflux pump cannot be expressed by the cells, the population density decays monotonically at all times as the concentration of antibiotic increases and there is no evidence of an increased IC_{90} through time. These are predictions that we can validate against experimental data, given an appropriate protocol, as we now show below.

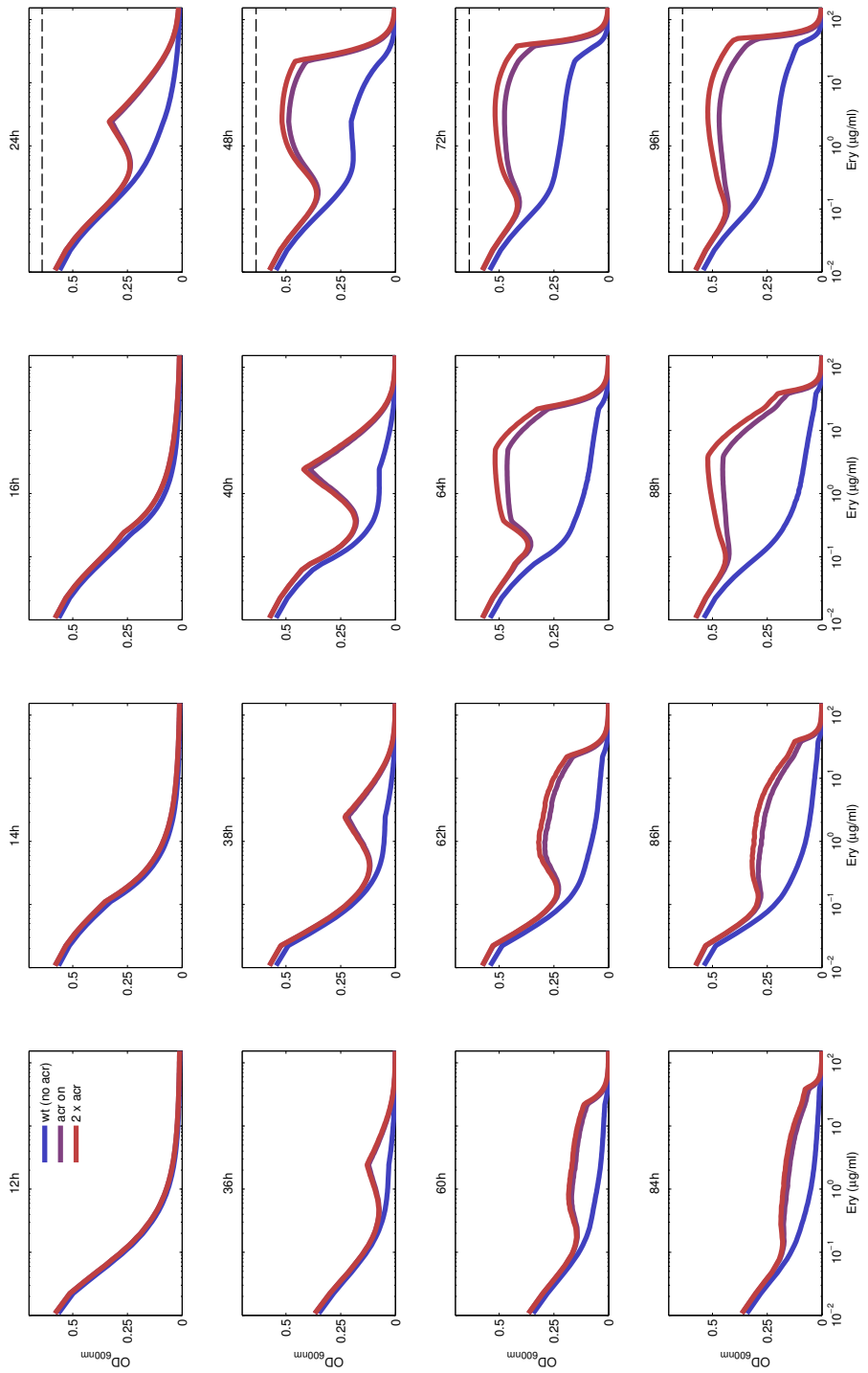

FIGURE 2.6. A prediction from the theoretical model defined in EQUATION 2.1. The concentration of antibiotic is represented on a logarithmic scale on the x-axis, whereas the growth in terms of OD_{600} is represented as a linear scale on the y-axis. This model predicts that the initial antimicrobial dose-response profile is monotone in accordance with standard tests that are used to quantify sensitivity to antibiotics in the lab. In time, following adaptation, cells with a higher number of pumps grow better at higher concentrations of antibiotic and they are selected through time, thus producing a non-monotone dose-response profile, eventually. The parameters are as follows:[74] $V = 1139.6 \mu g / OD_{600} / h$, $K_m = 0.53882 \mu g / mL$, $\kappa = 0.2 mL / \mu g$, $v = 3987.3 \mu g / OD_{600} / h$, $k_m = 19.681 (dimensionless)$, $g = 0.5 (dimensionless)$, $d = 0 / day$, $\varphi = 93.068 mL / OD_{600} / h$, $\delta = 0.0025 / gene$, $\Delta = 18 (dimensionless)$, and $c = 0.000315 OD_{600} / \mu g$ with initial conditions $B_{IC} = \{0.01, 0, 0\}$. The dashed line highlights the culture density in the absence of drug.

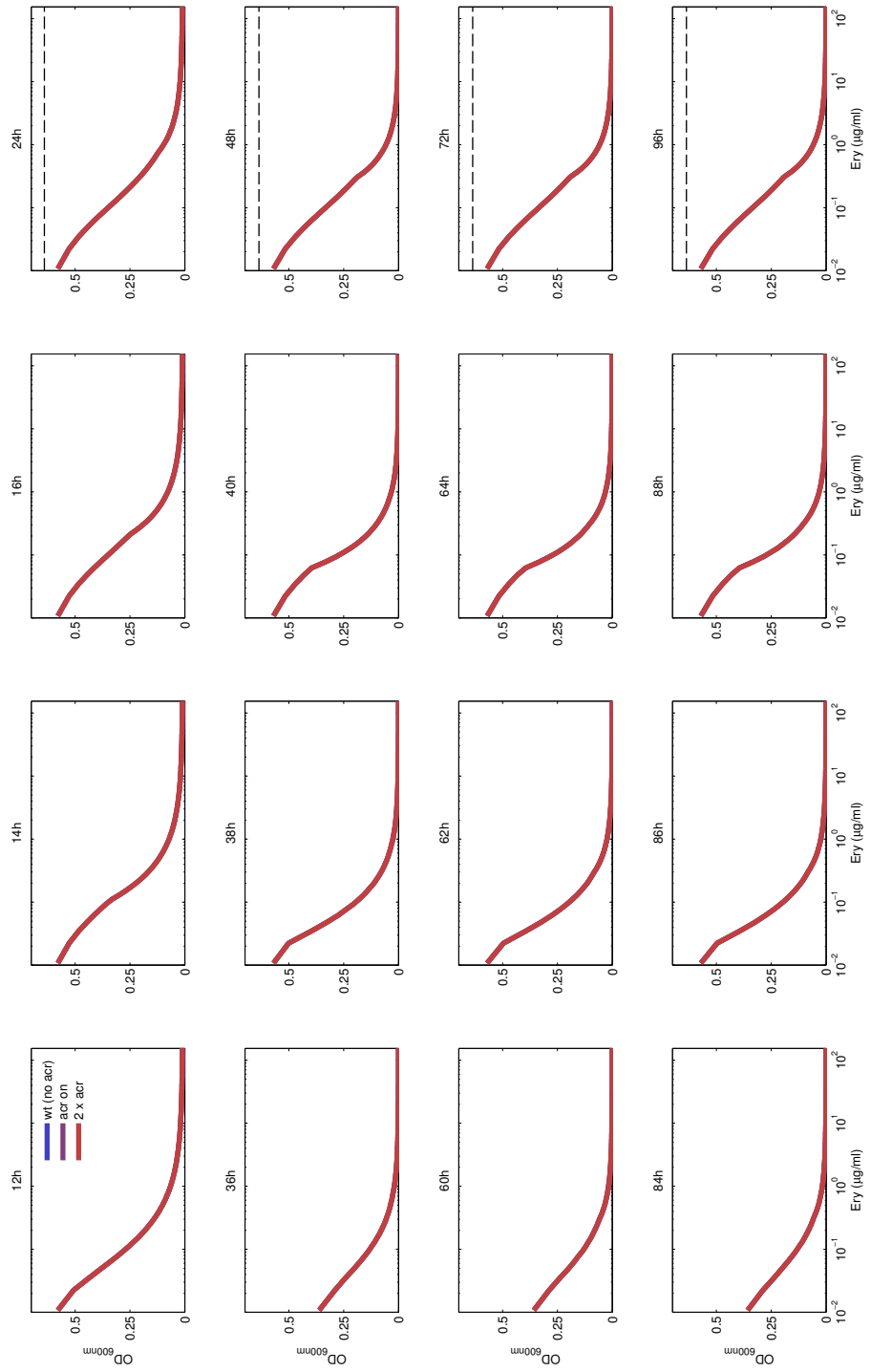

FIGURE 2.7. A second prediction from the theoretical model defined in EQUATION 2.1 when the ability of products of the *acr* operon to pump antibiotic has been removed from the model. The concentration of antibiotic is represented using a logarithmic scale on the *x*-axis, whereas growth in terms of OD_{600} is represented using a linear scale on the *y*-axis. The black line shows the total population density. Due to the inability of the cells to increase their ability to efflux the drug, and with the initial population lacking efflux pumps, the dose-response profile remains monotone at all times. In such a case, the IC_{90} shows little variation through time. Parameters as in FIG. 2.6 with only one modification: $\delta = 0/gene$. The dashed line highlights the culture density in the absence of drug.

2.5 Validating our theoretical hypothesis in the laboratory: the transition from monotone to non-monotone dose-response profile in *Escherichia coli*

To validate our hypothesis we used a standard experimental setup that is often employed in evolutionary microbiology studies.[69] For each of the bacterial strains shown in Table S.5 we created a 96-well microplate with minimal media containing 0.2% (w/v) of glucose, 0.1% (w/v) of casamino acids and eleven concentrations of erythromycin (both 0-2 and 0-50µg/mL, depending on the strain). Next, we inoculated this microplate with an overnight culture (>16h) of the corresponding strain and transferred the culture to another microplate with an identical setup at 24h intervals for seven days. Between each transfer, we monitored the growth of the cultures by measuring the optical density at 600nm (producing a density we denote OD_{600}, or just OD) every 20min. The results of this experiment are shown in Figs. 2.8 to 2.14. For every strain we compared the dose-response data to a monotone control profile, which was derived from the Hill function,[75] using a data-fitting routine coded using Matlab. The following is the mathematical definition of a Hill function used to model the dose-response data:

$$OD_{\text{model}}(C) = OD_0 \cdot \left(1 - \frac{I_{max} \cdot C^h}{IC_{50}^h + C^h}\right). \tag{2.2}$$

Here $OD_{\text{model}}(C)$ is the growth observed as a function of the erythromycin concentration (C), OD_0 the growth observed in the absence of erythromycin, I_{max} the maximum inhibition observed, IC_{50} the concentration of erythromycin achieving 50% of I_{max} and h the Hill coefficient which controls the 'sigmoidicity' of this dataset. This coefficient is non-dimensional and non-negative. Using Matlab to generate the aforementioned monotone control profile, we used our datasets to determine the best fit to the Hill model using a nonlinear regression method and we then quantified the difference between the data and the control profile by determining the area under the curve between the difference of the two ($AUC_d(E)$). This procedure allowed us to measure the 'non-monotonicity' of the dose-response data.

When we did this for the wild-type strain AG100 (see Fig. 2.8), bacterial growth as a function of the concentration of erythromycin has a monotonically decaying profile during the first 48h. After this time, there was a transition of that dose-response beyond which formed a non-monotone dose-response profile as a function of the

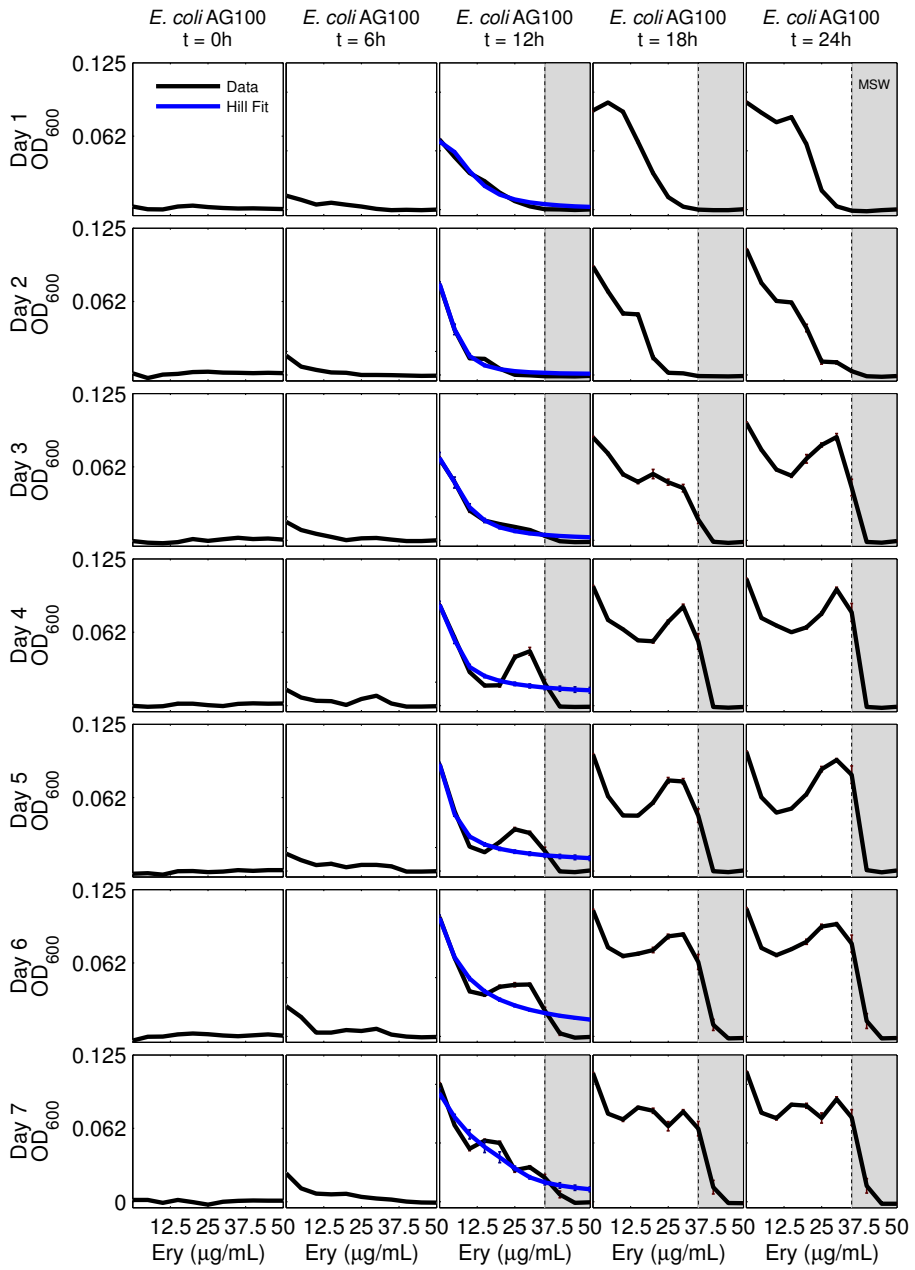

FIGURE 2.8. Experimental data on the growth of *E. coli* AG100 shown on the y-axis as the mean of OD_{600} ± standard error (n = 8, black), as a function of the concentration of erythromycin (Ery) on the *x*-axis. Data is plotted at the moment of inoculation (t = 0h) each season (one day per season) and every 6h thereafter. The vertical dashed line represents the IC_{99} measured after 24h of growth. This IC_{99} is often said to be the lower boundary of the *mutant selection window* (MSW), here represented in grey. In blue we represent the best Hill fit to data. This clearly shows a transition from monotone to non-monotone behaviour of the density data through time as the quality of the blue line datafit deteriorates through time.

concentration of erythromycin. This observation is compatible with the mathematical model defined in EQUATION 2.1. The observed deviation from monotonicity computed in this measure shows that $AUC_d(E)$ for AG100 crosses the zero point twice, leading to the development of a spike at t = 84h where this deviation is maximised (FIG. 2.10, $p < 0.001$; one-way ANOVA). The development through time of a non-monotone dose-response profile, including an increase in the IC_{99}, is also compatible with the theoretical model defined in EQUATION 2.1.

To validate our second prediction, we repeated the above experiment using the efflux knockout strain AG100-A, which produces nonfunctional of the proteins AcrA and AcrB. Therefore it has a nonfunctional AcrAB-TolC efflux pump system. With this strain, the growth measured by OD decayed monotonically at all measured times as a function of the concentration of erythromycin (FIG. 2.9). For the strain AG100-A, the deviation from the monotone control profile was considerably reduced (FIG. 2.10), and AUC_d reflected no defined shape ($p \approx 0.46$; one-way ANOVA testing for differences between treatments).

The data for these two strains, AG100 and AG100-A, is compatible with the predictions from our theoretical model and it shows the fundamental role played by the AcrAB-TolC efflux pump system in driving this phenomenon (the transition from monotone to non-monotone dose-response profile because of differential selection for the efflux pump). Our model assumes that the efflux pump is scalable through genomic amplification mutations whereby the number of copies of a gene or operon increases in the chromosome. Thus, we decided to monitor the relative abundance of AcrAB-TolC using the strains TB108 and eTB108, where AcrB has sfGFP as a fluorescent tag. Here, we assumed that an increment in the number of copies of the genes involved in this efflux pump is translated into a concomitant increment in the number of AcrAB-TolC efflux pumps (i.e. a genomic duplication event would result in an increase of the number of proteins conforming the AcrAB-TolC efflux pump system, therefore duplicating the fluorescence detected). However, the strains we used only allowed us to measure AcrB levels, they did not allow us to make any inferences regarding the structure of the chromosome during adaptation to the presence of the drug.

We repeated the previous protocol using the strain TB108, the results were not

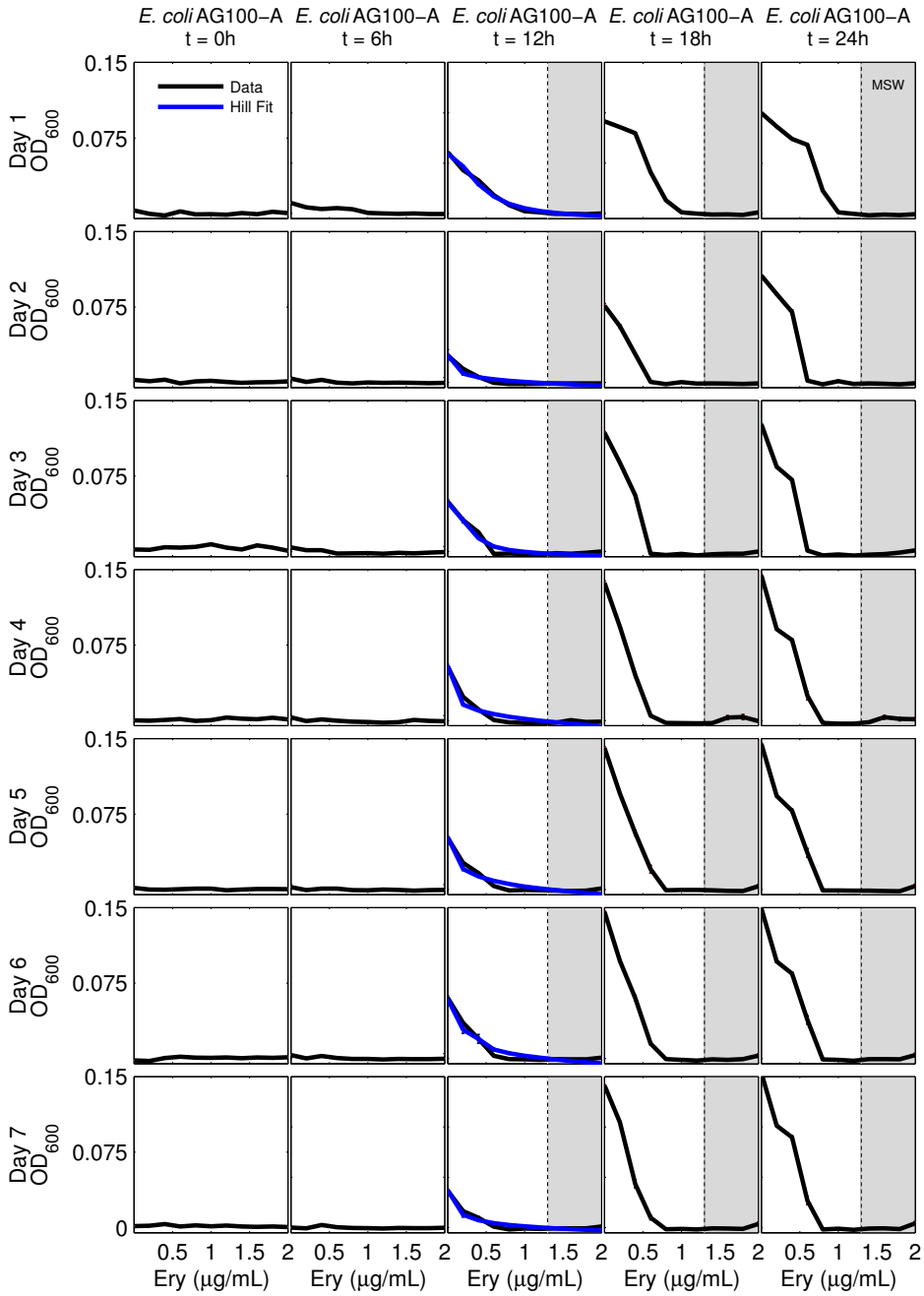

FIGURE 2.9. Experimental data on the growth of *E. coli* AG100-A shown on the y-axis as the mean of OD_{600} ± standard error (n = 8, black), as a function of the concentration of erythromycin (Ery) on the *x*-axis. Data is plotted at the moment of the inoculation (t = 0h) and every 6h thereafter. The vertical dashed line represents the IC_{99} measured after 24h of growth. This IC_{99} is often said to be the lower boundary of the *mutant selection window* (MSW), here represented in grey. In blue we represent the best Hill fit to data ± standard error (n = 8). (Note: we observed growth in the treatment containing the highest concentration of erythromycin in 1 out of 8 replicates after day 5).

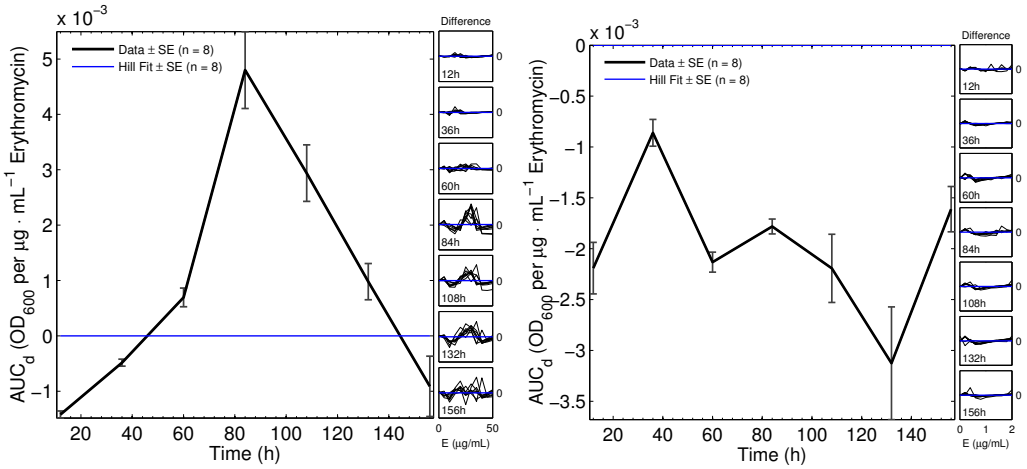

FIGURE 2.10. The difference between optical density data for the strain AG100 (left), AG100-A (right) and the best-fit monotone (Hill) profile (fitted with respect to OD_{600}) on the y-axis is plotted as a function of the concentration of erythromycin on the x-axis (shown as 'E' in the subplots on the right). The area under the curve of the difference between data and optimal datafit (AUC_d) is used to monitor the deviation from monotonicity as a function of time and the concentration of erythromycin (central plot). This shows maximal deviation is achieved at an intermediate time point.

conclusive. On the one hand, growth decays monotonically at all measured times as a function of the concentration of erythromycin, similar to our previous observation for the strain with nonfunctional efflux pumps AG100-A (FIG. 2.11). This dose-response profile was observed both for culture density (OD_{600}) and for absolute abundance of AcrB per cell (represented here as normalised GFP per OD). On the other hand, the resistance of this strain to erythromycin is ∼25 times higher than that measured for the strain AG100-A, but it is still more sensitive than the other K-12 wild-type strain, AG100. Furthermore, there was no significant deviation from the monotone control profile during the first six days both in OD_{600} and normalised GFP (FIG. 2.12, $p > 0.5$; one-way ANOVA testing for between-dose differences in deviation from the monotonic profile). Our interpretation was that the fluorescent tag, sfGFP, interfered with the normal function of AcrB and the whole AcrAB-TolC efflux pump system, thus diminishing the the strength of selection on the pump and therefore removing the effect we originally observed with AG100 above.

Nevertheless, at t = 156h a deviation from monotonicity was observed, which was different from earlier observations both in OD_{600} and OD-normalised GFP (i.e. the AcrB per cell proxy, FIG. 2.12). This deviation was produced by the cultures grown in the presence of 10µg/mL of erythromycin. We tested the sensitivity of this evolved

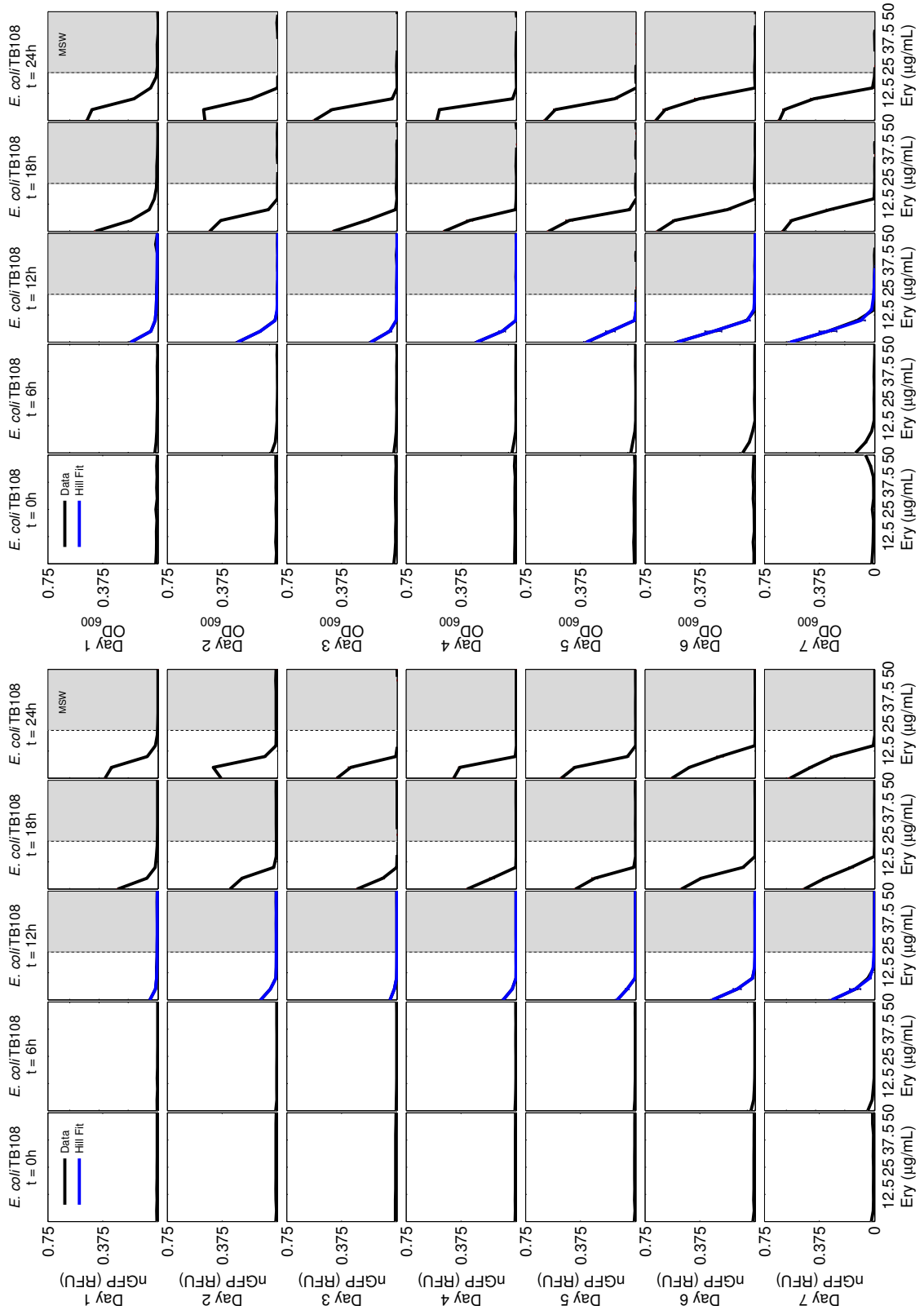

FIGURE 2.11. Experimental data on the growth of *E. coli* TB108 shown on the y-axis as the mean of OD_{600} ± standard error (n = 8, black), as a function of the concentration of erythromycin (Ery) on the *x*-axis. Data is plotted as OD_{600} (top) and as normalised GFP (nGFP, bottom) plotted at the moment of the inoculation (t = 0h) and every 6h thereafter. The vertical dashed line represents the IC_{99} measured after 24h of growth. In blue we show the best-fit Hill function.

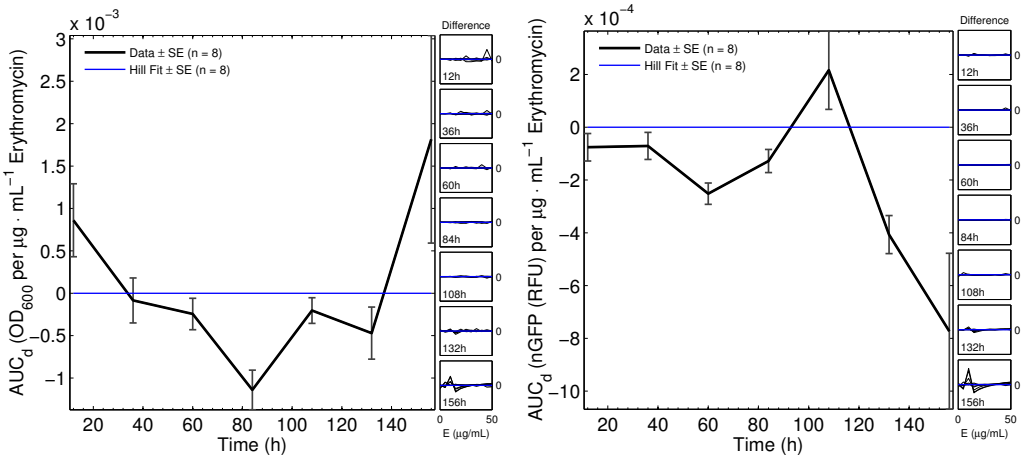

FIGURE 2.12. The difference between the optical density data for the strain TB108 and the best-fit monotone (Hill) profile in OD_{600} (top) and normalised GFP (nGFP, bottom) on the y-axis as a function of the concentration of erythromycin on the x-axis (E, subplots in the right). The area under the curve of this difference (AUC_d) is used to monitor the deviation from monotonicity as a function of time and the concentration of erythromycin (central plot).

culture of TB108 (called 'eTB108' hereafter) to erythromycin, the IC_{99} being identical to that for AG100 (FIG. 2.3 in p. 12). The new data was interpreted to potentially indicate a mitigation, by adaptation to erythromycin, of the interference between AcrB and its fluorescent tag, sfGFP, thus permitting the AcrAB-TolC efflux system to perform as expected. We had no clear indication as to the mechanism of this 'repair process' and at the time of writing this thesis, these strains have been submitted to a sequencing centre in Germany in order to assess what the genetic basis of those adaptations might be. The details of that study are considered outside of the scope of this thesis because, as we will now show, we are able to exploit this strain to correlate non-monotone dose-response profiles with hotspots for selection on AcrB, using this new strain.

This evolved strain, eTB108, was used to repeat the protocol and validate our assumption that the monotone to non-monotone profile transition is mediated by changes in the relative abundance of the AcrAB-TolC efflux pump system per bacterial cell. For this strain, in terms of culture density (OD_{600}), the growth measured by OD decays monotonically as a function of the concentration of erythromycin (FIG. 2.13). The properties of the dose-response profile do, however, change through time. In some aspects this resembled the changes observed in the prior K-12 wild-type strain AG100. For example, at t = 24h we observed a change in the slope of the dose-response profile that is nearly identical to that noted in AG100 (FIG. 2.13).

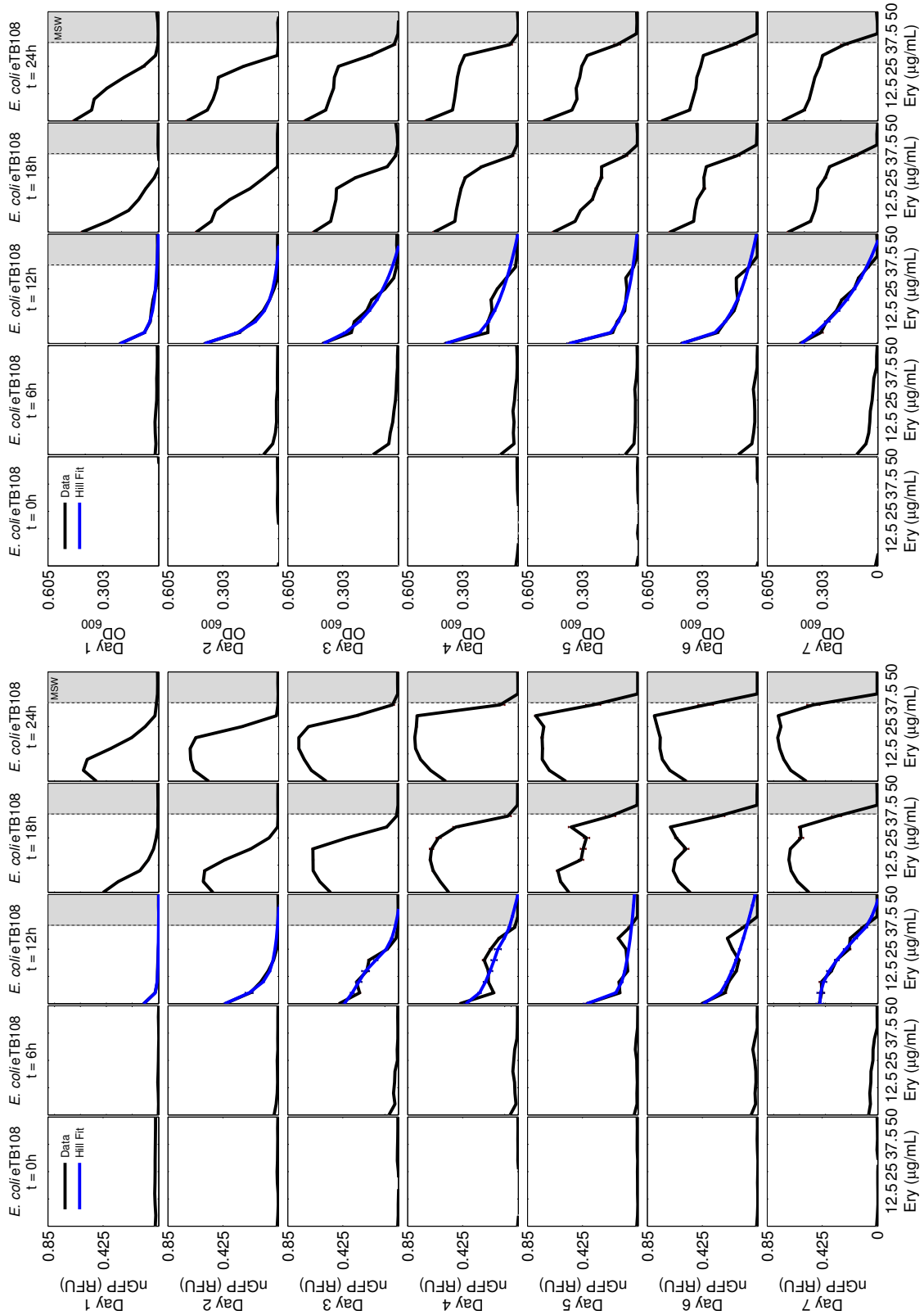

FIGURE 2.13. Experimental data on the growth of *E. coli* eTB108 shown in the y-axis as the mean of OD_{600} ± standard error (n = 8, black), as a function of the concentration of erythromycin (Ery) on the *x*-axis. Data for OD_{600} (top) and normalised GFP (nGFP, bottom) plotted at the moment of the inoculation (t = 0h) and every 6h thereafter. The vertical dashed line represents the IC_{99} measured after 24h of growth. In blue we show the best-fit Hill function.

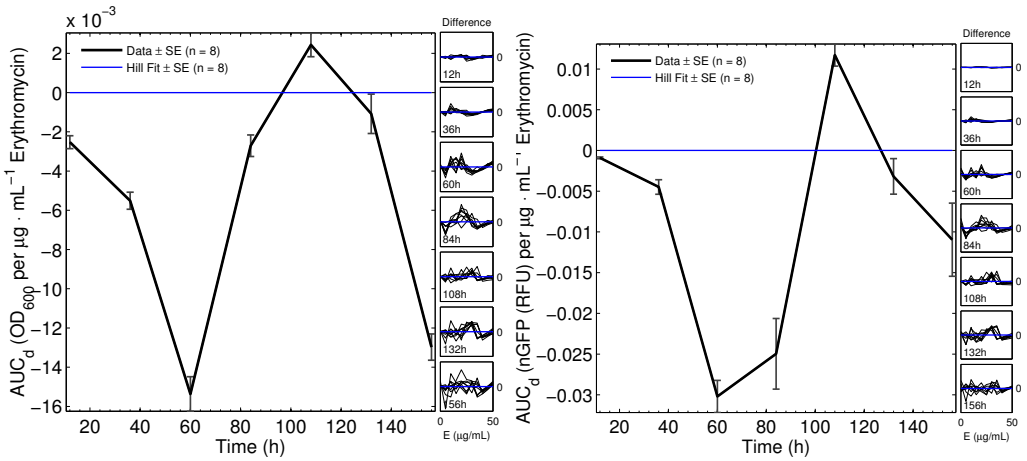

FIGURE 2.14. The difference between the optical density data for the strain eTB108 and the best-fit monotone (Hill) profile in OD_{600} (top) and normalised GFP (nGFP, bottom) on the y-axis as a function of the concentration of erythromycin on the x-axis (E, subplots in the right). The area under the curve of this difference (AUC_d) is used to monitor the deviation from monotonicity as a function of time and the concentration of erythromycin (central plot).

We compared this to the readings for OD-normalised GFP (the proxy of per-cell abundance of AcrB, FIG. 2.13). The development and expansion of a *plateau* in the dose-response data for culture density shown in this figure, follows the monotone to non-monotone transition profile in the abundance of AcrB, and therefore of AcrAB-TolC, seen in the same figure. A further observation of this figure, highlighted how the data crosses the monotone control profile twice, confirming the presence of a spike, or candidate selection hotspot. This is where the deviation from monotonicity is maximised (FIG. 2.14, $p < 0.001$; one-way ANOVA). Therefore, as predicted by our model, a change in abundance of the AcrAB-TolC efflux pump system may be the cause behind the phenomenon hereby described, namely a transition from a monotone to a non-monotone dose-response profile. The effect is clearer in the data related to AG100 than it is for eTB108.

2.6 NON-MONOTONE DOSE-RESPONSE PROFILES: INCREMENTS IN BACTERIAL GROWTH FROM INCREMENTS IN THE CONCENTRATION OF ANTIBIOTIC

A corollary of the existence of a non-monotone dose-response profile is the idea that increments in the concentration of an antibiotic can lead to increases in bacterial growth. This is counter-intuitive and the basis of the ‘paradox’ we described above. The purpose of this section is to dig a little deeper into the reasons why this might occur

using the strain eTB108. We were particularly interested in whether or not the increase in antibiotic dose leads to an increase, or a decrease, in the amount of efflux pump protein expressed per cell. Intuitively, we hypothesised a positive correlation between the number of these efflux pumps, and the dose of antibiotic supplied. But, in fact, we saw that this was untrue in the case of the strains of *E. coli* we used and the antibiotic erythromycin. We did verify that, at some specific doses, this hypothesis was true only after a period of adaptation to the drug.

To perform this analysis, we quantified changes in the dose-response profiles as a function of the concentration of erythromycin. We compared the data gathered for every concentration with a 'zero-slope' model, using *t*-tests to estimate whether the slopes are greater, lower, or equal to zero (FIGS.2.16 to 2.19). This test was performed for culture densities (OD_{600}), absolute abundances of AcrB (normalised GFP), and also the relative abundance of AcrB (a proxy for AcrAB-TolC per cell, assuming one copy of the operon in the chromosome in the absence of antibiotic).

To quantify the relative abundance of AcrB-sfGFP , thus of the AcrAB-TolC efflux pump system, we divided the absolute abundance of AcrB by culture density (OD_{600}). This normalises the abundance of AcrB, read as AcrB per cell, when the culture is grown in media without antibiotic. We used this number as a reference when comparing the quantity of AcrAB-TolC per cell in different growth conditions.

FIG. 2.15 contains a sub-network of the regulation network of the *acr* operon. Previously, we stated that the role of this pump is to detoxify the cell during metabolism and that AcrAB-TolC would be up-regulated when hazardous byproducts accumulate in the cell and down-regulated when these stressors are absent. What we observed when we calculated the relative abundance of AcrB per cell (and shown inFIG. 2.15) was more subtle than this. For example, in the absence of drug we saw that AcrB per cell stayed fairly constant through the lag phase period, between 0 and 10h after inoculation/transfer, but then up-regulated through exponential growth (10-17h after inoculation/transfer). This is consistent with the previous comment regarding AcrB regulation, and it remained at a static value through stationary phase. However, when a small amount of erythromycin was supplied into the growth medium, it delayed the exponential phase, and we saw a continual climb of AcrB per cell through stationary

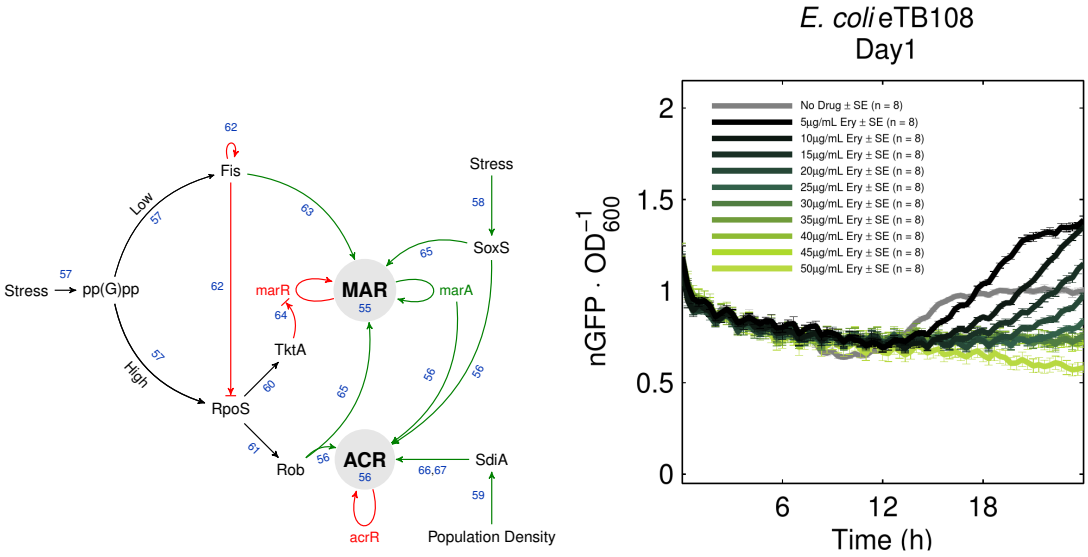

FIGURE 2.15. Top) A partial view of the regulation network of the *acr* operon (see p. 10 for details). **Bottom)** The expression profile of *AcrB-sfGFP* is shown as a function of time over 24h at different concentrations of erythromycin for the strain eTB108. A proxy for the relative abundance of AcrB-sfGFP per cell is shown on the *y*-axis as a function of time (bottom). Different concentrations of erythromycin are denoted by different colours. We note that the small oscillations observed are seemingly produced by mechanical components of the microplate reader and not by any oscillatory dynamic produced by the above network (see FIG. S.13).

phase. This rise in AcrB was much higher than had been the case in the absence of the drug. This appears to indicate that AcrB expression is, in a general sense, positively correlated with the presence of this antibiotic. Yet, the same figure showed that further increases in drug concentration actually lead to decreases in the amount of observed AcrB per cell, with greater drug leading to lower AcrB at all higher drug doses. As the network in FIG. 2.15 indicates, there is potential complex regulations of the AcrAB-TolC efflux pump due to the overlap between the *mar*, population density sensing, and resource stress networks to control pump expression levels.

The decay in the up-regulation rate of this efflux pumps can be explained by the mechanism whereby erythromycin inhibits cell growth (protein synthesis inhibition).[76] But why this reduction in up-regulation rate leads to higher relative numbers of pumps per cell is beyond the scope of this chapter. In CHAPTER 5 we explore the theoretical framework that proposes, based on thermodynamic constrains to be explained in that chapter, the existence of a trade-off between the rate of production of a biochemical pathway (i.e. to produce ATP or AcrB) and the production per molecule of substrate or *yield* of that pathway. A demonstration that such trade-off between rate and yield

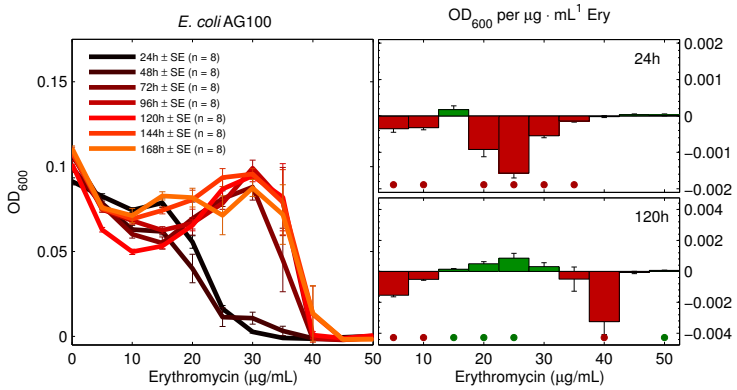

FIGURE 2.16. Erythromycin dose-response profiles for evolved *E. coli* AG100 measured every 24h. The growth measured as OD_{600} is shown on the *y*-axis as a function of the concentration of erythromycin, represented on the *x*-axis. For the subplots, the *y*-axis represent the point-to-point slope changes of the dose-response profiles and significantly positive (green) or negative (red) slopes are highlighted accordingly ($\alpha = 0.01$). These numbers indicate whether an increase or decrease in drug dose increases or decreases the OD values.

exists could provide an insight to, for example, why the addition of a protein synthesis inhibitor leads to an increase in total AcrB protein produced.

In these strains where sensitivity to erythromycin is reduced due to the increase in the relative number of multi-drug efflux pump AcrAB-TolC, following several days of adaptation to the drug, the drug-by-drug changes in AcrB expression described above can undergo changes as a function of the concentration of erythromycin (FIGS. 2.16, 2.17, 2.18, and 2.19). In particular, FIGURE 2.18 clearly shows the phenomenon to which we are referring: the initial negative correlation between drug and AcrB becomes a positive correlation at later times. This, however, is total AcrB expressed in the populations, not AcrB per cell.

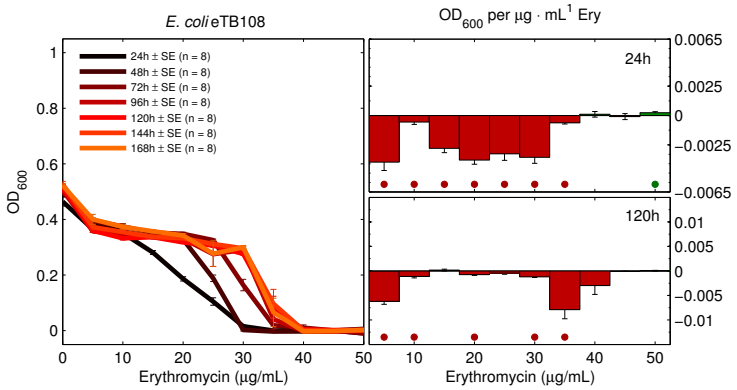

FIGURE 2.17. Erythromycin dose-response profiles for *E. coli* eTB108 measured every 24h. The growth measured as OD_{600} is represented on the *y*-axis as a function of the concentration of erythromycin, represented on the *x*-axis. For the subplots, the *y*-axis represent the point-to-point slope changes of the dose-response profiles and significantly positive (green) or negative (red) slopes are highlighted accordingly ($\alpha = 0.01$).

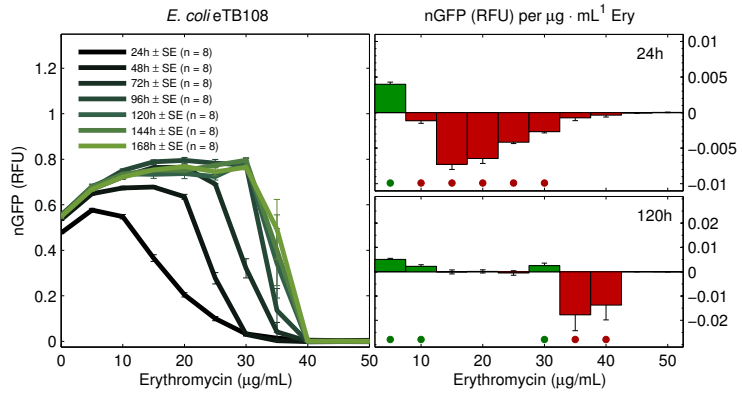

FIGURE 2.18. Erythromycin dose-response profiles for *E. coli* eTB108 measured every 24h. The absolute abundance of AcrB measured as normalised GFP (nGFP) is represented on the *y*-axis as a function of the concentration of erythromycin, represented on the *x*-axis. For the subplots, the *y*-axis represent the point-to-point slope changes of the dose-response profiles and significantly positive (green) or negative (red) slopes are highlighted accordingly ($\alpha = 0.01$).

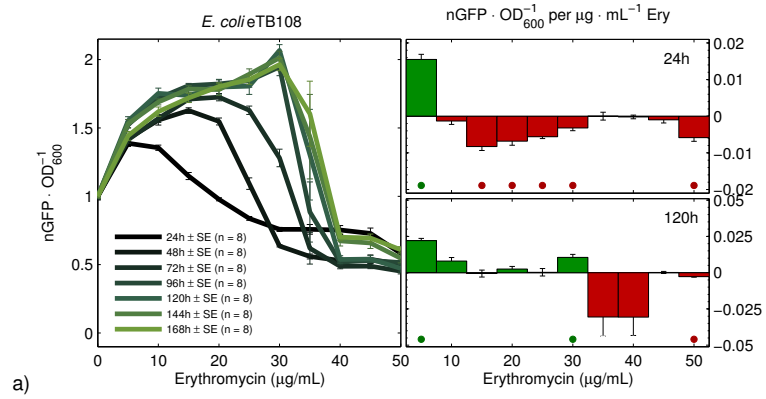

a)

FIGURE 2.19. Erythromycin dose-response profiles for *E. coli* eTB108 measured every 24h. The relative abundance of AcrB per cell measured as normalised GFP (nGFP) per OD_{600} is represented on the *y*-axis as a function of the concentration of erythromycin, represented on the *x*-axis. For the subplots, the *y*-axis represent the point-to-point slope changes of the dose-response profiles and significantly positive (green) or negative (red) slopes are highlighted accordingly ($\alpha = 0.01$).

Nevertheless, in FIG. 2.19 we observed the analogous change in correlation reported in the previous paragraph. It is clear that adaptation to this antibiotic is changing the way in which AcrB is regulated, consistent with known literature on adaptation of *E. coli* to protein-synthesis antibiotics where mutations in MarR have been observed following evolutionary experiments of this type.[74] Importantly, the same figure shows a clear increase in the relative abundance of AcrB per cell, shifting from 1 to almost exactly 2 'copies of *acrB* per cell' as a function of the concentration of erythromycin. This shift in the relative abundance of AcrB is directly related to the 'expansion' of the *plateau* formerly discussed with respect to the strain eTB108. The value '2' we observed here

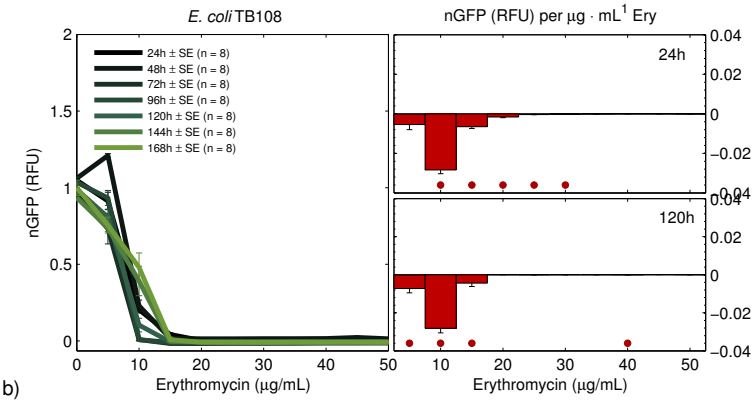

FIGURE 2.20. Erythromycin dose-response profiles for *E. coli* TB108 measured every 24h. The absolute abundance of AcrB measured as normalised GFP (nGFP) is represented on the *y*-axis as a function of the concentration of erythromycin, represented on the *x*-axis. For the subplots, the *y*-axis represent the point-to-point slope changes of the dose-response profiles and significantly positive (green) or negative (red) slopes are highlighted accordingly ($\alpha = 0.01$).

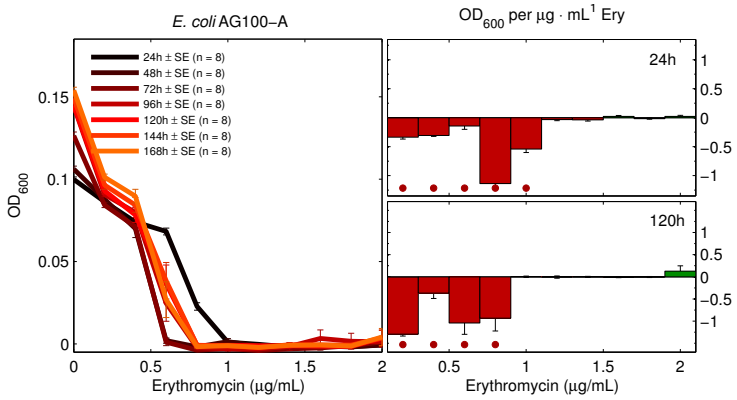

FIGURE 2.21. Erythromycin dose-response profiles for *E. coli* AG100-A measured every 24h. The growth measured as OD_{600} is represented on the *y*-axis as a function of the concentration of erythromycin, shown on the *x*-axis. For the subplots, the *y*-axis represent the point-to-point slope changes of the dose-response profiles and significantly positive (green) or negative (red) slopes are highlighted accordingly ($\alpha = 0.01$).

would seem to be closely related to the sweep through the population of a duplication mutation, but we have not proven this, as yet. If we implement the same experiments using the strain TB108, for which we do not observe the monotone to non-monotone dose-response transition, the values of these same slopes are negative at all times (see FIGS. 2.20, 2.21, and 2.22). This would indicate no measurable change in the regulation of the pump following a period of adaptation using this strain. It also indicates that increases in drug dose do correlate with a decrease in AcrB expression for this strain at all times in these experiments.

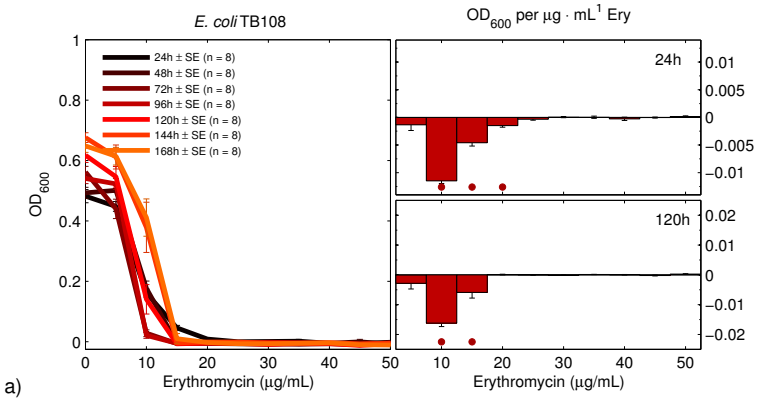

FIGURE 2.22. Erythromycin dose-response profiles for *E. coli* TB108 measured every 24h. The growth measured as OD_{600} is represented in the *y*-axis as a function of the concentration of erythromycin, represented in the *x*-axis. For the subplots, the *y*-axis represent the point-to-point slope changes of the dose-response profiles and significantly positive (green) or negative (red) slopes are highlighted accordingly ($\alpha = 0.01$).

2.7 ANALYSING PHENOTYPIC RATES OF ADAPTATION: THE MONOTONE TO NON-MONOTONE TRANSITION PROFILES REVEAL ADAPTATION 'HOTSPOTS' AND 'COLDSPOTS'

In the previous section we sought correlations between bacterial growth, AcrB expression levels and antibiotic concentration. We observed that these correlations could change significantly during periods of adaptation to antibiotics. Such changes in expression profiles of the pump system are the cause of the non-monotone dose-response profiles observed in those same experiments. Next we used a simple measure of adaptation, observed above, to demonstrate that the non-monotone profiles are due to doses that maximise selection on this pump. These we called 'evolutionary hotspots'.

To quantify the existence, or absence, of evolutionary hotspots we analysed the rate of adaptation measure (α, as defined in p. 13 and discussed above) calculated as the ratio between growth at t = 24h and the area under the curve (AUC) of the 24h OD data time series. An AUC version of growth rate, r_{AUC}, is defined as

$$r_{AUC} := \frac{OD(24h)}{\int_0^{24h} OD(t) \cdot dt}. \tag{2.3}$$

This measure of growth rate, applied to a 24h times series denoted $OD(t)$, has the appropriate units, namely 'per hour'. Using r_{AUC}, our analysis of the rate of adaptation of this particular phenotype for all the different strains used in this chapter revealed the existence of two 'windows' with opposite effects (as shown in FIGS. 2.23, 2.24, 2.25, and 2.26). We could use different definitions of r_{AUC}, so that if $x(t)$ is any series of

phenotype data, then we will also write $r_{AUC} := \frac{x(24h)}{\int_0^{24h} x(t) \cdot dt}$. Although this is not a growth rate, it is still a rate of change of $x(t)$.

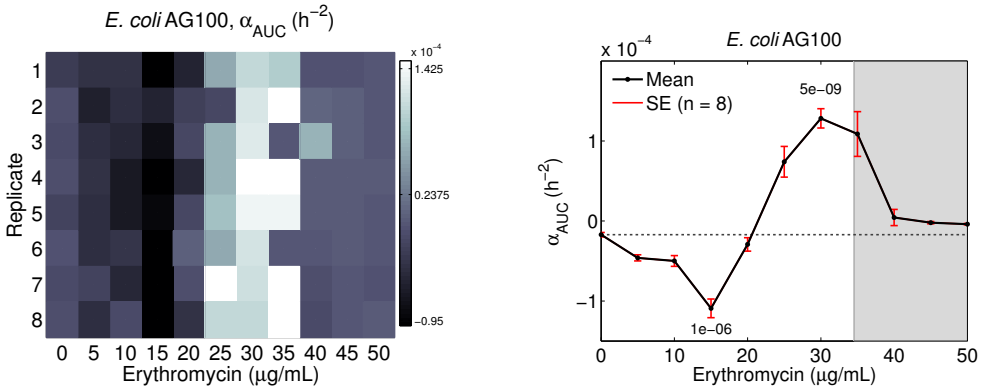

FIGURE 2.23. Selection statistics for *E. coli* AG100 as a function of the concentration of erythromycin: rate of adaptation per replicate based on r_{AUC} (α_{AUC}, left). Darker greys represent lower rates of adaptation, eight replicates shown, whereas brighter greys represent higher rates. Mean rate of adaptation as a function of the concentration of erythromycin (right). The numbers shown correspond to the *p*-values of an unpaired *t*-test ($\alpha = 0.05$). The error bars represent the standard error of the mean (n = 8), and the grey area represents the mutant selection window (MSW).

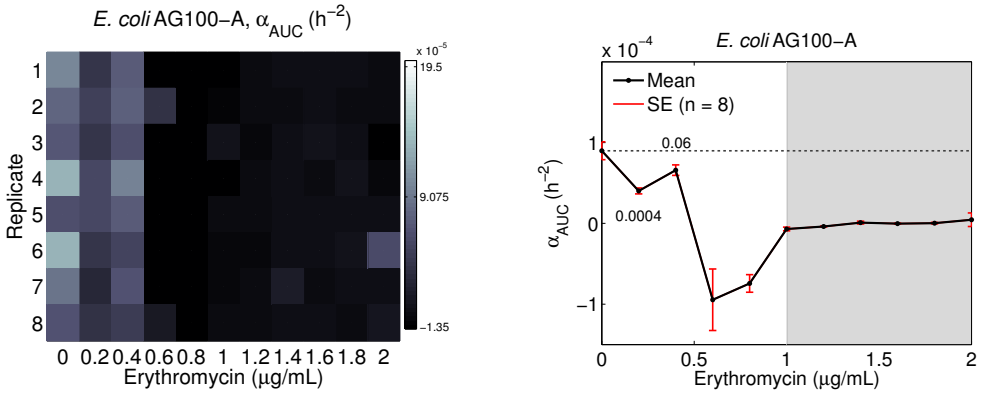

FIGURE 2.24. Selection statistics for *E. coli* AG100-A as a function of the concentration of erythromycin: rate of adaptation per replicate based on r_{AUC} (α_{AUC}, left). Darker greys represent lower rates of adaptation, eight replicates shown, whereas brighter greys represent higher rates. Mean rate of adaptation as a function of the concentration of erythromycin (right). The numbers shown correspond to the *p*-values of an unpaired *t*-test ($\alpha = 0.05$). The error bars represent the standard error of the mean (n = 8), and the grey area represents the mutant selection window (MSW).

In relative terms, the first window is located at very low concentrations of erythromycin, where the rate of adaptation to the low-drug environment is lower than in the antibiotic-free control. We considered this to be an *evolutionary coldspot*; the rate of adaptation may be increased either by adding or removing erythromycin from this coldspot. The second window sits between the evolutionary coldspot and the IC_{99}. In contrast to the coldspot, the rate of adaptation in this window is higher than in the

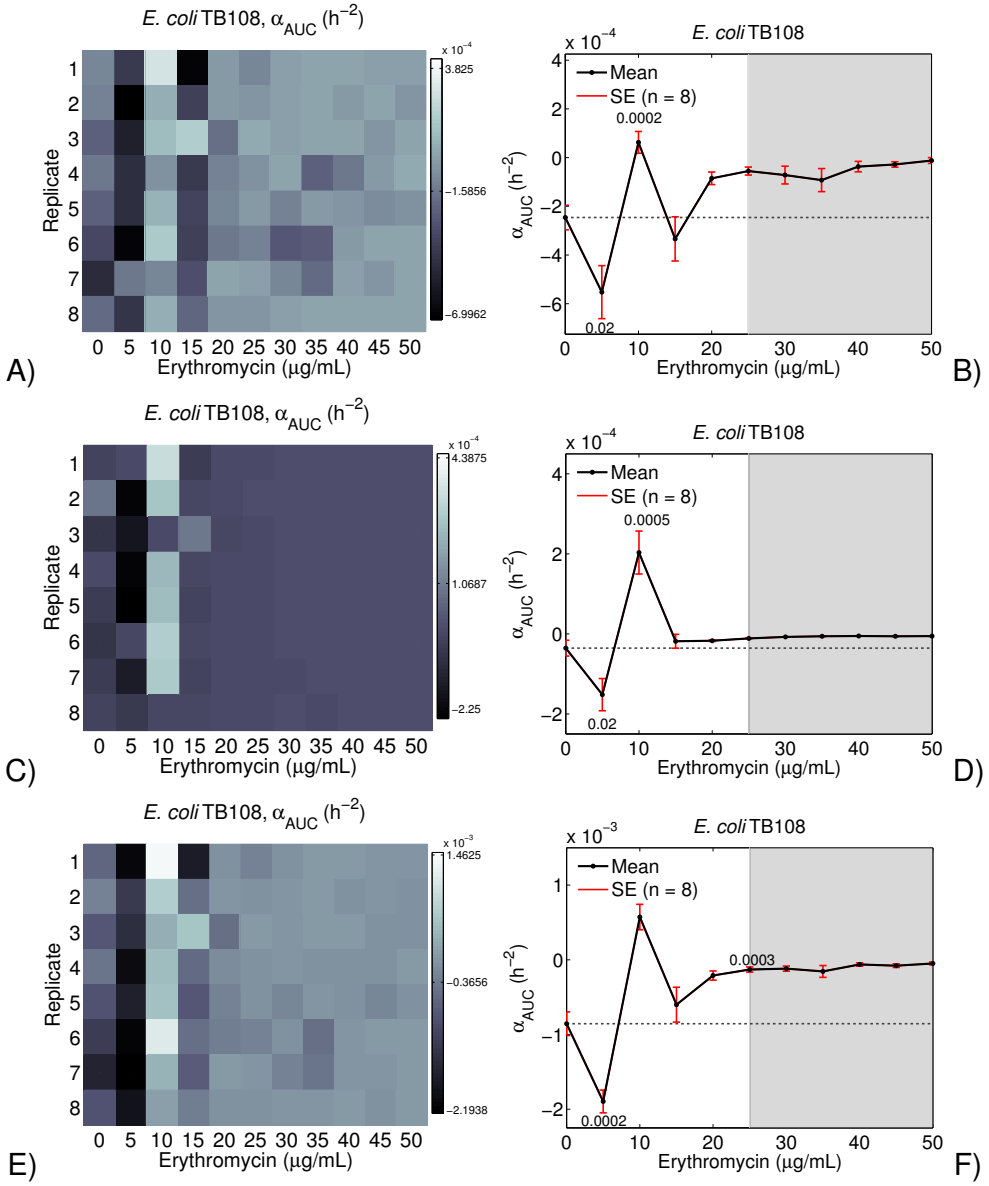

FIGURE 2.25. Selection statistics for *E. coli* TB108 as a function of the concentration of erythromycin: **A,C,E)** rate of adaptation per replicate based on r_{AUC} (α_{AUC}). Data for **A)** OD_{600}, **C)** absolute abundance of AcrB-sfGFP as normalised GFP (nGFP), **E)** relative abundance of AcrB-sfGFP as normalised GFP per OD units. Darker greys represent lower rates of adaptation, eight replicates shown, whereas brighter greys represent higher rates. **B,D,F)** Mean rate of adaptation as a function of the concentration of erythromycin (right column). The numbers shown correspond to the *p*-values for an unpaired *t*-test ($\alpha = 0.05$). The errorbars represent the standard error of the mean (n = 8), and the grey area represents the mutant selection window (MSW).

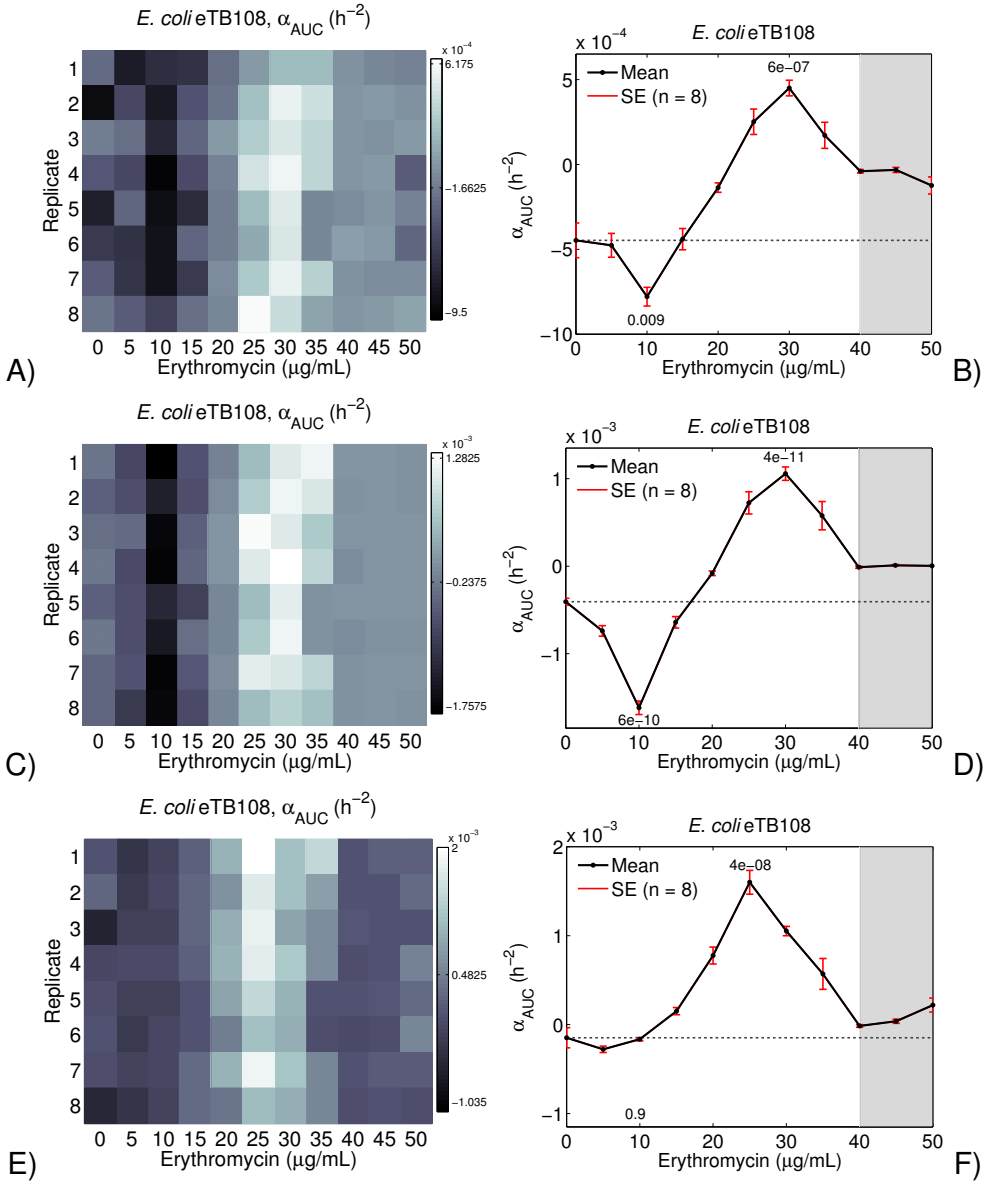

FIGURE 2.26. Selection statistics for *E. coli* eTB108 as a function of the concentration of erythromycin: **A,C,E)** rate of adaptation per replicate based on r_{AUC} (α_{AUC}). Data for **A)** OD_{600}, **C)** absolute abundance of AcrB-sfGFP as normalised GFP (nGFP), **E)** relative abundance of AcrB-sfGFP as normalised GFP per OD units. Darker greys represent lower rates of adaptation, eight replicates shown, whereas brighter greys represent higher rates. **B,D,F)** Mean rate of adaptation as a function of the concentration of erythromycin (right column). The numbers shown correspond to the *p*-values for an unpaired *t*-test ($\alpha = 0.05$). The errorbars represent the standard error of the mean (n = 8), and the grey area represents the mutant selection window (MSW)

antibiotic-free control. We considered this to be an *evolutionary hotspot* and, from this point, any change in the concentration of erythromycin leads to a reduced rate of adaptation, as can be seen in the same figures. The existence of these windows, hotspots and coldspots, is independent of the growth rate traits that we measured, whether this be culture density (OD_{600}), absolute abundance of AcrB (normalised GFP), or relative abundance of AcrB (normalised GFP per OD_{600}).

Importantly, for the latter trait, we measured the sweep to fixation as a function of time (t), and dose. We observed in FIG. 2.27 (bottom plot) that AcrB-sfGFP increased among the bacterial cells in a logistic fashion, in which a phase of non-linear increase is followed by a stable phase (sweep to fixation, see FIG. 2.5 in p. 14). This increase is, however, preceded by a non-linear decline of AcrB-sfGFP. The rate of sweep to fixation can be calculated using a logistic model,[23] so we included a simple non-linear term to account for the loss of AcrB-sfGFP. Denoting the relative abundance of AcrB-sfGFP as U, we fitted the following model to the data:

$$U(t) = U_0 + \overbrace{Ae^{-t\iota}}^{\text{Loss of AcrB}} + \overbrace{\frac{c}{1 + Be^{-t\psi}}}^{\text{Sweep of AcrB}} . \tag{2.4}$$

Here ι denotes the loss rate of AcrAB-TolC per OD_{600} unit, ψ the rate of sweep, c the number of relative copies of *acr* per cell, U_0 the relative abundance of AcrB at t = 0h, and A and B are phenomenological coefficients. In FIG. 2.27 we see that such a rate of sweep is maximised not only at the particular dose of 30µg/mL of erythromycin, within the evolutionary hotspot, but also within the particular times of 48 and 96h (2-4 days).

Other notable features of the same dataset are: i) at a dose of 5µg/mL of erythromycin, the levels of AcrB expression achieved a degree of stasis which may indicate a stable mutation-selection balance whereby AcrB duplications reside at approximately 50% frequency in the population. The same can be said for slightly higher doses with slightly higher percentages of the *acr* duplication. Finally, ii) we noted that high erythromycin doses lead to a stable down-regulation of the AcrB protein that is not overcome by adaptation. This is likely due to the low supply of mutants at these doses, which are the result of the small populate sizes.

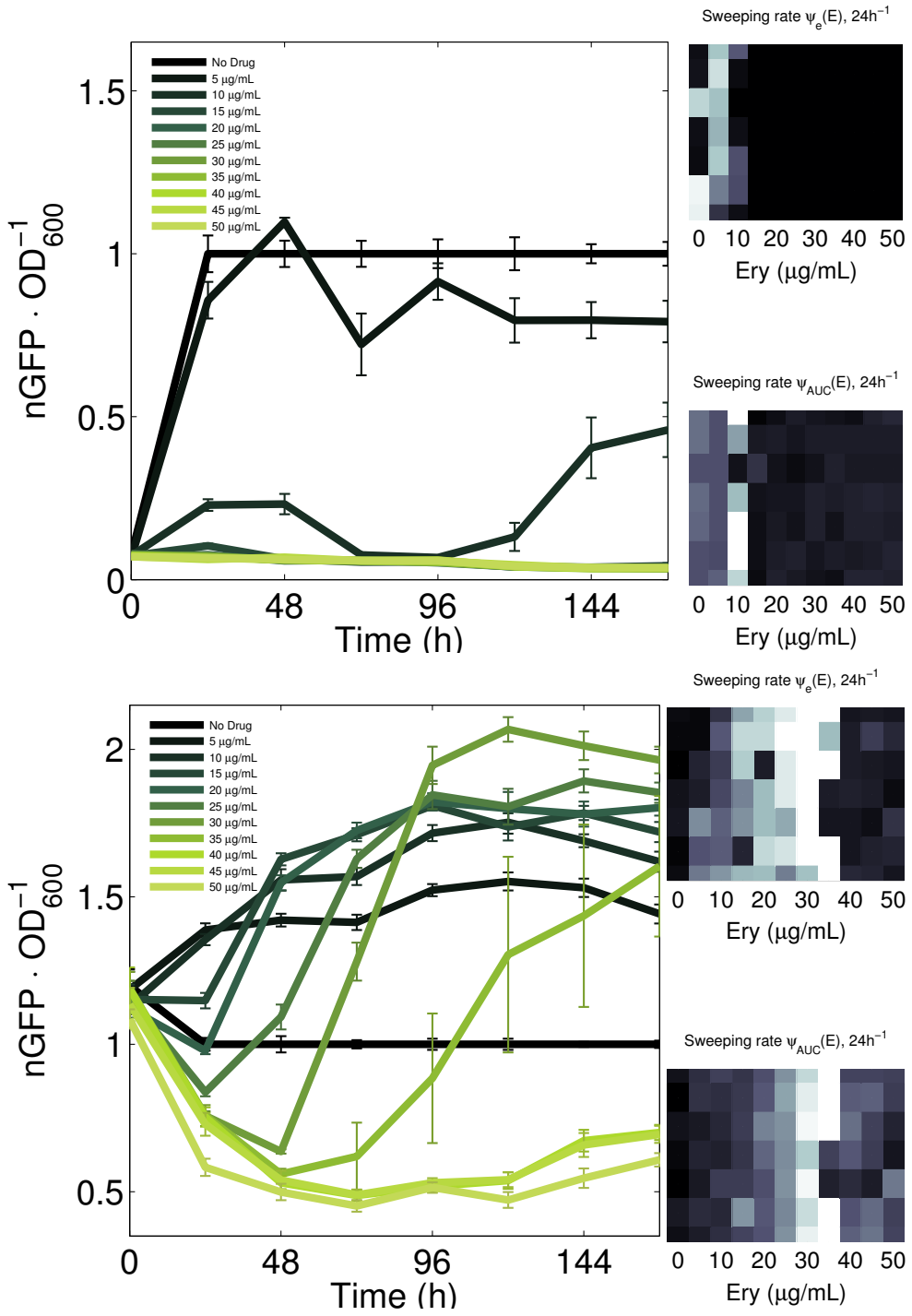

FIGURE 2.27. Estimation of the number of AcrB proteins per cell for populations the strains *E. coli* TB108 (top) and eTB108 (bottom) as time changes. The two main plots in the left-hand column represent the relative normalised GFP per OD_{600} in each population (y-axis, shown are means ± standard error, n = 8) as a function of time (x-axis) and the different concentrations of erythromycin have different colours. The subplots in the right-hand columns show sweep rates per replicate as a function of erythromycin (Ery) whereby lighter squares have higher values (8 replicates shown). The rate of sweep (ψ) is measured using AUC as implemented in EQUATION 2.4 (bottom), and the maximum rate of change in the time-series dataset for $nGFP \cdot OD^{-1}_{600}$ (y) for robustness as $\max_{0h \leq t \leq 168h} \frac{dy}{dt}$ (top).

2.8 Genomic data confirms duplication of the AcrAB-TolC multi-drug efflux pump loci

Our hypothesis of genomic duplication events was previously based on the mathematical model in Equation 2.1. The changes on the relative abundance of AcrB-sfGFP were based on the engineered, later evolved, strain *E. coli* eTB108 (Fig. 2.27). Dr Gunther Jansen, from the University of Kiel in Germany, performed the preliminary whole genome sequencing (WGS) using a pipeline designed elsewhere.[74] The data proved that the increase through time in the relative abundance of this pump was due to the duplication of the number of copies of the *acr* operon (Fig. 2.28A).

Using the routine described in Equation S.1, we observed the rate of sweep not as a linear but rather as a non-linear function of the dose. Fig. 2.28B shows that the non-linear sweep rate is maximised at certain concentrations of erythromycin. Concentrations above or below these result in, overall, lower sweep rates.

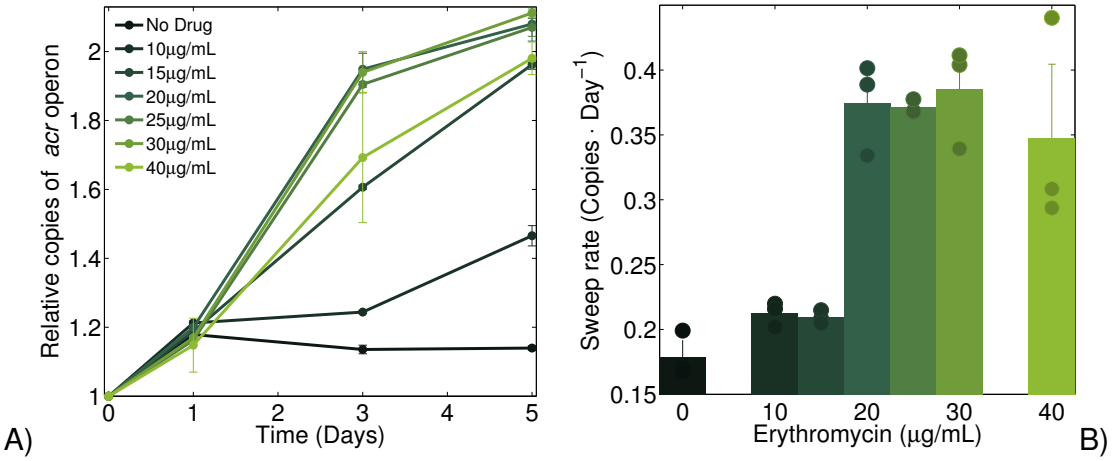

Figure 2.28. A) Genomic data for *E. coli* AG100. Coverage of the *acr* operon, relative to the genome background, as a function of the concentration of erythromycin and time (*x*-axis, mean ± s.e.m, n = 3). **B)** Rate of sweep as the increase in *acr* copies per day as a function of the concentration of erythromycin on the *y*-axis, of the *acr* operon based on the genomic data.

Using our proxy system, based on relative abundance of AcrB-sfGFP, we found the same optimal concentrations (Fig. 2.29A). This proxy also provided information that is not captured by the WGS data: the regulation of the AcrAB-TolC efflux pump due to the addition of erythromycin. In our experimental set up this pump is immediately down-regulated with the addition of the antibiotic and, only after a period of adaptation, the efflux pump is up-regulated. We are currently developing a similar pipeline to further

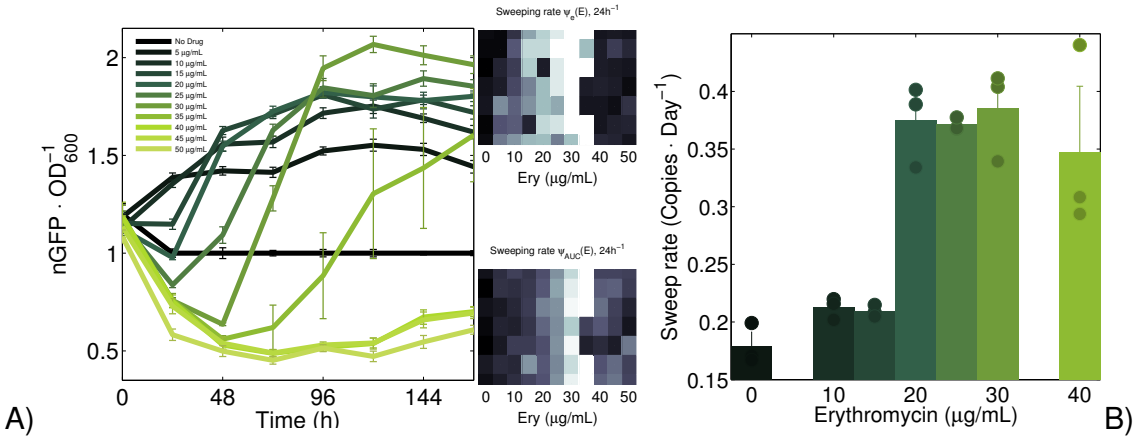

FIGURE 2.29. A) Estimation of the number of AcrB proteins per cell for populations the strains *E. coli* as time changes. The main plot in the left-hand column represents the relative normalised GFP per OD_{600} (y-axis, shown are means ± standard error, n = 8) as a function of time (x-axis) and the different concentrations of erythromycin have different colours. The subplots in the right-hand columns show sweep rates per replicate as a function of erythromycin (Ery) whereby lighter squares have higher values (8 replicates shown). The rate of sweep (ψ) is measured using both AUC (bottom), and finite difference approximations (top) for robustness. **B)** Rate of sweep, measured as the increase in *acr* copies per day as a function of the concentration of erythromycin on the y-axis, of the *acr* operon based on the genomic data.

analyse the WGS data, and reveal whether or not there are change in the regulation of the efflux pump and if these precede the duplication event.

2.9 CONCLUSIONS

In SECTION 1.1 we introduced the principle on which antibiotic sensitivity tests stand on, whereby higher dosages of the drug always lead to fewer bacterial cells. We demonstrated that this relationship may change and the monotone decrease of bacterial cell density, as a function of antibiotic dose, may become non-monotone. Consequently, we quantified a range or *window* of antibiotic concentrations in which, though time, the antibiotic has little effect on bacterial growth density. In our case, this transition is led by the duplication of the *acr* operon and subsequently selection on cells with extra copies (*mutation window*). Moreover, we also developed a theoretical framework that is able to predict, qualitatively, the evolution of resistance to antibiotics when the underlying mechanism of resistance is based on duplications of efflux pumps. Our resulting mutation window therefore refutes the arbitrarily set boundaries of the so-called *mutant selection window* introduced in SECTION 1.2.

Also, our whole genome sequence (WGS) datasets show the relationship between

acr operon copy number. These datasets show a monotone increase in the number of *acr* operons, provided the appropriate dose. This conflicts with the dataset obtained through the quantification of the fluorescent protein AcrB-sfGFP, in which a decrease in AcrB-sfGFP production precedes a monotone increase of AcrB-sfGFP. The later dataset is not only result of the number of copies of the *acr* operon, but it also summarises the expression and translation processes required for protein synthesis. Thus, the pipeline that we are currently developing will highlight mutations that may have occurred, presumably in the *acr* regulation network, to explain the difference between WGS and AcrB-sfGFP datasets.

III ANTIMICROBIAL SENSITIVITY IN THE PRESENCE OF COMPETITORS

SENSITIVITY TO ANTIBIOTICS is quantified by exposing an isolated bacterial strain to increasing concentrations of antibiotic. The use of mixed isolates in these tests is considered to lead to unreliable results and to be a poor indicator of clinical practice.[31] Whilst this seems logical from a quantification perspective, in practice pathogenic microbes are not found in isolation. Instead, they form part of ecological communities with intricate ecological relationships between a variety of microbial species that make up both the infection and the host's *microflora*.

We argue that during an infection, the integration of the pathogen within the host's microbial communities could quite easily affect the applicability of antibiotic sensitivity data. So, in this chapter we will demonstrate, both theoretically and empirically, that antibiotic sensitivity tests (ASTs) can both underestimate and overestimate the potency of antibiotics in polymicrobial contexts. We observed that which of these two outcomes occurs in practise depends crucially on the sensitivity of the second microbial isolate used in co-culture as a competitor for resources with the first.

So, when the competitor is not sensitive to the antibiotic used, due to either the presence of a resistance mechanism or an inherent lack of sensitivity (e.g. the use of antibacterials with fungal co-cultures), we observe that the bacteria targeted had an increased sensitivity to the antibiotic. We believe this phenomenon can be explained by *competitive suppression*.[77] This is a process whereby the growth rate of one microorganism is reduced by another acting as a 'resource thief' and, at least from a

growth-reduction perspective, this theft is a process that synergyses with the action of the antibiotic. However, when the aforementioned competitor species is as sensitive to the antibiotic as the bacteria targeted, we found that the latter was less sensitive to the drug. In this case each competitor is exposed, in relative terms, to lower concentrations of the antimicrobial and thus the competition process antagonised with the antibiotic.

We also observed that when the competition for resources is extended for several seasons, where each season represents one treatment of 24h duration, the synergistic effect of the competition can be further increased leading to even higher sensitivities to the antibiotic. This effect can be maintained if the competition lasts even longer still, in which case no significant change of sensitivity was observed.

We note that within this chapter, interestingly, none of the evolutionary drug-adaptation tests performed in the presence of competitors for resources created conditions that could lead to a monotone to non-monotone profile transition.

3.1 Problem: antibiotic sensitivity is quantified on isolated strains, but antibiotics are used against microbial communities

In nature, microorganisms, such as bacteria, proliferate in conditions surrounded by cells with the same and different genotypes. Like-genotypes naturally cluster due to the dynamics of two daughter cells emerging from a single mother cell. In any case, all these genotypes reside in permanent competition for resources such as amino acids, oxygen, carbon, salts and water.[78–81] In the clinic, however, antibiotic sensitivity tests are performed on specific clonal isolates. This procedure is sustained by the idea that therapies eradicate these isolates without significant disturbance of the patient's microflora.[31] Whilst this idea is now known to be incorrect,[82,83] antibiotic susceptibility tests remained highly standardised and do not reflect the change in the understanding of how antibiotics mediate between-species competition.

3.2 Hypothesis: ecological context can alter dose response profile

Motivated by whether or not the ecological context of a given microbial isolated can interfere with its sensitivity to antimicrobial drugs, we performed sensitivity tests both in the absence (monoculture) and in the presence (co-culture) of a competitor species. To

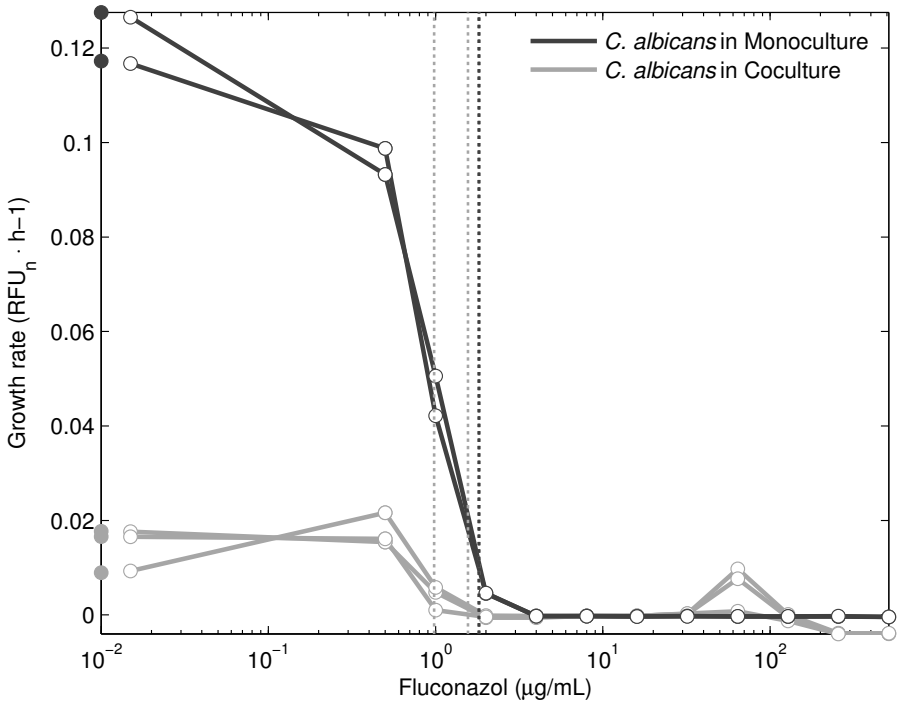

FIGURE 3.1. Dose-response profiles for *C. albicans* showing the change in growth rate as a function of the concentration of fluconazole in the absence (dark grey, n = 2), and in the presence (light grey, n = 3) of the fluconazole-resistant competitor *C. glabrata*. Growth rate in the absence of fluconazole is plotted on the y-axis. The vertical dotted lines represent the concentration at which 90% of the growth measured in the absence of fluconazole condition is inhibited, coloured accordingly (IC_{90} = 1.821 and 1.811 µg/mL in monoculture, IC_{90} = 1.563, 1.823, and 0.978 µg/mL in coculture). Data provided by Emily Cook, University of Exeter.

better understand this phenomenon, we also competed the human pathogenic *Candida albicans* with a fungal competitor, and strains of *E. coli* with a bacterial competitor (see FIGS. 3.1 and 3.2, strain details in TABLE 3.1). The sensitivity to the antimicrobial drug was measured as the concentration of drug able to inhibit 90% of the growth observed in the absence of drug (IC_{90} hereafter). Next we compared monoculture dose responses with co-culture dose-responses to assess changes in drug sensitivity due to the presence of a competitor species.

FIG. 3.1 illustrates the sensitivity of *Candida albicans* to the antifungal fluconazole, measured in the presence and in the absence of a competitor species. When this fungi was grown in the presence of *Candida glabrata* as competitor species, the resulting IC_{90} for *C. albicans* was lower than that measured in a monoculture. Note that in this case *C. glabrata* is naturally resistant to fluconazole. We will demonstrate that this is also the outcome when both competitors are bacteria later on in this chapter.

TABLE 3.1. Strains used for the validation of the competition model

Strain	***Genotype***	***Reference***
Escherichia coli Wyl	MC4100 *galK::YFP*, amp^R, pCS-λ	84
Escherichia coli GB(c)	MC4100 *galK::CFP*, amp^R, pGW155B	85
Candida glabrata	–	ATCC 2001
Candida albicans SBC153	*ura3Δ::imm434/ura3Δ::imm434 RPS1/rps1Δ::Clp10 ACT1/ACT1p-GFP-NAT1*	86

FIG. 3.2 displays the outcome of two competing bacterial species, each being sensitive to the antibiotic tetracycline to a similar degree. The competitors are the cyan fluorescence-tagged strain of *Escherichia coli* Wcl, and the human pathogen *Salmonella typhimurium*. As opposed to the previous figure, in which competitors had different sensitivities to the antimicrobial drug, the IC_{90} for the strain of *Escherichia coli* Wcl was higher in the presence of the competitor but that for *S. typhimurium* did not significantly change.

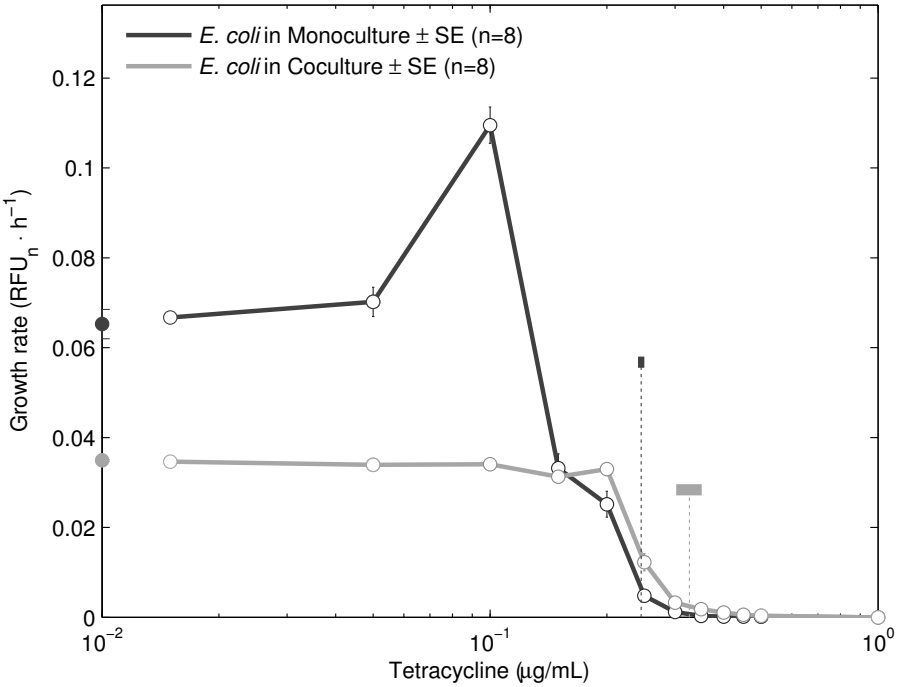

FIGURE 3.2. Dose-response profiles for *E. coli* Wcl showing the change in growth rate as a function of the concentration of tetracycline in the absence (dark grey), and in the presence (light grey) of the competitor *S. typhimurium*, where the latter is sensitive to this antibiotic. Growth rate in the absence of tetracycline is plotted on the y-axis. The vertical dotted lines represent the concentration at which 90% of the growth measured in the absence of tetracycline is inhibited, coloured accordingly: $IC_{90} = 0.245 \pm 0.004$ µg/mL in monoculture (mean ± 1.96 standard error), $IC_{90} = 0.326 \pm 0.024$ µg/mL in coculture. We analysed the difference between both IC_{90} using a Wilcoxon rank sum test with *ranksum* = 100, and $p = 1.55 \cdot 10^{-4}$.

These datasets suggest that ecological relationships with other microorganisms can modulate the sensitivity of a given microbial cell to an antimicrobial drug. They also suggest that such relationships can be complex, as demonstrated by the asymmetric modulation between the bacterial species *E. coli* Wcl and *S. typhimurium* in which only one of the species was affected by the competition. The cause of such asymmetry is beyond the scope of this PhD project, therefore we sought to simplify the protocol by instead using two strains of the same bacterial species in order to better understand how direct competition for a common resource can mediate drug resistance.

This common genetic background would provide identical metabolic profiles of each competitor and the sensitivity to antibiotics of one of the competitors can be controlled with the introduction of specific resistance genes on a plasmid. This artificially creates a competition that is analogue to the datasets represented above and is a simple proxy for the kind of microbial community that motivated this study. A theoretical

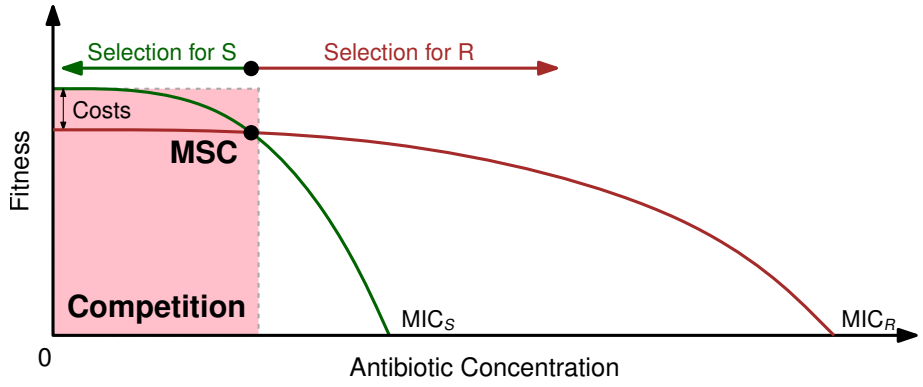

FIGURE 3.3. Model of the *minimal selective concentration* (MSC).[19] Fitness, typically measured as growth rate after 24h of growth, is represented in the y-axis as a function of the concentration of antibiotic, represented in the x-axis. This model assumes the existence of a 'cost of resistance',[87] whereby mutations conferring resistance to antibiotics are also associated with lower fitness. Thus, in the absence of antibiotics, the drug-sensitive competitor (hereafter denoted by 's') has a higher growth rate after, say, 24h of growth, than the resistant type (denoted by 'r'). However, the *s*-type has a higher sensitivity to the antibiotic and therefore $MIC_s < MIC_r$. As a consequence, the addition of antibiotic to a mixed culture of *s* and *r* forces a 'crossing point' between these two dose-response profiles. This crossing point defines the MSC, a concentration at which both competitors have the same fitness and whereafter selection on the resistant competitor begins. Note that MIC_s and MIC_r are measured in monoculture only. We conducted competition experiments at concentrations at which only the sensitive type is predicted to have changes in fitness (pink).

framework developed elsewhere[19] (FIG. 3.3) is relevant to the analysis of our proxy for a multi-species, drug-treated community.

We used the above framework to mimic selection on antibiotic resistance in mixed bacterial populations composed of species with different sensitivity to antibiotics. It has been proposed that mutations, or plasmids, that provide resistance to antibiotics are often associated with low relative growth rates in the absence of the antibiotic.[87] Thus the difference in sensitivities assumed by this framework results in different growth rates,[19] as part of an effect known as resistance mutations having fitness 'costs of resistance'.

FIG. 3.3 illustrates the case of a competition between two bacterial strains, each with different sensitivities to an antibiotic and the existence of costs of resistance. If antibiotic sensitivity is measured for each strain separately (in monoculture) using the *minimum inhibitory concentration* or MIC, then $MIC_S < MIC_R$ must be satisfied (S and R denote the sensitive and resistant strains, respectively). Moreover, the growth rate after 24h of growth in monoculture (r) must satisfy that $r_S > r_R$ due to the existence of costs of resistance. With these conditions, the resulting dose-response profiles cross each other when they are overlapped. The crossing point highlights the existence of a

concentration at which both strains have the same growth rate or fitness. Known as the *minimum selective concentration* or MSC, this concentration sets the drug dosing boundary at which selection on the resistant strains begins (FIG. 3.3). This allowed us to frame basic predictions of the drug dosages which select for or against the most resistant strain: below the MSC dose it is the drug-susceptible strain that has the higher growth rate, whereas above the MSC it is the drug-resistant.

However, this statement is based on fitness (growth rate) determined in monoculture. In terms of changes in sensitivity to the antibiotic that are observed in the presence and in the absence of competition, this framework makes no predictions. We therefore sought to also refine the notion of the MSC using our two-strain microbial community and asked whether the monoculture dose-response data is relevant to predict the MSC.

Our first approach to these questions was theoretical and we present a mathematical model, shown below, that implements the costs of resistance discussed above with the following rationale. We considered two monoclonal populations of bacteria with different sensitivities to an antibiotic, where the density of the sensitive population is denoted as S and R denotes that of the resistant population. The growth of these populations depends on a source of carbon, C, which these cells take from the environment using a transporter (FIG. 3.4). Thus, as we explained in the previous chapter, we defined the growth function for these two populations as $G_x(C_0) = \frac{VC_0}{K_m+C_0}$. Note that the growth parameters V and K_m for both populations, generically denoted as x, are identical. These parameters denote the maximal uptake and half-saturation constants, respectively. Then an antibiotic A is supplied at the concentration A_0. As mentioned in the previous chapter, A diffuses into the cells at a rate φ and binds to the transporter, with affinity κ, to reduce the growth of the cells. The resulting inhibition function is $\gamma(A) = \frac{1}{1+\kappa A^2}$, where 2 is the Hill coefficient.[75] The growth function of the sensitive population is herefore redefined as $G_s(C_0, A_0) = \frac{VC_0}{K_m+C_0} \cdot \gamma(A_0)$ whereas the growth of R remains as $G_r(C_0) = \frac{VC_0}{K_m+C_0}$ for simplicity. The concentration of A found in each population is noted as A_s or A_r, depending on whether the population is sensitive or resistant. However, as proposed by the authors of REFERENCE 19, the resistance of R will come at a cost that reduces the growth rate or *fitness* (Γ).

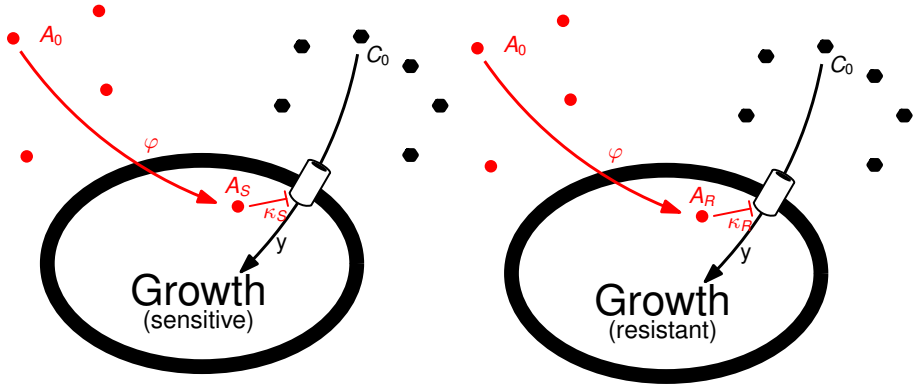

FIGURE 3.4. Diagram of the mathematical model formalised in EQUATION 3.1. A_0 and C denote the concentrations of antibiotic and carbon, respectively, in the environment. Each cell contains an enzyme (black) able to take C from the environment and process it to grow (the growth rate function is defined as $G(C) = y \cdot VC/(K_m + C)$, y denoting the yield per molecule of C, V the maximum rate at which C is processed, and K_m the enzymatic half-saturation constant). A_0 diffuses into the cells at a rate φ, binding to the enzyme and reducing the growth of the cell (a growth inhibition function is defined to be $\gamma(A) = 1/(1 + \kappa_j A_j^2)$, $G(C)$ being redefined as $G_j(C, A) = y \cdot VC_0/(K_m + C_0) \cdot 1/(1 + \kappa_j A_j^2)$). Here j denotes the type of bacterium, either sensitive (S) or resistant (R), $\kappa_R \ll \kappa_S$. We assume that antibiotic degrades through time at a rate d. Finally, the growth function $G_R(C, A)$ is modulated by the cost of resistance parameter $\Gamma > 0$.

To make this model compatible with experimental methodologies we assumed that a sample of the entire culture, either mono- or co-culture, is transferred to an environment with replenished antibiotic and resources. These transfers occur at 24h intervals and are indexed by the letter i, satisfying the expressions

$$S_i(t_{start}, C_{start}, A_{start}) = \eta \cdot S_{i-1}(t_{end}, C_{end}, A_{end})$$

, and

$$R_i(t_{start}, C_{start}, A_{start}) = \eta \cdot R_{i-1}(t_{end}, C_{end}, A_{end}).$$

Here, $0 < \eta \ll 1$ denotes the fraction of S and R transferred ($\sim 1\%$ of the culture), and $i \geqslant 1$ the number of transfers, or seasons. We formalised this model with the following set of ordinary differential equations (ODEs)

$$\frac{d}{dt}S = G_s(C, A_0) \cdot S, \tag{3.1a}$$

$$\frac{d}{dt}R = (1 - \Gamma) \cdot G_r(C, A_0) \cdot R, \tag{3.1b}$$

$$\frac{d}{dt}C = -\frac{V \cdot C}{k_m + C} \cdot (R + S), \tag{3.1c}$$

$$\frac{d}{dt}A_s = -d \cdot A_s + \varphi \cdot (A_0 - A_s) \cdot S, \tag{3.1d}$$

$$\frac{d}{dt}A_r = -d \cdot A_r + \varphi \cdot (A_0 - A_r) \cdot R, \tag{3.1e}$$

$$\frac{d}{dt}A_0 = -d \cdot A_0 - \varphi \cdot (A_0 \cdot (R + S) - (A_s S + A_r R)), \tag{3.1f}$$

We considered the cases where the initial inoculum was formed by i) the strain S (monoculture), ii) the strain R (monoculture), and iii) a mixture of equal proportions of both strains (50%S + 50%R) in co-culture, and solved the model numerically in Matlab using the function `ode113`, a variable order Adams-Bashforth-Moulton PECE solver.[88] This model makes several predictions. The first prediction was that antibiotic sensitivity increases depending on whether or not a second microbial population is present (FIG. 3.5). There is no explicit definition of how the strains interact with each other in our model, which leaves the use of a common source of carbon as the only explanation for this prediction. The reduction in growth by 'carbon theft' is known as *competitive suppression*[77] and it also enhanced the potency of the antibiotic according to our model (FIG. 3.6).

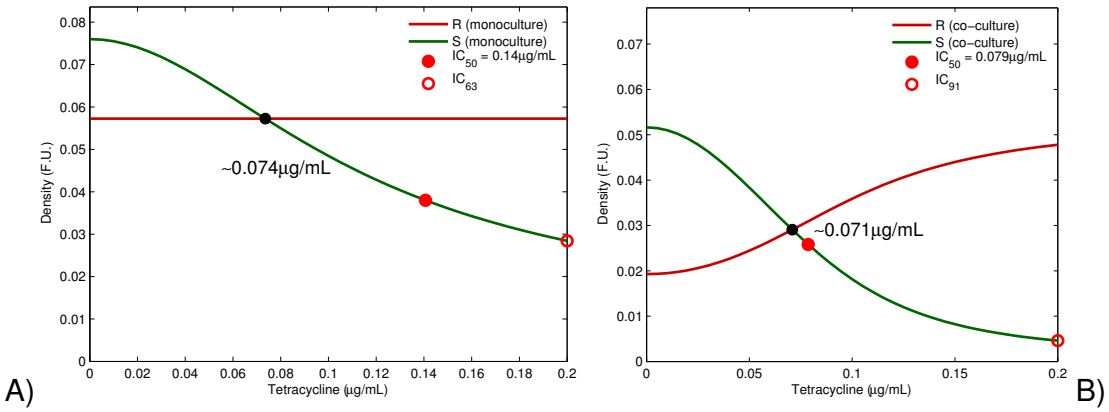

FIGURE 3.5. Our theory predicts that the S strain is more sensitive to tetracycline in the presence of a competitor than in its absence. **A)** The monoculture dose response of the S (plasmid-free) and R (resistant plasmid carrying) strains of *E. coli*. This shows that the R strain can be considered completely resistant over the range of dosages applied but the S strain has an IC_{50} over 0.14µg/mL of tetracycline. **B)** Co-culture experiment with the 50-50 inoculum of S and R strains, where the IC_{50} of the S strain has now shifted to 0.074µg/mL. Moreover, 0.2µg/mL tetracycline is the IC_{91} in co-culture whereas it is the IC_{63} in monoculture. The numerical values for the parameters are S_0 = 0.001 cells, R_0 = 0.001 cells, A_0 = 0.2µg/mL, C_0 = 100µg/mL, V = 2,400µg/cell/hour, K_m = 1µg/mL, γ= 0.75, φ = 10^3ml/cell, κ = 400mL/µg, d = 0.1 /h, η = 0.01, carbon conversion factor = 0.00075 cells/µg.

The other predictions apply if the competition lasts more than a 24h season. For example, our model predicted that the competitive suppression previously observed was intensified and sustained through time (FIG. 3.7). It also predicted the arrangement of the co-culture in three different 'niches' mediated by antibiotic dose. The most sensitive strain outcompeted its resistant counterpart in the first of these niches, which was defined at relative low concentrations of antibiotic. The next niche was defined

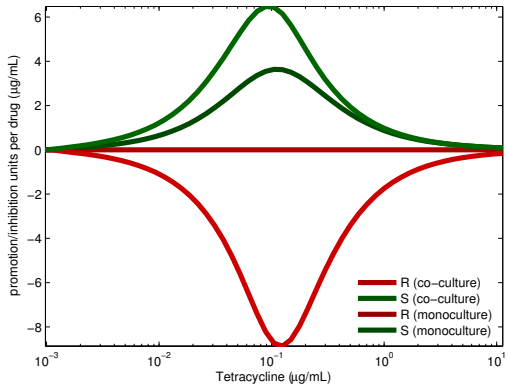

FIGURE 3.6. Predicted inhibition per molecule of drug in the absence, and in the presence, of a competitor with different sensitivities to the antibiotic tetracycline. The sensitive competitor (S) is inhibited with less tetracycline in the presence of a resistant competitor (R) due to *competitive supression*. Equally, the growth of R is promoted due to a similar phenomenon with opposite effect, namely *competitive release*,[35] whereby the eradication of a competitor (in this case by the use of antibiotics) leaves the unaffected competitor with more resources to grow.

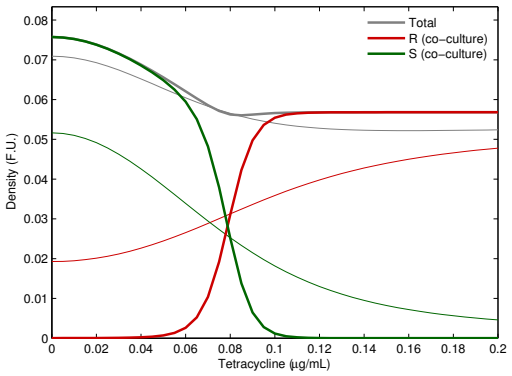

FIGURE 3.7. Theoretical prediction of the existence of a concentration of antibiotic at which, within a mixed culture, sensitive (s, green) and resistant (r, red) competitors have identical fitness (MSC). The thin and thick lines represent the predictions after one day and seven days of mixed growth, respectively. The crossing point defines the MSC, which is here predicted to be different after seven days of competition.

at relative high concentrations of antibiotic and was dominated by the most resistant strain. In this niche the sensitive strain was outcompeted. Finally, the third niche sat in between the previous two. In this niche both competitors were co-maintained, as opposed to the other niches in which only one of the strains survived.

The aforementioned *minimal selective concentration* (MSC) was located in the third niche. The arrangement of these niches, however, was not immediate. The precise boundary concentrations for each of them changed through time until they eventually reached an equilibrium, in which the concentrations defining the niches no longer changed. The MSC also changed through time and met an equilibrium, which depended on the volume of the culture transferred with every season. Thus the MSC

at equilibrium can be higher or lower than the MSC measured after a 24h season. With our transfer volume, previously defined as 1% of the culture, the model predicts an increase through time of the MSC. This latest prediction contradicts the role of the MSC, measured after 24h of growth, as the parameter defining where selection on resistance begins. Our model demonstrates that this concentration is dynamic and sits within a stable interface in which two competing species can be co-maintained. This interface separates the niche which selects for the most sensitive competitor from that which selects for the most resistant competitor. Finally, we sought to test these predictions in the laboratory.

3.3 Validating the theoretical model experimentally: we show antibiotic sensitivity in competition is not consistent with ASTs, and the IC_{90} can shift towards lower concentrations

Many bacterial species are able to produce antibiotic-like substances called 'bacteriocins' which are used to remove neighbouring competitor species.[81] These substances are highly specific and can lead to cross-resistance with antibiotics.[89] Thus, bacteriocins would be a confounding factor that could confound a study of competing microbial species in the presence of an antibiotic. To avoid such effects we decided to compete bacteria with a common genetic background. We used two strains derived from *E. coli* MC4100 that had different fluorescent markers inserted in the chromosome (Table 3.1). This allowed us to track each strain in mixed cultures. Moreover, one of the strains was modified to contain the plasmid-borne locus *tet(36)*, which confers resistance to the tetracycline class of antibiotic. We labelled this strain as Tet^r, and its sensitive counterpart as Tet^s.

Consequently these strains are consistent with our theoretical model in which the only difference between them was the degree of resistance to the antibiotic. Our experimental protocol also implemented other conditions introduced in our model. We began the co-culture experiment using a mixed culture which contained equal number of cells for Tet^r and Tet^s as inoculum. Also, the experiments were conducted for seven 24h seasons and the initial conditions of the following season were set by transferring 1% of the culture. We set up a 96-well microplate with minimal media containing

0.4% (w/v) of glucose, 0.1% (w/v) of casamino acids and eleven concentrations of tetracycline ranging from 0 (control) to 0.5 or 15µg/mL, depending on the strain. The cultures were incubated for 24h and later transferred to microplates with an identical conditions using a 96-well pin replicator. For experiments involving monocultures or co-cultures a sample for each strain was grown overnight (>16h), which were later used as inoculum.

As before with the above theoretical study, we first quantified the sensitivity to tetracycline of each bacterial strain separately. We naturally named this condition *monoculture* and denoted it by the letter *m*, as opposed to the condition where both strains were grown together in a mixed culture or *co-culture*. We noted the latter using the letter *c*. Next, the optical density was read at 600nm (OD_{600} or just OD) for each strain grown in monoculture as well as the fluorescence (RFU). The fluorescence was read at 505nm/540nm (excitation/emission wavelengths) for yellow fluorescent protein and at 430nm/480nm for cyan fluorescent protein. The OD_{600} readings were used to normalise the fluorescence signal (RFU_n) and correlate fluorescence with the densities of each bacterial strain in co-culture. We denoted yellow (YFP) and cyan (CFP) reads in the plate-reading device as y and c, respectively, and calibrated the values y_0 and c_0 so that $1 \times OD_{600} = y_0 \cdot \mathrm{YFP}_{max}$ and $1 \times OD_{600} = c_0 \cdot \mathrm{CFP}_{max}$. These values provided the number of OD_{600} units per yellow and cyan fluorescence unit. We read the data triple (y_r, c_r, OD_r) from the plate reader and defined the expected values of optical density (OD^e) for each strain as $y_{od} = y_r \cdot y_0$ and $c_{od} = c_r \cdot c_0$ so that $y_{od} + c_{od} = OD_r$ was satisfied. We also estimated the fraction of each strain in the mixed culture as

$$f_y = \frac{y_{od}}{y_{od} + c_{od}} \text{ and } f_c = \frac{c_{od}}{y_{od} + c_{od}}.$$

Finally we calculated the growth rate of each strain, r, using the following finite difference (forward Euler) approximation. We represented the change through time of RFU_n as $F(t)$ and defined its derivative as

$$F'(t) = \frac{F_{t+\Delta t} - F_t}{\Delta t}$$

where

$$r = \max_{0 \le t \le 24h} F'(t).$$

Here Δt is the read frequency in hours and r is expressed as maximum increase in RFU_n per hour. To test whether or not the MSC is sensitive to the way the growth rate is calculated, we also estimated the *per capita* growth rate using the routine in EQUATION S.1. This growth rate is expressed as doublings per hour.

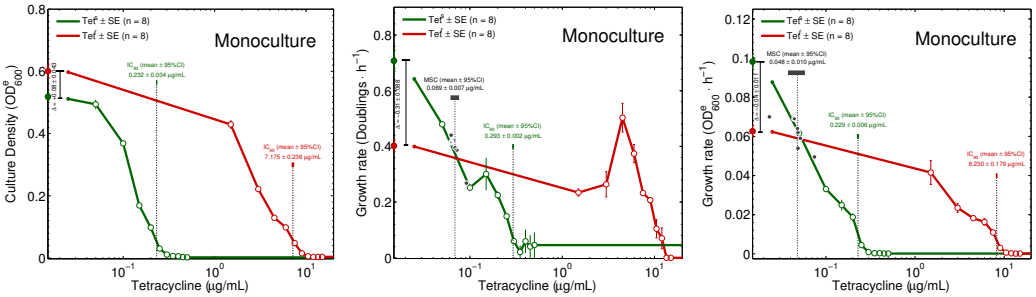

FIGURE 3.8. Overlapped dose-response profiles for Tet^r_m (red), and Tet^s_m (green) in monoculture. Culture growth is represented as **left)** optical density estimated from normalised fluorescence (OD^e_{600}), **centre)** *per capita* growth rate, and **right)** maximum increase in OD^e_{600} per hour on the *y*-axis, whereas the concentration of tetracycline is represented on a logarithmic scale on the *x*-axis. Upon detection, the MSC is represented in dark grey the IC_{90} for Tet^s in green, and that for Tet^r in red. For each case, we quantified the costs of resistance as the difference between Tet^r and Tet^s in the absence of tetracycline (data shown on the *y*-axis).

FIG. 3.8 displays the dose-response profiles of each strain grown in monoculture in the presence of the antibiotic tetracycline. For convenience, these profiles were overlapped and used to calculate parameters such as the MSC, and IC_{90}. We observed the MSC to be highly sensitive to the way it was calculated. The numerical value for this concentration was different between either form of growth rate and we were also unable to measure it using OD^e. The sensitivity to tetracycline was rather similar despite of the data used, Tet^s being $\sim$ 30 times more sensitive to the drug than Tet^r. Finally we measured the costs of resistance as the difference in growth rates and culture density between both strains in the absence of antibiotic. The resulting costs also were highly sensitive to whether we used culture density or growth rates.

Next, we repeated the previous measurements when the strains were grown in co-culture. Due to such difference in sensitivity, Tet^s set a limit as to how much tetracycline we could use, so we used a range of concentrations wide enough to be toxic for Tet^s but not for Tet^r. As predicted by our theoretical model, the resulting MSC and IC_{90} were different from those measured in monoculture (FIGS. 3.9 and 3.10). The IC_{90} was reduced between 30 to 50% depending on whether the concentrations were calculated using cell density or growth rate. The MSC was reduced in such conditions by 80%

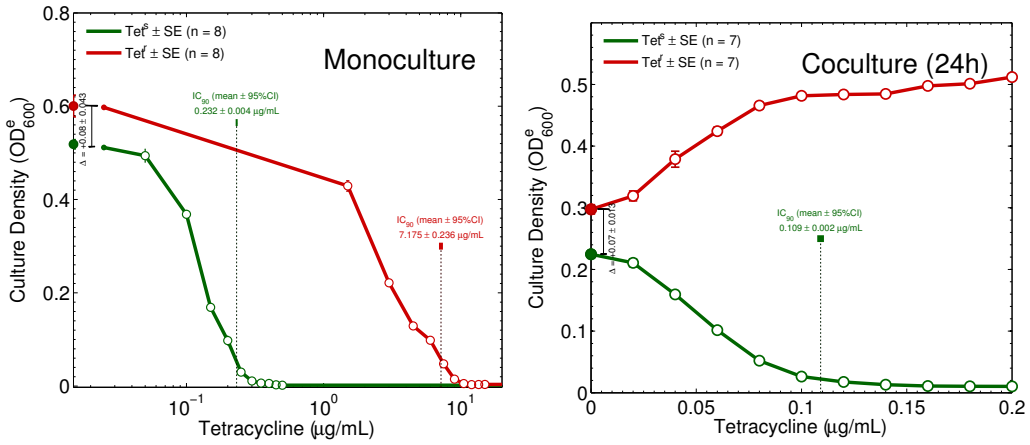

FIGURE 3.9. Left) Overlapped, culture density dose-response profiles for each competing strain grown in monoculture. For more information see FIG. 3.8. **Right)** Overlapped, culture density dose-response profiles for each competing strain grown in coculture over 24h. We quantified the costs of resistance as the difference between Tet^r and Tet^s in the absence of tetracycline (data shown on the *y*-axis). We used a Wilcoxon rank sum test to analyse the differences in IC$_{90}$ ($p = 1.55 \cdot 10^{-4}$ and *ranksum* = 100).

and was coupled with the nearly total reduction of the costs of resistance. Although this last observation is not entirely consistent with our mathematical model, the MSC did change when the strains were grown in co-culture just as our model predicted.

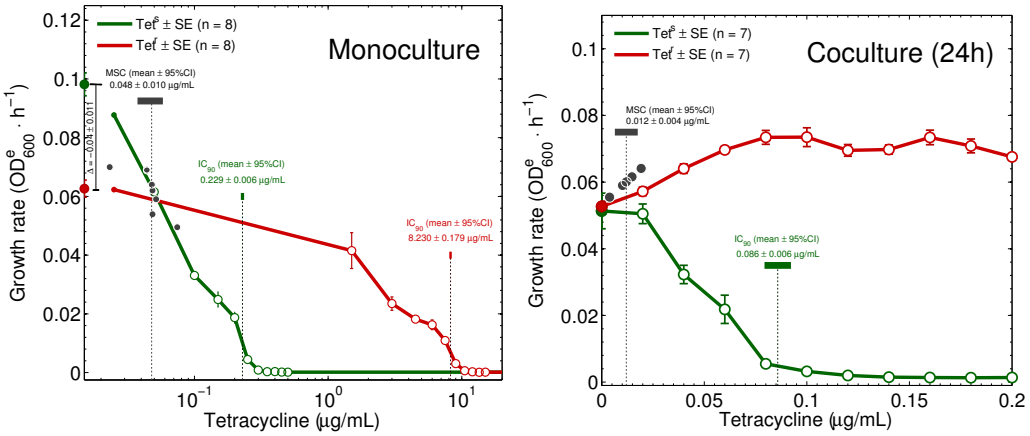

FIGURE 3.10. Overlapped, growth rate dose-response profiles for each competing strain grown in monoculture (left) and 24h of coculture (right). For more information see FIG. 3.8. Upon detection, the MSC is represented in dark grey the IC$_{90}$ for Tet^s in green, and that for Tet^r in red. We quantified the costs of resistance as the difference in between Tet^r and Tet^s in the absence of tetracycline (data shown on the *y*-axis). We used a Wilcoxon rank sum test to analyse the differences in IC$_{90}$ ($p = 1.55 \cdot 10^{-4}$ and *ranksum* = 100) and MSC ($p = 0.019$ and *ranksum* = 42).

The IC$_{90}$ for the most sensitive strain Tet^s was reduced in the presence of Tet^r in accordance with our theory. To quantify the inhibition per molecule of tetracycline, first we calculated the inhibition of growth in the presence of T µg/mL of tetracycline as G_T. If we label the growth in the absence of the drug as G_0, then $I(T) := 1 - G_T / G_0$. We

finally defined the inhibition per molecule of tetracycline as the ratio between $I(T)$ and T. When the antibiotic inhibits the growth of the culture this ratio is positive, otherwise it is negative. FIG. **??** shows that the effect of tetracycline on Tet^s was stronger in the presence of Tet^r, with the strongest inhibition being produced by a comparatively lower antibiotic dose.

FIG. 3.11 displays the raw data for the co-culture grown during seven 24h seasons, with transfers of $\sim$ 1% of the culture at 24h intervals. We presented the data as expected culture density (OD^e) obtained from fluorescence readings, relative frequency, *per capita* growth rate (doublings per hour) and growth rate (OD^e per hour) of each strain as a function of tetracycline dose. The dataset aligns well with the predictions of the model, which predicted the competitive suppression to be sustained and enhanced through time (FIG. 3.12). It also shows an increase in the number of molecules of tetracycline per cell, especially between the growth measured in monoculture and after 24h of co-culture (FIG. 3.13). To calculate this, we labelled the growth read at IC_{90} in each condition as G_{90} and used the ratio between IC_{90} and G_{90} as a proxy to estimate the concentration of tetracycline per cell.

In terms of culture density, Tet^s overcame the 'benefits of resistance' observed for Tet^r in the absence of tetracycline. This was coupled with the *emergence* of a crossing point (MSC) between the dose-response profiles of some of the replicates (FIG. 3.14). During the length of the experiment, the MSC shifted towards higher concentrations of tetracycline as predicted by our model (FIG. 3.7). When we measured the MSC using growth rates it remained unchanged during the seven days (FIG. 3.15). However, Tet^r was not able to outcompete Tet^s until the dose of tetracycline was well beyond the MSC. We interpreted this as the niche predicted by our model in which both competitors could be co-maintained, mediated by antibiotic dose, and where we would find the MSC. When the dose of tetracycline was higher we could no longer measure the presence of the most sensitive strain Tet^s and therefore these concentrations defined the niche which selects on the most resistant competitor Tet^r. The existence of a niche selecting for the most sensitive strain was not observed.

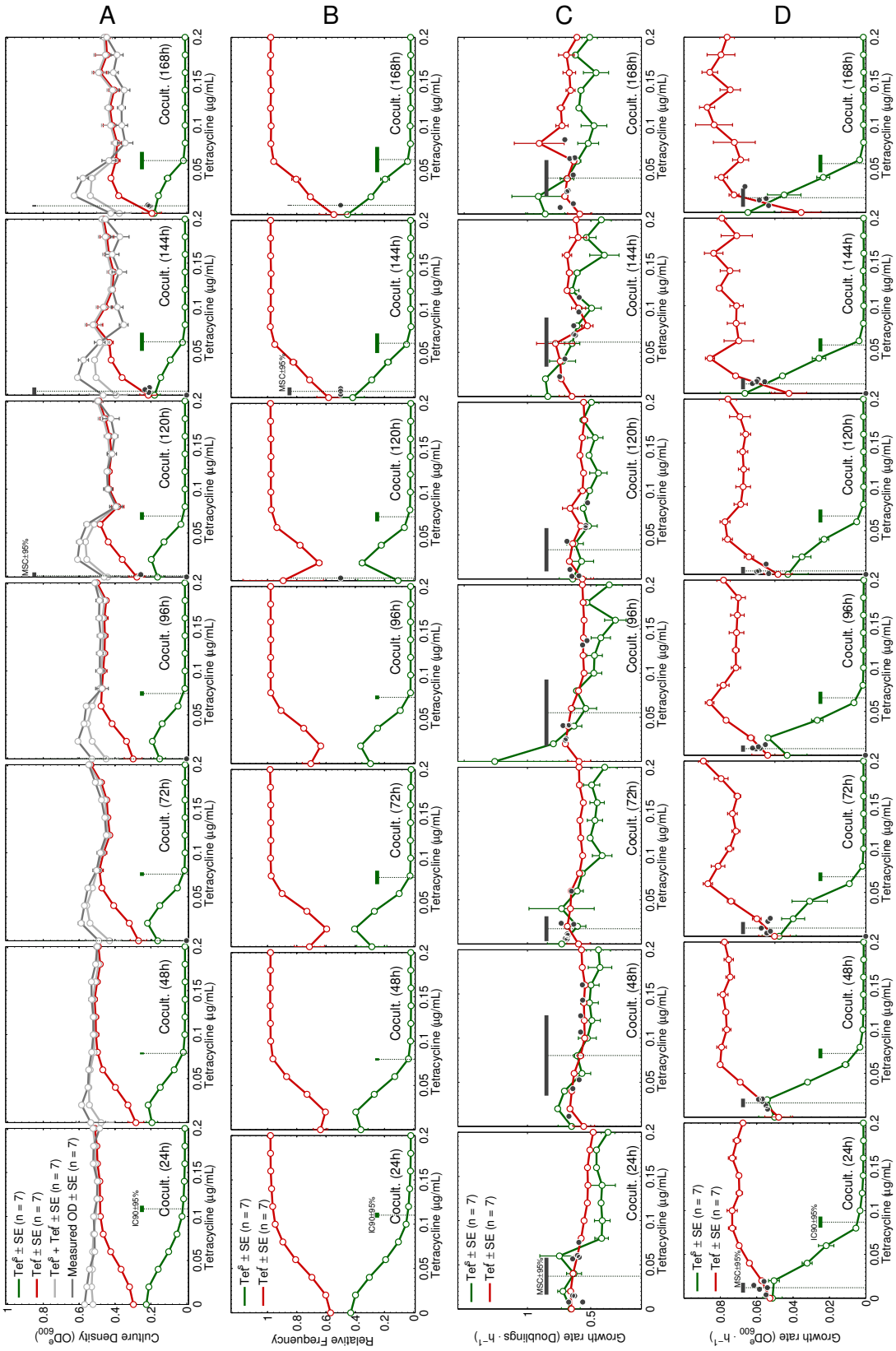

FIGURE 3.11. Overlapped dose-response profiles for Tet^r (red), and Tet^s (green) during the seven days of co-culture. Changes in **A)** optical density estimated from normalised fluorescence (OD$^e_{600}$), **B)** relative frequency, **C)** *per capita* growth rate, and **D)** maximum increase in OD$^e_{600}$ per hour as a function of the concentration of tetracycline. Upon detection, mean ± 95% confidence intervals are shown for the MSC, represented in dark grey, and the IC$_{90}$ for Tet^s, in green.

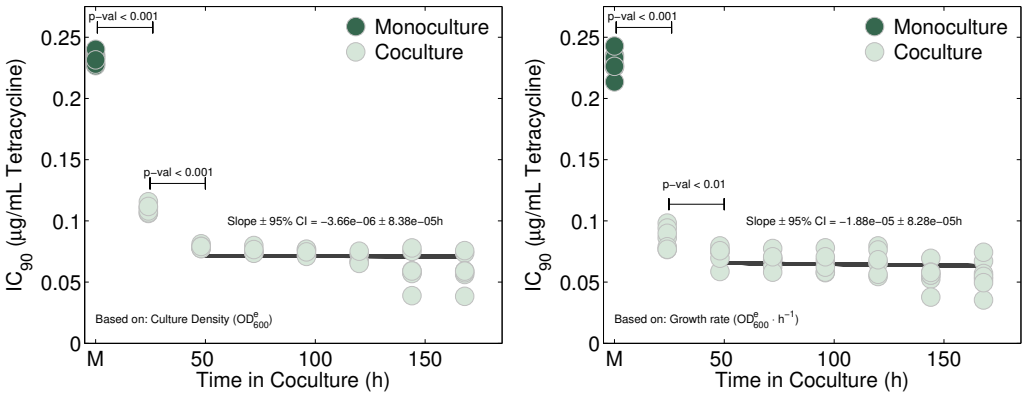

FIGURE 3.12. Change in the IC_{90} as a function of the growth conditions (monoculture or coculture) and competition length based on culture density (left), and maximum increase in OD^e_{600} per hour (right). We analysed the difference in the IC_{90} between that measured in monoculture (label M) and after 24h of coculture using a Wilcoxon rank sum test with $p = 1.55 \cdot 10^{-4}$ and *ranksum* = 100 for data based either on culture density (left) or growth rate as OD^e_{600} per hour (right). We also quantified differences in the IC_{90} measured after 48h of coculture, with $p = 3.10 \cdot 10^{-4}$ and *ranksum* = 92 for the data based on culture density (left), $p = 0.002$ and *ranksum* = 89 for data based on growth rate as OD^e_{600} per hour (right). The linear model $IC^c_{90} = a + bt$ is represented in dark grey, the parameter b not being significantly different from zero.

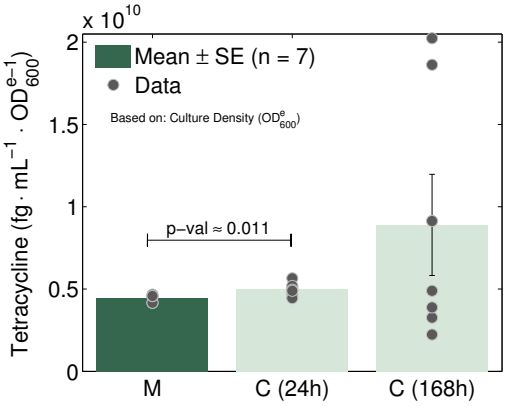

FIGURE 3.13. Relative concentration of tetracycline per optical density unit (OD^e_{600}) for the sensitive strain Tet^s in monoculture (labelled *M*), after 24 and 168 hours of competition (labelled C). The barplots represent mean ± standard error (n = 7), whereas the raw data is shown as circles. We analysed the differences between M and C(24h) using a Wilcoxon rank sum test with $p = 0.011$ and *ranksum* = 33.

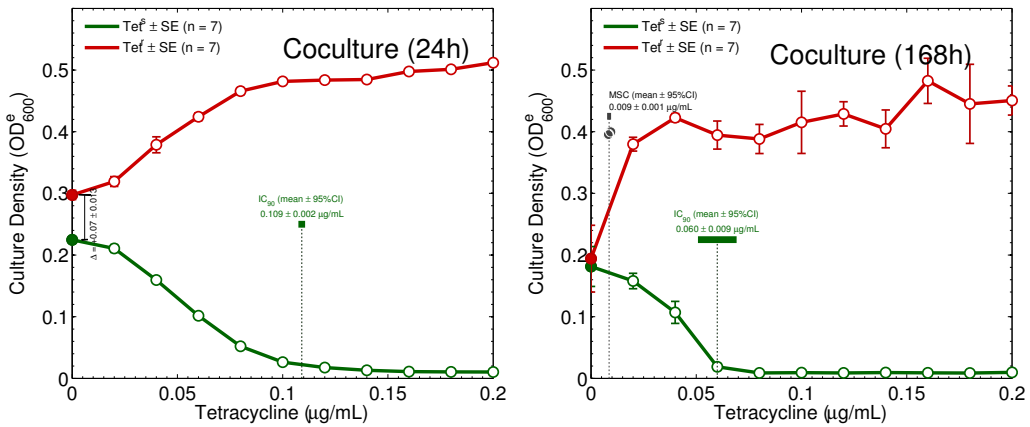

FIGURE 3.14. Overlapped, culture density dose-response profiles for each competing strain grown in coculture over 24h (left) and 168h (right). Upon detection, the MSC is represented in dark grey the IC_{90} for Tet^s in green, and that for Tet^r in red. For each case, we quantified the costs of resistance as the difference in between Tet^r and Tet^s in the absence of tetracycline (data shown on the *y*-axis). We used a Wilcoxon rank sum test to analyse the differences in IC_{90} ($p = 5.84 \cdot 10^{-4}$ and *ranksum* = 77). The costs of resistance are shown on the *y*-axis as the difference between Tet^r and Tet^s in the absence of tetracycline.

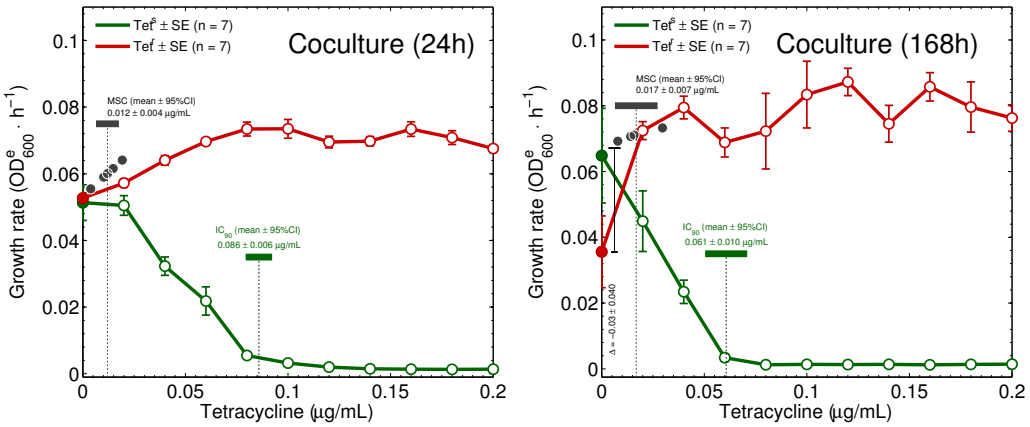

FIGURE 3.15. Overlapped, growth rate dose-response profiles for each competing strain grown in coculture over 24h (left) and 168h (right). Upon detection, the MSC is represented in dark grey the IC_{90} for Tet^s in green, and that for Tet^r in red. For each case, we quantified the costs of resistance as the difference in between Tet^r and Tet^s in the absence of tetracycline (data shown on the *y*-axis). We used a Wilcoxon rank sum test to analyse the differences in IC_{90} ($p = 0.00408$ and *ranksum* = 31) and MSC for which no statistical difference was found. The costs of resistance are shown on the *y*-axis as the difference between Tet^r and Tet^s in the absence of tetracycline.

3.4 Further predictions: the number of resistance plasmids per R cell is predicted to increase with the dose

Above we noted that the most resistant competitor, Tet^r, carries a plasmid-borne mechanism of resistance (*tet(36)*). Yet the mathematical model in Equation 3.1 does not include explicitly resistance as a function of the number of plasmids. We now rectify this omission by introducing the following theoretical model.

$$\frac{d}{dt}S = G_s(C, A_0) \cdot S \tag{3.2a}$$

$$\frac{d}{dt}R = \mathcal{M}\Big((1-\Gamma) \cdot G_r(C, A_0) \cdot R\Big) \tag{3.2b}$$

$$\frac{d}{dt}C = -\frac{V \cdot C}{K_m + C} \cdot \left(\sum_j R_j + S\right), \tag{3.2c}$$

$$\frac{d}{dt}A_s = -d \cdot A_s + \varphi \cdot (A_0 - A_s) \cdot S, \tag{3.2d}$$

$$\frac{d}{dt}A_r = -d \cdot A_r + \varphi \cdot (A_0 - A_r) \cdot \sum_j R_j, \tag{3.2e}$$

$$\frac{d}{dt}A_0 = -d \cdot A_0 - \varphi \cdot \left(A_0\left(\sum_j R_j + S\right) - \left(A_s S + A_r\left(\sum_j R_j\right)\right)\right), \tag{3.2f}$$

where the sum is taken over the number of R cells with different numbers of plasmids (j). During cell division, plasmids are replicated alongside the bacterial chromosome and equally segregated between the two daughter bacterial cells.[90] In the model we assume that such segregation is not perfect, and only one plasmid can be gained or lost at a time with equal probability σ. We modelled this as a Markov process with the following transition probability matrix

$$\mathcal{M} = \begin{pmatrix} 1 & \sigma & 0 & & \cdots & 0 \\ 0 & 1-\sigma & \sigma & 0 & & \vdots \\ & 0 & 1-\sigma & \sigma & \ddots & \\ & & 0 & 1-\sigma & \ddots & 0 \\ \vdots & & & \ddots & \ddots & \sigma \\ 0 & \cdots & & & 0 & 1-\sigma \end{pmatrix}$$

for a population of R formed by j subpopulations with $j-1$ plasmids per cell. Note that if the subpopulation with one plasmid per cell loses the plasmid, we assume that it cannot be recovered.

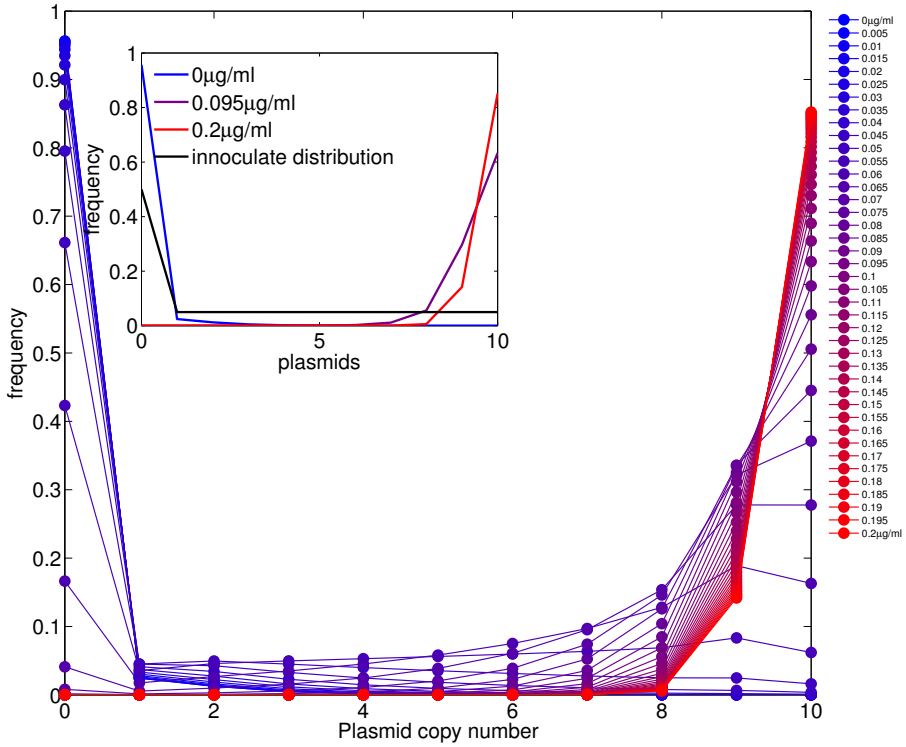

FIGURE 3.16. The main figure shows the 7-season distribution of the number of plasmids in the R-cell types when $\sigma = 0.01$. Note how these distributions are more skewed towards higher plasmid numbers as the dose of drug increases. The inset shows three particular plasmid distributions after 7 seasons, including the inoculum distribution which sees a random distribution of both s and r cell types, with a uniform distribution of plasmids in the latter case.

FIG. 3.16 illustrates the purpose of using this model. We solved this model numerically using the Matlab function `ode15s`, which uses numerical differentiation formulas (NDFs),[73] and used it to predict the existence of different distributions of plasmid numbers observed per cell at the end of seven seasons, which can be determined for each dosage. In the simulated case presented in this figure, we see that higher dosages (in red) led to higher numbers of plasmid per cell and vice versa. This occurs because because we assumed the plasmid had no copy number control and is therefore susceptible to copy number changes. These changes can occur during cell division, creating differential segregation of plasmid numbers within the dividing cell.

There are different ways of representing the same phenomenon and FIG. 3.17 shows that this new model predicts the existence of dynamics on the distribution of plasmids in the *Tet*^{r}-subpopulation as a function of the concentration of tetracycline that has a switch-like structure that occurs around 0.05μg/mL. The validation of this prediction is technically demanding, but we approximated it by measuring the mean copy number of

plasmids per cell using quantitative PCR (qPCR). We therefore calculated the number of plasmids using a protocol published elsewhere[91] (FIG. 3.18). The result of this qPCR-based protocol showed a significant positive correlation between the number of plasmids contained in each Tet^r cell after just 24h of competition with Tet^s (F-statistic *versus* constant model = 4.4, $p = 0.047$). Thus, selection on the plasmid can occur very rapidly and lead to changes in the distribution of plasmids per Tet^r-cell.

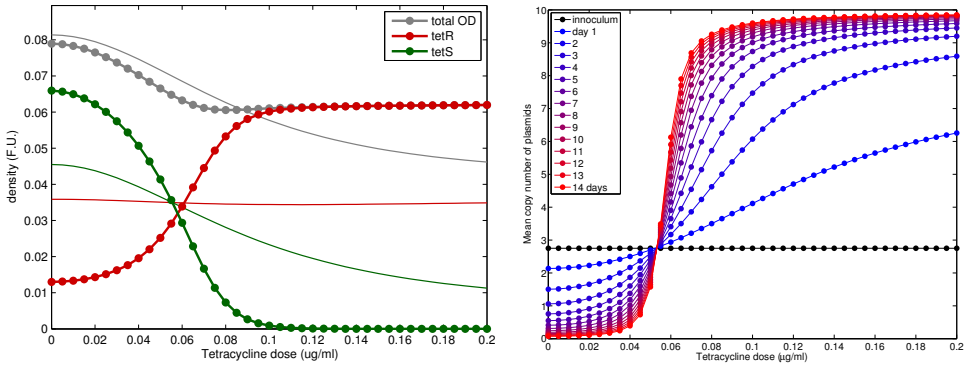

FIGURE 3.17. Left) New predicted outcome of a competition between the strains Tet^s and Tet^r. This prediction is not qualitative different from the previous version of the model. **Right)** Relative frequency of the plasmid as a function of the dose (coloured), assuming a uniform distribution at inoculation time (t = 0h).

3.5 CONCLUSIONS

During the introductory chapter, in SECTION 1.3, we highlighted a fundamental problem in antibiotic therapy design in which antibiotic sensitivity is quantified on an isolated bacterial population. The drug is, however, used on the natural microbiota of a patient (be this a person, pet or farm animal). Here we demonstrated, supported by a theoretical framework developed during this chapter, the sensitivity to antibiotics of a sensitive species can be further increased in the presence of other micro-organism when the latter is not affected by the drug. The stress produced by the antibiotic is added to the reduction of carbon and oxygen by the competing micro-organism due to an ecological phenomenon known as *competitive suppression*.

For convenience, in our case the micro-organism is resistant to the antibiotic tetracycline and thus we measured when the selection for this resistant bacterial species begins. This resistant species confronts a cost, a reduced growth rate, consequence of the plasmid-born resistance mechanism. In such circumstances it has been suggested that selection on resistance begins at a particular concentration resistance,

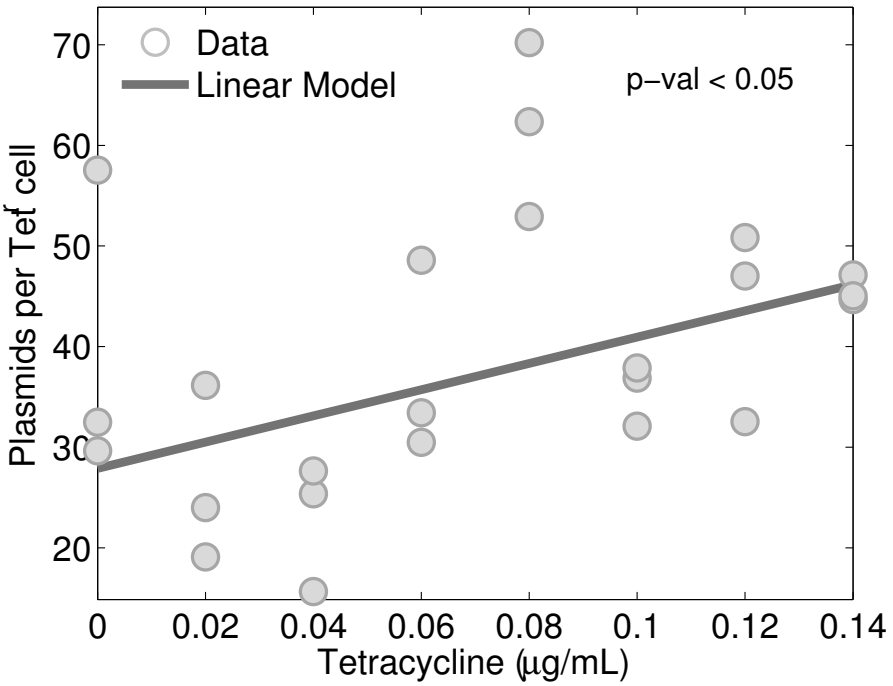

FIGURE 3.18. Relative copies of the plasmid pGW155B per cell of Tet^r after 24h of coculture with Tet^r. We robustly fitted the linear model $y = a + bx$ where the 95% confidence interval for a is (19.76, 41.35) and for b is (26.52, 284.56), with $R^2_{adj} = 0.198$. This highlights a weak, but significantly positive correlation between number of plasmids per cell and dose of tetracycline.

the so-called *minimal selective concentration* or MSC (FIG. 3.3). This concentration sets when both sensitive and resistant species have identical growth rate and, thus, higher dosages would select for the most resistant species. However, we showed that the MSC is not robust to different ways of measuring growth rate and therefore different definitions of growth rate yield different MSCs. Whether the MSC is calculated overlapping the dose-response profiles of both species, or empirically from a mixed culture also yield different MSCs. We also demonstrated that the MSC changes during the experiment. Thus, the MSC is a poor predictor of where selection on resistance begins.

In our case the resistant species harbours a plasmid with the ribosomal protection gene *tet36*. We also quantified how dose affects the plasmid copy number per cell but a weak correlation was found with the experimental setup presented in this chapter.

IV SELECTION ON THE DUPLICATION OF ACRAB-TOLC IN SPATIALLY DISTRIBUTED CULTURES

BY IMPLEMENTING AN analogy of the laboratory protocol used to determine antibiotic susceptibility, the so-called E-test, we are able to quantify aspects of selection for antibiotic resistance in a spatial drug gradient. Our main result is this. Although one might expect greater drug dose to correlate with lower population densities, we show that this expectation is not met in practice and the reasons for this are both ecological and evolutionary. We therefore show, using a combination of theoretical modelling and spatially-extended laboratory microbial growth experiments, that the growth rate of a bacterial population with genetically distinct subpopulations can be maximised at intermediate distances from the antibiotic drug. Moreover, each subpopulation, distinguishable by the number of resistance genes they carry, can have a maximal growth rate at a different spatial location.

One prediction from this observation is that microbes growing in an antibiotic gradient can exhibit, at least temporally, a certain 'bullseye' pattern formed from concentric rings. Experiments using *Escherichia coli* provide evidence for the existence of these rings and we show, using genetic manipulation of the resistance genes in question, that such a genetic manipulation can move the location of this pattern.

This chapter represented the work of an unusually large within-lab collaboration between the following people who each contributed to different aspects of the project. Their contributions are detailed as follows.

R. C. Reding Roman: implemented experimental protocols, analysed data, designed experiments and mathematical models;

M. Hewlett: designed and implemented experimental protocols, analysed data;

F. Gori: implemented computer codes to simulate mathematical models;

S. Gardner: developed a multi-fluorescence video capture device based on an Arduino controller and a commercial camera;

I. Gudelj: designed experiments, provided funding for the project from a NERC grant;

R. Beardmore: provided funding from an EPSRC grant, wrote and analysed mathematical and computer models.

4.1 Introduction: selection for resistance at different dosages

The purpose of this study is to test the following hypothesis: is it true that a greater antibiotic dose necessarily yields fewer bacterial cells? The Eagle effect, observed many years ago,[46] provides one of the earliest answers to this question, and that answer is negative for it can be the case that bacterial densities increase with increasing antibiotic dose. However, how Darwinian selection for resistance might also produce datasets like those reported by Eagle, and others, has received little attention in the literature. We therefore study this question from an evolutionary and ecological perspective, focusing on how resistance by efflux can contribute to datasets that also lead to the rejection of the above hypothesis. In short, we will conclude that a phenomenon known as *competitive release* can combine with selection on gene duplication mutations that mediate drug resistance by efflux to produce spatiogenomic patterns in which more drug need not correlate with fewer bacteria.

One of the most common assays performed in hospitals is the antibiogram,[92,93] it is an *in vitro* test for susceptibility to a range of antibiotics. At the core of antibiotic susceptibility testing is a simple laboratory test that determine zones of inhibition, these are often performed using manufacturers' so-called E-strips.[94] The E-strip is impregnated with a gradient of antibiotics and it is placed onto a bacterial lawn whereupon killing and growth inhibition of some of the bacteria can result. From this killing, a clearance appears on the lawn up to a certain drug concentration from which one can read concentrations at which the microbe is sensitive to the drug used.

As this protocol by its very design creates a spatial gradient of antibiotic, we are interested in ecological and evolutionary features that might result from the implementation of such a test. The bespoke implementation in our laboratory of an analogue of the test is illustrated in FIG. 4.1.

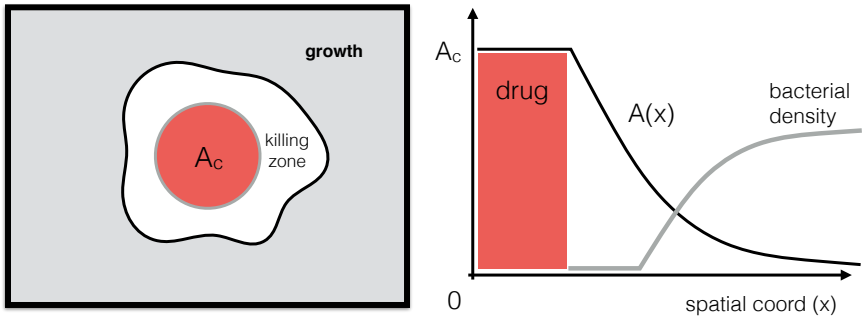

FIGURE 4.1. A schematic of our implementation of the antibiotic susceptibility test: an antibiotic drug held at high dosage at the centre of an agar plate diffuses out into a bacterial lawn, producing a killing zone or zone of inhibition where by the higher the dose, the larger the zone.

This drug susceptibility protocol is performed on an agar plate containing minimal growth medium, a carbon source, salts and amino acids. At the centre of the plate a circular region of agar is excised by hand and replaced with agar that has been impregnated with an antibiotic at a controlled dose, an antibiotic gradient therefore ensues across the plate.

It is thought that antibiotic gradients are associated with rapid selection for resistance, the idea being that a microbial population is exposed to small increments of drug which can be easily dealt with. A little like the tale in which a frog that can be boiled slowly by steadily increasing the temperature of the water of the pan in which it sits, so a microbe is thought to readily survive small increments in antibiotic dosage when an abrupt change would be lethal.[95]

We therefore use a laboratory model system in which changes in antibiotic resistance can be measured over short timescales. This system sees the bacterium *Escherichia coli* K12, strains TB108, MG1655 and AG100, treated with tetracycline and macrolide antibiotics, we use this combination because K12 has a clinically important efflux pump[96] formed from the products of the operon *acr* and the protein TolC.[97] Moreover, *acr* resides in a genomic region that can be recombined to produce duplications and triplications very rapidly under antibiotic selection pressure involving macrolides and

tetracyclines.[98]

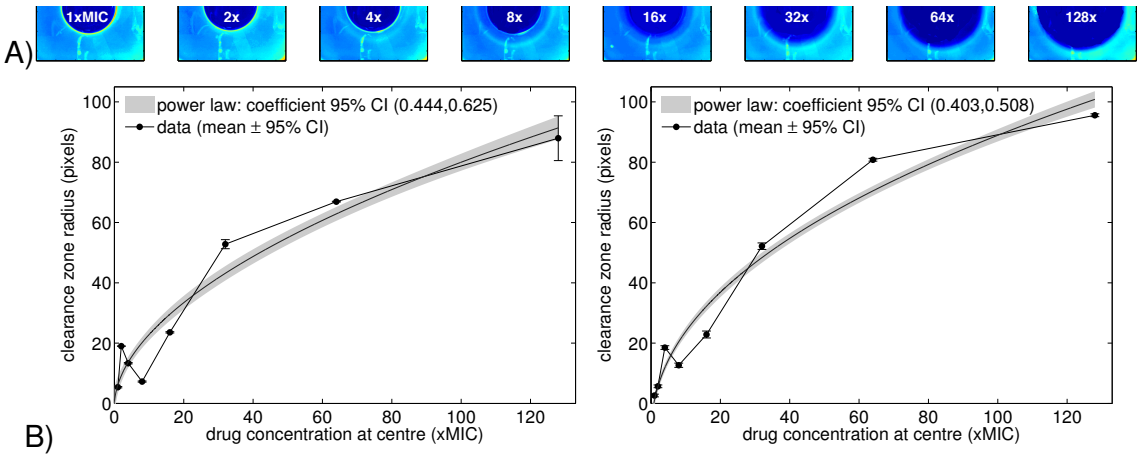

FIGURE 4.2. A) Raw data: an image of a bacterial lawn (in false colour) showing how the zone of inhibition on that lawn increases in area with increasing dose, here at 1, 2, 4,...., 128 times the MIC dose determined in liquid culture conditions. **B)** The increase in area for the tetracycline drug for strains MG1655 and AG100 follow a power law with coefficient close to a value of two: a quadratic. This is consistent with increases in zone of inhibition being described by a threshold killing model whereby escape of the drug fro the centre following a diffusion equation, as shown in the text (Statistical note: correlation coefficients are $R^2 = \{0.898, 0.959\}$ respectively, F-statistics versus constant models are $F = \{728, 1930\}$ and corresponding p-values are given by: $p = \{1.43 \cdot 10^{-82}, 3.45 \cdot 10^{-115}\}$.)

4.1.1 Inreases in the zone of inhibition of MG1655 and AG100 with dose are consistent with linear diffusion theory. The fundamental solution of the linear diffusion equation

$$A_t = \sigma A_{xx},$$

on an infinite two-dimensional domain with Dirac delta initial condition of mass A_c is given by the expression

$$A(t) = \frac{A_c}{4\pi\sigma t} \exp\left(-(x^2 + y^2)/4t\sigma\right)$$

which represents a temporally-modulated normal distribution. If we assume, as is natural, that extracellular and intracellular drug concentrations are highly correlated and, also, that the concentration of A leads to bacterial killing provided it is of a sufficiently high value, A_d say, a value known as the minimal bactericidal concentration (MBC), then the zone of inhibition, or killing, is given by those pairs (x, y) for which

$$A_d < \max_{t>0} \frac{A_c}{4\pi\sigma t} \cdot \exp\left(-(x^2 + y^2)/4t\sigma\right).$$

Let us write $r = \sqrt{x^2 + y^2}$. By taking the derivative with respect to t of the function $A(t)$ defined within the latter inequality and setting this derivative to zero, we find this maximum occurs when $t = r^2/4\sigma$. At this value of t there results $A(t) = A_c/(\pi r^2 e)$. Hence, equating $A_c/(\pi r^2 e)$ with A_d, we deduce that killing occurs up to a certain spatial radius, $r < r_d$ say, where

$$r_d = (A_c/(A_d \pi e))^{1/2}.$$

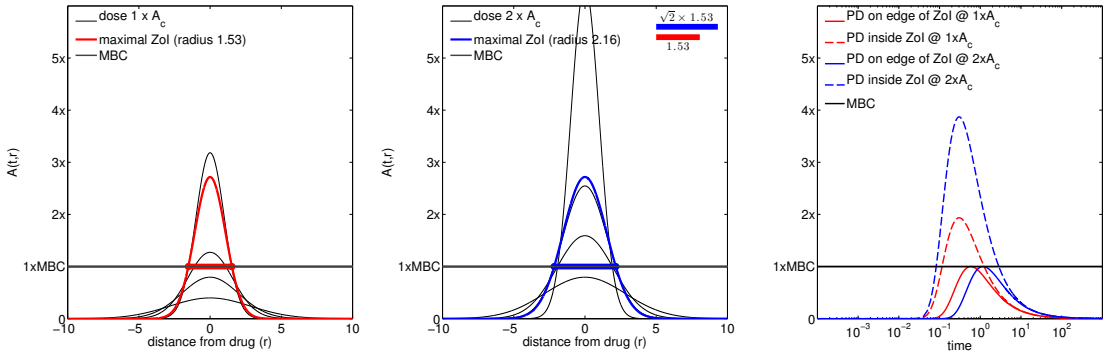

FIGURE 4.3. The leftmost plot shows the decay in drug concentration as a function of distance from the drug source, where the latter has been deployed at a value A_c. As the drug diffuses outwards, it maintains a value above the minimal bactericidal concentration (MBC) for a while, thus enlarging the zone of inhibition (ZoI), up to a maximum time point. Beyond this time, dose is too low to ensure bacterial killing occurs. The middle plot is analogous to the first, but with double the dose supplied, $2 \times A_c$. This calculation illustrates that the zone of killing increases in size by a factor $\sqrt{2}$ according to diffusion theory. The rightmost plot shows the dynamics of the drug dosage as a function of time both inside and also right at the very edge of the zone of inhibition.

If we therefore examine the plot of empirically-determined zones of inhibition, like those in FIG. 4.2, we ought to observe that the increase in radius of that zone with the dosage applied scales like the square root of the drug dose. From a nonlinear regression $p_1 + p_2 x^{p_3}$, we observe that the value $p_3 = 1/2$ lies within the 95% confidence interval for the estimate of this power coefficient. We therefore cannot reject the hypothesis that some value of the power coefficient provides a better fit than the theoretically-predicted square root law. We shall modify this simple diffusion-based theory later in order to provide more refined predictions of the nature of population dynamics in the growth region outside these zones of inhibition.

4.1.2 The AcrAB-tolC efflux system, the *acr* operon and its duplications. Outside the zones of inhibition where drug dosage is so high that bacterial killing is assured,

we anticipate a complex set of population dynamics between different tetracycline and macrolide resistance mechanisms available to the *E.coli* cell. In particular, the *E.coli* chromosome carries genes that encode proteins AcrA, AcrB and TolC which form a membrane-spanning efflux pump that includes tetracyclines and macrolides in the family of small molecule substrates that it can pump. Moreover, structure-altering mutations in AcrB are known to mediate clinical resistance to a range of antibiotics.[96].

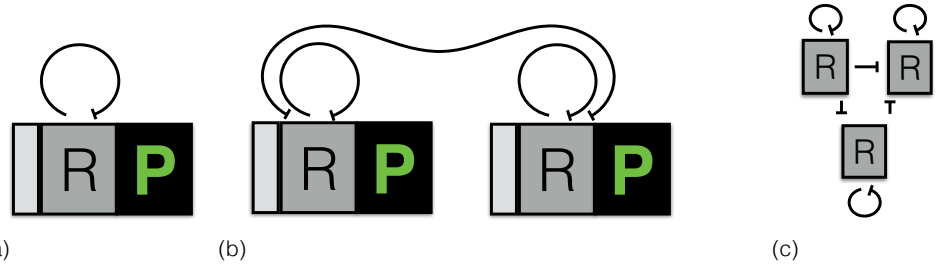

FIGURE 4.4. A) The basic structure of an operon: a promotor region in light grey, followed by a gene coding a protein that represses transcription of the same operon, followed by a second protein that encodes part of an efflux pump. We use the green font colour to highlight the fact that we have a strain which has GFP fused to the protein P, we also have strains without GFP fused to P. We have in mind that P represents the A and B proteins of the *acrRAB* operon. **B)** *E.coli* can duplicate the number of copies of the *acr* operon in its genome which leads to a novel network structure following duplication in which the two copies repress each other. **C)** Following a further duplication of one of the operons, a three-node network results with all nodes repressing each other.

The efflux proteins AcrA and AcrB are encoded within an operon *acr*, that we shall also write *acrRAB* to highlight the fact that the operon contains a triple of proteins, two of which form the pump but the first of which to be transcribed encodes a repressor of the same operon. Now, *acr* is contained within a genomic region in the *E.coli* chromosome that can be recombined into the chromosome to form a large mutation with a high mutation rate consisting of about 8% of the entire bacterial genome. Under strong selection for resistance as encoded by this pump, this region has been observed to be duplicated in doxycycline monotherapy and triplicated in a doxycycline-erythromycin cocktail treatment[98] within five days of exposure to these antibiotic conditions at low population densities.

When these operons are duplicated, triplicated, or held at an even greater copy number, this creates a growing network of ever stronger co-repression, as depicted in FIG. 4.4. Moreover, the *acr* operon is regulated by a complex stress network that includes the *mar* regulon and regulatory mutations in this operon, through *marR* can mediate expression of the AcrAB-TolC efflux pump.[98]

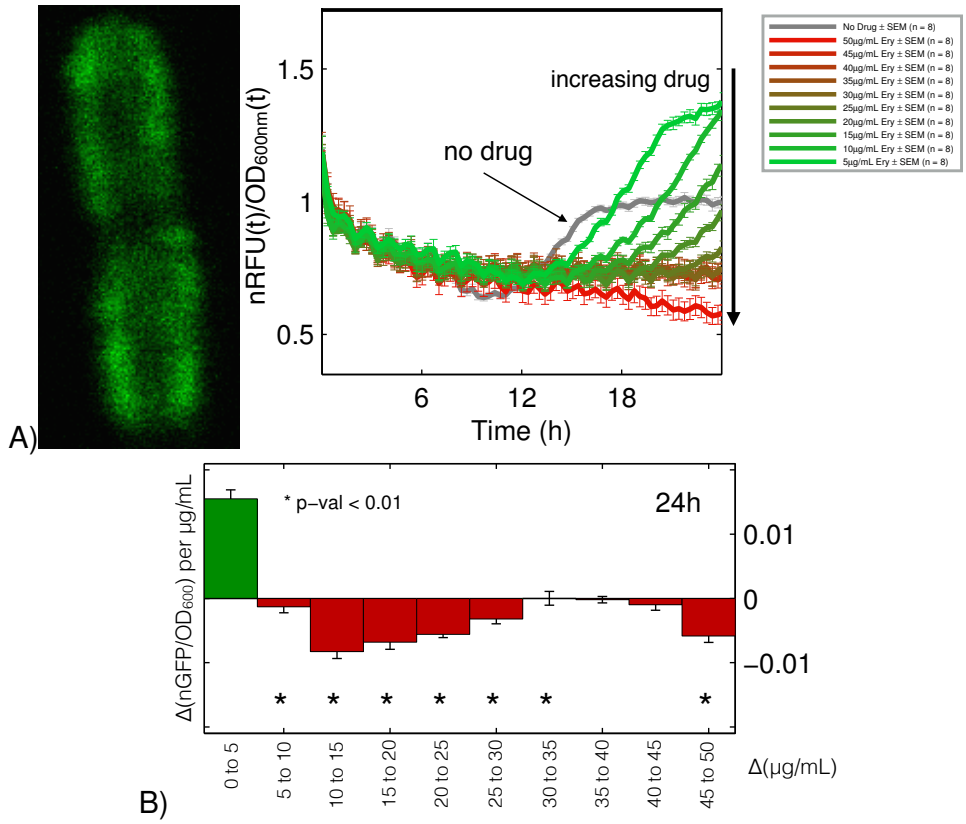

FIGURE 4.5. A) We took a fluorescence microphotography showing the localisation of GFP within a section of an *E. coli* cell close to the moment of division. Using this labelled strain of bacterium we are able to deduce how the dynamics of regulation of the protein AcrB correlates with the use of the macrolide, erythromycin (labelled 'ERY'). In the absence of the drug (grey curve) the protein is down-regulated through lag and exponential phase (less than 12h) before being up-regulated and then stabilising in stationary phase (12h and beyond). When drug dosage is applied, first at a low dosage of $5\mu g/ml$, the concentration of AcrB per cell increases substantially to level about 40% higher at its maximum in the absence of drug. However, as the dose is further increased we observed a negative correlation between drug and AcrB concentration per cell. (b) The negative correlation so-described is significant across a wide range of ERY dosages, as shown by the results of determining a t-statistic (for the derivative of GFP per cell with respect to dose) following a linear regression that is testing for the increase or decrease in AcrB concentration as dose changes.

In order to illustrate how this pump is regulated during different phases of bacterial growth and in different antibiotic concentrations, we present the data in FIG. 4.5. Using an altered MG1655 strain in which GFP is physically fused to AcrB, a strain denoted TB108. The latter strain, which allows us to infer data on efflux pump numbers per cell, shows that the pump decreases in concentration in lag and stationary phase, during the period up to 12h in FIG. 4.5(a). In the absence of drug as stationary phase is entered, the pump is up-regulated to a value deemed to be unity for this discussion. A region of stasis is reached from 18h onwards in which the pump concentration neither declines nor increases. When the drug erythromycin is used in the growth medium, a similar

dynamic of regulation of the pump is observed except that the final concentration per cell is much higher and it continues to increase in stationary phase, to a value about 40% higher than that observed in the absence of drug. Now, FIG. 4.5A and B both show that an increasing down-regulation of the *acrB* protein is observed as more drug is used in the growth medium. Thus, while it might be hypothesised that more drug necessarily leads to an increase in pumps expressed per cell, this statement is only true for certain dosages. The opposite is also observed in a single season of bacterial growth.

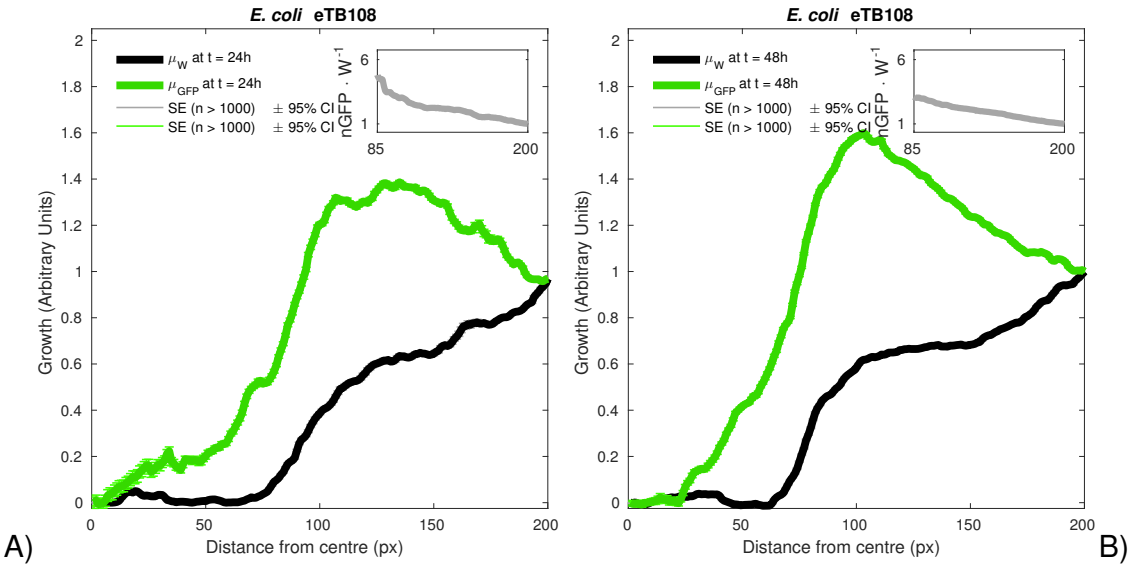

FIGURE 4.6. The analysis of the photographs from a spatial dose-response assay, using the strain eTB108, shows the expression of AcrB using the proxy of green fluorescence levels (shown next to optical density (i.e. white light) at **A**) 24h and **B**) 48h . This yields a per cell measure of AcrB concentration which is done by calculating fluorescence observed per optical density. This measure is shown in the inset of both plots which indicates a positive correlation between drug dose and pumps per cell. We designed an algorithm in Matlab, using the image analysis toolbox, to extract the information from the photographs FIG. S.16.

4.1.3 A duplication of the *acr* operon does not double protein *AcrB* concentration. Consider the following differential equation model of the *acr* operon shown in FIG. 4.4. The auto-repressive nature of structure, whereby the repressor R is transcribed, followed by the efflux protein, P, and then R represses the further transcription of the operon leads to one possible model of the following form:

$$\frac{d}{dt}P = -d_0 P + \rho M, \tag{4.1a}$$

$$\frac{d}{dt}M = -d_1 M + g\frac{V}{1+kP} + M_0. \tag{4.1b}$$

Here d_0 and d_1 are degradation rates of the protein, P, and of mRNA associated with the transcription of the operon. We assume that the concentration of the repressor protein, R is proportional to that of P, which is reasonable given they are encoded by the same operon. The parameter M_0 is a basis level of transition of the operon, $gV + M_0$ is the maximal rate of transcription, where the parameter g is a proxy for the number of copies of the operon held in the genome.

In steady-state, EQUATION 4.1a-b satisfies the following. First, $P = \rho M/d_0$, and therefore $M_0 + gV/(1 + kP) = d_1 m = d_1 d_0 P/\rho$. This is a quadratic in P which, when solved, gives

$$P = P^*(g) := \alpha + \sqrt{1 + \beta \cdot g},$$

where $\alpha = (k^{-1} - \rho M_0/(d_0 d_1))/(k^{-1} + \rho M_0/(d_0 d_1))$ and $\beta = \frac{4V\rho}{d_0 d_1 k}(k^{-1} + \rho M_0/(d_0 d_1))^{-2}$.

Let us now assume that $A(t)$ is the internal concentration of antibiotic in the cell and that A_0 is extracellular concentration of the drug, and then

$$\frac{d}{dt}A = \varphi(A_0 - A) - \rho A \cdot P. \tag{4.1c}$$

Then, in steady-state,

$$A = A^*(g) := \frac{\varphi A_0}{\varphi + \rho P} = \frac{A_0}{1 + \frac{\varphi}{\rho}(\alpha + \sqrt{1 + \beta \cdot g})}.$$

We therefore deduce, because of the auto-repressive nature of the efflux operon, that internal drug concentration and concentration of the efflux protein itself, scale as $\sqrt{g}$, the square root of the number of copies of the operon in the genome.

At this point we make the following remark. In the above, the value of M_0 is assumed to be small and should in fact be $g \cdot M_0$ in this analysis. This reflects the idea that if a gene is copied in the chromosome, then the basal transcription rate could well, indeed should, increase approximately linearly with the number of copies of the transcribed gene. This modification has the effect of changing the terms α and β above so that they also depend on g. However, if M_0 is small enough, then the above predicted square root dependence of $A^*(g)$ on g will be largely unaffected, although there clearly do exist parameter regions where that dependence will be lost. In short, the replacement $M_0 \to g \cdot M_0$ in the above manipulations makes clear in which parameter regimes that can happen. Throughout the remainder, for simplicity, we assume that α and β do not depend on g.

4.2 THEORETICAL PREDICTIONS: THE BULLSEYE PATTERN

4.2.1 The bullseye pattern: a heuristic derivation. Assume for now that environmental, meaning extracellular, antibiotics degrade sufficiently during the time of an experimental protocol in order for the diffusion equation with decay to be a reasonable description of the dynamics of the antibiotic molecules through space, ignoring uptake and efflux for the moment. Thus we suppose that the parameter that was denoted A_0 above now depends on space and time in such a way that

$$A_t = \sigma A_{xx} - dA,$$

where $A(x = 0, t) = A_c$ and $A(x \to \infty, t) = 0$ hold for all $t > 0$. In steady-state, this equation has solution

$$A = A(x) = A_c \cdot e^{-(\sigma/d)^{1/2}x}.$$

Consistent with the experimental protocol depicted in FIG. 4.1, if we assume the existence of a diffusing extracellular nutrient, call it S, then we may also introduce two further diffusion and decay parameters, this time for the carbon source glucose, and write $S = S(x) = S_c \cdot e^{-(\sigma/d)^{1/2}x}$. We use the latter form as a coarse approximation of the true nature of the nutrient concentration, S, because no cells can be found within the red, high-drug region in the centre of FIG. 4.1. However, cells are found inside the grey region and they will begin to ingest those nutrients and grow, this will create a nutrient gradient whereby more nutrients can be found inside the red region than outside it. Thus, we assume for now that the nutrient has a similar form to the drug profile. As this is a heuristic derivation, to makes matters simpler still we will assume

$$S = S(x) \approx S_c \cdot e^{-(\sigma/d)^{1/2}x}.$$

Now, suppose that bacteria grow through time according to Michaelis-Menten-Monod kinetics in the sense that their growth rate, G, can be written

$$G = G(S, A) = c \cdot \frac{vS}{\kappa + S} \cdot f(A),$$

where $f(A)$ is an A-dependent inhibition function which slows growth as a function of intracellular drug concentration, A. Thus, following the dependencies in this simple

model, G is a function of x. We are interested in where the maxima of this function, $G(x)$, might occur and so we now compute $\frac{\partial}{\partial x}G(S,A)$. So, we first note that

$$\frac{\partial}{\partial x}G(S,A) = f'(A)A'\frac{cvS}{\kappa+S} + f(A)\frac{cvS'}{\kappa+S} - f(A)S'\frac{cvS}{(\kappa+S)^2}$$

and as we are seeking maxima with respect to x of this quantity, we now determine whether, or not, the latter expression has zeros. This occurs if and only if

$$0 \;=\; f'(A)A'S + f(A)S' - f(A)S'\frac{S}{\kappa+S}. \tag{4.2}$$

Now, collating the information we have so far and using the fact that A represents intracellular drug concentration, by relating this to extracellular drug concentration, we have $A_0 = A_c \cdot e^{-(\sigma/d)^{1/2}x}$ and, therefore,

$$A = \frac{A_c \cdot e^{-(\sigma/d)^{1/2}x}}{1+\frac{\varphi}{\rho}(\alpha+\sqrt{1+\beta\cdot g})} = A^*(g)\frac{S}{S_c}.$$

Thus, EQUATION 4.2 has a solution if and only if the following quadratic in S does too:

$$0 \;=\; \frac{A^*(g)}{S_c}\cdot\frac{f'(A)}{f(A)}\cdot S(\kappa+S) + \kappa. \tag{4.3}$$

We have reached a point beyond which we cannot easily continue without specifying a form for the function $f(A)$ which denotes the rate of decrease in growth rate as a function of antibiotic. These are not generally well-understood[75] and, in the absence of any better model, we assume that we are working with a protein synthesis inhibitor that binds to a pocket on the ribosome and that growth rate is proportional to the number of drug-free ribosomes. If we impose mass-action kinetics onto the following standard schema whereby antibiotic, A, binds to the ribosome, R, to form the inhibited complex, $[AR]$,

$$A + R \underset{k_{-1}}{\overset{k_1}{\rightleftharpoons}} [AR]$$

then one can readily derive

$$\frac{R}{R+[AR]} = \frac{1}{1+qA}$$

as being the fraction of antibiotic-free ribosomes. We therefore set $f(A) = 1/(1+qA)$ where q is a parameter. Given this set of assumptions, we deduce that equation (EQUATION 4.3) is equivalent to

$$S\cdot(\kappa+S) = q\kappa\left(qS + \frac{S^c}{A^*(g)}\right). \tag{4.4}$$

Equation (EQUATION 4.4) can be re-written with respect to antibiotic too, whereupon it takes the form

$$A \cdot \left(\kappa S_c^{-1} A^*(g) + A\right) = q\kappa\,(1 + A)\,. \tag{4.5}$$

It is clear from the linearity and quadratic nature of their respective left and right hand side that equations (EQUATION 4.4) and (EQUATION 4.5) have solutions that depend on g and, as illustrated in FIG. 4.7, the growth rate function G, defined above, can have local maxima in space that are located in different places for different values of g. In order words, an antibiotic can create a spatio-genomic pattern with a multi-bump structure with respect to the drug gradient.

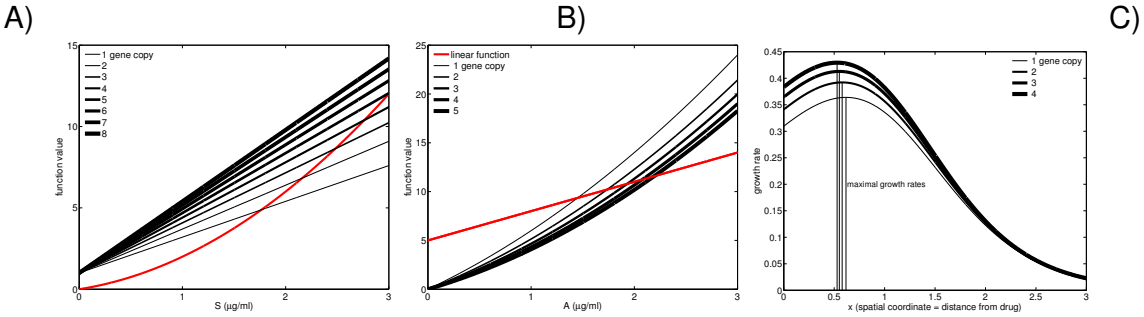

FIGURE 4.7. A) The intersection of the line and the quadratic functions give the values of the environmental sugar concentration, S, for which growth rate has a local extremum (a maximum). In this illustrate example, it is only in those regions for which S lies between 2 and $3\mu g/ml$ (at the intersection of the red and black lines) for which growth rate can have a local maximum and, then, it is only for a certain range of the number of additional gene copies. **B)** The analogous plot to that given in A), but showing dependence on A rather than S. **C)** From A) and B) we deduce that, for the correct values of A and S, there can be local spatial maxima with respect to growth rates whose location can change with the number of copies of the resistance operon, *acr*.

Whether, or not, the potential for such a multi-bump structure is realised in practise depends on many parameters within the model. For example, not only is an antibiotic gradient required in the theory, a resource gradient has to be created by virtue of the fact that the use of high antibiotic dosages kills so many cells that their resources are 'released'. This also requires the presence of cells some distance from the drug source in exactly the manner depicted in FIG. 4.1.

In that figure, the indicated 'killing zone' contains no bacterial cells but it does contain antibiotic and glucose, and other nutrients, in the agar that will both diffuse outwards to create the requisite gradients. The glucose, or any other sugar, gradient is created by virtue of the greatest population densities being present furthest from the drug at the start of the experiment.

4.2.2 A theoretical genetics model of drug efflux. Having used a highly stylised form of mathematical modelling to infer that a spatio-genomic pattern, in the form of a bullseye, can appear in an antibiotic gradient because of a spatial nutrient gradient, as illustrated in FIG. 4.7, we now turn to a mathematical model that is more explicit in its ability to capture both the diffusing nature of different bacterial and chemical species and the manner in which ecological dynamics mediate the potential existence of the bullseye pattern.

To begin the specification of the model, we first define the radial diffusion operator, written L, of a function $f(r)$, by

$$L(f) = \frac{\partial^2 f}{\partial r^2} + \frac{1}{r}\frac{\partial f}{\partial r}.$$

This is defined for sufficiently smooth functions, f that satisfy $f'(0) = 0$ and $f'(r_0) = 0$ where $r_0 > 0$ is a positive constant that defines the radius of the circular domain in which the diffusion processes are assumed to take place.

The following partial differential equations are now used to describe the spatial dynamics of antibiotic inhibition to which we allude above:

$$\frac{\partial}{\partial t}B_0 = G_0(S, a_0)B_0 + \delta(1+\Delta)B_1 - \delta B_0 + \rho_b L(B_0), \tag{4.6a}$$

$$\frac{\partial}{\partial t}B_1 = G_1(S, a_1)B_1 - \delta(1+\Delta)B_1 + \delta B_0 + \rho_b L(B_1), \tag{4.6b}$$

$$\frac{\partial}{\partial t}a_0 = -\eta a_0 + B_0\varphi(a_{\text{ext}} - a_0) - B_0\frac{vp_0}{k+p_0}a_0 + \delta(1+\Delta)a_1 - \delta a_0 + \rho_a L(a_0), \tag{4.6c}$$

$$\frac{\partial}{\partial t}a_1 = -\eta a_1 + B_1\varphi(a_{\text{ext}} - a_1) - B_1\frac{vp_1}{k+p_1}a_1 - \delta(1+\Delta)a_1 + \delta a_0 + \rho_a L(a_1), \tag{4.6d}$$

$$\frac{\partial}{\partial t}a_{\text{ext}} = -\eta a_{\text{ext}} - \sum_{i=0}^{1} B_i\varphi(a_{\text{ext}} - a_i) - \sum_{i=0}^{1} B_i\frac{vp_i}{k+p_i}a_i + \rho_e L(a_{\text{ext}}), \tag{4.6e}$$

$$\frac{\partial}{\partial t}S = -\frac{vS}{\kappa+S}\sum_{i=0}^{1} B_i + \rho_u L(S), \tag{4.6f}$$

subject to initial conditions as depicted in the schema of the protocol in FIG. 4.1 and using no-flux (Neumann) boundary conditions so that no mass can spill out of the simulated experimental agar plate at any time.

The model (EQUATION 4.6) captures the densities of two bacterial subpopulations having density $B_i(t)$ at time t and expressing different numbers of copies of an efflux gene or operon, where the $i = 1$ genotype has one more than the $i = 0$ genotype,

where this gene codes a protein, or protein complex, that transports drug from the cell. The intracellular drug concentrations for each subpopulation B_i is denoted by a_i and is measured per unit volume. The variable a_{ext} is the extracellular concentration of drug, S denotes the concentration of a limiting carbon source, glucose in our experimental systems.

Note that we assumed that mutations increasing the number of efflux pump-encoding genes ($B_0 \rightarrow B_1$) are less likely than those reducing the number of such genes ($B_1 \rightarrow B_0$). We have done this because the genomic region in which *acr* resides is unstable in the sense that replication of the chromosome usually leads to just one copy of the operon, and mother cells with a duplication are more likely to have two 'daughter' cells where one such daughter is without that duplication than to have two daughters where both daughters carry it. In other words, there is strong physiological purifying selection acting against the duplication mutation.

EQUATION 4.6a and b) describe the variation of bacterial density with respect to time. The model assumes that this variation is caused by three phenomena, one for each term of the equation. The first part of these equations describes the temporal variation of bacterial density B_i due to the growth and division of bacteria with intracellular drug concentration a_i and in an environment with glucose concentration S. This phenomenon is modelled as an exponential growth of the bacterial population, with cellular growth rate

$$G_j(S, A) := c_j \cdot \frac{1}{1 + pA} \cdot \frac{vS}{k + S},$$

where c is cell yield per glucose supplied, v and k are the maximal uptake rate and half-saturation constants associated with Michaelis-Menten uptake of the single carbon source S, and p is the reciprocal of the half-saturation constant due to the inhibition from ribosome-antibiotic binding.

To represent the cost of expressing the efflux gene, we chose the yield of c_i of each sub-population, B_i, to satisfy the condition that their respective yields are ordered such that the greater resistance genotype has a lower per-glucose cell yield, in other words $c_1 < c_0$. We have assumed this because the chromosomal recombination events that produce increases in the copy of the *acr* operon carry with them 8% of the entire set of genes held in the chromosome. It is highly likely that the duplication will therefore

come at a large 'protein cost' whereby many proteins will be over-expressed following the duplication that have no selective advantage and yet energy in the form of carbon and ATP is used in order to express those genes.

The second terms of EQUATION 4.6a and EQUATION 4.6b describe the variation of B_i caused by down/up-regulation of the efflux gene in some of the bacteria. The down-regulation of the efflux gene in some of the B_1 cells make them become B_0, while B_0 that up-regulate that gene become B_1. The process of up-regulation of efflux genes is assumed to occur randomly as a Poisson process at a certain rate δ per cell per hour (the probability of expression and amplification of the gene per cell per unit time are assumed, for simplicity, to be the same); similarly, the down-regulation is a Poisson process with rate $\delta(1+\Delta)$, a value necessarily greater than δ. The final terms of EQUATION 4.6a and EQUATION 4.6b give the variation of $b_i(t)$ due the radial diffusion of b_i with rate ρ_b.

The process of up-regulation of efflux genes and both increases and decreases in the copy number of the efflux genes are assumed to occur randomly as a Poisson process at a certain rate δ per cell per hour (the probability of expression and amplification of the gene per cell per unit time are assumed, for simplicity, to be the same).

We assume a functional form for p_j that is monotone increasing and bounded in j, controlled by a dimensionless constant g (the Michaelis-Menten function $p_j = (j-1)/(1+g(j-1))$). Thus p_j is also dimensionless and the quantity $p_j/(k+p_j)$ is the probability of finding a pump in the state where it momentarily is bound to drug. The rationale for this is that the polymerase transcription complex, assumed limited in number, has to compete for each gene copy, thus providing a limit on the number of efflux genes that can be simultaneously expressed.

The remaining variables in EQUATION 4.6 have the following meaning: φ is the antibiotic diffusion rates across the cell membrane, v is the maximal antibiotic efflux rates and k is half-saturation constants associated with efflux pump-antibiotic molecule binding; V and K are the maximal uptake rate and half-saturation constant associated with Michaelis-Menten uptake of the single carbon source, glucose S; $G_j(S,A)$ is the per hour growth rate of each cell detailed above; δ is the rate of amplification of the efflux gene and $\delta(1+\Delta)$, a value necessarily greater than δ, is the rate of decay of

the efflux protein expressed by this gene. Finally, therefore, $n-1$ is the maximum copy number of the gene.

We solved EQUATION 4.6 numerically in python using the package `odeint` from the SciPy library (`www.scipy.org`), which uses a linear multistep method (predictor-corrector) or backward differentiation formula methods (the Gear methods) depending on whether the problem is stiff or non-stiff. In the resulting prediction, shown in FIG. 4.8, there is a clear difference in the nature of the spatio-genomic pattern depending on whether the antibiotic efflux operon present in the chromosome can be duplicated, or not. In the case where it cannot be duplicated, the spatial pattern is simple and consists of a single 'growth ring' where bacterial densities have achieved a local optimum. This is consistent with the analysis illustrated in FIG. 4.7, but it indicates that only one of the predicted rings is realised using the diffusion model (EQUATION 4.6). FIG. 4.8 shows that in order to achieve something like the bullseye pattern predicted by FIG. 4.7, we must use a strain of bacterium that is able to duplicate the efflux operon, *acr*. These provide testable experimental predictions that we address in the following section.

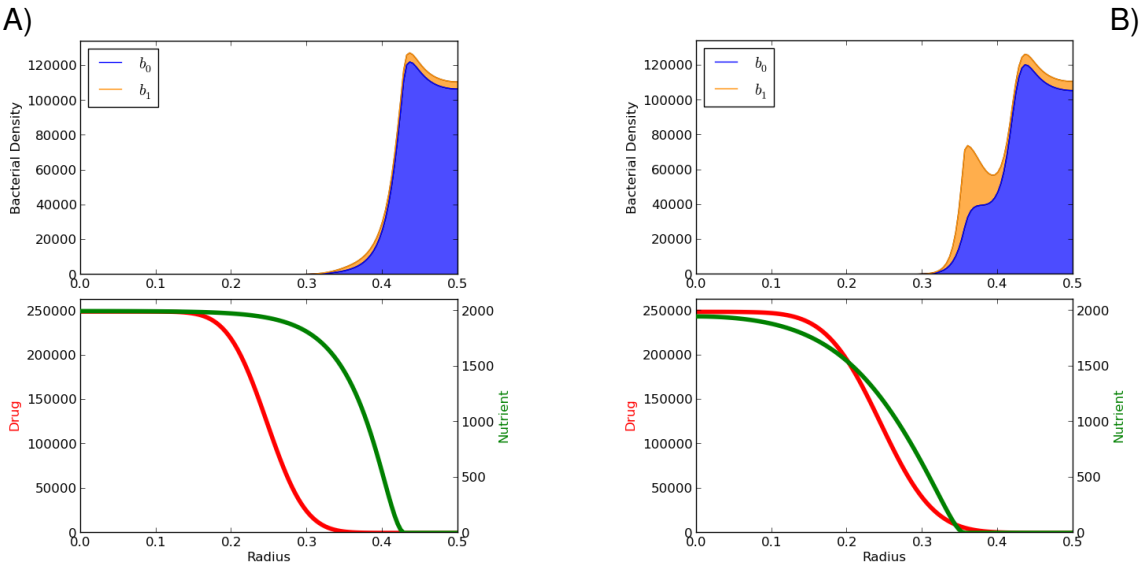

FIGURE 4.8. Bullseye pattern formation due to the duplication of the *acr* operon as predicted by EQUATION 4.6. The distance from the centre of the plate is represented on the $x-$axes, whereas on the $y-$axes we represent the nutrient and drug concentrations, and bacterial density all in arbitrary units. The first ring (**A** top) is due to the increased bacterial growth produced by the higher availability of nutrients (**A**, bottom plot in green) and extremely low concentrations of drug (**A** bottom plot in red) in the boundary of the killing zone. More nutrients are available beyond this boundary, but the concentrations of drug in these coordinates impede the growth of the bacterial cells. Only when the cells carry a second copy of this operon (b_1), translated into higher drug resistance, they are able to grow conforming an 'inner rings' of bacteria (**B** top) until the concentration of drug is too high for these resistant cells (**B** bottom).

4.3 Experimental Data

We now provide an analysis of the result of some bacterial growth experiments that, we believe, show evidence of the bullseye pattern predicted in theory. Before we are able to do this, we first present some mathematical measures of monotonicity that we can apply to dose-response curves in order to provide a quantitative description of how many rings a spatial dose-response pattern possesses.

4.3.1 Mathematical measures of (non-)monotonicity.

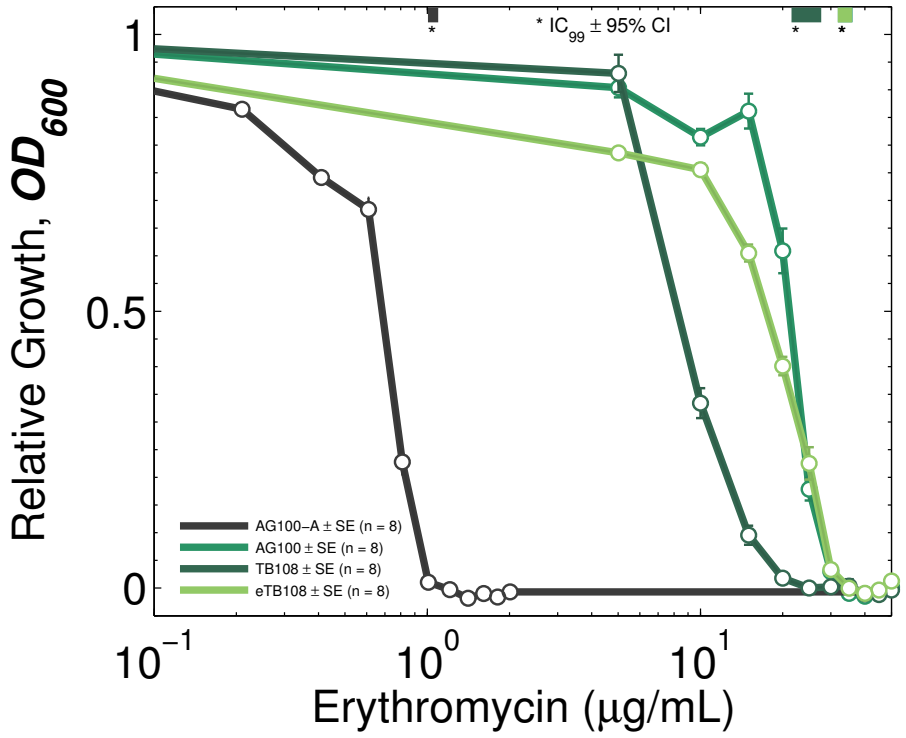

Figure 4.9. A (relative) dose-response of three strains of *E.coli* with respect to the drug erythromycin using units of optical density measured at 600nm. The *acr* knockout strain AG100-A is most sensitive to the drug, followed by TB108 which has a GFP physically fused to AcrB, followed by the strain MG1655. These antibiotic sensitivity tests, required for experiments in Chapter 2, show that, overall, bacterial growth declines monotonically with increasing drug supply over a 24h incubation period.

4.3.1.1 A First Numerical Measure of Non-Monotonicity: the Hill function. The basic idea of an empirical antibiotic dose-response is encapsulated in Fig. 4.9. In it, an exponential scale of increasing dosages is presented on the x-axis and the y-axis contains data relating to the growth of the microorganism in question, in that case optical density although other measures, such as growth rate, are also used in the

antibiotic literature. It is common, as we have also done using the dose-response data in FIG. 4.10(a), to assume that the data decreases monotonically with dose and to numerically fit a Hill function to it. A Hill function takes the form

$$H(A) = H_0 \cdot \frac{K^n}{K^n + A^n}$$

where H_0, K and n are three parameters to be determined as part of the data fit. Using this fit, we can then estimate IC_x values which are the dosages that give an x% reduction in growth. In other words, IC_x satisfies the relationship $H(IC_x) = \frac{x}{100} \cdot H_0$, thus the value of K is the IC_{50} of the data.

However, as FIG. 4.10B shows, Hill functions are not accurate descriptors of dose-response data when one is interested in studying, as we are here, the effect selection for resistance has at different dosages. For the latter figure shows the effect on the Hill function-like data, gathered at 24h, after that *E.coli* data has been evolved in the presence of erythromycin for a further 72h. The details of how this is done are contained in the methods section, but it is clear from the figure that the monotone nature of the data has changed; while there is short-term monotonicity of dose-response the strength of selection at different dosages differs in such a way that monotonicity is not preserved through adaptive and evolutionary changes. This observation is consistent with the theory of SECTION 4.2.1 which shows that the maximal growth rates for different genotypes can occur at different dosages and it is difference of these growth rates between genotypes that determine the strength of selection for resistance.

We therefore require statistical methods for quantifying the the non-monotonicity properties of dose-responses. One could, of course, use the goodness of fit, or poorness of fit, of a Hill curve to dose-response data but this would not capture information about the oscillatory properties of the dose response. Another approach is to perform a best-monotone function fit to data, this could be achieved as follows.

4.3.1.2 A Second Numerical Measure of Non-Monotonicity: monotone data fitting. Suppose that $(u_0, u_1) \in H := \mathbb{R} \times L^2((0,1), \mathbb{R})$, we can define a monotonic function $M(u) \in W^{1,1}((0,1), \mathbb{R})$ by

$$M(u_0, u_1)(x) = u_0 + \int_0^x u_1(y)^2 dy.$$

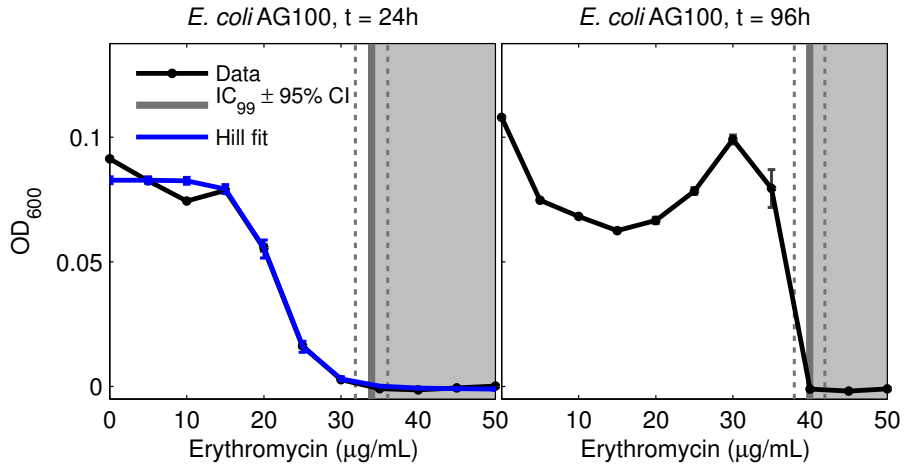

FIGURE 4.10. An erythromycin dose-response curve of the *E.coli* AG100 strain with a Hill function fit super-imposed onto the data. The latter is used to determine an IC_{99} within a certain confidence and define the classic mutant selection window (grey). Drug dose is shown on a linear scale on the x-axis, optical density at 24h is shown on the y-axis. Data from experiment described in CHAPTER 2 (FIG. 2.8).

Note that $\frac{d}{dx}M(u_0, u_1) = u_1^2 \geq 0$ almost everywhere and u_1^2 is an element of L^1 by definition, justifying our claims on the properties of M.

Now, any dataset resulting from the experimental construction of a dose-response curve gives rise to a function in $W^{1,1}$ through linear interpolation: if (x_i, y_i) defines a discrete set of points with $0 = x_1 < x_2 < ... < x_N = 1$ representing a series of antibiotic dosages, we take the maximal dose to be $x_N = 1$ which should be thought of simply as a normalisation to unity, then the linear interpolant of the data points y_i is not only a continuous function, but it is in fact Lipschitz. It is therefore a member of the space $W^{1,\infty}$ which is contained within $W^{1,1}$. We can therefore apply the operator M to experimental data.

Given a function $d(\cdot) \in W^{1,1}$, supposed to represent an empirical dose response dataset, we then define the best monotone approximation of d to be the element $(v_0, v_1) \in H$ that achieves

$$\min \left\{ \|M(u_0, u_1) - d\|_{L^2} : (u_0, u_1) \in H, \|M(u_0, u_1)\|_\infty \leq \|d\|_\infty \right\}.$$

If we define $r(u_0, u_1) := \|M(u_0, u_1) - d\|_{L^2}$ then r is a sum and composition of convex and linear functionals and operators and H is a Hilbert space on which infimising sequences of M are bounded and from these observations one can prove that there is a unique minimiser of r. Moreover, approximations to this can be readily computed

using a direct optimisation algorithm if d is the piecewise linear interpolant of a discrete dataset. We call the value of r so obtained the measure of monotonicity of the function or dataset d. It is not a fine measure of how the data oscillates, but it is a measure of how 'not monotone' the data is.

In order to illustrate that the appearance of non-monotone dose-response profiles with mid-dose local maxima can appear for a range of antibiotic drug molecules, we applied this numerical measure of non-monotonicity to a video of *E.coli* AG100 growth in the presence of kanamycin, see FIG. 4.12. The raw data is contained within a video, a few frames of which are illustrated in FIG. 4.11. Consistent with the theories developed earlier, this data exhibits a transition from monotone to non-monotone dose response.

4.3.1.3 A Third Numerical Measure of Non-Monotonicity: the oscillation profile. Although a metric with respect to monotonicity allows one to quantify the loss of monotonicity in the dose-response profile through time, the above theoretical modelling arguments have indicated that there is the opportunity, given the right environmental conditions, for the presence of subtle structures within those nonlinear profiles. For example, the non-monotonicity may be due to selection for certain copies of specific drug resistance operons occurring at different drug dosages. In order to discern those effects, which are predicted to be associated with multi-bump dose-response patterns, we need a finer measure of these oscillation that we can apply to experimental data.

We therefore turn to the winding number of a given function, call the function $f(t)$ and let $W(f)$ denote its winding number about the number α. We consider f to be normalised in two ways such that its domain is $[0,1]$ and, over this domain, $\inf(f) = 0$ and $\sup(f) = 1$. Its winding number is the value $W(f,\alpha) = w(f-\alpha, f')$ where

$$w(x,y) = \int \frac{xdy - ydx}{x^2 + y^2}.$$

We say that the oscillation profile of $f(t)$, is the function of α defined by

$$\mathcal{O}(f)(\alpha) := W(f,\alpha)$$

defined for all values of α, but potentially non-zero only for $\alpha \in \mathrm{ran}(f)$ where $\mathrm{ran}(f) := (\inf(f), \sup(f)) = (0,1)$. Note that $\mathcal{O}(f)(\alpha) = 0$ for values of α outside that range,

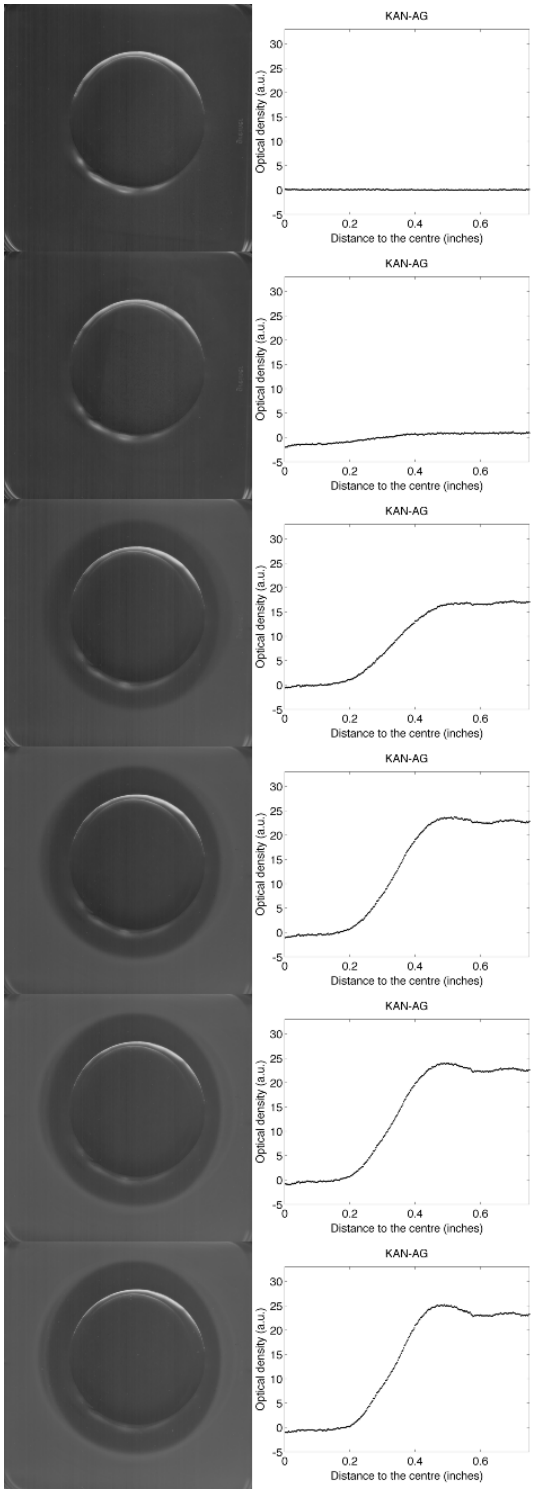

FIGURE 4.11. Frames from a video showing the transition from monotone to non-monotone dose response in the inhibition of *E.coli* growth by kanamycin held in the central circular region. The top-most image was taken at time, $t = 0h$, the bottom-most at $t = 24h$. The right column shows the mean dose-response determined from each image in the left-hand column.

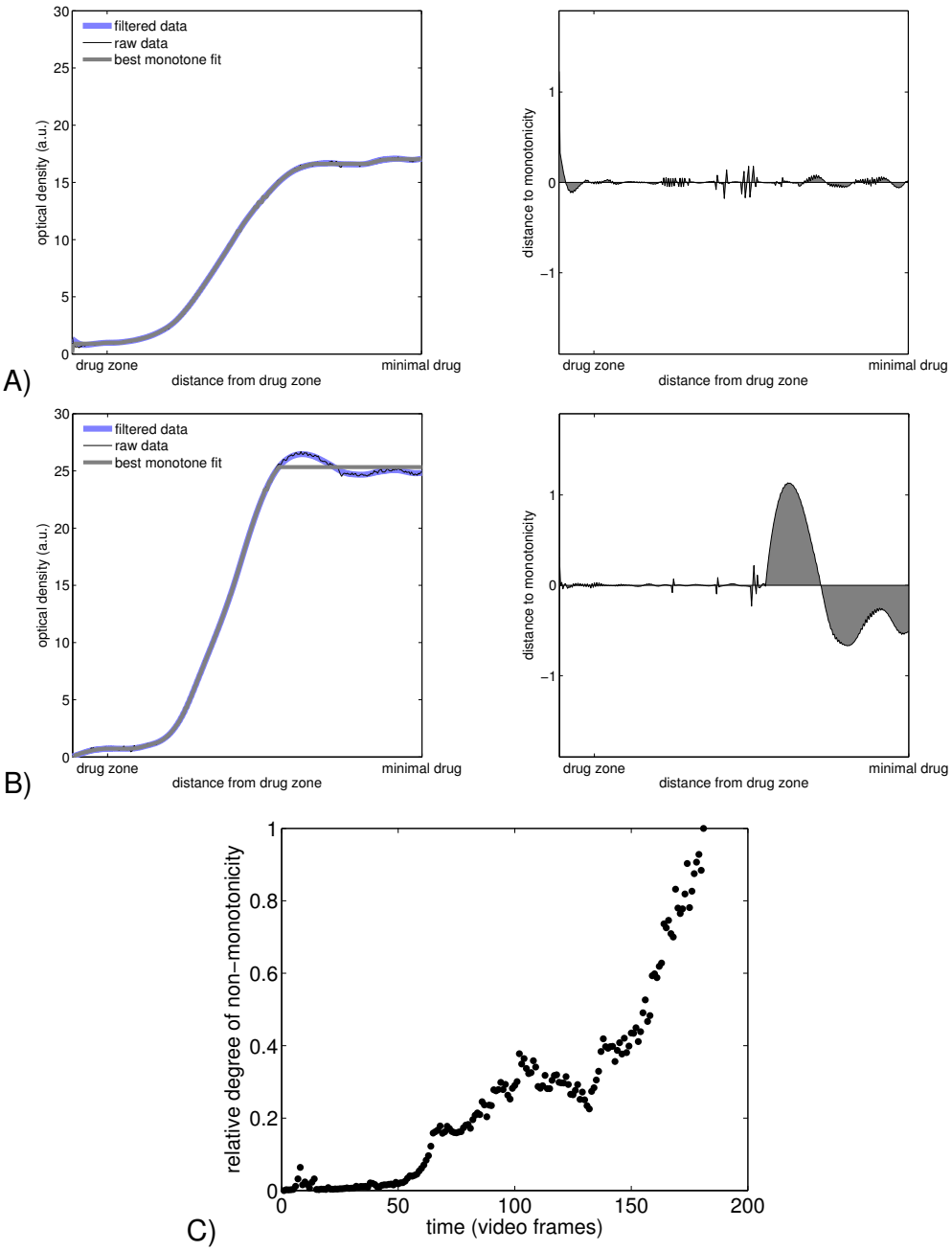

FIGURE 4.12. The result of quantifying the transition in the dose-response data of FIG. 4.11. Plot **A)** shows how the data exhibits a low degree of non-monotonicity at early on the in the experiment because the best monotone fit to data is a good descriptor of the dose-response. Plot **B)** shows, at a later time, that the best monotone fit to data gives a relatively poor fit. The right-hand images in A) and B) show the difference between filtered data and the best monotone fit. **C)** Tracing the goodness of fit of the best monotone descriptor of the dose-response data shows deterioration through time, indicative of a transition from monotone to non-monotone dose-response.

inside that range $O(f)$ only takes integer values. If we now define a sequence $O_n := \int_{O(f)(\alpha)<n} O(f)(\alpha)d\alpha$, with $O_0 = 0$, and then set

$$B_n = O_{n+1} - O_n,$$

we call the latter the *bumpiness spectrum* of the function f.

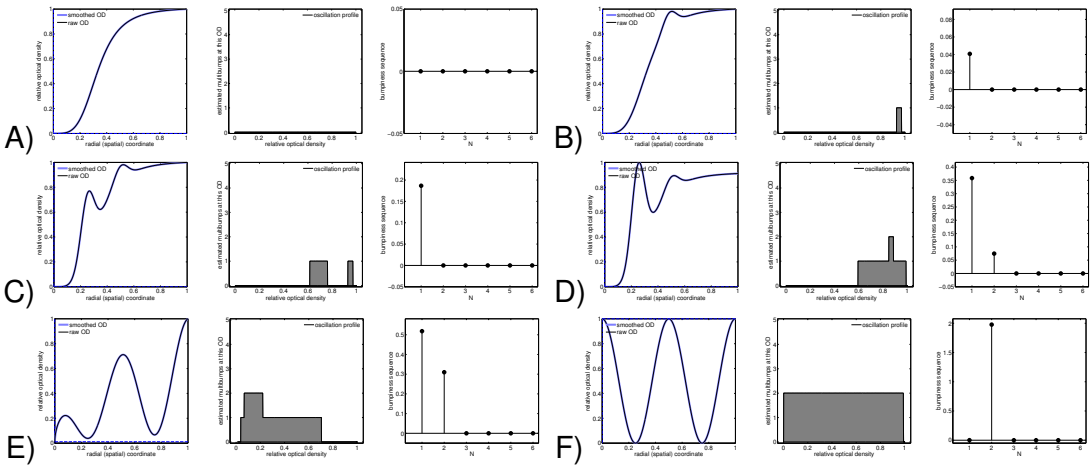

FIGURE 4.13. Measures of non-monotonicity (the oscillation profile and bumpiness measure) using the winding number of some synthetic data. In each of (A-F) one can see, in the left column of the two images, a function representing a particular dose-response pattern with zero drug at the $x = 0$ position and higher drug where $x \gg 0$. Plot (**A**) shows a monotone dose-response which is reflected in the oscillation profile equation, shown in the middle figure of plot A), to the zero function. Plots (**B-F**) have increasing degrees of non-monotonicity which is reflected in the oscillation profile in the right-hand figure of each plot whereby the grey regions have increasing area. In each window, the right-most plot corresponds to the bumpiness spectrum. Plot (F) accords with what one might expect from intuition: the bumpiness spectrum of a $\cos(2\pi \cdot x)$ function, suitably normalised, is $(0, 2, 0, ...)$ as it exhibits exactly two bumps. Plot (a) shows that the bumpiness spectrum of a monotone function is the zero sequence $(0, 0, ...)$.

In order to illustrate how the oscillation profile and the bumpiness spectrum might be used to provide insight into the non-montone and multi-bump nature of empirical data, we turn to FIG. 4.13. It shows synthetic examples of both monotone dose-repsonse profiles and also non-monotone profiles. The figure also shows how the bumpiness spectrum encapsulates the oscillatory character of those profiles in a manner that is reminiscent of Fourier series coefficients.

4.3.2 Applying the bumpiness spectrum to laboratory spatial dose-response data. We will now claim that the bumpiness spectrum so-defined can be used to corroborate visual evidence for an emergent pattern exhibiting concentric rings of increasing radius when *E.coli* grows in a spatial antibiotic gradient, as predicted by the above theory.

First, the experimental data for this is a pair of images that we present in FIG. 4.14A and B. The left-hand image shows the optical density profile as a function of the distance from the source of the drug at the centre of the plate whereby drug

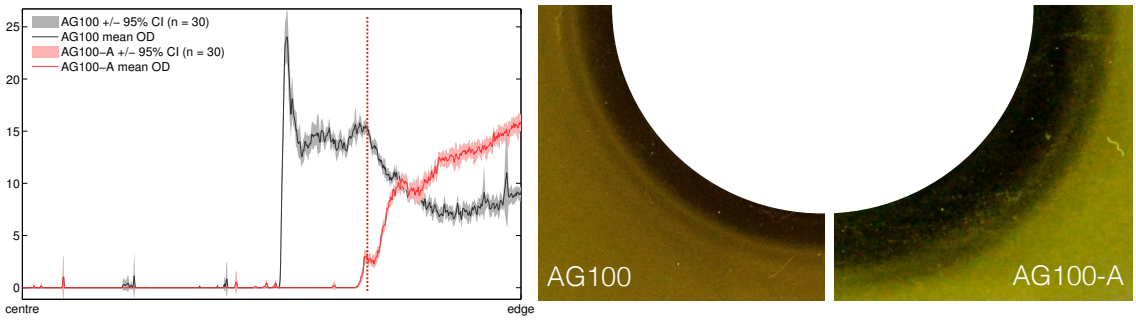

FIGURE 4.14. The left-hand image shows the mean optical density of two bacterial strains at 24h, AG100 and AG100-A, the latter does not have a functional *acr* operon whereas the former does. The two right-hand images are false colour representations of two different agar plates on which the respective strains were cultured.

dosage necessarily decreases towards the edge of the plate. Images taken from these agar plates are shown in the right-hand image of the same figure whereby the white semi-circular region is the drug source. This figure illustrates bacterial population density at 24h and, to the eye, appears to exhibit bullseye ring patterns. This appears consistent with the density images on the left, and although the *acr* knockout strain has an essentially increasing density profile with decreasing drug, as may be expected, the AG100 wild-type strain has an altogether different, and clearly non-monotone, character.

To quantify this apparent non-monotonicity, effectively in order to produce numerical measures of what the human eye perceives in FIG. 4.14B, we present FIG. 4.15. It shows the oscillation profile of the population density data as a function of the spatial coordinate for the two *E.coli* strains AG100 and AG100-A, FIG. 4.15 is an analysis of data taken from FIG. 4.14A).

The population density data relating to AG100-A in the left-hand image of FIG. 4.15 looks almost monotone to the human eye and, indeed, FIG. 4.15(a) shows little quantitative evidence of non-monotonicity. There is some evidence of a mutli-bump profile to be seen in the bumpiness spectrum, but certainly not to the same extent as that seen in the analogous data for strain AG100. This data can be seen in FIG. 4.15(b). The latter data alluded to, for AG100, shows in quantitative terms what appears to the human eye in FIG. 4.14 whereby distinct rings highlighting regions of growth can be seen for this strain, consistent with predictions made earlier using mathematical models.

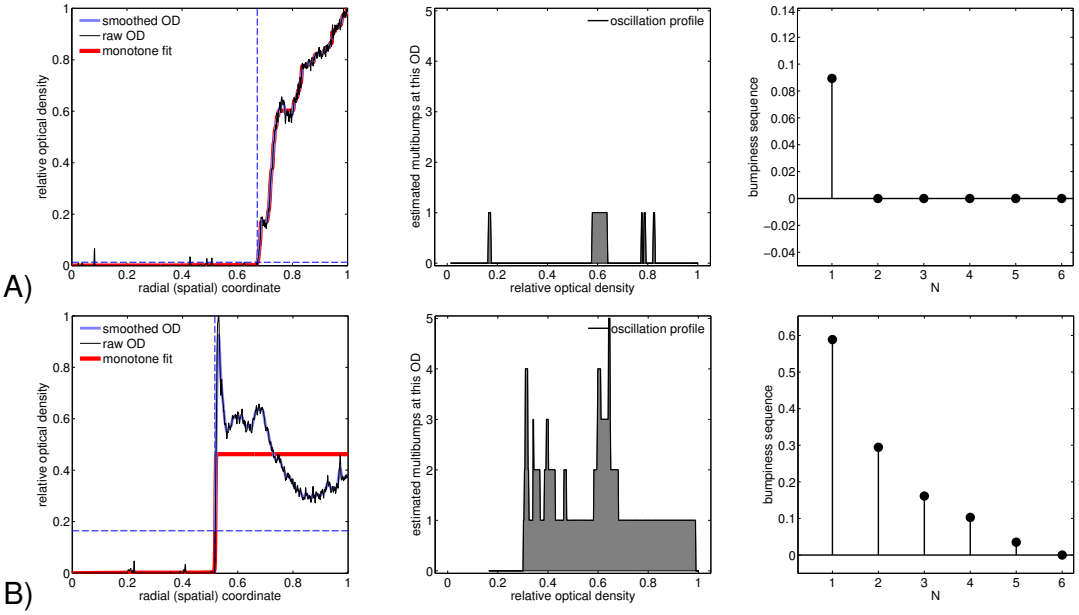

FIGURE 4.15. A) The left-most plot shows an analysis of the dose-response profile which constitutes the observed mean optical density as a function of the spatial distance from the source of the drug (at position zero), and in this case it is derived from strain AG100-A that lacks the efflux pump operon, *acr*. The left-hand plot shows (in red) the best monotone function fit to data, filtered data (in blue) and the dash blue lines indicate the leftmost point where the optical density has been established to be significantly above zero using a t-test with significance level $p = 0.05$. To the right of this point we assume that optical density is significantly positive. The middle plot is the oscillation profile $O(f)(\alpha)$ for this AG100-A data and the rightmost plot is the bumpiness spectrum that is derived from the oscillation profile. Neither of the latter two measures are consistent with the presence of oscillations. **B)** This is the analogous analysis to A) but now for the strain AG100 that possesses the *acr* operon.

4.4 CONCLUSIONS

The experiments described in CHAPTER 2 were carried out in 96-well microplates. There, we set up a range of concentrations of antibiotic in which the concentration in each well does not change. So here we created a 2D gradient of antibiotic, observing that the non-monotone profile also occurs in a spatial context giving rise to bullseye patterns. Using a fluorescence-tagged bacterial strain that allows us to track the relative amount of AcrB, key component of the AcrAB-TolC efflux pump, we could also observe that the relative abundance of this pump increases with higher dosages.

A key observation lies on the agreement between our empirical dataset and linear diffusion theory, whereby an increase in antibiotic dose not involve a proportional increase in bacterial killing or growth inhibition. To put this into context, the medical orthodoxy in the clinic involves the use of aggressive chemotherapies for “radical pathogen cure”.[26] This practice is translated into higher dosages during a treatment

with antibiotics. Yet, in a spatial context such as the human body, doubling the dose of antibiotic therapies does not necessarily lead to doubling inhibition as we demonstrated in this chapter.

V EFFECTS OF THE AVAILABILITY OF FUNCTIONAL RIBOSOMES ON THE ROBUSTNESS OF METABOLIC RATE-YIELD TRADE-OFFS: IMPLICATIONS FOR GROWTH RATE INHIBITING ANTIBIOTICS.

WE HAVE USED erythromycin, tetracycline and a tetracycline-derivative antibiotic, doxycycline, during this PhD project. These drugs are known to target different binding pockets in the bacterial ribosome and lead to the inhibition of protein synthesis.[99,100] The ribosome is genetically encoded by seven *rrn* operons in the bacterium *Escherichia coli*[101,102] and each of these operons is able to form a fully functional ribosome. In this chapter we asked how the concentration of functional ribosomes within the cells affected growth rate, a question motivated by the use of antibiotics. The quantification of antibiotic-free ribosomes can be technically demanding, so instead of using antibiotics we used strains in which the number of *rrn* operons had been manipulated to limit the maximum production of these proteins.

Using a set of strains derived from the wild-type *E. coli* MG1655, which contain cells with from two to seven (the wild-type) *rrn* operons, here we observe a potential 'paradoxical' increase in both growth rate and yield (biomass produced per molecule of carbon source) as the number of *rrn* operons is reduced. Our dataset also provides empirical evidence that supports previous theoretical studies on metabolic 'rate-yield' trade-offs (RYTO),[37,38,103] which turn out to be highly dependent on the environmental

richness of a carbon source supplied to the bacterial cells. Based on the evidence presented in this chapter, we hypothesised that our observations could also be mediated by the presence of ribosome-binding antibiotics but this particular hypothesis has not been tested.

5.1 Question: can antibiotics mediate metabolic trade-offs, like the rate-yield trade-off?

Ribosomes are essential for the synthesis of proteins within the bacterial cell[104] and this process is known to be coupled to bacterial growth rate.[39] A reduction in the number of functional ribosomes, for example due to the presence of a ribosome-binding antibiotic, translates into lower bacterial growth rates.[41] However, while this relationship seems self-evident, the situation is not quite so clearcut because there can be an optimal number of ribosomal operons in very simple growth conditions supported by minimal media.

The notion of 'trade-offs' in evolutionary biology stem from an idea that two beneficial traits cannot both be improved simultaneously during evolution.[105,106] Under normal circumstances, the idea is that one previously-optimised trait can only improve at the expense of the other; the traits are therefore said to antagonise each other. As an example of this, cell growth rate is often compared with yield, defined as the biomass produced per unit of carbon source supplied. Based on thermodynamic constraints,[107] a theoretical study has suggested the existence of a metabolic trade-off between growth rate and cell yield[38] supported by the following rationale.[107]

Adenosine triphosphate (ATP) is the most common energy 'currency' in the cell and it is produced during the biological oxidation of a carbon source. If this carbon source is glucose, oxidised using the glycolitic pathway, we can describe the process as the chemical reaction

$$\{glucose\} + 2ADP + 2P \rightleftharpoons \{2lactate\} + [2ATP]$$

if glucose is metabolised in the absence of oxygen, or as

$$\{6O_2 + glucose\} + [36ADP + 36P] \rightleftharpoons \{6CO_2 + 6H_2O\} + [36ATP]$$

if glucose is metabolised in the presence of oxygen. The driver and driven reactions

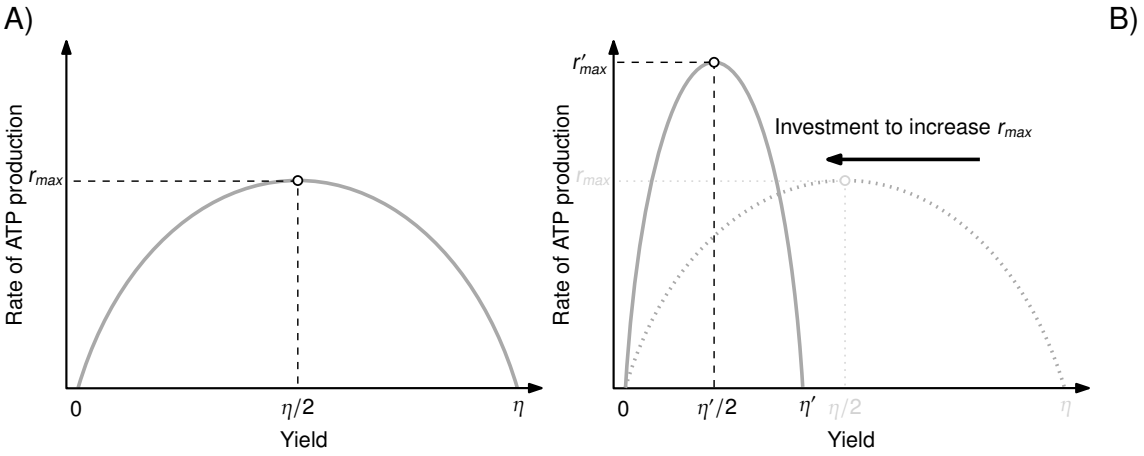

FIGURE 5.1. Diagram of the metabolic rate-yield trade-off theory. A) Rate of ATP production is shown on the *y*-axis as a function of the yield, η, on the *x*-axis. This function reaches its maximum at $\eta/2$.[37] **B)** The dynamics of ATP production depicted in A) may change if part of the ATP synthesised is used to increase the production rate. This investment of ATP comes at a cost of lower maximum yields.[38]

are indicated with curly and squared brackets respectively. In order for these reaction to happen, the change in free energy (ΔG) for the driver reaction is $\Delta G_0 < 0$, whereas that for the driven reaction is $\Delta G_1 > 0$. The efficiency of the reaction is therefore $\mu = -\frac{\Delta G_1}{\Delta G_0}$ and the production of ATP $J^{ATP} = \Delta G_1 \upsilon$, where υ denotes the reaction speed. If the affinity of the reactions is defined as $A = -(\Delta G_0 + \Delta G_1)$, and finite time thermodynamics (FTT) and near-equilibrium irreversible thermodynamics (NEIT) are used as described in REFERENCE 107, J^{ATP} can be redefined as the parabolic function $J^{ATP} = r \cdot \eta \cdot (\eta_{max} - \eta)$.

In this parabola η denotes the yield of ATP production per glucose supplied to the pathway and *r* the maximum rate of ATP production (FIG. 5.1A).[37,107] Therefore any investment of ATP towards the increase of the production rate necessarily leads to lower ATP yields (FIG. 5.1B), hence the trade-off.[37] This rationale has been extended to the theory of metabolic pathways. For example the fermentation of glucose involves high growth rates at the cost of lower yields, whereas the oxidative phosphorylation of the glucose allows higher yields at the expense of lower growth rates.[38] The study of a trade off between the rate of ATP production and yield therefore gave rise to the study of a trade off between cell growth rate and yield.

Given the relationship between growth rate and the number of functional ribosomes, we asked whether or not is it possible that ribosome-binding antibiotics can mediate

a metabolic trade-off between bacterial growth rate and yield. Our hypothesis is that these type of antibiotics could lead to slowly dividing, and yet more efficient cells. Data supporting the previous theories on this topic, however, is scarce.[42] First we needed to validate the hypothesis in the laboratory.

5.2 Differences in ribosomal content, mediated by the *rrn* operons, shape fitness landscape and robustness of metabolic rate-yield trade-off profiles

To quantify metabolic rate-yield trade-offs (RYTOs) we used the derivative strains of *E. coli*, described in Table 5.1, in cultures grown for 24h. These bacteria were grown in minimal media with increasing concentrations of glucose, ranging from 0 to 3mg/mL (0-0.3% w/v), complemented with equally increasing concentration of casamino acids, from 0 to 0.75mg/mL.

Table 5.1. Strains of *Escherichia coli* used to perform the experiments described in this chapter. All strains from Reference 41. Number of *rrn* operons removed from the wild-type strain MG1655 indicated by Δ.

Strain	***Genotype***
E. coli MG1655	K-12 *F- λ− ilvF0 rfb-50 rph-1*
E. coli Δ1	MG1655 Δ*rrnE*
E. coli Δ2	MG1655 Δ*rrnGB*
E. coli Δ3	MG1655 Δ*rrnGBA*
E. coli Δ4	MG1655 Δ*rrnGADE*
E. coli Δ5	MG1655 Δ*rrnGADEH*, ptRNA67

During a 24h period, we measured the optical density at 600nm (OD_{600}) at a frequency of 20min per readout. We therefore designed an algorithm in Matlab to fit the mathematical models to cell growth data of the following form:

$$OD(t) = a + bt, \text{ with } r = b/a, \tag{5.1a}$$

$$OD(t) = a + be^{rt}, \tag{5.1b}$$

$$OD(t) = a + \frac{K}{1 + be^{-rt}}, \tag{5.1c}$$

where t denotes the time in hours, r the *per capita* growth rate, K the carrying capacity

of the culture, a is an estimate of the optical density of the culture at $t = 0$ and b a phenomenological coefficient. We used these models because they describe three possible growth curves that we could observe in the experiment. For example EQUATION 5.1(a) describes the case in which OD_{600} does not vary through time due to the lack of cell growth, or when this is slow enough to be undetectable by our plate-reader device. The other two models describe the case in which cell growth can be detected, but it describes different curves. If the growth is slow enough and the nutrients supplied are not depleted during a 24h period, we expect an exponential-like growth curve, best described by EQUATION 5.1(b). But if the nutrients are depleted during this period, after an exponential growth phase, bacteria enter a maintenance mode in which culture density remains at a stationary level. This case is best described by EQUATION 5.1(c).

We thus need to select objectively one of these model to extract meaningful information from our datasets, so we designed an algorithm to score each model using the corrected 'Akaike Information Criterion' (AICc). The Matlab routines `fitlm` and `fitnlm` provide information about the AICc, where

$$AIC := N \cdot log\left(det\left(\frac{1}{N}\sum_{1}^{N}\varepsilon(t,\theta_N)(\varepsilon(t,\theta_N))^T\right)\right) + 2n_p + N\cdot(n_y\cdot(log(2\pi)+1))$$

and

$$AIC_c := AIC + 2n_p\cdot\frac{n_p+1}{N-n_p-1}.$$

Here N denotes the number of values in the estimation dataset, $\varepsilon(t)$ a n_y – by – 1 vector of prediction errors, θ_N the estimated parameters, n_p the number of estimated parameters, and n_y the number of model outputs. The best model was then defined as that with the lowest AICc.[108] Next, we extracted the corresponding information for *per capita* growth rate (r) and carrying capacity (K). In cultures grown with 0mg/mL of glucose we defined, for convenience, that K would be the optical density measured after the 24h incubation period. Finally we related our dataset for growth rate and carrying capacity to the concentration of glucose.

FIG. 5.2 shows the relationship between carrying capacity and glucose supplied to the media. This data is worthy of mention because it contains information on the rate-yield trade off (the RYTO) we were seeking. The carrying capacity is a measure

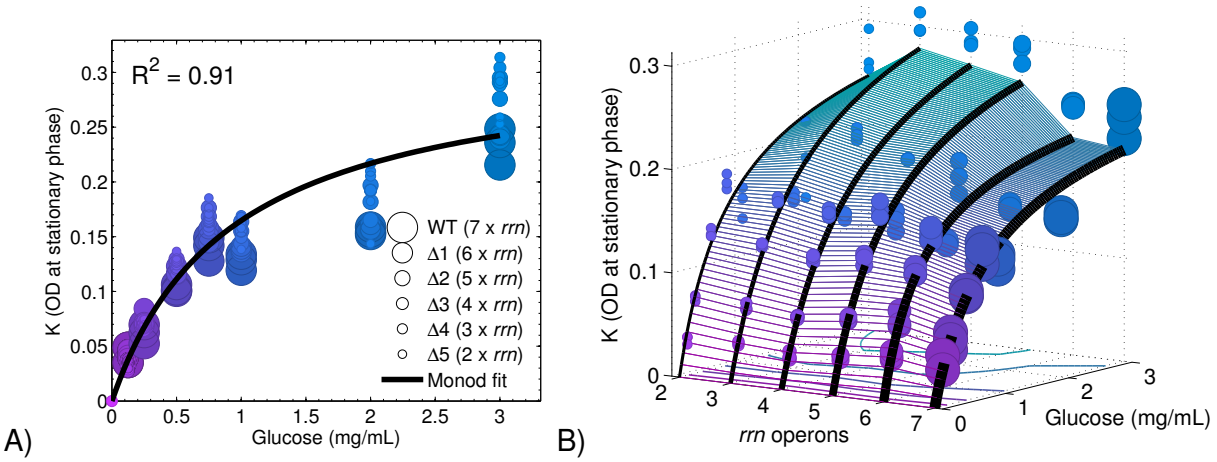

FIGURE 5.2. A) Non-linear, monotonic increase in the carrying capacity, K, shown on the y-axis, as a function of the concentration glucose of glucose supplied to the media, shown on the x-axis. **B)** Landscape of possible carrying capacities as a function of both glucose supplied and copies of the *rrn* operon. Contour lines show the combination of glucose and number of *rrn* operons with identical K.

of the maximal cell density supported by each concentration of glucose. The ratio between this capacity and glucose thus defines the number of cells produced per unit of glucose, or yield. A constant yield would mean that the number of cells produced by unit of glucose does not depend on the latter. If this were the case a straight line would a good descriptor of our data in FIG. 5.2, but it was not. In fact our data was best described by the Monod model in which the rate of change in cell density (dB/dt) is defined as

$$\frac{dB}{dt} = B\frac{r_{max}C}{k_m + C}$$

where B denotes bacterial cell density, r_{max} the maximum *per capita* growth rate, C the concentration of carbon and k_m the associated half-saturation constant.[109,110] Consequently, we observed that cells grown at higher glucose concentrations had lower yields. Defining explicitly the yield as the ratio between K and glucose, FIG. 5.3 displays the dependence of yield on glucose concentration for all the strains used. The maximum yield was achieved with the lowest concentrations of glucose and *vice versa*. This transition defined a hyperbolic profile where the lower boundary set a minimum, limiting yield. FIGS. 5.2 and 5.3 highlight the consistency of the profiles generated irrespective of the number of *rrn* operons carried by the different strains. The number of these operons, however, had subtle effects on how yield changes as a function of the glucose supplied. We observed that strains with fewer copies of the operons

normally had higher yields and carrying capacities (FIG. 5.4). The same phenomenon was reported in the literature as a paradox,[111] but it is consistent with the idea that an excess of synthesis of ribosomes sets a metabolic burden in environment with little nutrients.[112,113] The phenomenon is still poorly understood.

Next we analysed the changes in *per capita* growth rate as a function of glucose concentration and observed a concentration at which this growth rate was maximised (FIG. 5.5). There was a range of concentrations of glucose in which this measure of growth rate increased with the glucose supplied, but if the glucose was further increased the growth rate declined, resulting in the aforementioned optimum glucose supply. We demonstrated that this is consequence of a RYTO by fitting to our data the model[42]

$$\text{Growth rate}(S) = c(S) \cdot \frac{V_{\max} S}{k_m + S}$$

where the conversion factor from sugar, S, which is glucose, to biomass, $c(S)$, is given by

$$c(S) = c_{\text{lo}} \frac{S}{1 + pS} + c_{\text{hi}} \frac{1}{1 + pS}.$$

Here p is a model parameter that controls the rate of decrease in cell yield, $c(S)$, as a function of increases in sugar, S. The parameters c_{lo} and c_{hi} are the lowest and highest yields, respectively, that the model can achieve. In order to turn this yield model into a growth rate, the value of $c(S)$ is multiplied by an uptake rate of sugar into the cell and this is taken to be of the standard Monod form, whereby V_{max} is the maximal uptake rate and k_m is the half-saturation constant associated with that uptake response.

This model of the dependence of yield on glucose was also used to fit the yield data shown in FIG. 5.3. From FIGS. 5.3 and 5.5 it is clear that the form we presented for $c(S)$ was consistent with our data for both growth rate and yield. Note that $c(S)$ is one possible theoretical form of a RYTO and it was derived elsewhere.[42] The form of $c(S)$ is a monotonic function that can either increase or decrease and it describes a *within-strain RYTO* in the case whereby it is an decreasing function. FIG. 5.3 shows that the data was consistent with the decreasing form of this model. Further analysis of our data also revealed the existence of an optimal number of *rrn* operons that maximised both yield and *per capita* growth rate (FIGS. 5.3B and 5.5B). To highlight this we used a linear model for the yield (FIG. 5.4) and a non-mechanistic quadratic model for

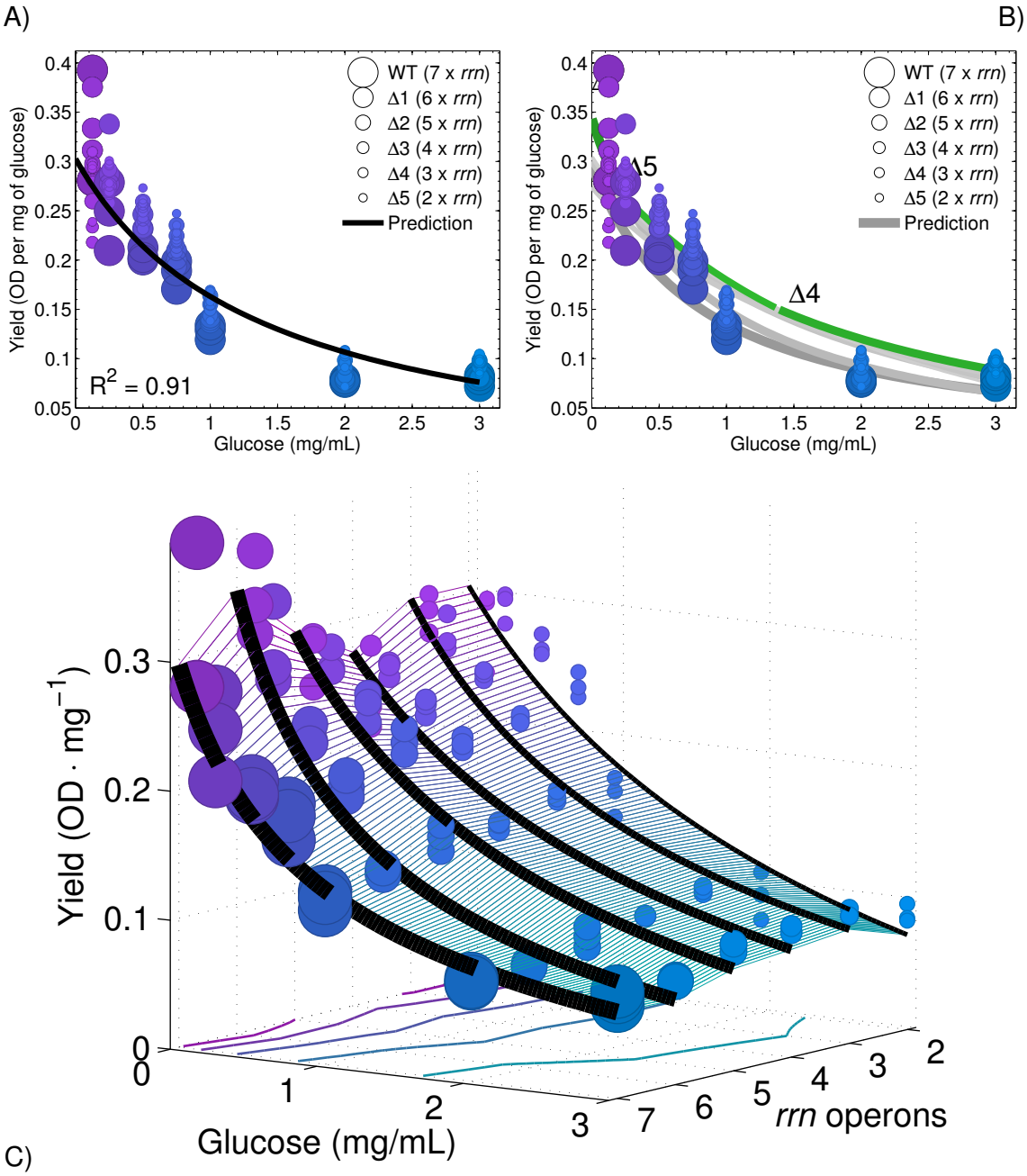

FIGURE 5.3. A) Representation of yield, measured as the ratio between K and glucose supplied, on the y-axis and the glucose supplied to the media, on the x-axis. The decrease in yield as a function of glucose supplied describes a hyperbola that is consistent with formerly hypothesised RYTOs based on a branched pathway, each branch leading to different yields.[42,114] **B)** Upon variation in environmental conditions, here in glucose supplied, the relative maximum yield (green, strains in black) is achieved by strains with different number of *rrn* operons. Per-strain hyperbola, as formalised in p. 97, shown in grey. **C)** Landscape of possible yields achieved as a function of the glucose supplied and the number of *rrn* operons. Contour lines show the combination of glucose and number of *rrn* operons with identical yield.

per capita growth rate (FIG. 5.6). The dataset presented in FIG. 5.6 resembles the prediction of a theory[115] in which bacterial growth rate depends on the abundance of

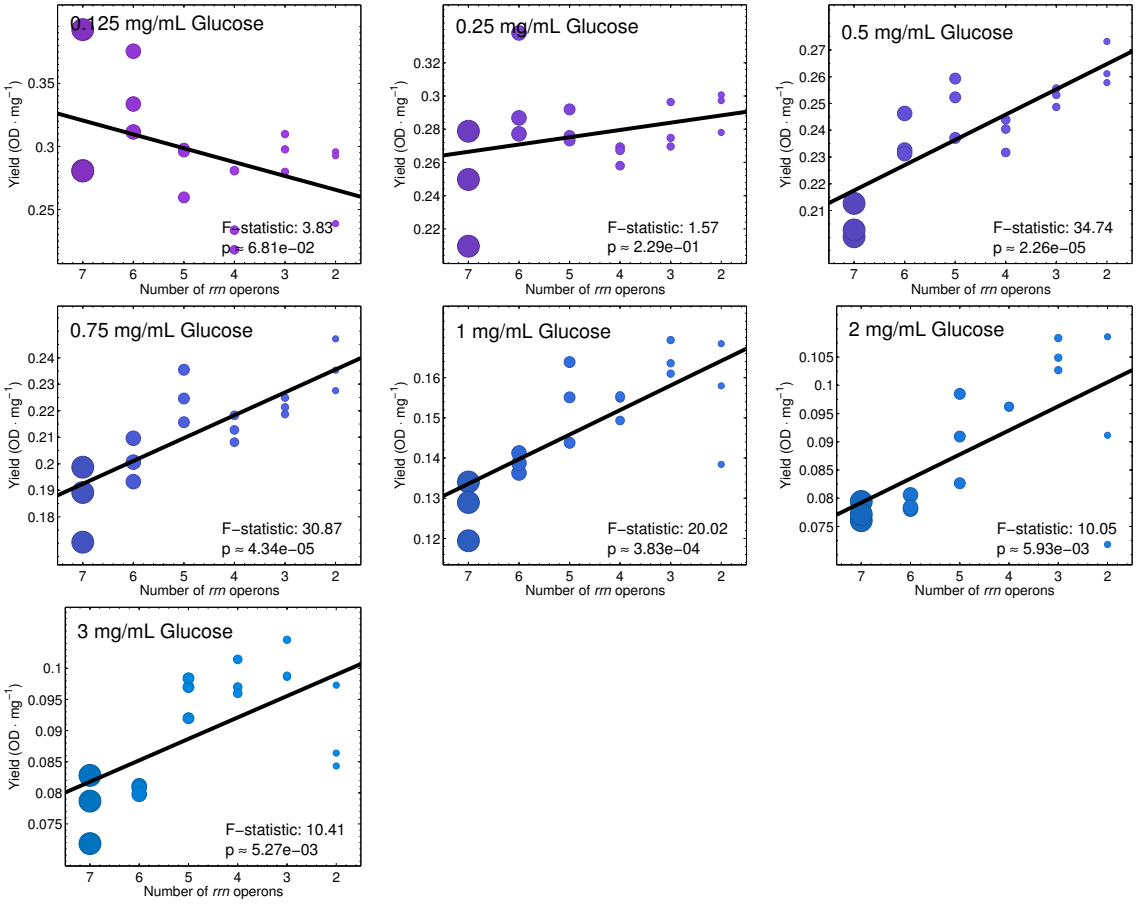

FIGURE 5.4. Representation of the change in yield, shown on the *y*-axis, as a function of the number of *rrn* operons. Each subplot shows this relationship when different concentrations of glucose is supplied of the media. Overall, there is a linear, significant increase in yield as the number of *rrn* operons is reduced when the concentration of glucose is above 0.25 mg/mL (black). However, we observed no significant change when this concentration is equal or lower than 0.25mg/mL.

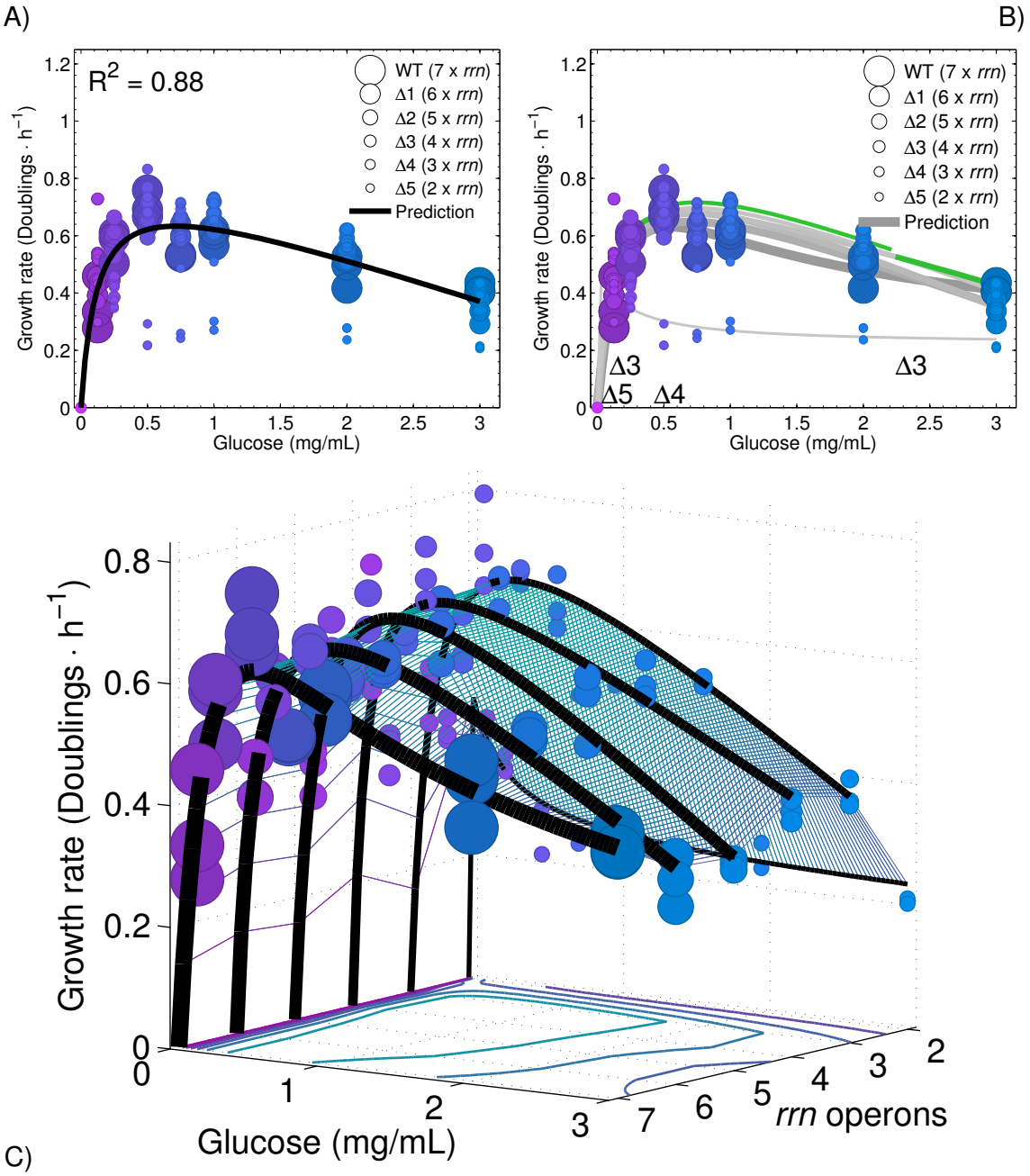

FIGURE 5.5. A) Change in *per capita* growth rate, shown on the *y*-axis, as a function of the glucose supplied to the media, on the *x*-axis. We modified Monod's growth model (in black, see p. 97) to include, explicitly, the glucose-dependence property of the yield. We observed an absolute, overall optimum *per capita* growth rate at ≈0.5 mg/mL of glucose. **B)** Upon variation in environmental conditions, here in glucose supplied, the relative maximum *per capita* growth rate (green, strains in black) is achieved by strains with different number of *rrn* operons. Per-strain hyperbola, as formalised in p. 97, shown in grey. **C)** Landscape of possible *per capita* growth rates achieved as a function of the glucose supplied and the number of *rrn* operons. Contour lines show the combination of glucose and number of *rrn* operons with identical yield.

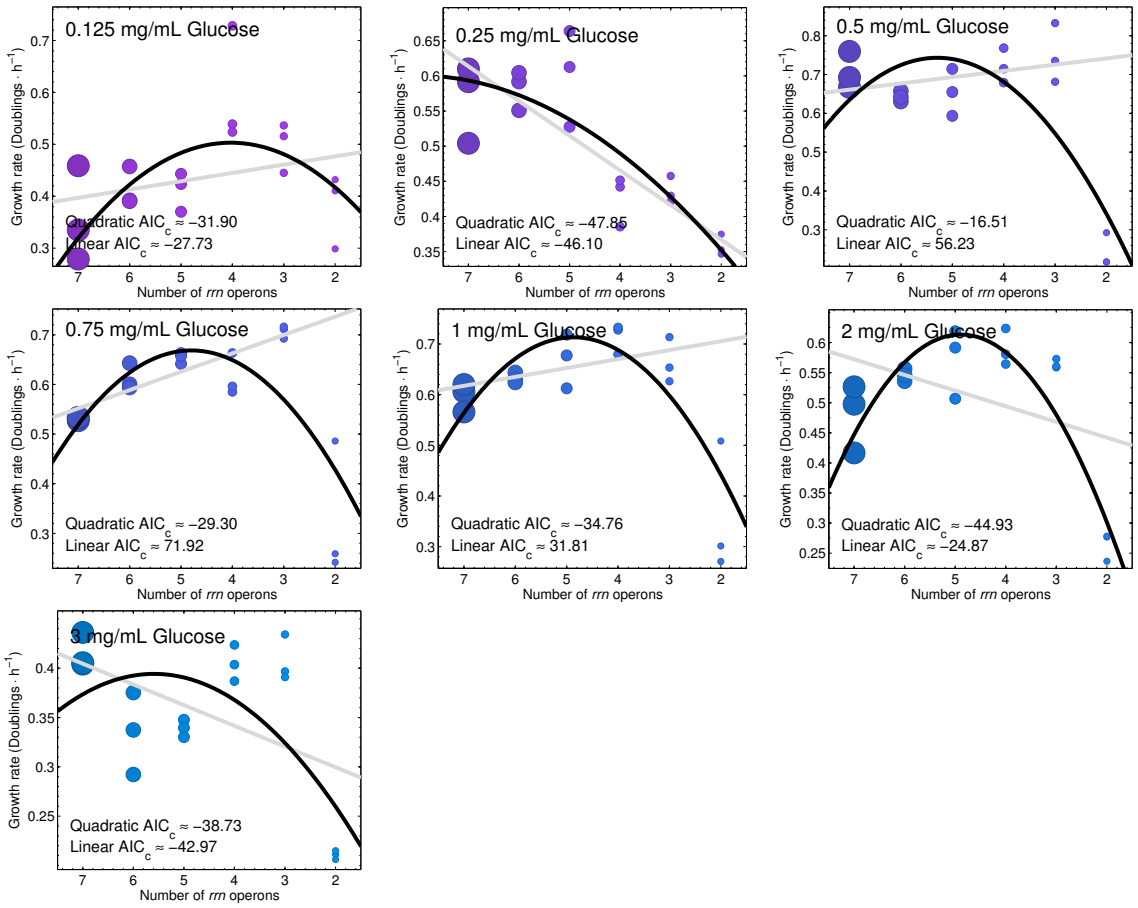

FIGURE 5.6. Representation of the change in *per capita* growth rate, shown on the *y*-axis, as a function of the number of *rrn* operons. Each subplot shows this relationship when different concentrations of glucose is supplied of the media. We compared whether the change in *per capita* growth rate is linear (light grey) or non-linear (black). We tested the non-linearity of the data by fitting the quadratic model $r(G) = a + b \cdot G + b \cdot G^2$ to the data. Here r denotes *per capita* growth rate, G the concentration of glucose, a *per capita* growth rate when $G = 0$, and b and c phenomenological coefficients.

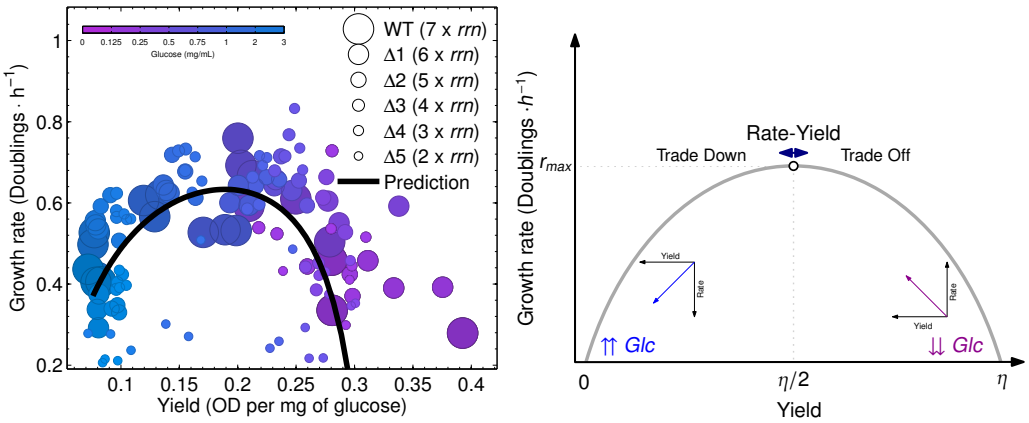

FIGURE 5.7. Left) Relationship between the *per capita* growth rate, measured as doublings per hour on the *y*-axis, and yield, defined as cell density in OD units generated per mg of glucose after 24h of growth, on the *x*-axis. The black line represents the predicted, overall RYTO profile based on the predictions for yield (FIG. 5.3A) and *per capita* growth rate (FIG. 5.5A). **Right)** When we compare the data in A) with the concentration of glucose, we observe RYTO at low glucose concentrations, whereas at higher concentrations the RYTO turns into a rate-yield trade down (RYTD).

ribosomes as it follows:

$$\text{Growth rate}(S) = \left[\frac{\phi_R^{max} - \phi_R^{min}}{1/\gamma + 1/\nu}\right]\frac{S}{K_m + S}$$

Where the growth rate is a parabolic function of the ribosomal fraction (ϕ_R), controlled by us through the *rrn* operons, provided the translation efficiency (γ) and yield (ν) are constant. The differences between FIG. 5.6 and this theory may lie in the fact that yield can be a function of the abundance of resources, as we will demonstrate in this chapter (FIG. 5.3).

Following this analysis we were able to compare changes in *per capita* growth rate as a function of the yield (FIG. 5.7). Overall, the data described a parabolic profile which resembled the expectations from the theories introduced at the beginning of this chapter (FIG. 5.1A). Including the information about glucose supply in each case, we distinguished three phases in our RYTO dataset also predicted by the models. First there was a rate-yield trade-off (RYTO) with very low concentrations of glucose, whereby increases in yield necessarily involved a decrease in *per capita* growth rate, and *vice versa*. On the other hand, a decline in *per capita* growth rate was coupled with a decrease in yield with high glucose supply. This therefore described a rate-yield trade-down (RYTD). Growth rate and yield could also be uncoupled when the concentration of glucose was in between the previous extreme cases.

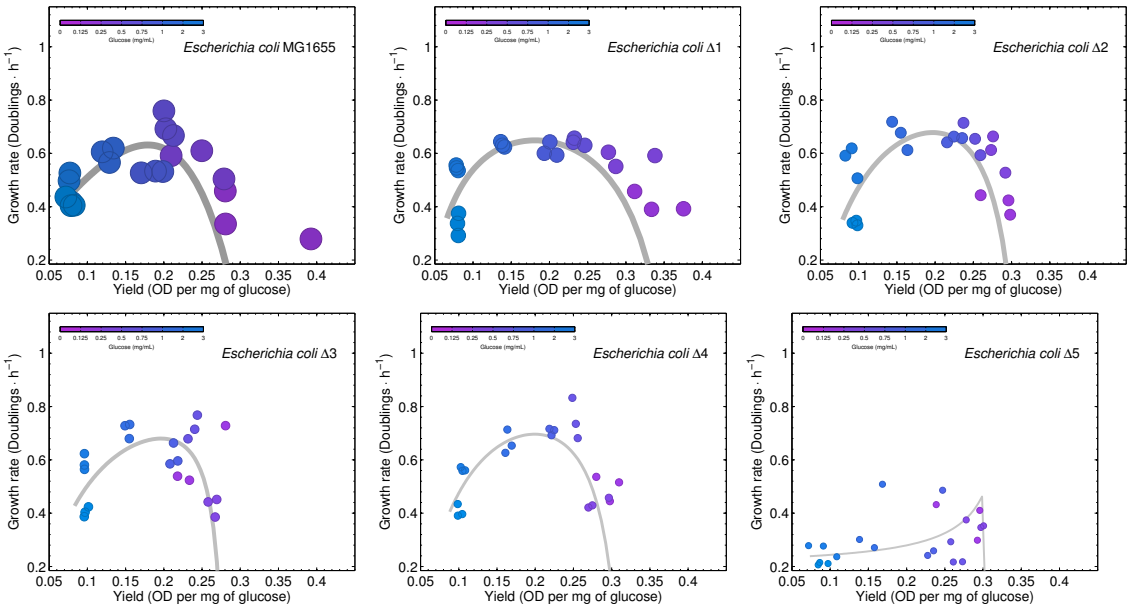

FIGURE 5.8. Relationship between the *per capita* growth rate, measured as doublings per hour on the *y*-axis, and yield, defined as cell density in OD units generated per mg of glucose after 24h of growth, on the *x*-axis. Each subplot represents this relationship for every strain, and hereby demonstrates the robustness of this RYTO.

The shape of the general RYTO profile was maintained in all the strains used except for the one with the fewest ribosomal RNA operons, Δ5, this showed the remarkable robustness of the relationship between growth rate and yield (FIG. 5.8). We later asked whether or not the differences in yield and *per capita* growth rate due to loss of *rrn* operons could lead to *between-strains* RYTOs. FIG. 5.9 highlights the difficulty of studying *between-strain* trade-offs. Whilst we have a good understanding of the *within-strain* RYTO/RYTD, it was difficult to discern the existence of a self-consistent set of trade-offs, or trade-downs, from the data presented in FIG. 5.9. The statements that can be made from linear regression analyses, as to the presence or absence of a *between-strain* trade-off, were sensitive to the algorithms used due to the presence of potential outliers.

Moreover, there is no theory of how a rate-yield trade-off would be mediated by the number of ribosomal RNA operons. As a consequence, as of yet we have no understanding of what mechanisms support the data presented in FIG. 5.9.

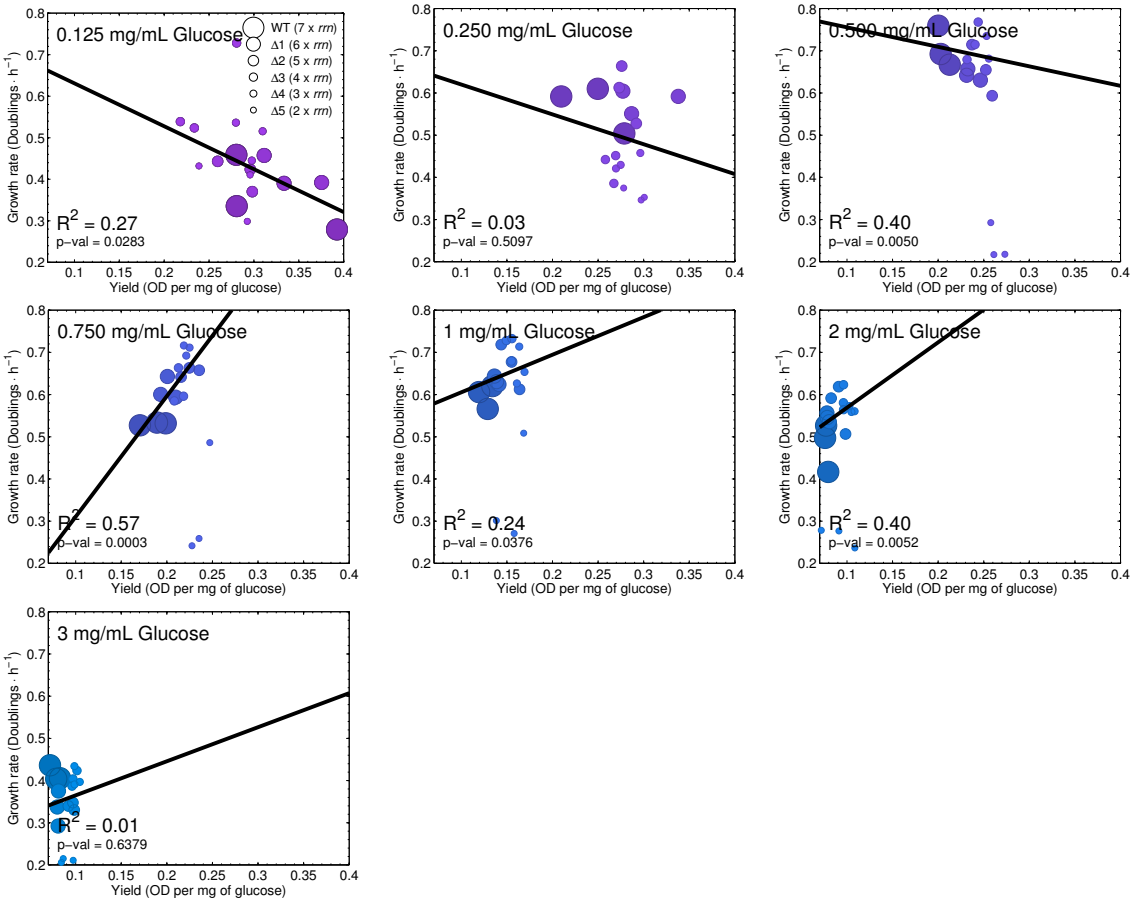

FIGURE 5.9. Relationship between the *per capita* growth rate, measured as doublings per hour on the *y*-axis, and yield, defined as cell density in OD units generated per mg of glucose after 24h of growth, on the *x*-axis. Each subplot represents this relationship as a function of the number of *rrn* operons and glucose supply.

5.3 Robustness of the RYTO to different measurements of growth rate

Whilst the definition of cell yield is straightforward, the definition for growth rate can be subject to some interpretation. The above analysis is based on *per capita* growth rates, defined as the number of estimated cell divisions per unit of time *per capita*. This estimation assumes a density-dependent growth rate, but we could also have quantified the growth rate in ecological terms using finite difference approximations applied directly to OD data. These approximations quantify differences in optical density as a function of time, using a mathematical model-free estimate of the culture growth rate. We therefore note the rate of change in OD as a function of time, written $OD'(t)$, as being

$$OD'(t) = \frac{OD_{t+\Delta t} - OD_t}{\Delta t}$$

where Δt is the read frequency in hours. The maximum growth rate of the culture, r_{max}, is defined as

$$r_{max} = \max_{0 \leq t \leq 24h} OD'(t).$$

The parameter r_{max} is expressed as the maximum increase in OD_{600} units per hour. In Fig. 5.5 we quantified how the *per capita* growth rate parameter, taken from the logistic model in Equation 5.1c, has an absolute maximum at a specific concentration of glucose and, if the glucose was further increased, the growth rate declined. We demonstrated that this observation is consistent with a non-constant yield. However, if we quantify the growth rate differently (r_{max}) the resulting dataset is no longer consistent with a non-constant yield. In fact, it is consistent with Monod's original growth model, which assumes a constant yield (Fig. 5.10). The relationship of other parameters with the abundance of *rrn* operons also applies here and fewer operons lead to higher r_{max}.

Consequently, the relationship between r_{max} and yield did not resemble a parabola, as shown in Fig. 5.7. We did observe a trade-off between r_{max} and yield, but the profile generated had different properties, the most significant being the lack of trade-down between rate and yield when the glucose supplied was high. Thus, this profile is not compatible with the theories introduced in this chapter (Fig. 5.1). It is, nevertheless, compatible with the analogue from physics known as 'maximum power transfer theorem'. The use of this theorem in biology defined the 'maximum power principle',[116,117]

which proposes that open, self-organised systems tend to operate with an efficiency that maximises the useful power or *biomass production*.[37,117]

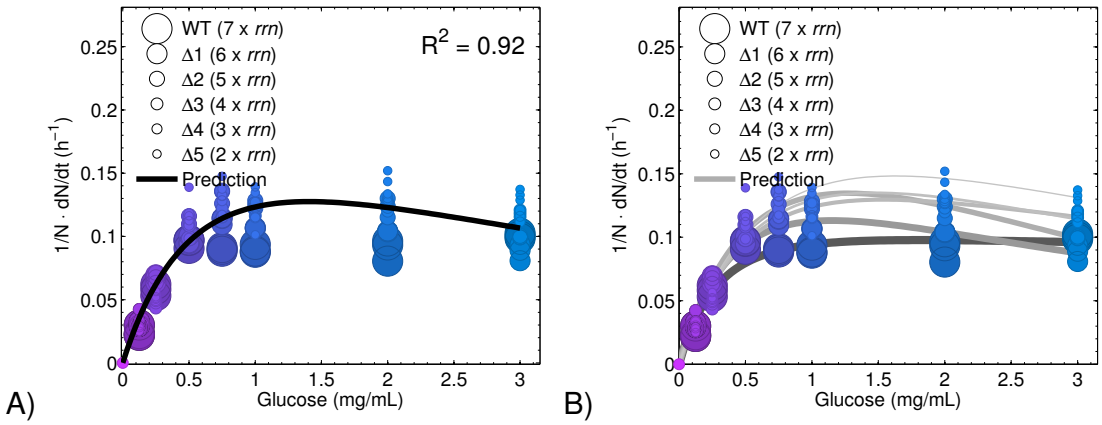

FIGURE 5.10. A) Culture growth rate, r_{max}, shown on the y-axis as a function of glucose supply, shown on the x-axis. The black line represents the overall growth rate as predicted by Monod's growth, as opposed to that predicted per strain, represented in **B)**.

If we consider the yield (y) to be a proxy for growth efficiency, the production of biomass (P) in our cultures can be estimated as $P = r_{max} \cdot y$.[37,117] Thus the production of biomass reflects the number of cells produced by each cell per hour, per unit of glucose. The resulting dataset reflects the existence of a production-efficiency trade-off (PETO, FIG. 5.11). The profile described by the PETO contained all the properties that we previously described for a RYTO (FIG. 5.7): three different phases leading to a trade-off, trade-down, independence of power and yield as a function of the glucose supplied. Also, we observed the effect of the abundance of ribosomal RNA whereby fewer *rrn* operons led to higher production of biomass, likely due to a reduction of the metabolic burden caused by the synthesis of ribosomal proteins in conditions of low nutrients.[112,113] We do not have a theory to explain the existence of a PETO, so we used a non-mechanistic quadratic model to detect whether or not the relationship between biomass production and yield conforms a parabola.

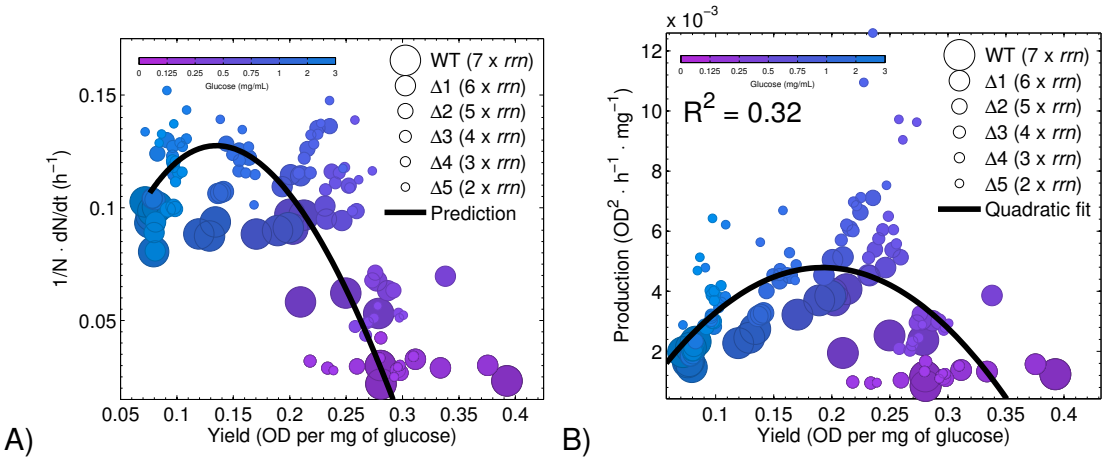

FIGURE 5.11. A) Relationship between the population growth rate, r_{max}, shown on the y-axis, and yield on the x-axis. The size of the data points is indicative of the number of *rrn* operons, from seven copies in the wild-type strain MG1655 (labelled WT) to just two copies in the strain with five deletions, Δ5.Relationship between power output,[37] shown on the y-axis, and yield, on the x-axis. The black line represents the quadratic model $P(Y) = a + b \cdot Y + b \cdot Y^2$, P denoting the power output, Y the yield, a the growth rate when $y = 0$, and b and c phenomenological coefficients. The 95% confidence for a is (-0.003, 0.0004), for b (0.042, 0.086), and for c (-0.220, -0.110). The trend is analogous to that observed in FIG. 5.7.

5.4 CONTRIBUTION OF EACH *rrn* OPERON TO THE YIELD

The wild-type strain of *E. coli* used in this chapter, MG1655, contained seven *rrn* operons.[101,102] Until now the yield has been defined in absolute terms as OD_{600} units produced per mg of glucose. However, this definition does not account for differences in the abundance of ribosomal RNA operons. Now, we defined the yield *per operon*, or relative yield, as the ratio between the yield and the number of *rrn* operons present in each strain.

If FIG. 5.3 showed the existence of a negative correlation between ribosomal RNA abundance and absolute yield, this correlation was maintained when yield *per operon* was used (FIG. 5.12). Also, the use of relative yield to quantify RYTOs resulted in the aggregation of the data in two separate clusters which are characterised by the number of *rrn* operons (FIG. 5.13). Strains with three to seven operons were contained within one cluster, whereas the strain with two operons was contained in the other. These clusters are also characterised by different combinations of *per capita* growth rate and relative yield. The first cluster contained strains with lower relative yields than those in the second cluster, which contained strains with lower *per capita* growth rates. We observed no change in the existence, or lack of thereof, *between-strains* RYTOs (FIG.

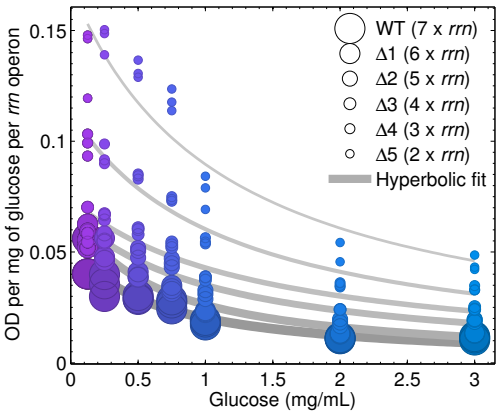

FIGURE 5.12. Relative yield, defined as OD units generated per mg of glucose per *rrn* operon, is shown on the *y*-axis as a function of the glucose supplied to the media, on the *x*-axis. Lines represent the best model fit: exponential (light grey) or sigmoidal (dark grey), chosen depending on the corrected Akaike Information Criterion (AICc).

5.14).

For completeness we repeated the analysis of the RYTOs using r_{max} to estimate the growth rate and relative yield (FIG. 5.15). The use of relative yield did not produce qualitative changes in the profiles observed previously.

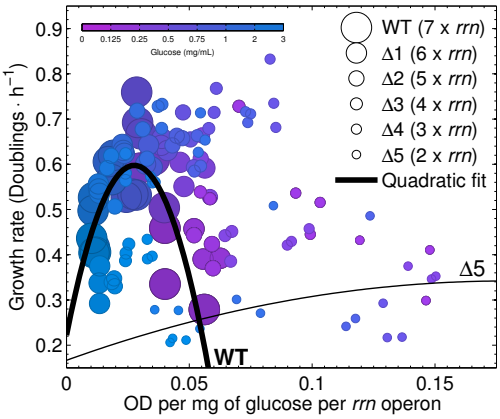

FIGURE 5.13. Shape of the RYTO profile when relative yields are taken into account. The strains containing seven to three *rrn* are clustered within a group with high *per capita* growth rate but low relative yield, whereas the strain with two *rrn* operons, Δ5, forms a second cluster characterised by lower *per capita* growth rates and higher yields. Black lines correspond to the estimation from a quadratic model. Regression for the wild-type (WT): R^2 = 0.56, F-statistic *versus* constant model: 11.7, p = 0.000562. Regression for Δ5: R^2 = 0.27 , F-statistic *versus* constant model: 3.44, p = 0.0541.

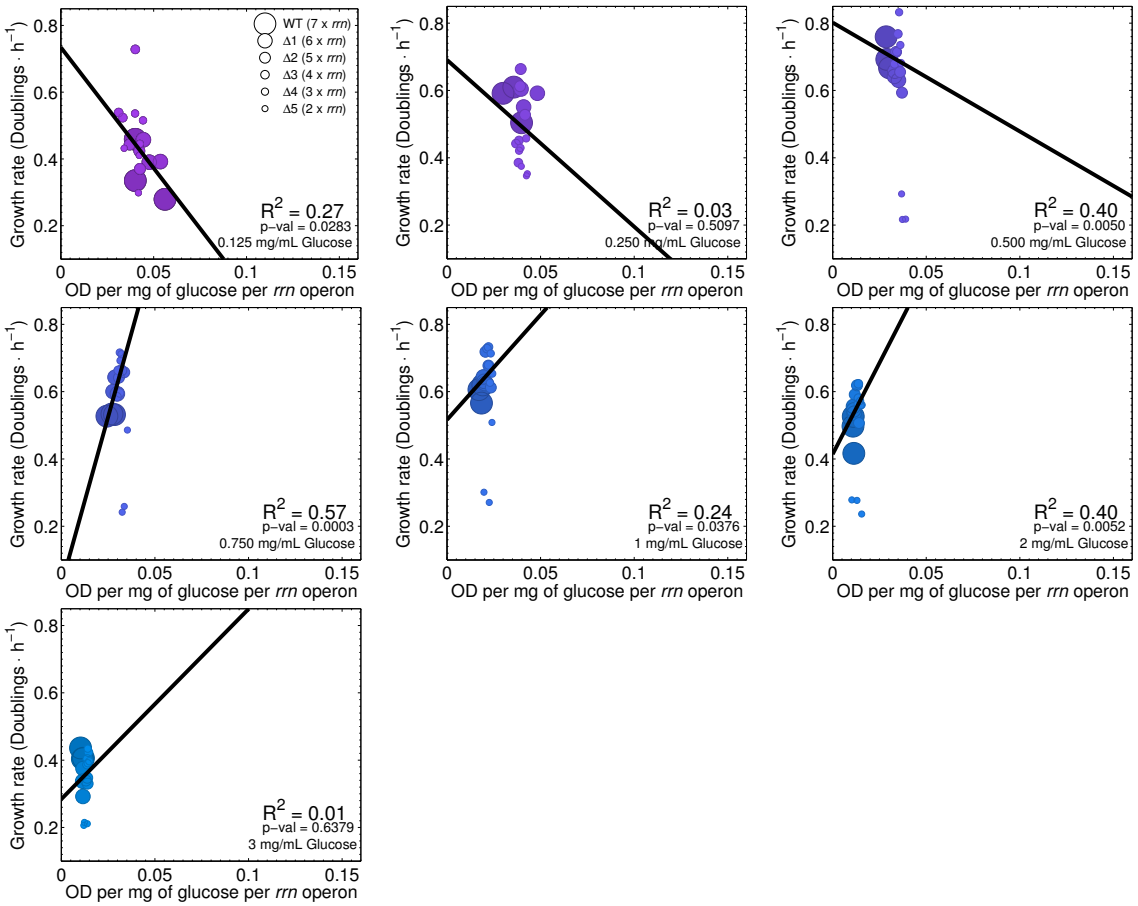

FIGURE 5.14. Effect of the number of *rrn* operons on the metabolic rate-yield trade-off when relative yield is taken into account. Each plot represents this effect when different concentration of glucose is supplied to the media. In each subplot, *per capita* growth rate is represented on the *y*-axis, whereas the yield, defined as cell density in OD units generated per mg of glucose after 24h of growth, is represented on the *x*-axis.

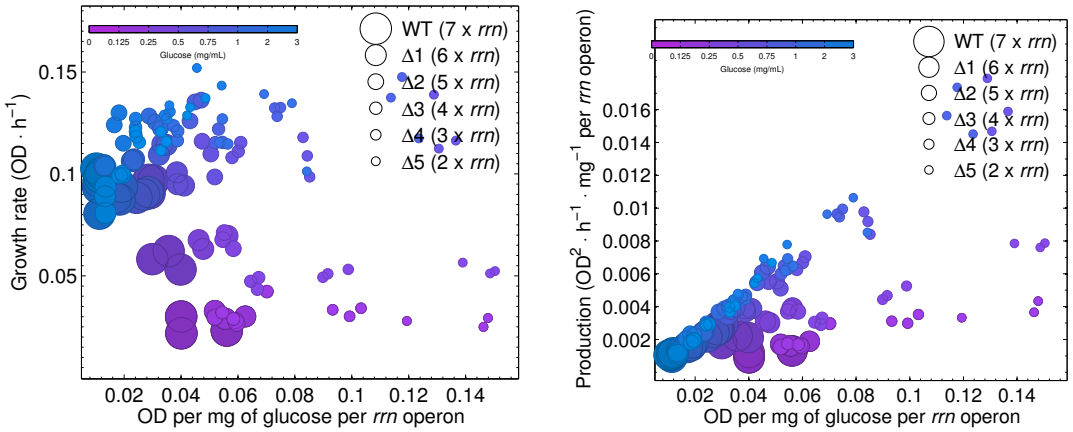

FIGURE 5.15. Left) Relationship between the population growth rate, measured as the maximum increment in OD per hour, shown on the *y*-axis, and relative yield, defined as cell density in OD units generated per mg of glucose after 24h of growth, on the *x*-axis. **Right)** Relationship between biomass production,[37] shown on the *y*-axis, and relative yield, on the *x*-axis.

FIGURE 5.16

5.5 Conclusions

During this chapter we analysed the relationship existing between growth rate and biomass yield. We observed that these traits can be positively or negatively correlated depending on the abundance of a carbon source, like glucose, generating a parabolic profile. The phenomenon is due to the existence of branched metabolic pathways whereby a carbon source, glucose, is processed with different efficiencies that we quantified as culture OD per mg of glucose supplied (yield).

When the efficient branch of the pathway is being used we found that growth rate and yield are negatively correlated, whereas if the inefficient pathway is being used these traits are positively correlated. This means that if one of the traits is manipulated, say by the addition of an growth-inhibitor antibiotic, the yield could change accordingly depending on whether the cells are using the efficient or inefficient pathway. In Chapter 2, for example, we observed how the *rate* of production of AcrB, component of the multi-drug efflux pump AcrAB-TolC, is reduced by a protein synthesis inhibitor antibiotic (Fig. 2.15). However, the *total amount of protein* produced per cell (therefore total efflux pumps per cell) was higher until the concentration of the antibiotic was too high.

Finally we found this phenomenon to be robust not only to artificial changes in growth rate and yield, through the manipulation of the ribosomal RNA *rrn* copy number, but also to how growth is measured. Whether is *per capita* growth rate or biomass production, the parabola is maintained.

VI CONCLUDING REMARKS

6.1 Evolutionary landscapes

One of the central themes in evolutionary biology has been the notion of an evolutionary landscape[118]. Such landscapes are based on the idea that absolute fitness can be represented, typically on a Cartesian z-axis, as a function of two constraining traits on the x- and y-axes. In this thesis we provide data for two types of evolutionary landscapes.

In Chapter 2 we provided datasets that showed the adaptive strength of the bacterium *Escherichia coli* growing in the presence of the antibiotic erythromycin (Figures 2.21 to 2.19). Motivated by a theoretical model, the sensitivity to erythromycin was quantified over a 24h incubation period and we demonstrated that such sensitivities can change through time. This change can have different causes but in our case this is determined by the efflux pump AcrAB-TolC. Originally used for the evacuation of metabolic byproducts, this pump is recycled by the cell very rapidly to remove molecules of antibiotic.

The representation of the rate of adaptation (α) in Figures 2.24 to 2.26 highlighted an evolutionary landscape in which very specific concentrations of erythromycin were able to maximise selection on this efflux pump (evolutionary 'hotspot') but other concentrations were able to diminish the cell's capacity to adapt (evolutionary 'coldspot'). None of these spots were related to the minimum inhibitory concentration (MIC) as previously suggested elsewhere,[17,18]. Moreover, we also saw that the strength of selection on resistance can be a non-linear and non-monotone function of the dose.

We also presented another type of landscape. In CHAPTER 5 we showed a fitness landscape in which we could read the dependence of fitness, as *per capita* growth rate, not only on a mutable genetic element but also on the environment (FIG. 5.5C). The data indicated that different environments had different fitness landscapes associated with them. It also indicated that a different genotype could be optimal for each environment regardless of how optimality is interpreted, whether with respect to yield (FIG. 5.3B) or growth rate (FIG. 5.5B). If we imagine selection, or indeed some form of historical selection, acting upon copy number variants of the *rrn* operon, we can use this representation of our data to tentatively hypothesise a reason why bacteria might have different numbers of these operons.

According to our data, this number would depend on the glucose concentration of the environment. For example, FIG. 5.3B predicted that strains Δ1 and Δ4 had the optimal number of operons in environments where yield is a good predictor of fitness, depending on the availability of carbon in the environment. On the other hand, FIG. 5.5B showed that Δ3, Δ4 and Δ had the optimal number of operons for growth rate depending on the availability of carbon in the environment.

We further hypothesised that in environments whereby extracellular resources like glucose fluctuate in a seasonal manner, the resulting fluctuating selection might act to support a polymorphism on the number of operons which may allow, for example, Δ3, Δ4 and Δ5 to be stably maintained in the same polymorphic community. We have not, however, tested this prediction.

6.2 ROBUSTNESS OF ANTIBIOTIC SENSITIVITY TESTS

Considering the capacity of bacterial cells to adapt, it seems hard to believe that the optimal control of such a dynamic system can be achieved by constant, non-responsive control strategies such as those suggested by ASTs.[11] For example, the optimal inhibiting concentration of erythromycin for the wild-type strain AG100 was ~37μg/mL, as we described in CHAPTER 2. This concentration, optimal for a 24h incubation period, became sub-optimal after three days of treatment due to the duplication and selection of the multi-drug efflux pump AcrAB-TolC. Although ours was a laboratory setup, similar changes in sensitivity during antibiotic therapies has also been reported

in the clinic.[119–121]

But time was not the only factor altering the outcome of ASTs. We also demonstrated the role of competitors for resources and how these may sensitise, or otherwise, bacterial cells. The result of this 'sensitising' process would depend on the competitor's own sensitivity to the antibiotic. When two competing bacteria were equally sensitive to an antibiotic they could appear more resistant to the drug when they are grown together (FIG. 3.2). However, if each of them are differentially drug-sensitive competitors, the most sensitive competitor appears to be additionally sensitised (FIGURES 3.1, 3.9, and 3.10). For this latter case, the effect is maintained through time (FIGURES 3.15 and 3.12).

We therefore hypothesise, tentatively, that appropriately engineered non-pathogenic cells, merely acting as resource thieves, or 'niche occupiers', might be used to *sensitise* pathogenic cells in combination with antibiotics *in vivo*.

6.3 IN SPATIALLY DISTRIBUTED CULTURES, THE NON-LINEAR SELECTION ON ACRAB-TOLC IS MANIFESTED AS BULLSEYE PATTERNS

We have used a prediction from the results of several theoretical models to show that bacterial growth in an antibiotic gradient can result in a visible spatial pattern, moreover this pattern can be used to reject the hypothesis that more antibiotic necessarily equates to less bacterial population growth also in a spatial context.

The laboratory model system we have used is not based on the occurrence of single nucleotide polymorphisms (SNPs) as the drivers of the evolutionary processes that produce this spatial pattern, but rather a drug efflux operon that is rapidly duplicated by recombination in the face of antibiotic stresses is the mechanism of resistance selected for by evolution. It is selection on this operon that creates the requisite spatial pattern. Moreover, we have introduced a series of quantitative measures of monotonicity to help discern in quantitative terms what is apparent to the human eye in images of bacterial growth on agar plates in antibiotic gradients.

Our results are not directly relevant to the interpretation of antibiograms in a clinical context, although we have shown that an increase in drug dosage increases the size of the zone of bacterial growth inhibition according to a square root law, consistent

with diffusion theoretic models of bacterial killing. However, our observations are key to understanding conditions for which an increase in drug concentration will not necessarily reduce bacterial densities. After all, all practical uses of antibiotics create decaying dose profiles as one moves further way from the point source of an antibiotic drug. So, while it may be thought that one can mitigate, or even obviate, the process of selection for drug resistance by always passing to ever greater dosages,[1,122] those dosages must eventually decay to zero in regions of treatment located not too far from the source whereby one might be able to observe the effects we allude to in our study.

SUPPLEMENTARY DATA

I SUPPLEMENTARY CHAPTER 2

I.1 Model fit. This chapter includes the plots that we used to visually validate the fitting process described in SECTION 2.7. We denoted the readings as a function of time as $R(t)$, and fitted the following models to our data using a routine coded using Matlab (see below)

$$R(t) = R_0 + bt, \text{ with } r = b/R_0, \tag{S.1a}$$

$$R(t) = R_0 + b^{rt}, \tag{S.1b}$$

$$R(t) = R_0 + \frac{K}{1 + b \cdot e^{-rt}}. \tag{S.1c}$$

Here R_0 denotes the readings at the beginning of the experiment, r *per capita* growth rate, K the carrying capacity, and b a phenomenological coefficient. We considered the best model to be that with the lowest corrected Akaike Information Criterion (AICc). FIGURES S.1 to S.8 show a comparison between raw data, and prediction from the best model.

I.2 Routine code and raw data.

I.2.1 Calculate growth rates.

```
function [AUC, Beta, YPred] = FitData(Data, B)
% Beta(Blank, coeff, r, r_diff, G, Data(24h));
  warning('off');
    i = length(Data);
    x = 24*(i:(n-1))/(n-1); % This transform time to h.
    y = Data;
```

```
7
8   %% Fit models!
9   try
10    % Constant model
11    mdl_C = fitlm(x,y); % y = blank + r*t (r DEPENDS ON UNITS OF Y-AXIS!)
12    param_C = abs(mdl_C.Coefficients.Estimate);
13    AIC_C = mdl_C.ModelCriterion.AICc;
14    Rsq_C = mdl_C.Rsquared.Adjusted;
15    YPred_C = mdl_C.Fitted;
16        % Compute duplication time as r/blank = 1/t
17        param_C(3) = str2num(sprintf('%.3f', param_C(2))) / str2num(sprintf('%.3f', param_C(1))); % r =
              divisions per timeunit (1/h)
18  catch
19    AIC_C = NaN;
20    Rsq_C = NaN;
21    disp('NaNs found in Linear Model.');
22  end
23
24  try
25    % Exponential model (nested constant model)
26    B_e = B(1:3)/1;
27    modelfun_E = @(b,X)(abs(b(1)) + abs(b(2)) * exp(X*abs(b(3))));
28    mdl_E = fitnlm(x,y,modelfun_E, B_e);
29    param_E = abs(mdl_E.Coefficients.Estimate);
30    AIC_E = mdl_E.ModelCriterion.AICc;
31    Rsq_E = mdl_E.Rsquared.Adjusted;
32    YPred_E = mdl_E.Fitted;
33  catch
34    AIC_E = NaN;
35    Rsq_E = NaN;
36    disp('NaNs found in Exponential Model.');
37  end
38
39  try
40    % Logistic model (nested constant model)
41    modelfun_L = @(b,X)(abs(b(1)) + abs(b(4)) ./ (1 + abs(b(2))*exp(-X*abs(b(3)))));
42    mdl_L = fitnlm(x,y,modelfun_L, B);
43    param_L = abs(mdl_L.Coefficients.Estimate);
44    AIC_L = mdl_L.ModelCriterion.AICc;
45    Rsq_L = mdl_L.Rsquared.Adjusted;
46    YPred_L = mdl_L.Fitted;
47  catch
48    AIC_L = NaN;
49    Rsq_L = NaN;
50    disp('NaNs found in Logistic Model.');
51  end
52
```

```
    % Which is more accurate?
    [AIC_Crit, ~] = min([AIC_C, AIC_E, AIC_L]);

    % Select the appropriate model:
    if AIC_Crit == AIC_C
      Param = param_C; % Param(Blank, r)
      YPred = YPred_C;
      FitName = 'Linear Fit';
    elseif AIC_Crit == AIC_E
      Param = param_E; % Param(Blank, Lambda, r)
      YPred = YPred_E;
      FitName = 'Exponential Fit';
    elseif AIC_Crit == AIC_L
      Param = param_L; % Param(Blank, C, r, K)
      YPred = YPred_L;
      FitName = 'Logistic Fit';
    end

    % Sort out parameters.
    Timestep = 1/3; % h;
    Param(1) = YPred(1);
    Param(5) = max(diff(YPred(15:end)) ./ Timestep); % Growth rate (/h): Euler Method
    AUC = YPred(end) ./ trapz(x, YPred); % Growth rate (1/h): AUC Method.
    Param(6) = YPred(end); % Yield after 24h.

  warning('on');
end
```

I.2.2 Calculate AcrB-sfGFP up-regulation rate.

```
function [AUC, Param, YPred] = PumpRegulation(Data, B)
% B(K, c, r, B0, r_diff, G, Data(24h));
   warning('off');

    n = length(Data);
    x = 24*(0:(n-1))/(n-1);
    y = Data;

    %% Fit models!
    try
      % Constant model
      mdl_C = fitlm(x,y); % y = blank + r*x
      param_C = abs(mdl_C.Coefficients.Estimate); % Growth rate: estimated from data.
      AIC_C = mdl_C.ModelCriterion.AIC;
      YPred_C = mdl_C.Fitted;
        % Compute duplication time as r/blank = 1/t
```

```
17          param_C(3) = str2num(sprintf('%.3f', param_C(2))) / str2num(sprintf('%.3f', param_C(1))); % r =
                divisions per timeunit (1/h)
18      catch
19        AIC_C = NaN;
20        disp('NaNs found in Linear Model.');
21      end
22
23      try
24        % DownUp model
25        modelfun_L = @(b,X)(abs(b(4)) + abs(b(5))*exp(-X*abs(b(6))) +  abs(b(1)) ./ [1 + abs(b(2))*exp(-X*abs(b
                (3)))]) ;
26        mdl_L = fitnlm(x,y,modelfun_L, B);
27        param_L = abs(mdl_L.Coefficients.Estimate);
28        AIC_L = mdl_L.ModelCriterion.AIC;
29        YPred_L = mdl_L.Fitted;
30      catch
31        AIC_L = NaN;
32        disp('NaNs found in Logistic Model.');
33      end
34
35      % Which is more accurate?
36      [AIC_Crit, AIC_idx] = min([AIC_C, AIC_L]);
37
38      % Select the appropriate model:
39      if AIC_Crit == AIC_C
40        Param = param_C; % Param(Blank, r)
41        YPred = YPred_C;
42        Param(3) = Param(2); % For convenience: r always 3rd item.
43        FitName = 'Linear Fit';
44      elseif AIC_Crit == AIC_L
45        Param = param_L; % Param(Blank, C, r, K)
46        YPred = YPred_L;
47        FitName = 'DownUp Fit';
48      end
49
50      % Sort out parameters.
51      Timestep = 1/3; % h;
52      Param(4) = YPred(1);
53      Param(7) = max(diff(YPred) ./ Timestep); % Growth rate (OD/h): Euler Method
54      AUC = YPred(end) ./ trapz(x, YPred); % Growth rate (1/h): AUC Method
55
56    warning('on');
57  end
```

I.2.3 Implementation of mathematical model.

```
1  % Main function
```

```
function [timeOut,stateOut] = NonMonotoneDR(parameters,IC)
    if nargin == 1
        IC = parameters.initialCondition;
    end

    timeOut = [];
    stateOut = [];

    for days = 1:parameters.days
        [times,states] = SolveMdl(parameters, IC);

        IC = states(end,:);

        IC(1) = parameters.SZero;
        IC(2) = parameters.AInitial;
        IC(3) = parameters.BInitial;

        dilution = parameters.dilution*parameters.dilRatios(days);

        IC(parameters.cells) = IC(parameters.cells)*dilution;
        IC(parameters.internalA) = IC(parameters.internalA)*dilution;
        IC(parameters.internalB) = IC(parameters.internalB)*dilution;

        timeOut = [timeOut ; parameters.Time*(days-1) + times];
        stateOut = [stateOut ; states];
    end

end


% Call ode15s solver
function [t,state] = SolveMdl(parameters,IC)
    %Solve Model
    if nargin == 1
        IC = parameters.initialCondition;
    end
    refine = 4;
    options = odeset('NonNegative',ones(size(IC)),'RelTol',1e-10,'Refine',refine);
    [t,state] = ode15s(@(t,y)Mdl(parameters, y),[0 parameters.Time],IC, options);
end


% Inhibition function (Gamma(A))
function gamma = gamma(parameters,A)
    gamma = 1./(1 + parameters.ka*A);
end
% Transported sugar uptake function
```

```
function uptakeRate = uptakeRate(parameters,S)
    uptakeRate = S.*parameters.Vmax./(S+parameters.K);
end
% Growth function
function Gvector = Growth(parameters,S,A)
    Gvector = parameters.conversion*uptakeRate(parameters,S).*gamma(parameters,A);
end
% Protein production function
function p = P(parameters,j)
    p = j./(1+parameters.g * j);
    %one gene means one protein, with diminishing returns:
    p = p/p(1);
    p = p - 1;
end
% Efflux function
function eff = Efflux(parameters,i,v,k)
    Q = P(parameters,i);
    eff = v*Q./(k+Q);
end


% Model
function newState = Mdl(parameters, state)

    Phi = parameters.Phi;
    Delta = parameters.Delta;
    delta = parameters.delta;
    decayA = parameters.decayA;

    Nd = parameters.Ndims;

    S = state(1);
    a = state(2);

    Aj = state(4:Nd+3);
    ej = state((2*Nd+4):(3*Nd+3));

    I = 1:Nd;
    EffluxPump = Efflux(parameters,I', parameters.Va, parameters.Ka) ;
    Gvector = G(parameters, S, Aj(2:end-1));

    dSdt = -uptakeRate(parameters,S)*sum(ej);
    dadt = -a*decayA + Phi*(sum(ej.*(Aj - a))) + sum(EffluxPump.*Aj.*ej);

    dAjdt = -Aj*decayA + Phi*ej.*(a - Aj) - EffluxPump.*Aj.*ej;

    de1dt = G(parameters, S, Aj(1))*ej(1) - Delta*ej(1) + Delta*(1+delta)*ej(2);
```

```
96      deNdt = G(parameters, S, Aj(end))*ej(end) - Delta*(1+delta)*ej(end) + Delta*ej(end-1);
97
98      dejdt = Gvector.*ej(2:end-1) - Delta*((2+delta)*ej(2:end-1) - ej(1:end-2) - (1+delta)*ej(3:end));
99
100     newState = [dSdt ; dadt ; dbdt ; dAjdt ; dBjdt ; de1dt ; dejdt ; deNdt];
101
102 end
```

I.2.4 Raw data.

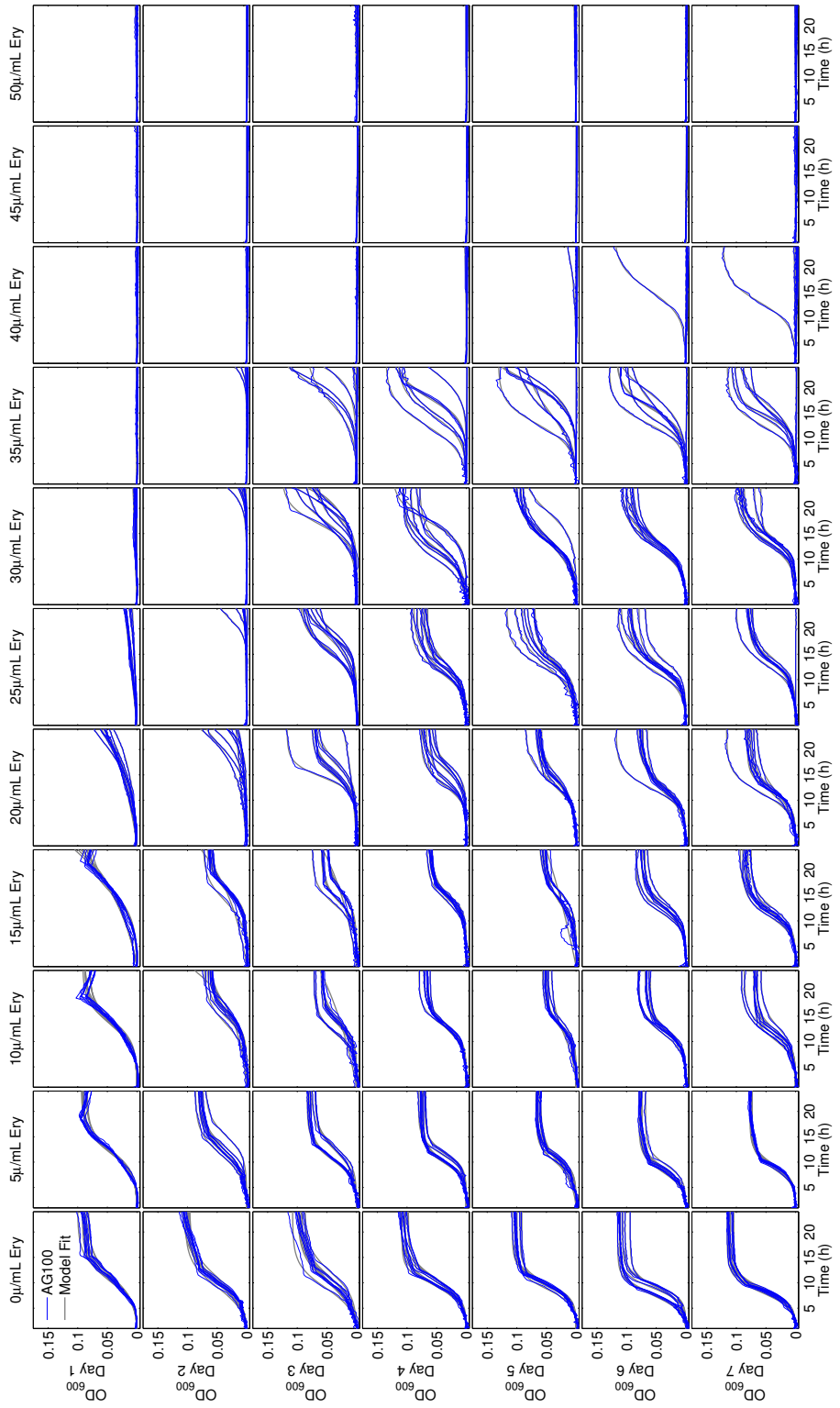

FIGURE S.1. Growth profiles for *E. coli* AG100 based on OD_{600} measured every 20min (1/3h), for 24h, during 7 days. Each subplot contains the growth profile of eight replicates as a function of time, and as a function of the dose of erythromycin (columns). The different rows show the fit, and the data for different days ranging from days 1 to 7. We used the degree of overlap of the data (grey) and the model (blue) to validate the appropriateness of the models that we used to calculate the growth rate in each case.

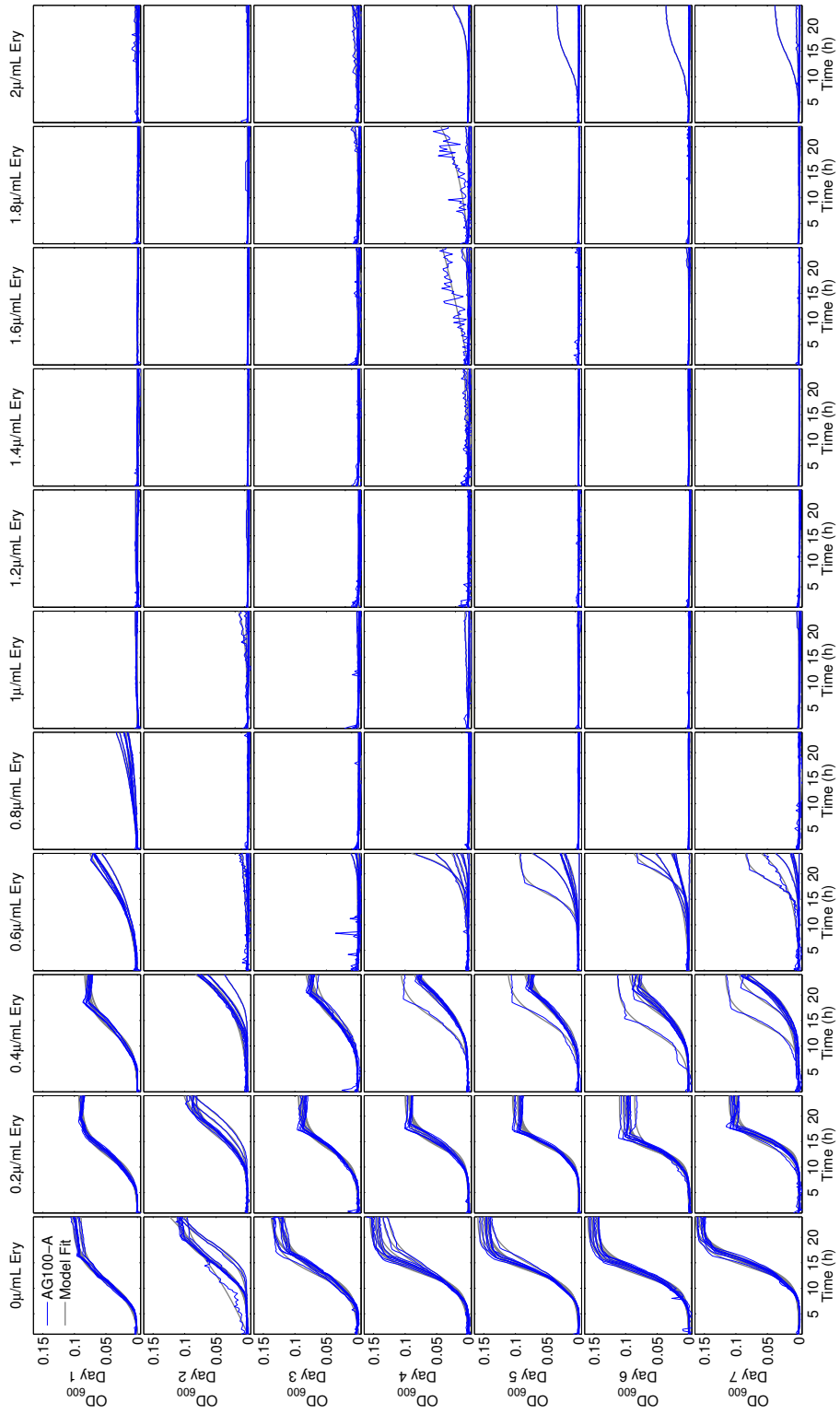

FIGURE S.2. Growth profiles for *E. coli* AG100-A based on OD_{600} measured every 20min (1/3h), for 24h, during 7 days. Each subplot contains the growth profile of eight replicates as a function of time, and as a function of the dose of erythromycin (columns). The different rows show the fit, and the data for different days ranging from days 1 to 7. We used the degree of overlap of the data (grey) and the model (blue) to validate the appropriateness of the models that we used to calculate the growth rate in each case.

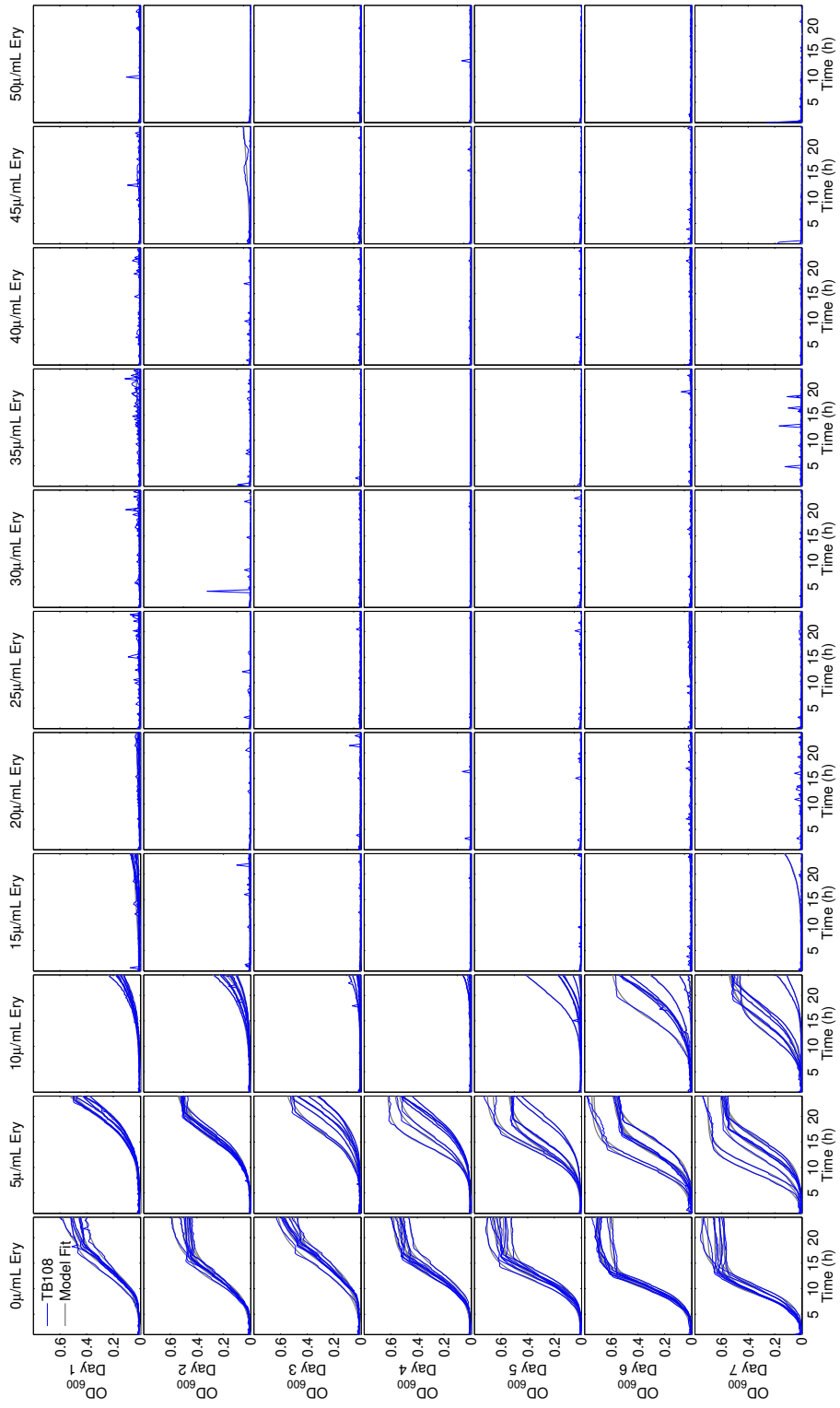

FIGURE S.3. Growth profiles for *E. coli* TB108 based on OD_{600} measured every 20min (1/3h), for 24h, during 7 days. Each subplot contains the growth profile of eight replicates as a function of time, and as a function of the dose of erythromycin (columns). The different rows show the fit, and the data for different days ranging from days 1 to 7. We used the degree of overlap of the data (grey) and the model (blue) to validate the appropriateness of the models that we used to calculate the growth rate in each case.

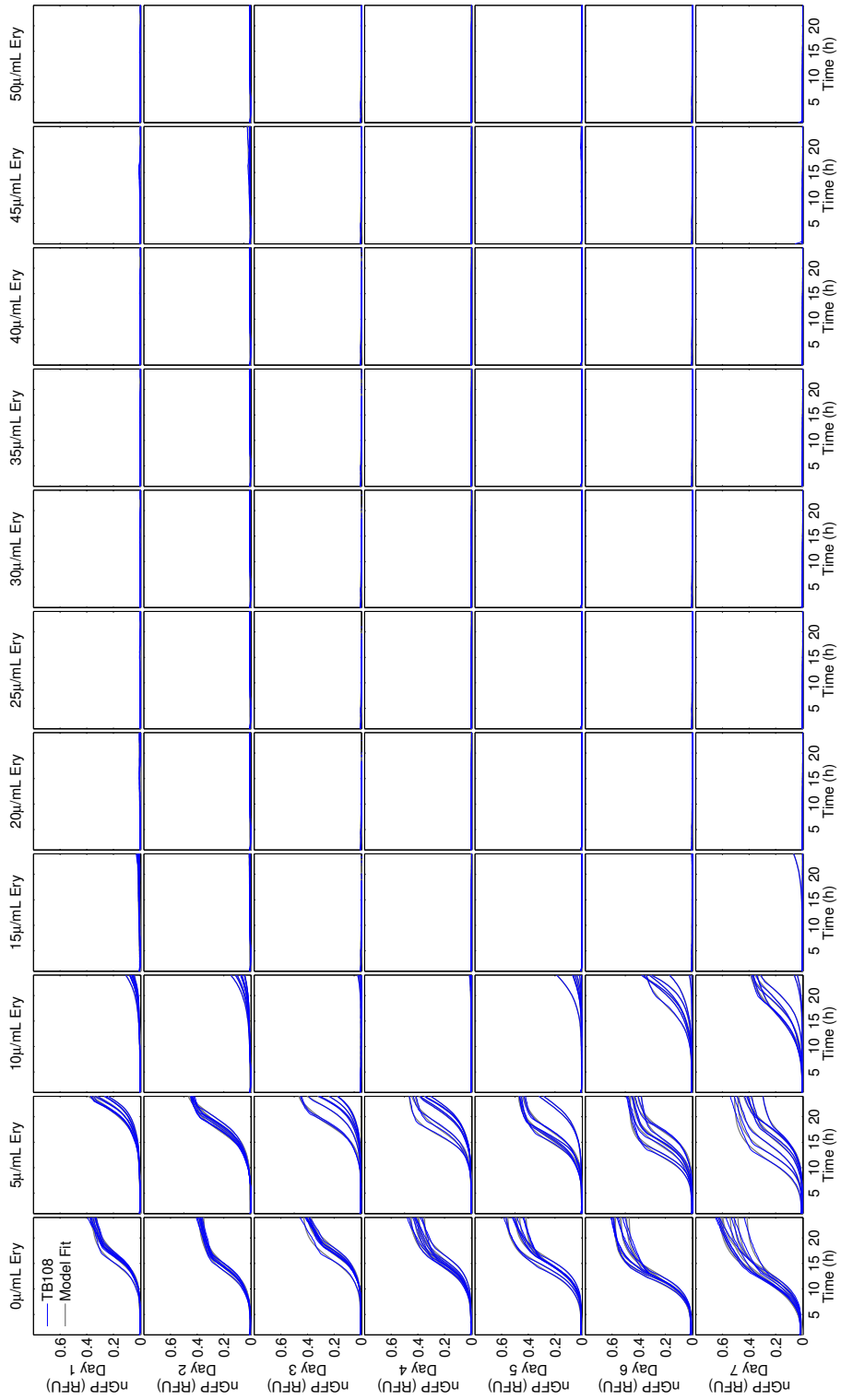

FIGURE S.4. Growth profiles for *E. coli* TB108 based on normalised fluorescence (nGFP) measured every 20min (1/3h), for 24h, during 7 days. Each subplot contains the growth profile of eight replicates as a function of time, and as a function of the dose of erythromycin (columns). The different rows show the fit, and the data for different days ranging from days 1 to 7. We used the degree of overlap of the data (grey) and the model (blue) to validate the appropriateness of the models that we used to calculate the growth rate in each case.

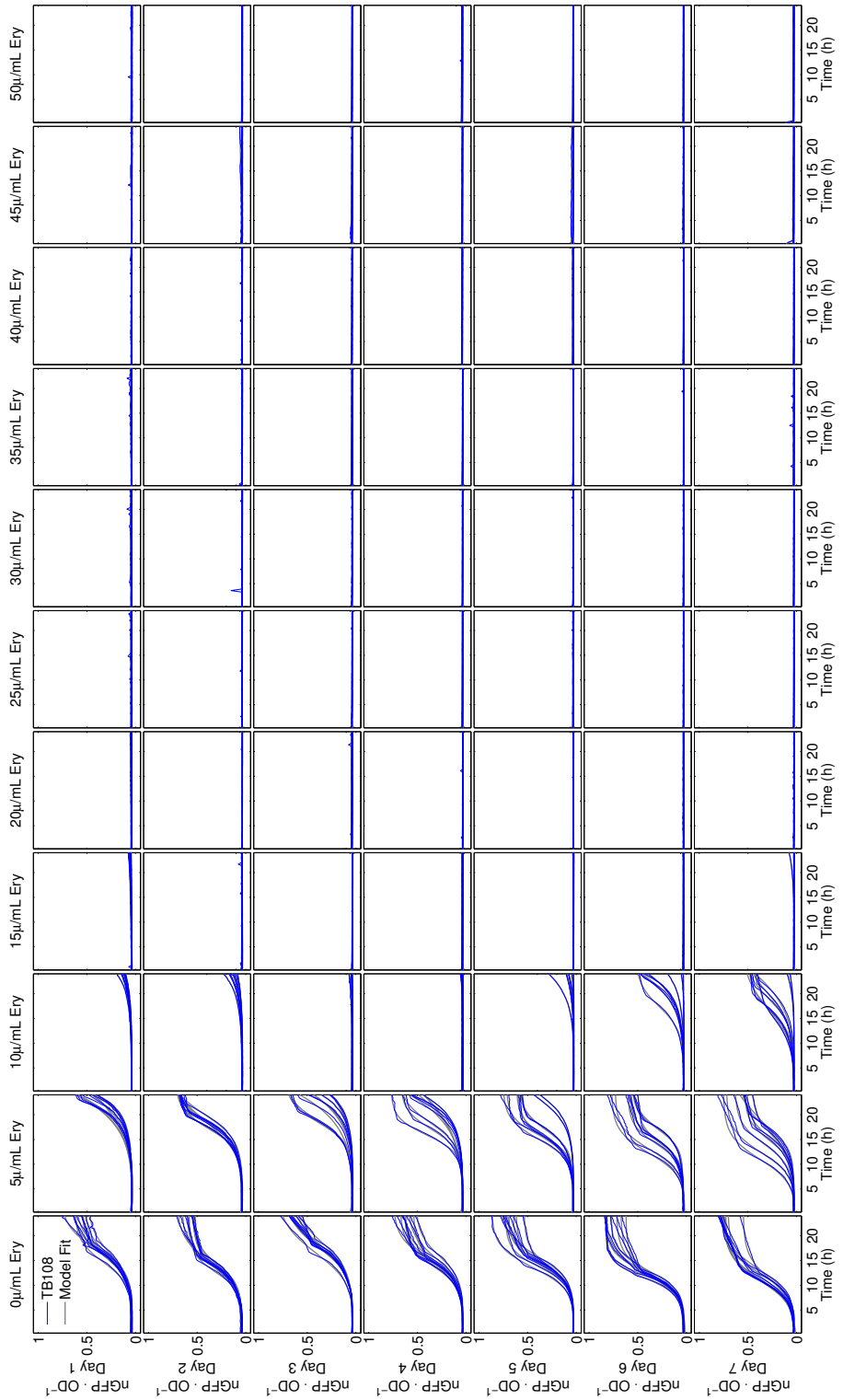

FIGURE S.5. Growth profiles for *E. coli* TB108 based on relative fluorescence per OD_{600} unit (nGFP · OD^{-1}) measured every 20min (1/3h), for 24h, during 7 days. Each subplot contains the growth profile of eight replicates as a function of time, and as a function of the dose of erythromycin (columns). The different rows show the fit, and the data for different days ranging from days 1 to 7. We used the degree of overlap of the data (grey) and the model (blue) to validate the appropriateness of the models that we used to calculate the growth rate in each case.

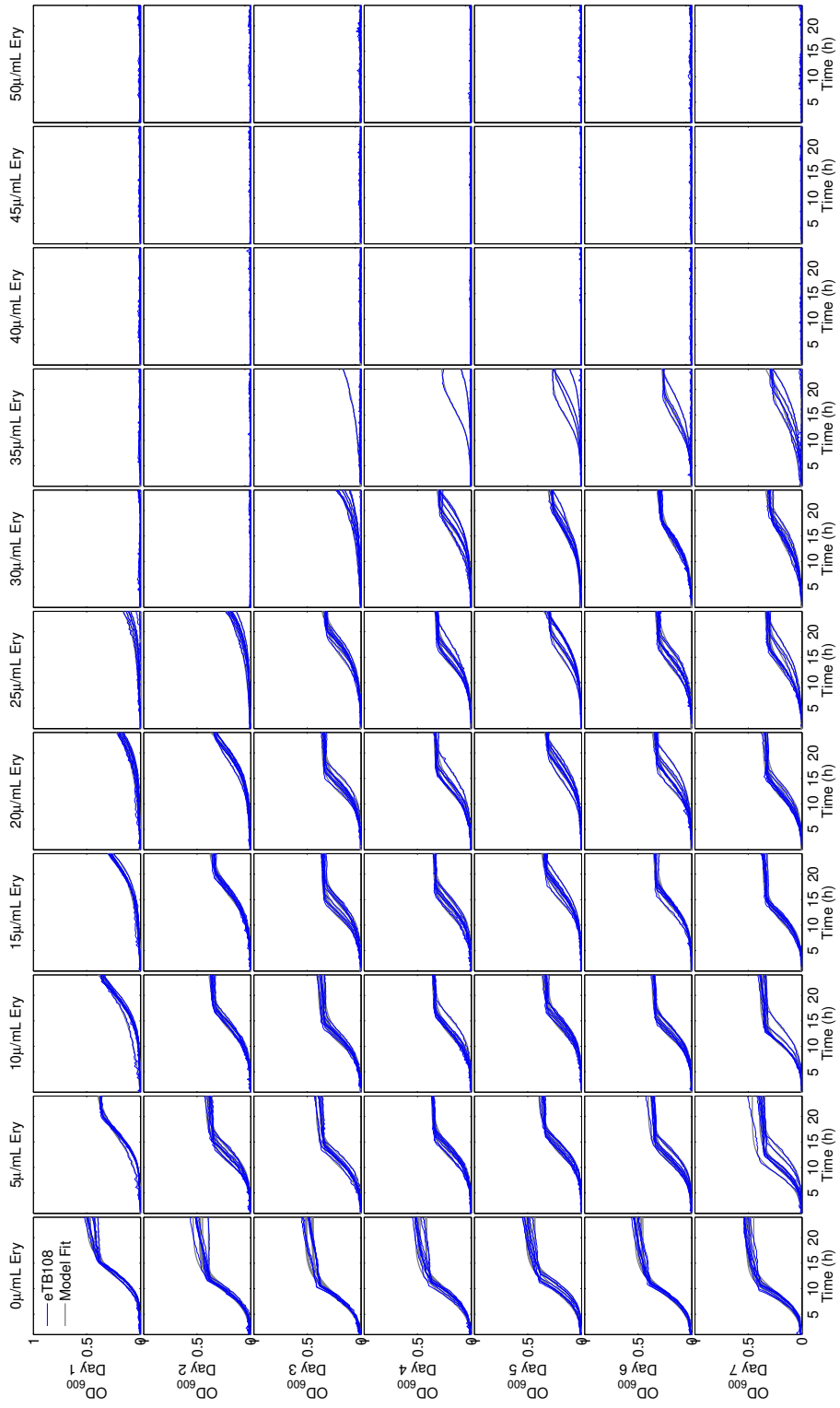

FIGURE S.6. Growth profiles for *E. coli* eTB108 based on OD_{600} measured every 20min (1/3h), for 24h, during 7 days. Each subplot contains the growth profile of eight replicates as a function of time, and as a function of the dose of erythromycin (columns). The different rows show the fit, and the data for different days ranging from days 1 to 7. We used the degree of overlap of the data (grey) and the model (blue) to validate the appropriateness of the models that we used to calculate the growth rate in each case.

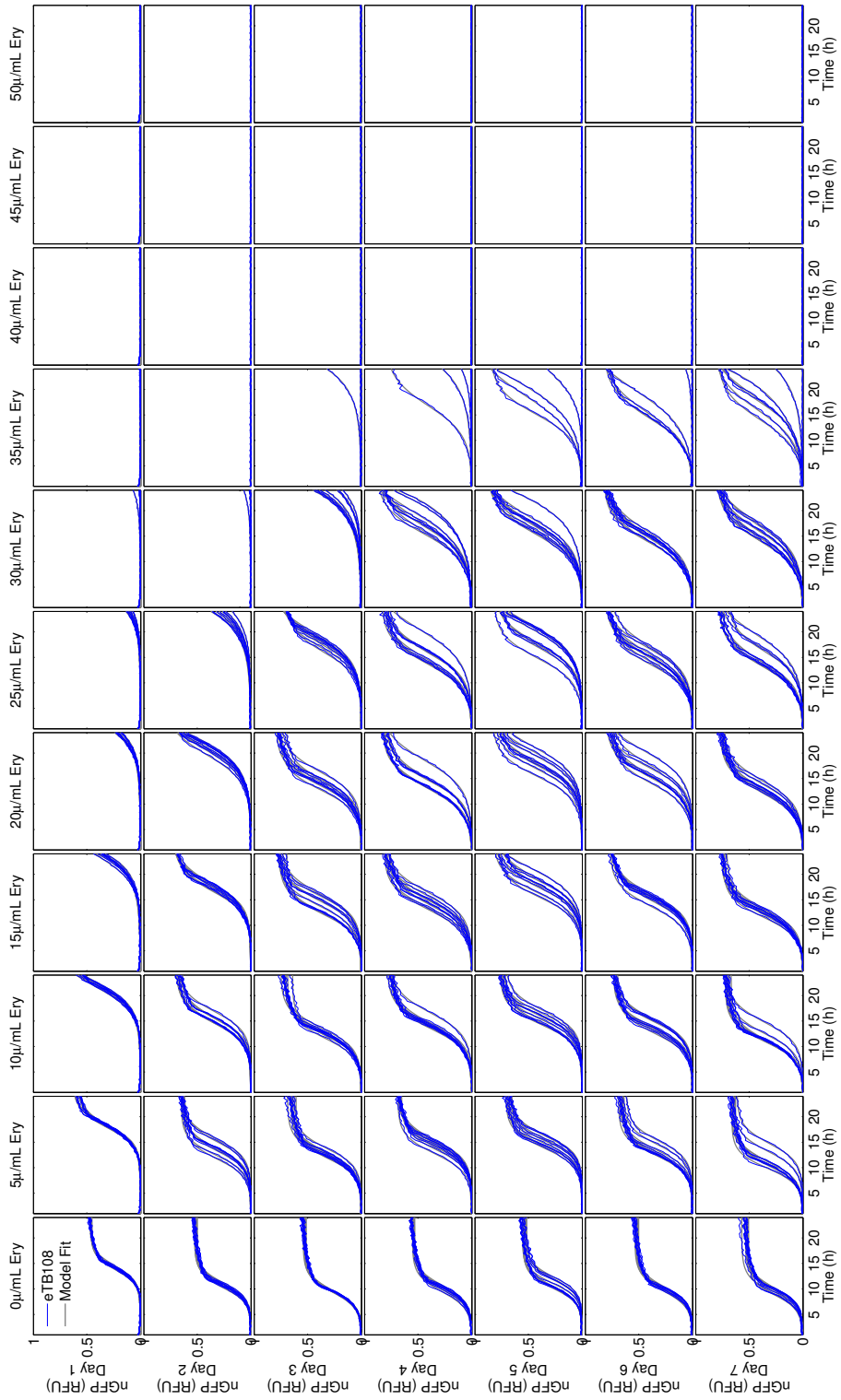

FIGURE S.7. Growth profiles for *E. coli* eTB108 based on normalised fluorescence (nGFP) measured every 20min (1/3h), for 24h, during 7 days. Each subplot contains the growth profile of eight replicates as a function of time, and as a function of the dose of erythromycin (columns). The different rows show the fit, and the data for different days ranging from days 1 to 7. We used the degree of overlap of the data (grey) and the model (blue) to validate the appropriateness of the models that we used to calculate the growth rate in each case.

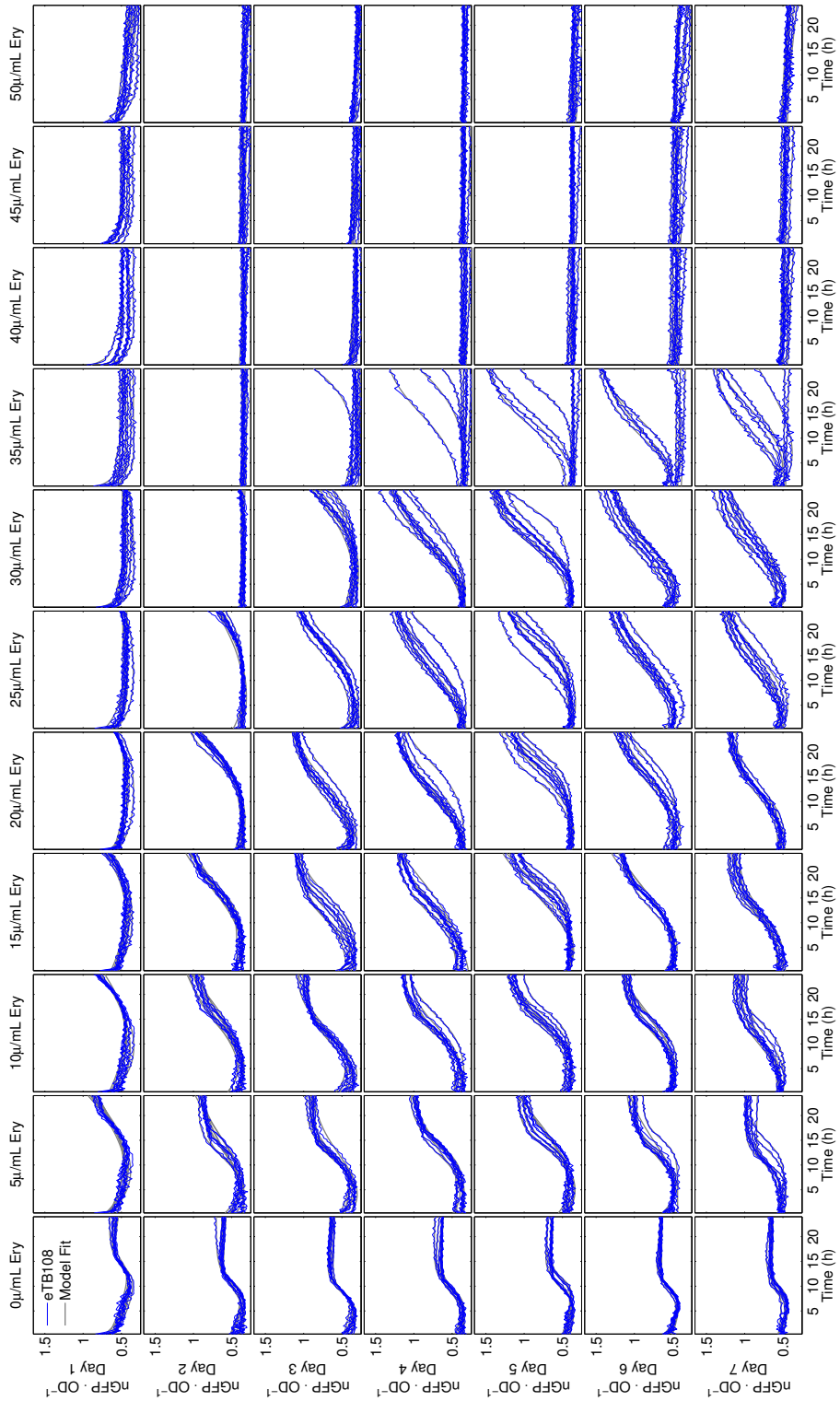

FIGURE S.8. Growth profiles for *E. coli* eTB108 based on relative fluorescence per OD_{600} unit (nGFP · OD^{-1}) measured every 20min (1/3h), for 24h, during 7 days. Each subplot contains the growth profile of eight replicates as a function of time, and as a function of the dose of erythromycin (columns). The different rows show the fit, and the data for different days ranging from days 1 to 7. We used the degree of overlap of the data (grey) and the model (blue) to validate the appropriateness of the models that we used to calculate the growth rate in each case.

I.3 Rate of adaptation (α): robustness. The following plots show the rate of adaptation (α, see SECTION 2.3), per replicate, measured using *per capita* growth rate (here labelled as 'fit'), finite difference approximation (labelled as 'r_e'), and area under the curve (labelled AUC).

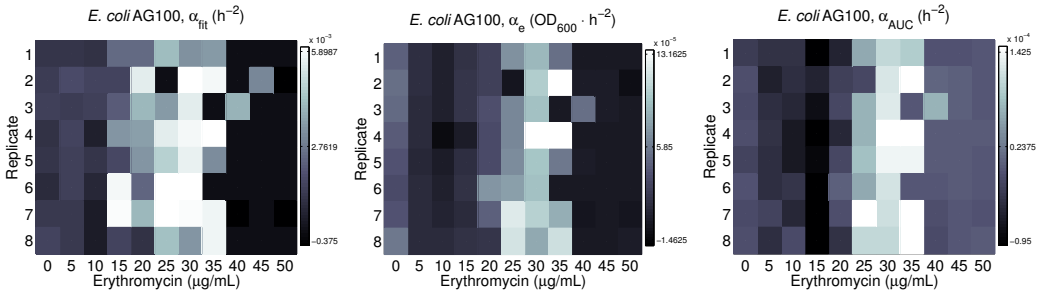

FIGURE S.9. Adaptive landscapes for *E. coli* AG100 according to the best model fit (left), finite difference approximation (centre), and area under the curve (right). The analysis reflects the robustness of the existence, and location of the evolutionary 'coldspots' and 'hotspots' as a function of the dose of erythromycin. The colorbar indicates the rate of adaptation, black being the lowest rate of adaptation and white being the highest.

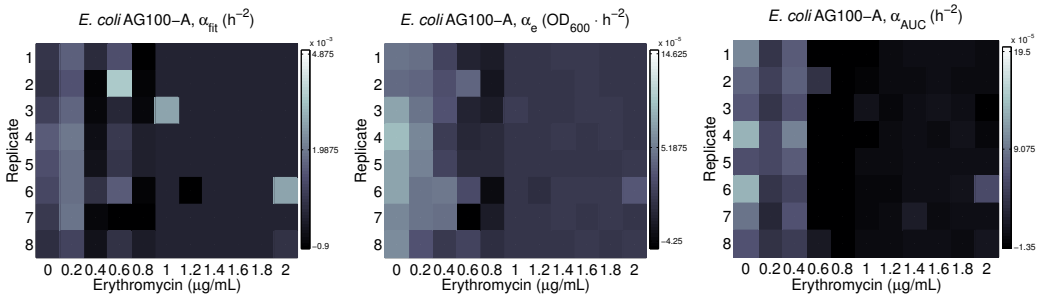

FIGURE S.10. Adaptive landscapes for *E. coli* AG100-A according to the best model fit (left), finite difference approximation (centre), and area under the curve (right). The analysis reflects the robustness of the existence, and location of the evolutionary 'coldspots' and 'hotspots' as a function of the dose of erythromycin. The colorbar indicates the rate of adaptation, black being the lowest rate of adaptation and white being the highest.

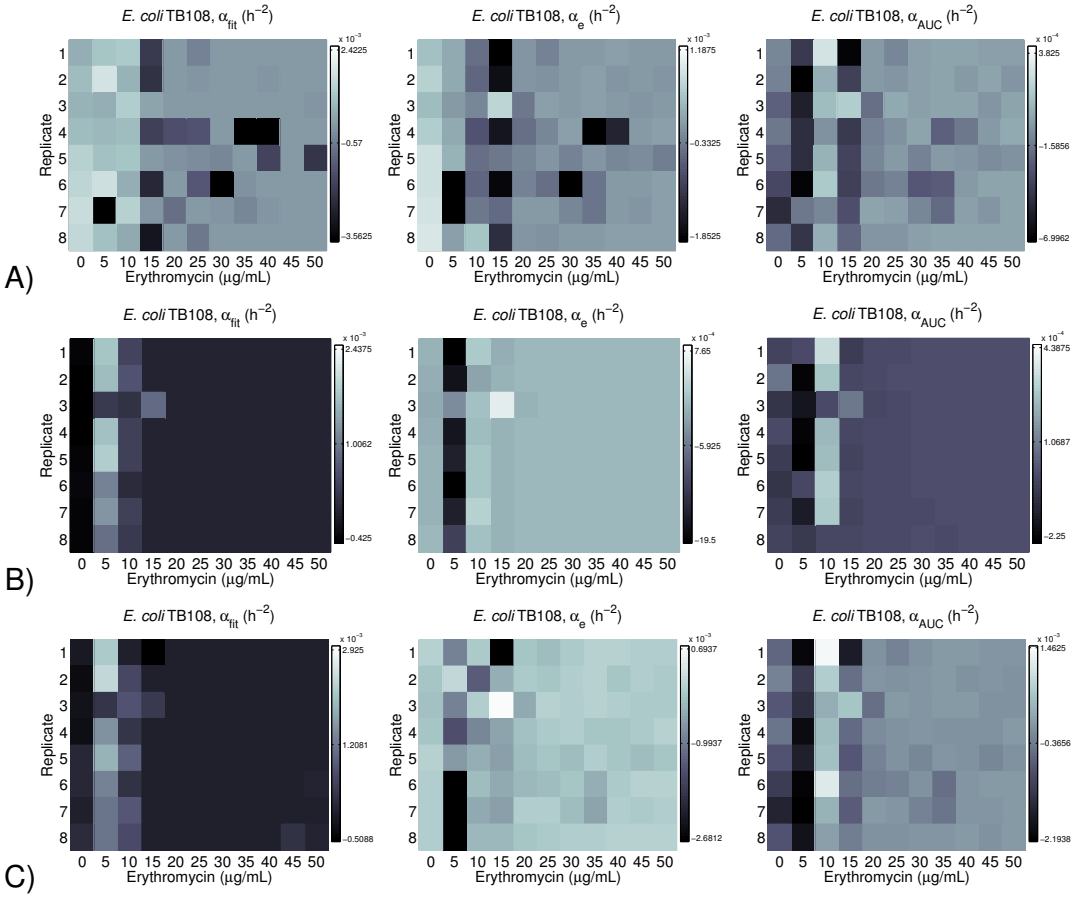

FIGURE S.11. Adaptive landscapes for *E. coli* TB108 according to the best model fit (left), finite difference approximation (centre), and area under the curve (right) based on readings for OD_{600} (**A**), normalised fluorescence (**B**), and relative fluorescence per OD_{600} unit (**C**). The analysis reflects the robustness of the existence, and location of the evolutionary 'coldspots' and 'hotspots' as a function of the dose of erythromycin. The colorbar indicates the rate of adaptation, black being the lowest rate of adaptation and white being the highest.

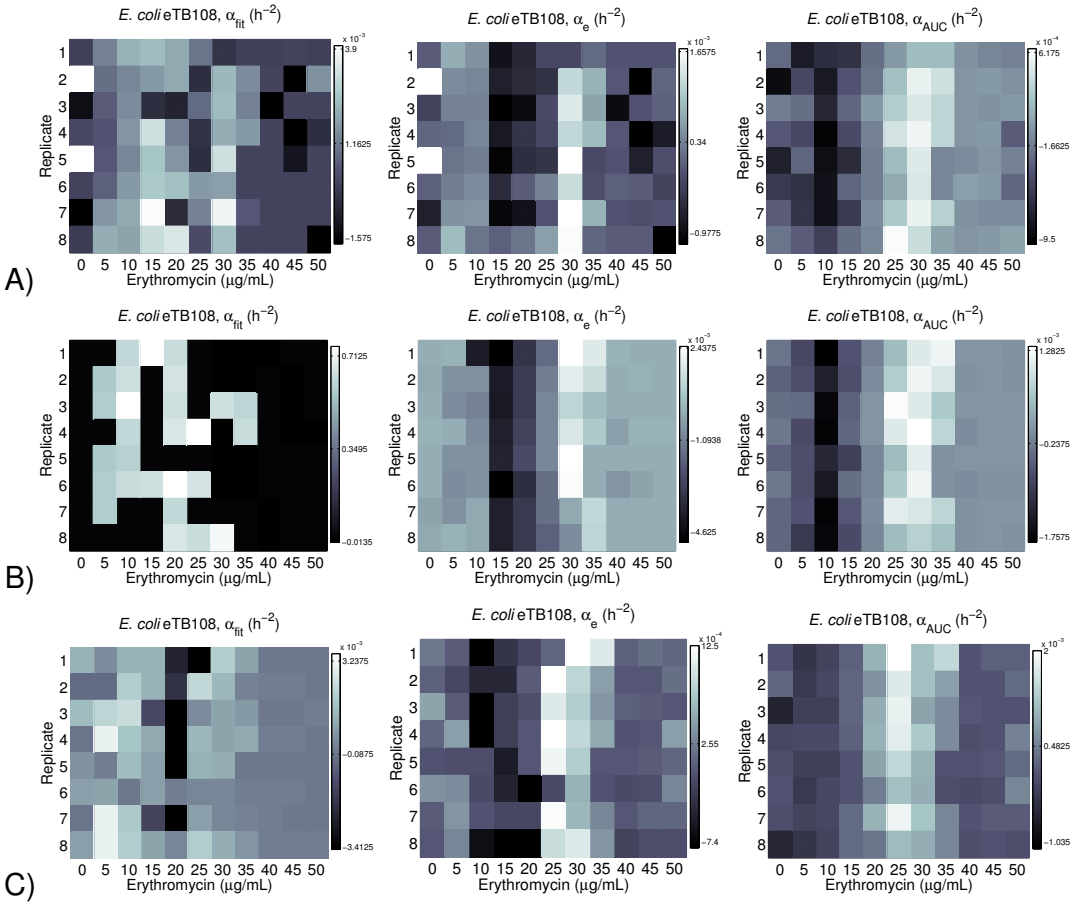

FIGURE S.12. Adaptive landscapes for *E. coli* eTB108 according to the best model fit (left), finite difference approximation (centre), and area under the curve (right) based on readings for OD_{600} (**A**), normalised fluorescence (nGFP, **B**), and relative fluorescence per OD_{600} unit (**C**). The analysis reflects the robustness of the existence, and location of the evolutionary 'coldspots' and 'hotspots' as a function of the dose of erythromycin. The colorbar indicates the rate of adaptation, black being the lowest rate of adaptation and white being the highest.

I.4 Oscillations in fluorescence readings: Discrete Fourier Transform. We a Fourier analysis on the data shown in FIGURES 2.15 and S.8 to answer whether, or not, the oscillations observed have a biological origin. We computed the discrete Fourier transform of our dataset using the `fft` function as implemented in Matlab 2014a.

Represented in FIG. S.13 we show the existence of two main oscillations taking place, at different frequencies, during our experiment. The first has the highest intensity and occurs at a frequency of ∼10h (∼0.1 peaks per hour). This corresponds with the up-regulation of the AcrAB-TolC efflux pump. The second has a lower intensity, and occurs at a frequency of ∼3/4 of an hour.

We compared the spectra so-represented with that of the inocula-free culture condition (negative control, FIG. S.14). Here we do not observe the first, intense oscillation but we do observe the second. Given the absence of cells in this condition, we must conclude that these small oscillations are mechanically produced by our microplate reader and not by the subtle regulation of the AcrAB-TolC efflux pump.

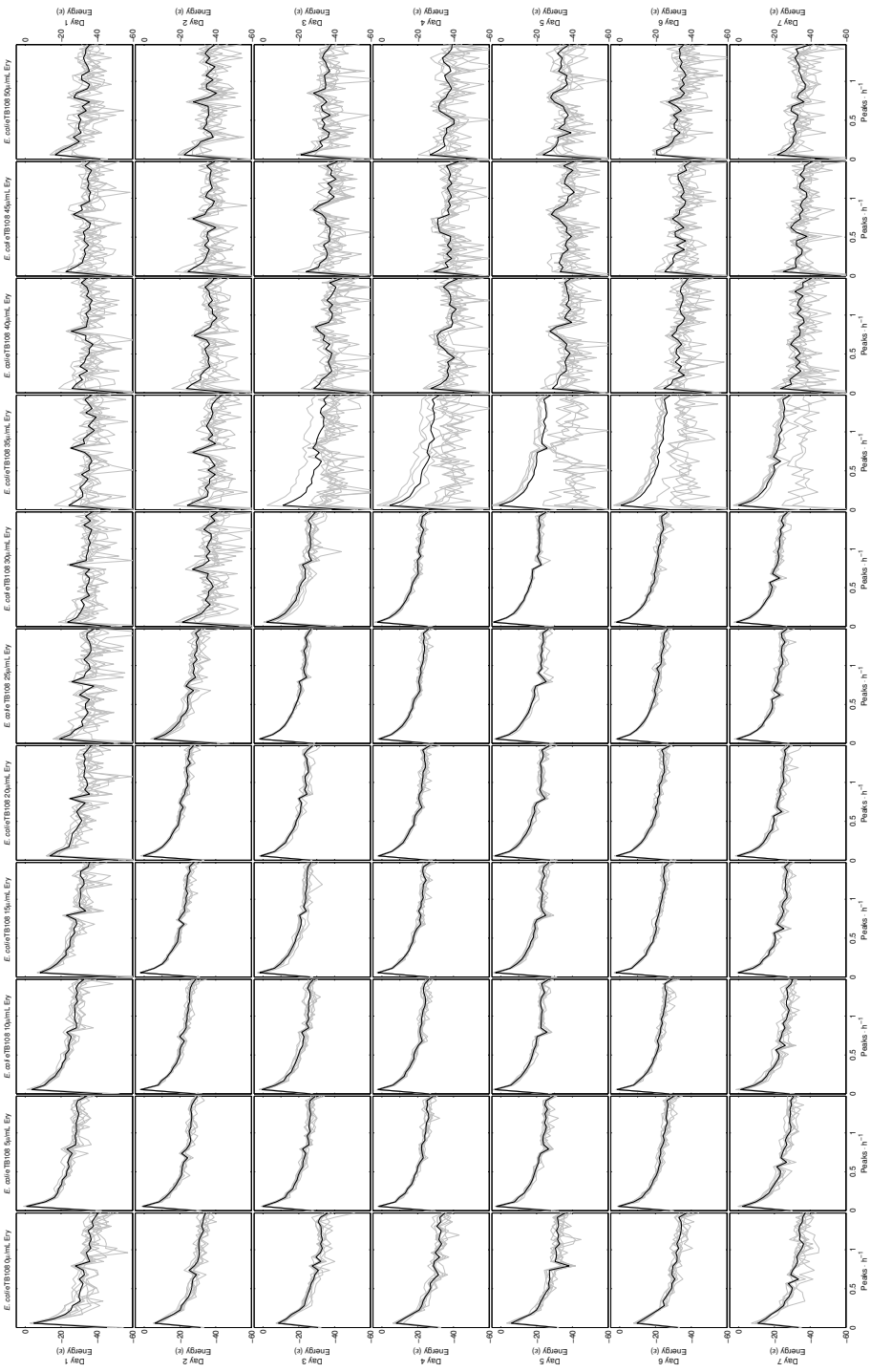

FIGURE S.13. Fast Fourier transform (FFT) spectra for *E. coli* eTB108. The frequency of the oscillations is shown on the *x*-axis and the energy of such oscillations on the *y*-axis. Each column represents the FFT for the data measured in different days, in different concentrations of erythromycin (here shown in rows). A feature is shared overall: a peak every ~3/4 of an hour. This feature corresponds to the small oscillations observed in FIGURES 2.15 and S.8. Mean signal in black, per replicate signal in light grey.

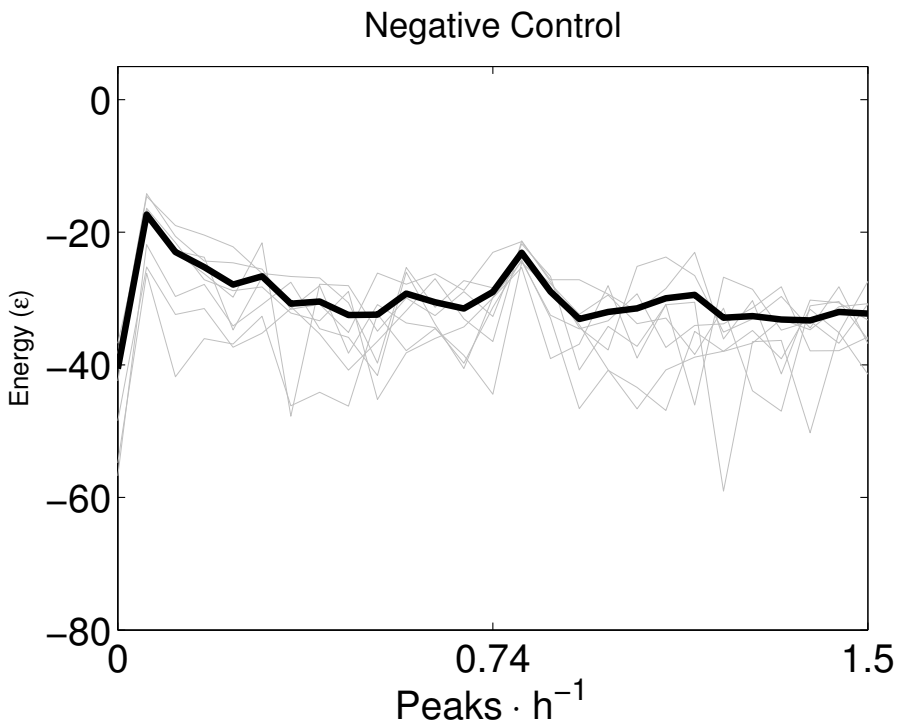

FIGURE S.14. Fast Fourier transform (FFT) spectrum for the inocula-free, negative control. The frequency of the oscillations is shown on the *x*-axis and the energy of such oscillations on the *y*-axis. The presence of the same signature, a peak every 3/4 of an hour, suggests a mechanical cause for these oscillations. Mean signal in black, per replicate signal in light grey.

II SUPPLEMENTARY CHAPTER 3

II.1 Implementation of mathematical model.

```
% Defining Markov process
function p = setMarkov(N,p)

    if nargin < 1
        N = 11;
    end

    p.sigma = 0.01;%rate of plasmid loss/gain through segregation
    p.N = N;%max number of plasmids

    if N == 1
        p.M = 1;
        p.Markov = 1;
    else
        p.M = (diag(-2*ones(N,1)) + diag(ones(N-1,1),1) + diag(ones(N-1,1),-1))/2;
        p.M(1,1) = 0;
        p.M(2,1) = 0;
        p.M(end,end) = -1;
        p.M(end-1,end) = 1;

        p.Markov = eye(N) + p.sigma*p.M;
    end

end

% Model for plasmid distribution
function f = PlasmidDistribution(u,p)

    e = p.e;
    V = p.V;
    K = p.K;
    gamma = p.gamma;
    phi = p.phi;
    kappa = p.kappa;
    d = p.d;
    Markov = p.Markov;

    N = p.N;
    sigma = p.sigma;

    c = u(1:N);
    Aint = u(N+1);
    Aext = u(N+2);
```

```
    S = u(N+3);

    U = V*S/(K+S);
    G = e*U;

    % Maximal cost of resistance gamma value (relative to 1)
    % cost of carrying _maximal number_ of available plasmids
    if N > 1
        s = (0:(N-1))/(N-1);
    else
        s = 1;
    end

    s = s';
    GRy = G/(1+kappa*Aint^(2));
    GRc = s.*gamma*G + (1-s).*GRy;

    dc = Markov*(c.*GRc);

    dAint = -d*Aint + phi*sum(c)*(Aext-Aint);
    dAext = -d*Aext - phi*sum(c)*(Aext-Aint);
    dS = -U*sum(c);

    f = [dc;dAint;dAext;dS];

end

% Model (plasmids not included)
function f = RHS(u,p)

    e = p.e;
    V = p.V;
    K = p.K;
    gamma = p.gamma;
    phi = p.phi;
    kappa = p.kappa;
    d = p.d;

    c = u(1);
    y = u(2);
    Aint = u(3);
    Aext = u(4);
    S = u(5);

    U = V*S/(K+S);
    G = e*U;

```

```
    dc = gamma*c*G;
    dy = y*G/(1+kappa*Aint^(2));
    dAint = -d*Aint + phi*(c+y)*(Aext-Aint);
    dAext = -d*Aext - phi*(c+y)*(Aext-Aint);
    dS = -U*(c+y);

    f = [dc;dy;dAint;dAext;dS];

end
```

II.2 Raw data.

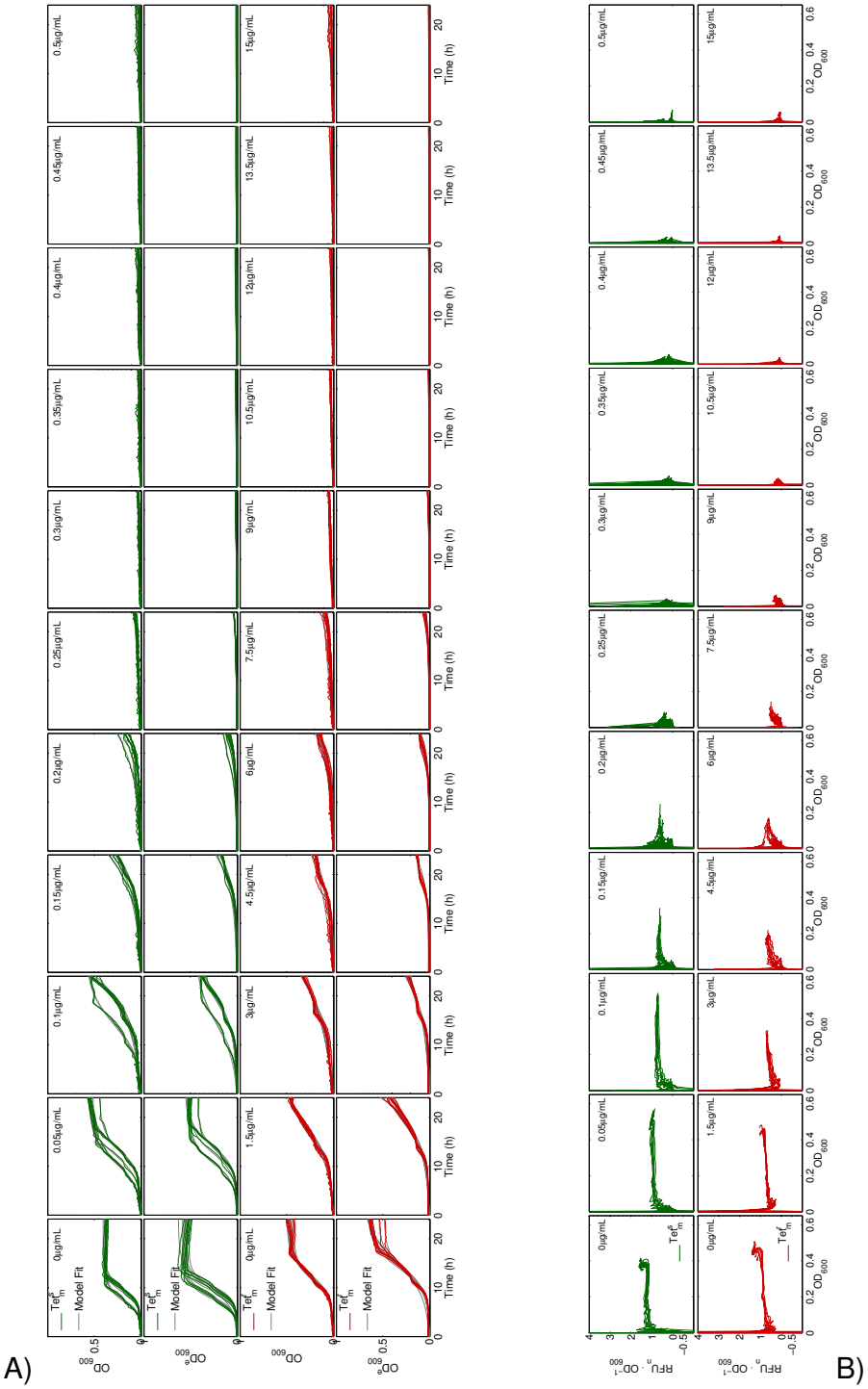

FIGURE S.15. A) Model fit for the tetracycline sensitive (Tet^s_m, green), and the tetracycline resistant (Tet^r_m, red) strains grown in monoculture. Model fitted to optical density at 600nm (OD_{600}) and optical density estimated from fluorescence (OD^e_{600}). **B**) Ratio of normalised fluorescence units (RFU_n) per optical density unit. This ratio is robust to changes in optical density.

III SUPPLEMENTARY CHAPTER 4

III.1 Image processing routine.

```
function [mData, ci95Data] = Radial_Profile_Plot (ImageBW, ImageRef)
  % This function finds the origin of the inner circle, and integrates
  % a n radians wide arc, with origin (X0, Y0), to generate a
  % profile plot from the origin and a radius iR.

  % Required variables.
  [Height, Width] = size(ImageBW);
  % Find inhibition origin.
  [Origin, Radius, ~ ] = imfindcircles(ImageRef, [100 200],...
                                       'Sensitivity', 0.985);
  % Make sure I process one circle ONLY.
  Origin = Origin(1, :);
  Radius = Radius(1);
  % Defining X0 and Y0 based on the existence of 'Origin'
  X0 = floor(Origin(1));
  Y0 = floor(Origin(2));
  Step = 1;
  iR = floor(Radius * 1.15); % Inner Radius (>1 to avoid circle boundary)
  oR = floor(Radius * 2.25); % Outter Radius

  mData = zeros(oR, 1); % Preallocation
  seData = zeros(oR, 1); % Preallocation

  % For Normalisation
    Arc = round(2*pi*oR); % 2pir = circumference.
    Theta = linspace(5/3*pi, 11/6*pi, Arc); % Pi = 180 degrees
    Rho = ones(1, Arc) * round(oR);
    [ X Y ] = pol2cart(Theta, Rho);
    X = round(X) + X0;
    Y = round(Y) + Y0;
      oX = X;
      oY = Y;

  % Acr integration and creation of profile
  for r = oR:-Step:iR
    Arc = round(2*pi*r); % 2pir = circumference.
    Theta = linspace(5/3*pi, 11/6*pi, Arc); % Pi = 180 degrees
    Rho = ones(1, Arc) * round(r);
    [ X Y ] = pol2cart(Theta, Rho);
    X = round(X) + X0;
    Y = round(Y) + Y0;
    OD = im2double(improfile(Image_OD_Blurred, X, Y));
    GFP = im2double(improfile(Image_GFP_Blurred, X, Y));
```

```
    Data = GFP ./ OD;

    mData(r) = mean(Data);
    seData(r) = std(Data) ./ sqrt(Arc - 1) .* 1.96;
  end

  % Computing cell density:
  mData(r) = mean(Data);
  seData(r) = std(Data) ./ sqrt(Arc - 1) .* 1.96;

  iN = round(2*pi*iR);
  oN = round(2*pi*oR);

  mData = mData(iR:end);
  ci95Data = seData(iR:end);

end
```

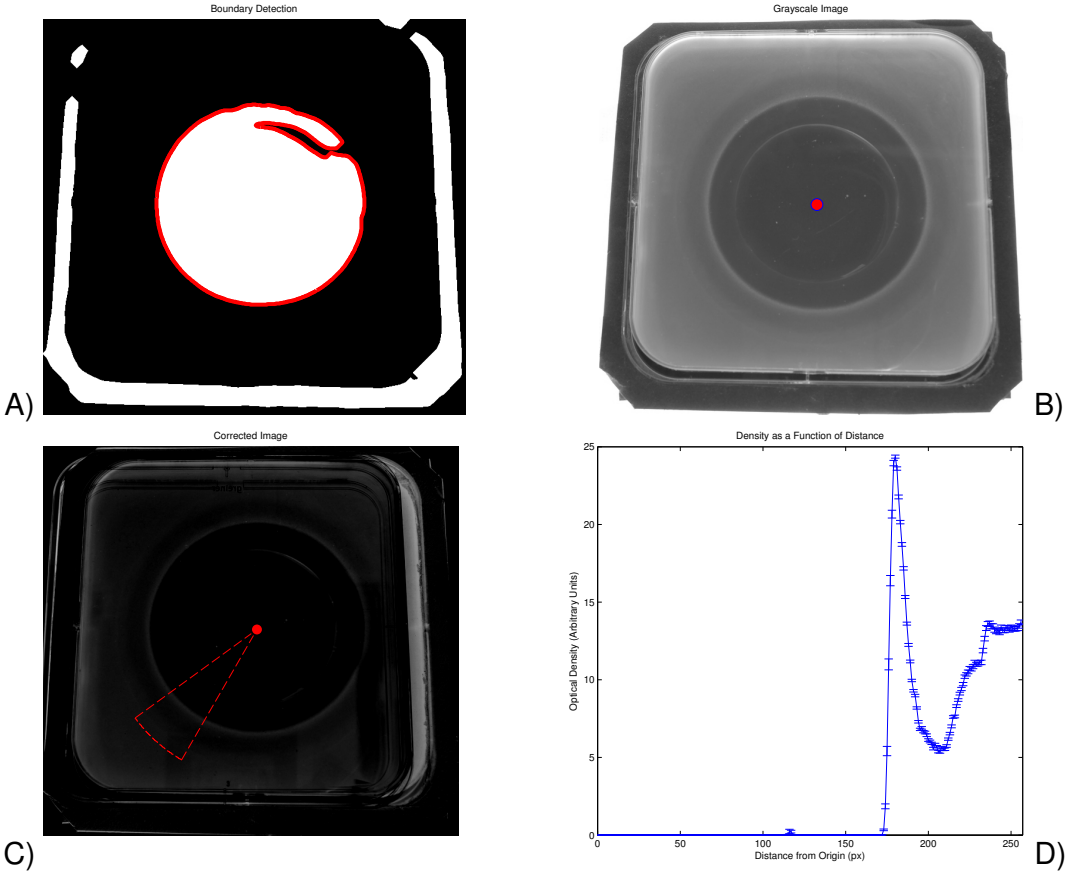

FIGURE S.16. Pilot experiment for the development of the image analysis pipeline. **A**) Binary mask created to detect circular shapes from **B**) grey scaled photographs. **C**) The image is corrected by subtracting the photo taken at t = 0h and read. **D**) Profile plot, showing mean growth ± standard error on the $y-$axis as a function of the distance to the centre of the inhibition zone, on the $x-$axis.

IV SUPPLEMENTARY CHAPTER 5

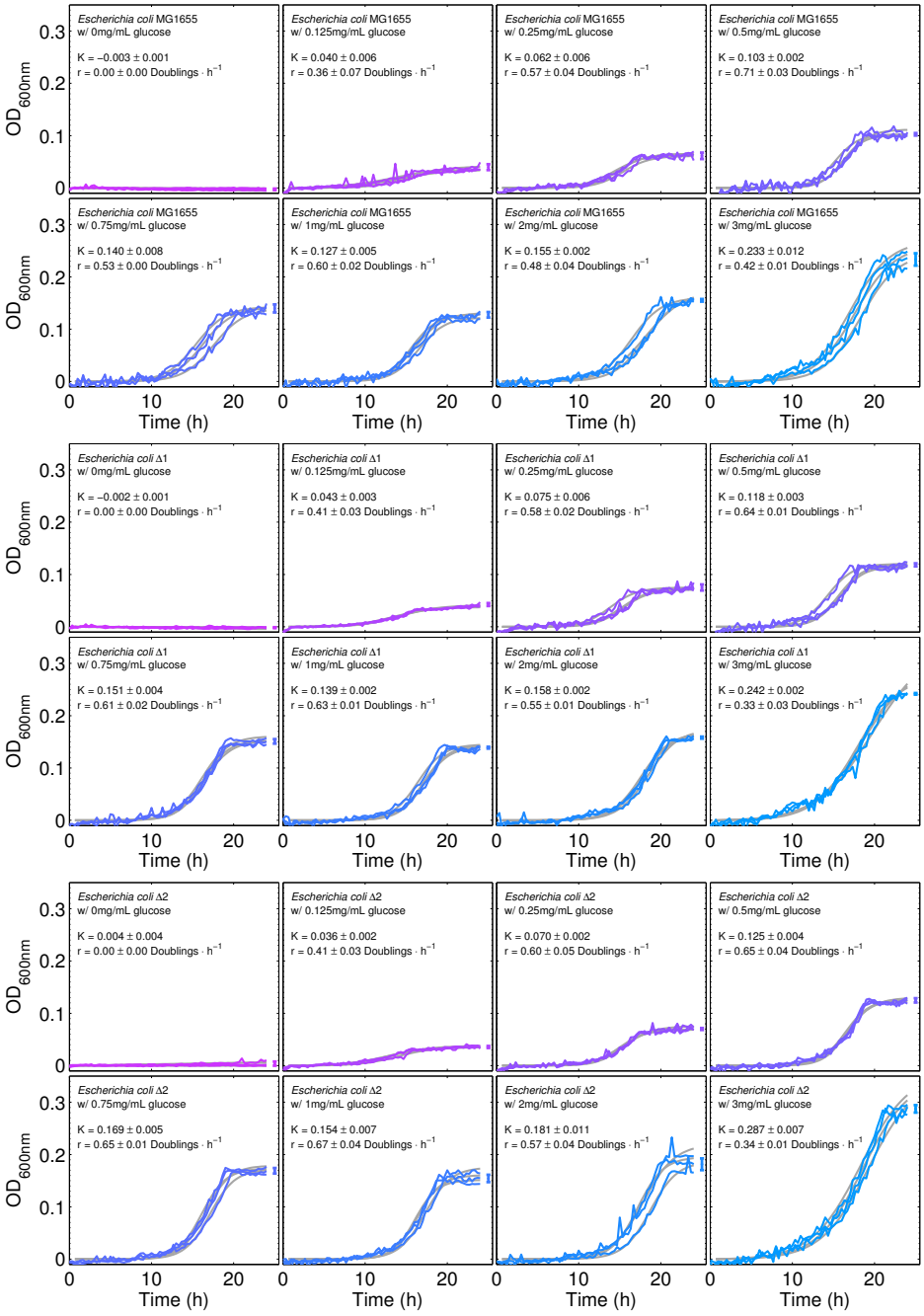

FIGURE S.17. Raw Data. MG1655, Δ1, Δ2.

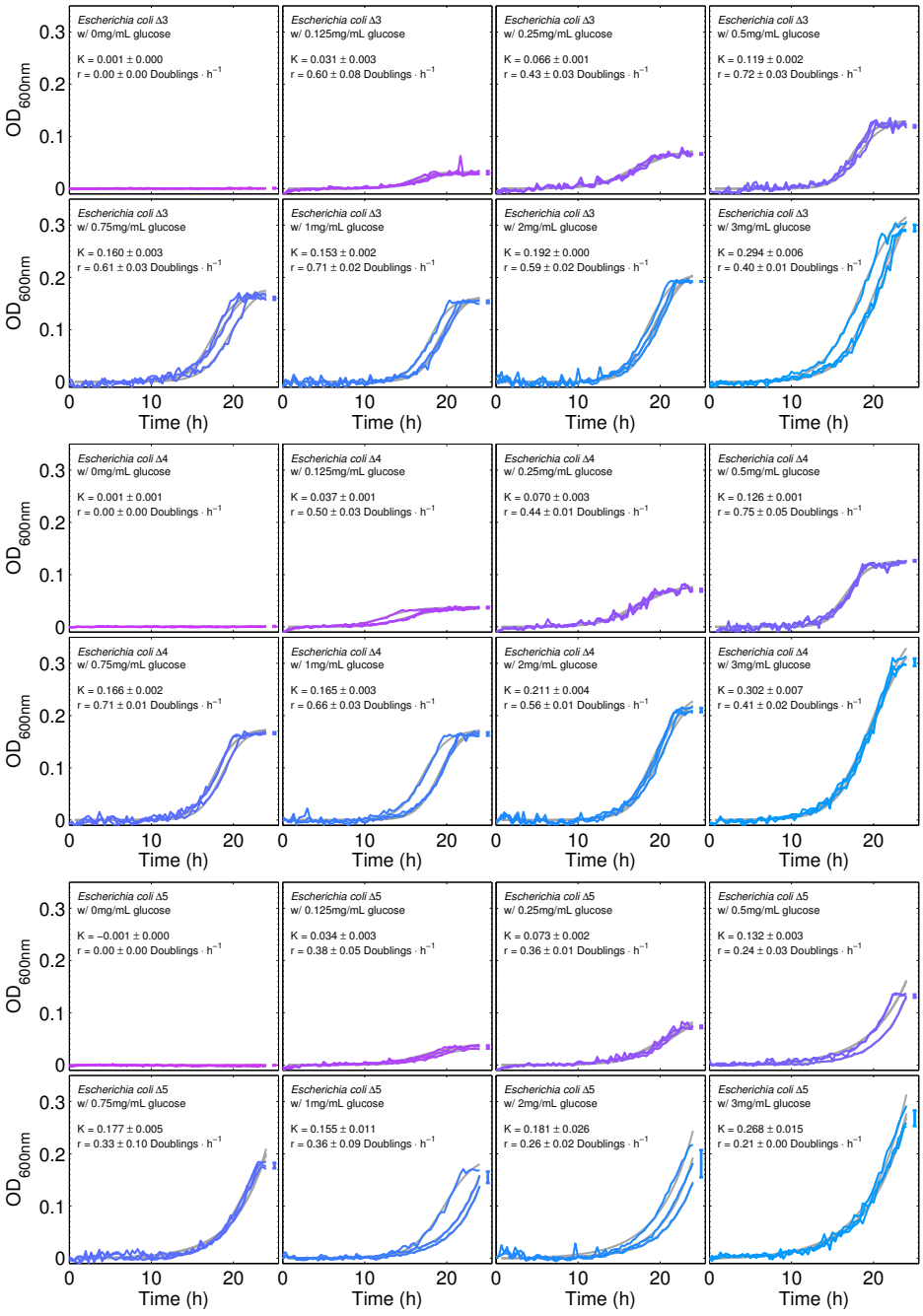

FIGURE S.18. Raw Data. Δ3, Δ4, Δ5.

METHODS

V MEDIA

V.1 Rich media. We used Lysoneny Broth (LB), LB Agar, and LB Soft Agar as rich media following the recipes described in the table below. In every case, we prepared the media using deionised water for a total volume of 1 litre, pH adjusted using NaOH, and autoclaved at 121^{o}C for 20 min prior to use.

TABLE S.1. Recipe for rich media

LB	***LB Agar***	***LB Soft Agar***
25g LB Powder	as for LB	as for LB
-	12g Agar Powder	6g Agar Powder

V.2 Minimal media. As a minimal media we used M9, M9 Agar, and M9 Soft Agar supplemented with casamino acids (CA) as a source of nitrogen and sulphur, and glucose (Glc) as the main source of carbon (see SUBSECTION V.3 for further information about the stocks of glucose and casamino acids).

Non-supplemented M9 (M9 salts) was prepared by mixing two components, A and B. I prepared each of these components as described in TABLE S.2, using deionised water for a total volume of 1 litre. For convenience, we prepared a stock of M9 salts fifty times concentrated (50X), and autoclaved at 121^{o}C for 20min. When required, we diluted accordingly in deionised water a mixture containing equal volumes of each component to prepare M9 salts (1X). This new solution was also autoclaved at 121^{o}C

for 20min prior to use.

To prepare M9 Agar and M9 Soft Agar, we added the same quantity of Agar powder as described in TABLE S.1 to 1 litre of M9 salts (1X), and autoclaved at 121^{o}C for 20min prior to use.

TABLE S.2. Recipe for M9 minimal media 50X

Component A	***Amount***	***Supplier***	***Component B***	***Amount***	***Supplier***
K_2HPO_4	350g	Sigma (P3786)	Trisodium Citrate	29.4g	Sigma (S1804)
KH_2HPO_4	100g	Sigma (P9791)	$(NH_4)_2SO_4$	50g	Sigma (A4418)
–	–	–	$MgSO_4$	10.45g	Fisher Scientific (M/1050/53)

V.3 Stock solutions for glucose and casamino acids. We supplemented M9 salts (1X), M9 salts (1X) Agar, and M9 salts (1X) Soft Agar with two specific nutrients: glucose and casamino acids. I diluted different proportions of glucose and casamino acids in 1 litre of M9 salts (1X) to prepare two different stocks of 20% glucose (200mg/mL) as described below.

TABLE S.3. Recipe for stocks of 20% glucose

Component	***10% CA***	***5% CA***	***Supplier***
Glucose	200g	200g	Fisher Scientific (G/0500/53)
Casamino acids	100g	50g	Duchefa (C1301.0250)

Both glucose and casamino acids are thermolabile substances. Consequently, we filter sterilised these stock solutions, and not autoclaved, to prevent degradation. When required, we added aseptically the appropriate volume of stock to either M9 salts (1X), M9 salts (1X) Agar, or M9 salts (1X) Soft Agar.

Typically, the media used in the experiments was M9 salts (1X) supplemented with 0.2% (2mg/mL) of glucose, and 0.1% (1mg/mL) of casamino acids.

VI ANTIBIOTICS

During the experiments presented in this thesis, we used a number of different clinically relevant antibiotics. Erythromycin (Ery), doxycycline (Dox), and tetracycline

(Tet) are used to treat infectious diseases produced by pathogens such as *Neisseria gonorrhoeae*, *Vibrio cholera*, meticillin-resistant *Staphylococcus aureus* (MRSA), multidrug-resistant *Acinetobacter baumannii*, among others.[123–129]

TABLE S.4. Antibiotic stock solutions, and typical working dilutions.

Drug	Solvent	Stock solution	Working dilution	*Supplier*
Erythromycin	Pure Ethanol	$10\text{mg} \cdot \text{mL}^{-1}$	$1 / 0.5 / 0.03\text{mg} \cdot \text{mL}^{-1}$	Duchefa (E0122.0010)
Doxycycline	Water	$5\text{mg} \cdot \text{mL}^{-1}$	$8 \times 10^{-3} / 8 \times 10^{-4}\text{mg} \cdot \text{mL}^{-1}$	Sigma (D9891-5G)
Tetracycline	Water	$5\text{mg} \cdot \text{mL}^{-1}$	$8 \times 10^{-3} / 8 \times 10^{-4}\text{mg} \cdot \text{mL}^{-1}$	Duchefa (T0150.0025)

We prepared stock solutions for Ery, Dox and Tet as described in TABLE S.4 (above), using pure ethanol or deionised water for a volume of 10mL. The stock solutions were stored at -20^{o}C as recommended by the manufacturer, the solutions for Dox and Tet being filter sterilised and aliquoted. To prepare the working dilutions, samples from these stock solutions were diluted accordingly using the same media that would later be used for the experiment. The working dilution was further diluted in media to prepare the final concentrations of the antibiotic.

VI.1 Dilution of antibiotic stock solutions. We typically used ten different concentrations of antibiotic. To avoid over- or mis-representation of a concentration (i.e. too many low concentrations or too few high concentrations), we prepared the antibiotic as it follows: we defined ten concentrations, $\boldsymbol{c} = (1, \dots, 10)$, the highest concentration being denoted by h, and the lowest concentration being denoted by $l = h \cdot 10^{-1}$. The final concentration is calculated as $l \times \boldsymbol{c}$. We defined this range after several iterations in which the stock solution of antibiotic was diluted 10, 100 and 1000 times. The density of the cultures was measured using the filter-based microplate reader ELX808 from BioTek for CHAPTER 2 and the monochromator-based microplate reader Tecan Infinite 200 PRO for CHAPTERS 2, 3 and 5. The cultures were read in 96-wells microplates by Greiner bio-one (655101).

The working dilution was diluted accordingly using the same media used in the experiment for a volume of 10mL.

VII Plate readers protocols

The plate readers were programmed to perform the following steps.

VII.1 BioTek ELX808.

- Set temperature at 30^{o}C.
- Kinetic Window (length of experiment): 24h, with readings every 20min.

    - Shaking time: 300s (5min). Shaking strength: medium (strength options are low, medium and high). With high culture droplets can be found on the lids.

    - Read using the 600nm filter.

The plate reader iterates the steps within the kinetic loop (shaking and reading), shaking for 5min to homogenise the culture, reading, and then leaving the cultures at 30^{o}C for ≈15min (20min total).

VII.2 Tecan Infinite 200 PRO.

- Set temperature at 30^{o}C.
- Kinetic Window (length of experiment): 24h, with readings every 20min.

    - Shaking time: 300s (5min). Shaking: linear at 680rpm.

    - Read each well once at 600nm in a 2x2 matrix, 1450µm from the border.

The plate reader iterates the steps within the kinetic loop (shaking and reading), shaking for 5min to homogenise the culture, reading, and then leaving the cultures at 30^{o}C for ≈15min (20min total). Reading each well in four different points (2x2 matrix) reduced the noise of the data.

VIII Strains

On reception, all the strains used for this thesis were grown overnight (>16h) in 10mL of M9 salts (1X) supplemented with 0.2% Glc and 0.1% CA, at 30^{o}C and 180rpm. We froze three samples at −80^{o}C after adding 500µL of 80% glycerol for a total volume of 1.5mL.

IX Microbiological techniques

IX.1 Cell culture.

TABLE S.5. Strains of *Escherichia coli*. The strain TB108 was kindly provided by Dr. Tobias Bergmiller. The strain eTB108 is an evolved sample of TB108 after six transfers in media containing 10µg/mL of erythromycin.

Strain	***Genotype***	***Reference***
E. coli AG100	K–12 *argE3 thi–1 rpsL xyl mtl* Δ*(gal-uvrB) supE44*	68
E. coli MG1655	K–12 *F-* λ*- ilvG0 rfb–50 rph–1*	130
E. coli MC4100	*F- [araD139]*$_{B/r}$ Δ*(argF–lac)169* λ*- e14- flhD5301* Δ*(fruK–yeiR)725(fruA25) relA1 rpsL150(strR) rbsR22* Δ*(fimb–fimE)632(::IS1) deoC1*	131
E. coli AG100–A	AG100 Δ*acrAB::Tn903*	68
E. coli Wyl	MC4100 *galK::YFP*, amp^R, pCS-λ	84
E. coli GB(c)	MC4100 *galK::CFP*, amp^R, pGW155B	85
E. coli TB108	MG1655 *acrB–sfGFP–FRT*	Unpublished
E. coli eTB108	MG1655 *acrB–sfGFP–FRT* ± ***?***	This thesis

IX.1.1 Solid media. A frozen sample was taken using a flamesterilised loop, and spread over a Petri dish containing 25mL of sterile, antibioticfree LB Agar. This Petri dish was incubated overnight at 30^{o}C, and the resulting colonies were picked to perform tests and calibrations described in the following sections.

IX.1.2 Liquid media. A frozen sample, or a colony in solid LB Agar, was taken using a flamesterilised loop and spread in the corresponding liquid media. This media was typically M9 supplemented with different concentrations of Glc, CA, and the appropriate antibiotic if required. 10mL of this media was inoculated in a universal tube (30mL), incubated in aerated conditions overnight at 30^{o}C.

IX.2 Colony counting. To quantify the number of colony forming units (CFUs) 0.1mL from a liquid culture was diluted in 100-fold or 10-fold dilutions, depending on the culture's optical density measured at 600nm. In triplicate, a 0.1mL droplet from the final dilution, ranging typically from 10^{-5} to 10^{-9}, was mixed in a Petri dish with 25mL of sterile LB Soft Agar. The cultures were incubated overnight at 37 ^{o}C.

Photos of these Petri dishes were taken and processed computationally with a

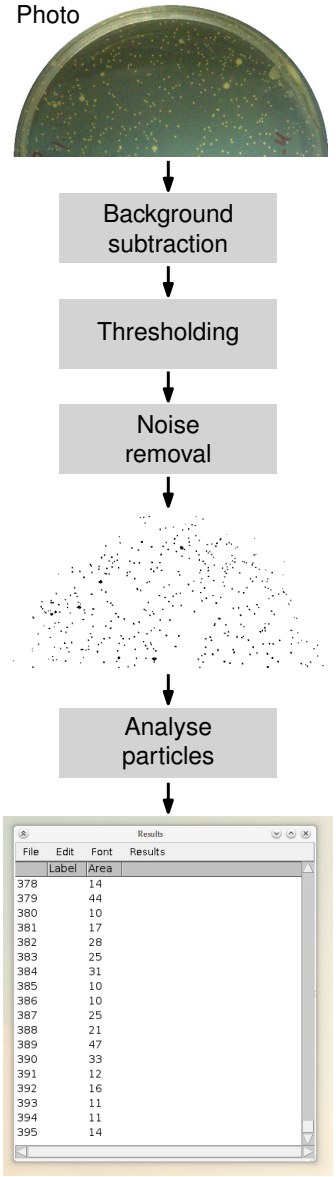

FIGURE S.19. Algorithm designed to count CFUs from photographs using ImageJ.

routine created in ImageJ[132] (FIG. S.19). The cell density in the original culture was calculated using the following formula, assuming that each colony is developed from a single bacterial cell:

$$\text{Density (Cells} \cdot \text{mL}^{-1}) = \frac{\text{Colonies}}{\text{Dilution Factor}} \times 10 \tag{S.2}$$

X CALIBRATIONS

X.1 Fluorescence. Upon reception of a fluorescent strain we reviewed the literature, including original publication, to find the appropriate wavelenghts (λ) for excitation (λ_{ex}) and emission (λ_{em}) of the corresponding fluorochrome. When the appropriates wavelengths were not provided, an overnight culture of the fluorescent strain was screened in the monochromator-based reader by Tecan.

Once λ_{ex} and λ_{em} were known, we compared the fluorescence from overnight cultures of the corresponding fluorescence strains with that coming from a parental, non-fluorescent strain. Three replicates of 150µL each were read in a 96-well microplate and read at 505nm/540nm to measure the fluorescence produced by the yellow fluorescence protein (emission/excitation wavelengths), and at 430nm/480nm for the cyan fluorescent protein. No fluorescence was detected in the non-fluorescent parental strain. Therefore the fluorescence detected comes from the corresponding fluorescent protein and not by another protein or by metabolic byproduct.

X.2 Dose-response curve. In SUBSECTION VI.1, we introduced how we defined the range of concentrations of the antibiotic to be used. To define the highest concentration, h, we prepared the concentrations in $\boldsymbol{c}$ from increasing 10-fold dilutions of the stock solution of antibiotic. If c_h is the highest concentration at which we observed growth during this process, we interpolated the concentrations of antibiotic between 0 and the concentration c_{h+1} until we could observe the transition from maximum growth to lack thereof.

Once we identified the range of concentrations, $\boldsymbol{c}$, we prepared the corresponding number of 96-well microplates depending on the length of the experiment. If several days were required, we used a 96-pin replicator to transfer the culture from a previous 96-well microplate.

X.3 Quantitative PCR (qPCR).

X.3.1 DNA extraction. The DNA from 10 mL of culture was processed with the DNA extraction kit 'GeneJET' (ThermoScientific #K0729), and quantified using the 'Qubit' system. The DNA extracts were later diluted accordingly to normalise the concentration

TABLE S.6. Primers and probes designed using 'Primer3'. Amplicon ranging from 100 to 141bp. T_m indicates the estimated melting temperature.

Target gen	Sequence (5′ → 3′)	T_m (^oC)	Feature
tatB	CGATGAAGCGTTCCTACGTT	60.27	Forward
	TCATGCGCAGCTTCATTATC	59.94	Reverse
	AAGGCGAGCGATGAAGCGCA	70.70	Probe
tet(36)	ATTGGGCATCTATTGGCTTG	59.22	Forward
	CCGATTCACAGGCTTTCTTG	60.76	Reverse
	AGCCTTTGCCAATTGGGGCG	70.37	Probe

of DNA across the samples, so we have the same concentration of DNA in every sample.

X.3.2 Primers and probes. Upon reception, primers and probes were diluted in sterile, DNAse-free deionised water pH 8.0, to prepare 25pmol/µL stocks. We later aliquoted, and stored at -20^oC these stocks. Probes are molecular beacons, tagged with the fluorochrome HEX in 5′, and the quencher BHQ1 in 3′.

The Primers and probes were designed using PRIMER3 as implemented in UGENE.[133] We targeted *tatB* as a chromosomal reference using the reference genome sequence for the bacterium *Escherichia coli* strain MG1655 (NCBI reference sequence: NC_000913.2). For the plasmid pGW155B, we targeted the locus *tet(36)* using a reference sequence published elsewere.[134] The sequences in TABLE S.6 where tested by PCR and qPCR against so-called no template controls (NTC), containing no DNA, and strains of *E. coli* lacking the aforementioned plasmid. The efficiency of the reaction is close to 100% (FIG. S.20) and therefore the material for these loci is considered to double per cycle.[135]

X.3.3 Reaction mix. The qPCR reaction mix was prepared as detailed by the manufacturer for the 'Luminaris Color Probe Low ROX' kit (ThermoScientific #K0342, see TABLE S.7), and we calculated the volume required for the primers following the EQUATION S.3.

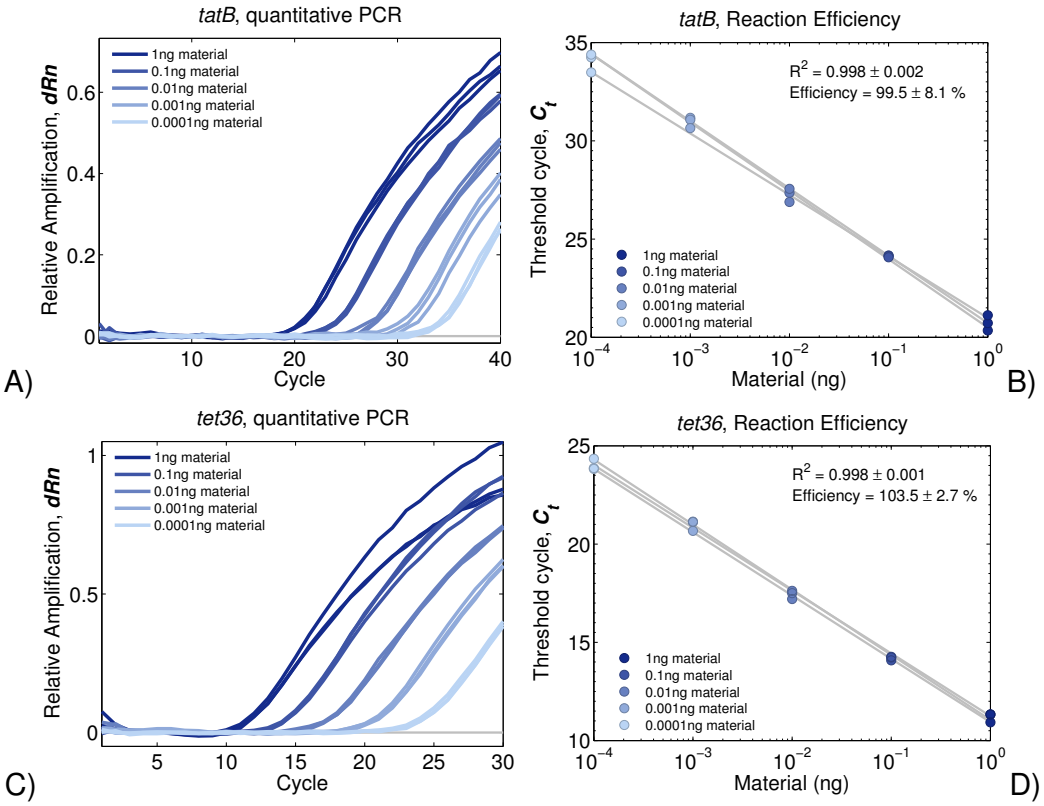

FIGURE S.20. Baseline corrected, normalised amplification curves (dRn) for the chromosomal locus *tatB* (**A**), followed by that for the plasmid-borne locus *tet(36)* (**C**). The efficiency of the qPCR for each loci, in subplots **B** and **D**, shows the efficiency of the reaction (E_f) calculated as $E_f = 10^{-1/Slope} - 1$.

$$M = \frac{mol}{vol(L)} \rightarrow mol = \underbrace{10^{-7}M}_{0.1\mu M} \cdot (\underbrace{2 \cdot 10^{-5}L}_{20\mu L}) = \underbrace{2 \cdot 10^{-12}mol}_{2pmol} \tag{S.3}$$

Therefore, the concentrations for the primers specified in TABLE S.7 correspond to 6pmol or 0.24µL from the 25pmol stock solutions; whereas for the probe 4pmol or 0.16µL from such stocks. The qPCR was set up using the conditions described in TABLE S.8.

TABLE S.7. Recommended recipe for Luminaris Color Probe Low ROX (ThermoScientific).

Component	**Volume (µL)**
PCR Master Mix	10
Primer F	Final Concentration = 0.3µM
Primer R	Final Concentration = 0.3µM
Probe	Final Concentration = 0.2µM
Template DNA	$\leqslant$ 200ng per reaction
Nuclease-free Water	to 20

TABLE S.8. qPCR thermal cycling conditions.

Step	**Temperature (^{o}C)**	**Time (min)**	**N. of cycles**
UDG pre-treatment	50	2	1
Enzyme activation	95	10	1
Denaturation	94	0.5	
Annealing	60	0.5	} 40
Extension	72	1	
Final Extension	72	10	1

X.4 Spatial plates. We performed the spatial plates on Petri dishes containing M9 (1X) soft agar supplemented with 0.2% glucose (w/v) and 0.1% casamino acids (w/v), inoculated with of an overnight culture (0.1mL per litre). The centre of the Petri dish was surgically removed with a sterile universal tube, and refilled with non-inoculated media containing 64µg/mL of the antibiotic doxycycline. This plate was incubated at 30^{o}C in a device developed as part of this PhD project, and photos were taken during 5 days at 2h intervals. These photos were later analysed with a routine coded using Matlab.

ADDENDA

XI ADDITIONAL ANALYSIS FOR CHAPTER 2

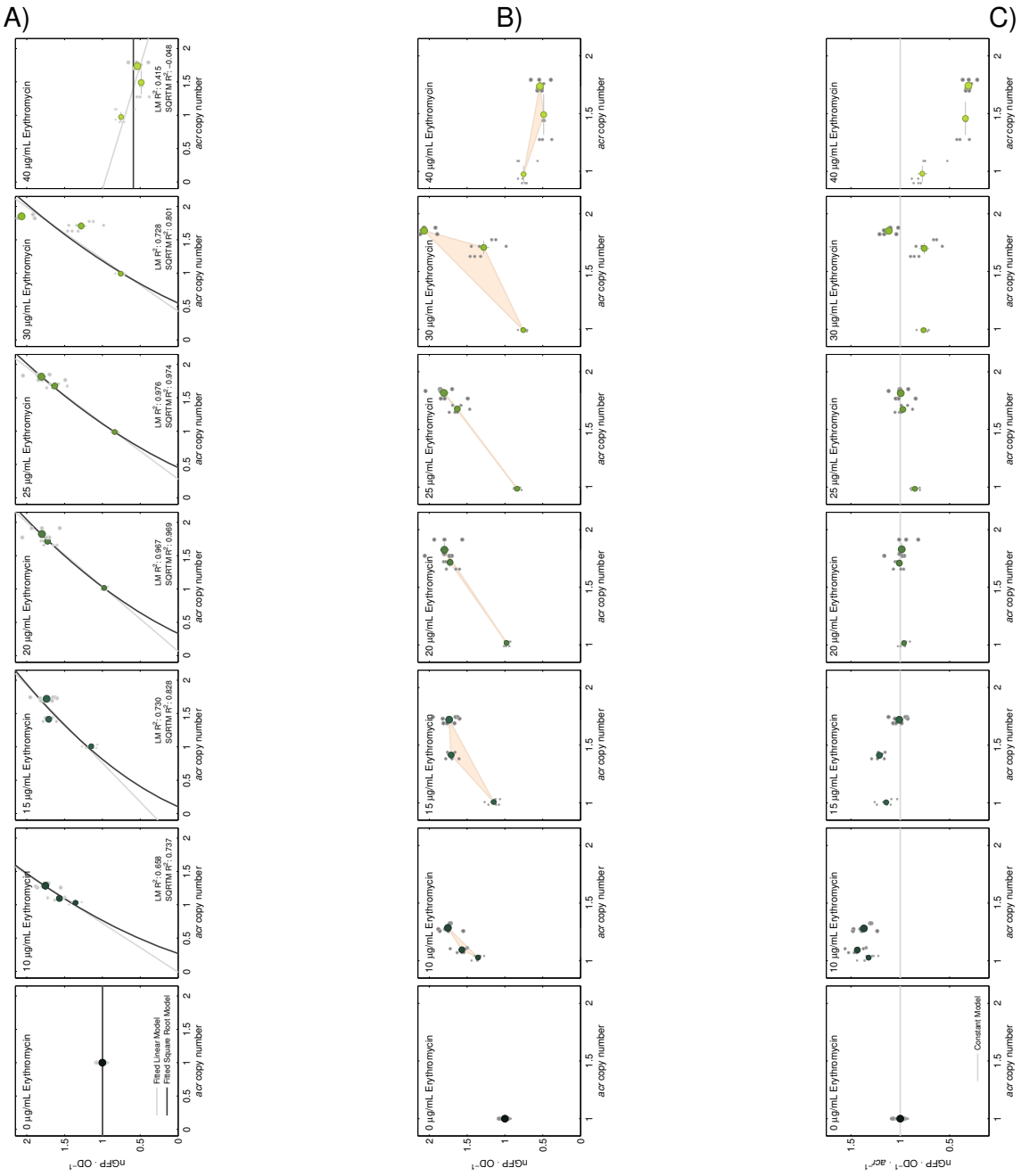

FIGURE S.21. A) Representation of the relative abundance of efflux pumps ($nGFP^{-1} \cdot OD^{-1}$), on the $y-$axis, as a function of *acr* operon copy number on the $x-$axis during the first five days of the experiment. The raw data is represented as grey dots and their size indicates if the culture was sampled after one, five or seven days of growth. Mean ± standard error of the mean shown in green and grey, respectively. The dataset is compared to the predictions from a linear (light grey) and square root (dark grey, model in p. 72) models. The goodness of fit was quantified using R^2. **B)** Concavity analysis (orange) using the `convhull` function in `matlab`. The hull highlights a transition, from a concave to convex, in the relationship between the relative abundance of efflux pumps per operon copy number. This transition is also captured when the relative expression of efflux pumps per *acr* operon is considered (**C**). Further genomic analysis will reveal the specific mutations responsible for the transition.

XII Additional Analysis for Chapter 3

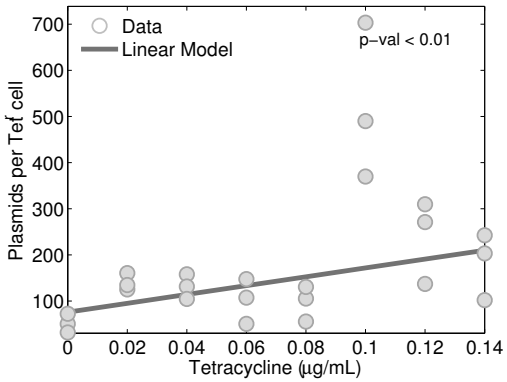

Figure S.22. Relative copies of the plasmid pGW155B per cell of Tet^r after 120h of coculture with Tet^r. We robustly fitted the linear model $y = a + bx$ where the 95% confidence interval for a is (8.68, 153.07) and for b is (143.33, 1762.40), with $R^2_{adj} = 0.307$. The number of plasmids per cell has increased through time and the increase was stronger with higher dosages of tetracycline. This observation is compatible with the model in Equation 3.2.

XIII Additional Analysis for Chapter 5

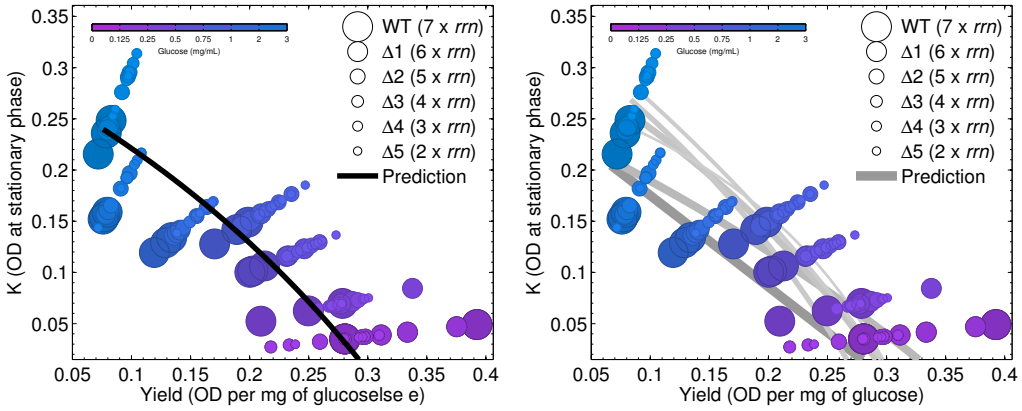

Figure S.23. Left) Relationship between carrying capacity (K), on the $y-$axis and cell yield, on the $x-$axis. Overall, there is a negative correlation between K and yield that is approximately linear as shown by the model in Equation 5.2 (black). In **Right)** we show the prediction per strain. We observed that higher population densities were achieved in conditions that led to low cell yield, such as a high concentration of glucose. However, the model does not capture the role of the *rrn* operons: the highest population size were achieved with 7-6 copies of this operon with low concentrations of glucose, but with more glucose the highest population sizes were achieved with fewer of these operons.

REFERENCES

1. Ehrlich, P. Address in Pathology: on Chemotherapy. *Br. Med. J.* **2**, 353–359 (1913).

2. Walsh, C. T. & Wencewicz, T. A. Prospects for new antibiotics: a molecule-centered perspective. *J. Antibiot.* **67**, 7–22 (2014).

3. Borman, E. K. Comparative studies on the natural and acquired resistance of certain strains of Escherichia Coli to the bacteriostatic and germicidal effects of cations. *J. Bacteriol.* **23**, 315 (1932).

4. Neu, H. C. The crisis in antibiotic resistance. *Science* **257**, 1064–1073 (1992).

5. *Antimicrobial resistance: global report on surveillance* (World Health Organization, 2014).

6. Bush, K. *et al.* Tackling antibiotic resistance. *Nat. Revs. Microbiol.* **9**, 894–896 (2011).

7. Garrod, L. P. Reactions of bacteria to chemotherapeutic agents. *Br. Med. J.* **1**, 205 (1951).

8. Annotations: Antibiotic Treatment of Boils. *Br. Med. J.* **2**, 98–103 (1958).

9. Ehrlich, P. The Barben Lectures ON EXPERIMENTAL RESEARCHES ON SPECIFIC THERAPEUTICS. *The Lancet* **169**, 1634–1636 (1907).

10. Garrod, L. P. Action of Penicillin on Bacteria. *Br. Med. J.* **1**, 107 (1945).

11. Clinical and Laboratory Standards Institute. *Performance Standards for Antimicrobial Susceptibility Testing; Twenty–Second Informational Supplement M100–S22* (2012).

12. Huijben, S. *et al.* Aggressive chemotherapy and the selection of drug resistant pathogens. *PLoS Pathog.* **9**, e1003578 (2013).

13. Alp, E., van der Hoeven, J. G., Verweij, P. E., Mouton, J. W. & Voss, A. Duration of antibiotic treatment: are even numbers odd? *J. Antimicrob. Chemother.* **56**, 441–442 (2005).

14. Tabor, E. & Rice, L. B. Bacteria by the book. *Science* **322**, 853–4 (2008).

15. Bryson, V. & Demerec, M. Bacterial resistance. *The American journal of medicine* **18**, 723–737 (1955).

16. Maccabe, A., Gould, J. & Forfar, J. ERYTHROMYCIN-RESISTANT STAPHYLOCOCCUS AUREUS. *The Lancet* **278**, 7–9 (1961).

17. Baquero, F. & Negri, M.-C. Challenges: Selective compartments for resistant microorganisms in antibiotic gradients. *Bioessays* **19**, 731–736 (1997).

18. Zhao, X. & Drlica, K. Restricting the selection of antibiotic-resistant mutants: a general strategy derived from fluoroquinolone studies. *Clin. Infect. Dis.* **33**, S147–S156 (2001).

19. Gullberg, E. *et al.* Selection of resistant bacteria at very low antibiotic concentrations. *PLoS Pathog.* **7**, e1002158 (2011).

20. Wright, S. Evolution in Mendelian populations. *Genetics* **16**, 97–159 (1931).

21. Fisher, R. A. The Distribution of Gene Ratios for Rare Mutations. *Proceedings of the Royal Society of Edinburgh* **50**, 205–220 (1930).

22. Wright, S. Statistical theory of evolution. *J. Am. Stat. Assoc.* **26**, 201–208 (1931).

23. Kimura, M. Process leading to quasi-fixation of genes in natural populations due to random fluctuation of selection intensities. *Genetics* **39**, 280 (1954).

24. Wright, S. Genic and organismic selection. *Evolution* 825–843 (1980).

25. Wargo, A. R., Huijben, S., de Roode, J. C., Shepherd, J. & Read, A. F. Competitive release and facilitation of drug-resistant parasites after therapeutic chemotherapy in a rodent malaria model. *Proc. Natl. Acad. Sci. U.S.A.* **104**, 19914–19919 (2007).

26. Read, A. F., Day, T. & Huijben, S. The evolution of drug resistance and the curious orthodoxy of aggressive chemotherapy. *Proc. Natl. Acad. Sci. U.S.A.* **108**, 10871–10877 (2011).

27. Ankomah, P. & Levin, B. R. Exploring the collaboration between antibiotics and the immune response in the treatment of acute, self-limiting infections. *Proc. Natl. Acad. Sci. U.S.A.* **111**, 8331–8338 (2014).

28. Brown, R., Sands, M. & Ryczak, M. Community-acquired pneumonia caused by mixed aerobic bacteria. *CHEST Journal* **90**, 810–814 (1986).

29. Rice, T. W. *et al.* Critical illness from 2009 pandemic influenza a (h1n1) virus and bacterial co-infection in the united states. *Crit. Care Med.* **40**, 1487 (2012).

30. Maggi, R. G., Mascarelli, P. E., Havenga, L. N., Naidoo, V. & Breitschwerdt, E. B. Co-infection with anaplasma platys, bartonella henselae and candidatus mycoplasma haematoparvum in a veterinarian. *Parasit Vectors* **6**, 103 (2013).

31. Shahidi, A. & Ellner, P. D. Effect of mixed cultures on antibiotic susceptibility testing. *Applied Microbiology* **18**, 766–770 (1969).

32. Pope, C. F., McHugh, T. D. & Gillespie, S. H. Methods to determine fitness in bacteria. In *Antibiotic Resistance Protocols*, 113–121 (Springer, 2010).

33. Nilsson, A. I. *et al.* Reducing the fitness cost of antibiotic resistance by amplification of initiator trna genes. *Proc. Natl. Acad. Sci. U.S.A.* **103**, 6976–6981 (2006).

34. Rosenthal, A. Z. & Elowitz, M. B. Following evolution of bacterial antibiotic resistance in real time. *Nat. Genet.* **44**, 11–13 (2012).

35. Day, T., Huijben, S. & Read, A. F. Is selection relevant in the evolutionary emergence of drug resistance? *Trends in Microbiology* **23**, 126–133 (2015).

36. Andersson, D. I. & Hughes, D. Antibiotic resistance and its cost: is it possible to reverse resistance? *Nat. Revs. Microbiol.* **8**, 260–271 (2010).

37. Torres, J. Natural selection and thermodynamic optimality. *Nuovo Cimento.* **13**, 177–185 (1991).

38. Pfeiffer, T., Schuster, S. & Bonhoeffer, S. Cooperation and competition in the evolution of ATP-producing pathways. *Science* **292**, 504–507 (2001).

39. Kaczanowska, M. & Ryden-Aulin, M. Ribosome biogenesis and the translation process in escherichia coli. *Microbiol. Mol. Biol. Rev.* **71**, 477–494 (2007).

40. Marr, A. Growh rate of escherichia coli. *Microbiol. Rev.* **55**, 316–333 (1991).

41. Bollenbach, T., Quan, S., Chait, R. & Kishony, R. Nonoptimal microbial response to antibiotics underlies suppressive drug interactions. *Cell* **139**, 707–718 (2009).

42. Meyer, J. R., Gudelj, I. & Beardmore, R. Biophysical mechanisms that maintain biodiversity through trade-offs. *Nat. Commun.* **6**, 6278 (2015).

43. Blair, J. M., Webber, M. A., Baylay, A. J., Ogbolu, D. O. & Piddock, L. J. Molecular mechanisms of antibiotic resistance. *Nat. Revs. Microbiol.* **13**, 42–51 (2015).

44. Alekshun, M. N. & Levy, S. B. Molecular mechanisms of antibacterial multidrug resistance. *Cell* **128**, 1037–1050 (2007).

45. Murakami, S., Nakashima, R., Yamashita, E. & Yamaguchi, A. Crystal structure of bacterial multidrug efflux transporter AcrB. *Nature* **419**, 587–593 (2002).

46. Eagle, H. A Paradoxical Zone Phenomenon in the Bactericidal Action of Penicillin in Vitro. *Science* **107**, 44–45 (1948).

47. Yourassowsky, E., Vanderlinden, M. P., Lismont, M. J. & Schoutens, E. Paradoxical action of penicillin G on Staphylococcus aureus: a time study of the effect of a zonal antibiotic concentration gradient on bacterial growth. *Antimicrob. Agents Chemother.* **8**, 262–5 (1975).

48. Shah, P. M. Paradoxical effect of antibiotics. I. The'Eagle effect'. *J. Antimicrob. Chemother.* 259–60 (1982).

49. Annear, D. Paradoxical effect of antibiotics II. Comment and bibliography. *J. Antimicrob. Chemother.* **10**, 260–262 (1982).

50. Nikaido, H. Multiple antibiotic resistance and efflux. *Curr. Opin. Microbiol.* **1**, 516–523 (1998).

51. Webber, M. & Piddock, L. The importance of efflux pumps in bacterial antibiotic resistance. *J. Antimicrob. Chemother.* **51**, 9–11 (2003).

52. Du, D. *et al.* Structure of the AcrAB-TolC multidrug efflux pump. *Nature* **509**, 512–515 (2014).

53. Piddock, L. J. Multidrug-resistance efflux pumps? not just for resistance. *Nat. Revs. Microbiol.* **4**, 629–636 (2006).

54. Murakami, S., Nakashima, R., Yamashita, E., Matsumoto, T. & Yamaguchi, A. Crystal structures of a multidrug transporter reveal a functionally rotating mechanism. *Nature* **443**, 173–179 (2006).

55. Alekshun, M. N. & Levy, S. B. Regulation of chromosomally mediated multiple antibiotic resistance: the mar regulon. *Antimicrob. Agents. Chemother.* **41**, 2067 (1997).

56. Ma, D., Alberti, M., Lynch, C., Nikaido, H. & Hearst, J. E. The local repressor AcrR plays a modulating role in the regulation of acrAB genes of Escherichia coli by global stress signals. *Molecular microbiology* **19**, 101–112 (1996).

57. Magnusson, L. U., Farewell, A. & Nyström, T. ppGpp: a global regulator in Escherichia coli. *Trends Microbiol.* **13**, 236–42 (2005).

58. Nunoshiba, T., Hidalgo, E., Cuevas, C. A. & Demple, B. Two-stage control of an oxidative stress regulon: the Escherichia coli SoxR protein triggers redox-inducible expression of the soxS regulatory gene. *J. Bacteriol.* **174**, 6054–6060 (1992).

59. Delisa, M. P., Valdes, J. J. & Bentley, W. E. Mapping stress-induced changes in autoinducer AI-2 production in chemostat-cultivated Escherichia coli K-12. *J. Bacteriol.* **183**, 2918–2928 (2001).

60. Jung, I. L., Phyo, K. H. & Kim, I. G. RpoS-mediated growth-dependent expression of the Escherichia coli tkt genes encoding transketolases isoenzymes. *Curr. Microbiol.* **50**, 314–8 (2005).

61. Kakeda, M., Ueguchi, C., Yamada, H. & Mizuno, T. An Escherichia coli curved DNA-binding protein whose expression is affected by the stationary phase-specific sigma factor sigma S. *Mol. Gen. Genet.* **248**, 629–34 (1995).

62. Xu, J. & Johnson, R. C. Identification of genes negatively regulated by Fis: Fis and RpoS comodulate growth-phase-dependent gene expression in Escherichia coli. *J. Bacteriol.* **177**, 938–47 (1995).

63. Martin, R. G. & Rosner, J. L. Fis, an accessorial factor for transcriptional activation of the mar (multiple antibiotic resistance) promoter of Escherichia coli in the presence of the activator MarA, SoxS, or Rob. *J. Bacteriol.* **179**, 7410–9 (1997).

64. Domain, F., Bina, X. R. & Levy, S. B. Transketolase A, an enzyme in central metabolism, derepresses the marRAB multiple antibiotic resistance operon of Escherichia coli by interaction with MarR. *Mol. Microbiol.* **66**, 383–94 (2007).

65. Alekshun, M. N. & Levy, S. B. The mar regulon: multiple resistance to antibiotics and other toxic chemicals. *Trends in microbiology* **7**, 410–413 (1999).

66. Wei, Y., Lee, J.-M., Smulski, D. R. & LaRossa, R. A. Global impact of sdiA amplification revealed by comprehensive gene expression profiling of Escherichia coli. *J. Bacteriol.* **183**, 2265–2272 (2001).

67. Rahmati, S., Yang, S., Davidson, A. L. & Zechiedrich, E. L. Control of the AcrAB multidrug efflux pump by quorum-sensing regulator SdiA. *Molecular Microbiology* **43**, 677–685 (2002).

68. Cohen, S. P., Levy, S. B., Foulds, J. & Rosner, J. L. Salicylate induction of antibiotic resistance in Escherichia coli: activation of the mar operon and a mar-independent pathway. *J. Bacteriol.* **175**, 7856–62 (1993).

69. Hegreness, M., Shoresh, N., Damian, D., Hartl, D. & Kishony, R. Accelerated evolution of resistance in multidrug environments. *Proc. Natl. Acad. Sci. U.S.A.* **105**, 13977–13981 (2008).

70. Peña-Miller, R., Lähnemann, D., Schulenburg, H., Ackermann, M. & Beardmore, R. Selecting against antibiotic-resistant pathogens: Optimal treatments in the presence of commensal bacteria. *Bull. Math. Biol.* **74**, 908–934 (2012).

71. Van Bambeke, F., Balzi, E. & Tulkens, P. M. Antibiotic efflux pumps. *Biochemical pharmacology* **60**, 457–470 (2000).

72. Nierlich, D., Rutter, W. & Fox, C. *Molecular Mechanisms in the Control of Gene Expression*. ICN-UCLA symposia on molecular and cellular biology (Elsevier Science, 2013). Fig. 3 in p.139.

73. Shampine, L. F. & Reichelt, M. W. The matlab ode suite. *SIAM J. Sci. Comput.* **18**, 1–22 (1997).

74. Pena-Miller, R. *et al.* When the most potent combination of antibiotics selects for the greatest bacterial load: the smile-frown transition. *PLoS Biol.* **11**, e1001540 (2013).

75. Goutelle, S. *et al.* The Hill equation: a review of its capabilities in pharmacological modelling. *Fundam. Clin. Pharmacol.* **22**, 633–648 (2008).

76. Benveniste, R. & Davies, J. Mechanisms of antibiotic resistance in bacteria. *Annu. Rev. Biochem.* **42**, 471–506 (1973).

77. Jinks, J. Competitive suppression and the determination of linkage in micro-organisms. *Nature* (1952).

78. Moore, G. T. Microorganisms of the soil. *Science* **36**, 609–616 (1912).

79. Conn, H. The distribution of bacteria in various soil types. *Agron J* **5**, 218–221 (1913).

80. Kellerman, K. F. & Leonard, L. T. The prevalence of bacillus radicicola in soil. *Science* **38**, 95–98 (1913).

81. Hibbing, M. E., Fuqua, C., Parsek, M. R. & Peterson, S. B. Bacterial competition: surviving and thriving in the microbial jungle. *Nat. Revs. Microbiol.* **8**, 15–25 (2010).

82. Edlund, C. & Nord, C. Effect on the human normal microflora of oral antibiotics for treatment of urinary tract infections. *J. Antimicrob. Chemother.* **46 Suppl 1**, 41–48 (2000).

83. Pérez-Cobas, A. E. *et al.* Gut microbiota disturbance during antibiotic therapy: a multi-omic approach. *Gut* **62**, 1591–1601 (2013).

84. Chait, R., Craney, A. & Kishony, R. Antibiotic interactions that select against resistance. *Nature* **446**, 668–671 (2007).

85. Chait, R., Shrestha, S., Shah, A. K., Michel, J.-B. & Kishony, R. A Differential Drug Screen for Compounds That Select Against Antibiotic Resistance. *PLOS One* **5**, e15179. doi:10.1371/journal.pone.0015179 (2010).

86. Milne, S. W., Cheetham, J., Lloyd, D., Aves, S. & Bates, S. Cassettes for pcr-mediated gene tagging in candida albicans utilizing nourseothricin resistance. *Yeast* **28**, 833–841 (2011).

87. Andersson, D. I. & Levin, B. R. The biological cost of antibiotic resistance. *Curr. Opin. Microbiol.* **2**, 489–493 (1999).

88. Shampine, L. F. & Gordon, M. K. *Computer solution of ordinary differential equations: the initial value problem* (WH Freeman San Francisco, 1975).

89. Koch Gudrun *et al.* Evolution of Resistance to a Last-Resort Antibiotic in Staphylococcus aureus via Bacterial Competition. *Cell* **158**, 1060–1071 (2015).

90. Ghosh, S. K., Hajra, S., Paek, A. & Jayaram, M. Mechanisms for chromosome and plasmid segregation. *Annu. Rev. Biochem.* **75**, 211–241 (2006).

91. Millán, A. S. *et al.* Positive selection and compensatory adaptation interact to stabilize non-transmissible plasmids. *Nat. Commun.* **5** (2014).

92. Pakyz, A. *et al.* Diversity of antimicrobial use and resistance in 42 hospitals in the united states. *Pharmacotherapy* **28**, 906–912 (2008).

93. Sarraf-Yazdi, S. *et al.* A 9-year retrospective review of antibiotic cycling in a surgical intensive care unit. *J. Surg. Res.* **176**, e73–e78 (2012).

94. White, R. L., Burgess, D. S., Manduru, M. & Bosso, J. A. Comparison of three different in vitro methods of detecting synergy: time-kill, checkerboard, and e test. *Antimicrob. Agents. Chemother.* **40**, 1914–8 (1996).

95. Toprak, E., Veres, A., Michel, J.-B., Chait, R. & Kishony, R. Evolutionary paths to antibiotic resistance under dynamically sustained drug selection. *Nat. Genet.* **44**, 101–106 (2012).

96. Blair, J. M. *et al.* Acrb drug-binding pocket substitution confers clinically relevant resistance and altered substrate specificity. *Proc. Natl. Acad. Sci. U.S.A.* **112**, 3511–3516 (2015).

97. Li, X.-Z. & Nikaido, H. Efflux-mediated drug resistance in bacteria: an update. *Drugs* **69**, 1555–1623 (2009).

98. Laehnemann, D. *et al.* Genomics of Rapid Adaptation to Antibiotics: Convergent Evolution and Scalable Sequence Amplification. *Genome Biol. Evol.* **6**, 1287–1301 (2014).

99. Connamacher, R. H. & Mandel, H. G. Binding of tetracycline to the 30S ribosomes and to polyuridylic acid. *Biochem. Biophys. Res. Commun.* **20**, 98–103 (1965).

100. Pestka, S. & Lemahieu, R. A. Effect of erythromycin analogues on binding of [(14)c]erythromycin to escherichia coli ribosomes. *Antimicrob. Agents Chemother.* **6**, 479–488 (1974).

101. Kiss, A., Sain, B. & Venetianer, P. The number of rrna genes in escherichia coli. *{FEBS} Lett.* **79**, 77–79 (1977).

102. Acinas, S. G., Marcelino, L. A., Klepac-Ceraj, V. & Polz, M. F. Divergence and redundancy of 16s rrna sequences in genomes with multiple rrn operons. *J. Bacteriol.* **186**, 2629–2635 (2004).

103. Waddell, T. G., Repovic, P., Meléndez-Hevia, E., Heinrich, R. & Montero, F. Optimization of glycolysis: New discussions. *Biochem. Educ.* **27**, 12–13 (1999).

104. Neidhardt, F. C. & Magasanik, B. Studies on the role of ribonucleic acid in the growth of bacteria. *Biochimica et Biophysica Acta* **42**, 99–116 (1960).

105. Reznick, D. Costs of reproduction: an evaluation of the empirical evidence. *Oikos* 257–267 (1985).

106. Bohannan, B., Kerr, B., Jessup, C., Hughes, J. & Sandvik, G. Trade-offs and coexistence in microbial microcosms. *Antonie van Leeuwenhoek* **81**, 107–115 (2002).

107. Angulo-Brown, F., Santillán, M. & Calleja-Quevedo, E. Thermodynamic optimality in some biochemical reactions. *Nuovo Cimento.* **17**, 87–90 (1995).

108. Akaike, H. A new look at the statistical model identification. *IEEE Trans. Automat. Contr.* **19**, 716–723 (1974).

109. Monod, J. *Recherches sur la croissance des cultures bactériennes*. Ph.D. thesis (1941).

110. Monod, J. The growth of bacterial cultures. *Annu. Rev. Microbiol.* **3**, 371–394 (1949).

111. Kjeldgaard, N. O., MaalØe, O. & Schaechter, M. The transition between different physiological states during balanced growth of salmonella typhimurium. *Microbiology* **19**, 607–616 (1958).

112. Koch, A. R. & Deppe, C. S. *In vivo* assay of protein synthesizing capacity of *escherichia coli* from slowly growing chemostat cultures. *J. Mol. Biol.* **55**, 549–562 (1971).

113. Stevenson, B. S. & Schmidt, T. M. Growth rate-dependent accumulation of rna from plasmid-borne rrna operons in escherichia coli. *J. Bacteriol.* **180**, 1970–1972 (1998).

114. MacLean, R. C. & Gudelj, I. Resource competition and social conflict in experimental populations of yeast. *Nature* **441**, 498–501 (2006).

115. Scott, M., Klumpp, S., Mateescu, E. M. & Hwa, T. Emergence of robust growth laws from optimal regulation of ribosome synthesis. *Mol. Syst. Biol.* **10**, 747 (2014).

116. Lotka, A. J. Contribution to the energetics of evolution. *Proc. Natl. Acad. Sci. U.S.A.* **8**, 147–151 (1922).

117. Odum, H. T. & Pinkerton, R. C. Time's speed regulator: The optimum efficiency for maximum output in physical and biological systems. *Am. Sci.* **43**, 331–343 (1955).

118. Wright, S. *The roles of mutation, inbreeding, crossbreeding, and selection in evolution*, vol. 1 (na, 1932).

119. Sanders, C. C. & Sanders, W. E. Emergence of resistance during therapy with the newer beta-lactam antibiotics: role of inducible beta-lactamases and implications for the future. *Rev. Infect Dis.* **5**, 639–648 (1983).

120. Chow, J. W. *et al.* Enterobacter bacteremia: Clinical features and emergence of antibiotic resistance during therapy. *Ann. Intern. Med.* **115**, 585–590 (1991).

121. Thomas, J. K. *et al.* Pharmacodynamic evaluation of factors associated with the development of bacterial resistance in acutely ill patients during therapy. *Antimicrob. Agents Chemother.* **42**, 521–527 (1998).

122. Fleming, S. A. Nobel Lecture: Penicillin. In *Nobel Lectures, Physiology or Medicine 1942-1962* (Elsevier Publishing Company, 1964).

123. Wood, G., Hanes, S., Boucher, B., Croce, M. & Fabian, T. Tetracyclines for treating multidrug-resistant Acinetobacter baumannii ventilator-associated pneumonia. *Intensive Care Medicine* **29**, 2072–2076 (2003).

124. Ruhe, J. J., Monson, T., Bradsher, R. W. & Menon, A. Use of Long-Acting Tetracyclines for Methicillin-Resistant Staphylococcus aureus Infections: Case Series and Rev. Infect Dis.the Literature. *Clin. Infect. Dis.* **40**, 1429–1434 (2005).

125. Wormser, G. P. *et al.* The Clinical Assessment, Treatment, and Prevention of Lyme Disease, Human Granulocytic Anaplasmosis, and Babesiosis: Clinical Practice Guidelines by the Infectious Diseases Society of America. *Clin. Infect. Dis.* **43**, 1089–1134 (2006).

126. Lewis, D. A. & Lukehart, S. A. Antimicrobial resistance in Neisseria gonorrhoeae and Treponema pallidum: evolution, therapeutic challenges and the need to strengthen global surveillance. *Sexually Transmitted Infections* **87**, ii39–ii43 (2011).

127. Kitaoka, M., Miyata, S. T., Unterweger, D. & Pukatzki, S. Antibiotic resistance mechanisms of Vibrio cholerae. *Journal of medical microbiology* **60**, 397–407 (2011).

128. Frank, U. & Tacconelli, E. The Most Frequent Pathogens – Choice of Antibiotics. In *The Daschner Guide to In-Hospital Antibiotic Therapy*, 71–76 (Springer Berlin Heidelberg, 2012).

129. Cunha, B. Oral doxycycline for non-systemic urinary tract infections (UTIs) due to P. aeruginosa and other Gram negative uropathogens. *European journal of clinical microbiology & infectious diseases* 1–4 (2012).

130. Blattner, F. R. *et al.* The Complete Genome Sequence of Escherichia coli K-12. *Science* **277**, 1453–1462 (1997).

131. Casadaban, M. J. Transposition and fusion of the lac genes to selected promoters in Escherichia coli using bacteriophage lambda and Mu. *J. Mol. Biol.* **104**, 541–55 (1976).

132. Abràmoff, M. D., Magalhães, P. J. & Ram, S. J. Image processing with ImageJ. *Biophotonics international* **11**, 36–43 (2004).

133. Okonechnikov, K., Golosova, O., Fursov, M. & the UGENE team. Unipro ugene: a unified bioinformatics toolkit. *Bioinformatics* **28**, 1166–1167 (2012).

134. Whittle, G. *et al.* Identification of a new ribosomal protection type of tetracycline resistance gene, tet(36), from swine manure pits. *Appl. Environ. Microbiol.* **64**, 4151–4158 (2003).

135. Stratagene. *Methods and Applications Guide* (2004).